

**Dynamics of  
isolated quantum many-body systems  
far from equilibrium**

**Dissertation**

zur Erlangung des mathematisch-naturwissenschaftlichen Doktorgrades

*“Doctor rerum naturalium”*

der Georg-August-Universität Göttingen

im Promotionsprogramm ProPhys

der Georg-August University School of Science (GAUSS)

vorgelegt von

**Markus Schmitt**

aus Düsseldorf

Göttingen, 2017

## **Betreuungsausschuss:**

Prof. Dr. Stefan Kehrein,  
Institut für Theoretische Physik,  
Georg-August-Universität Göttingen

Prof. Dr. Reiner Kree,  
Institut für Theoretische Physik,  
Georg-August-Universität Göttingen

## **Mitglieder der Prüfungskommission:**

### *Referent:*

Prof. Dr. Stefan Kehrein,  
Institut für Theoretische Physik,  
Georg-August-Universität Göttingen

### *Korreferent:*

Prof. Dr. Reiner Kree,  
Institut für Theoretische Physik,  
Georg-August-Universität Göttingen

### *2. Korreferent: (kein Mitglied der Prüfungskommission)*

Prof. Dr. Martin Eckstein,  
Institut für Theoretische Physik,  
Friedrich-Alexander-Universität Erlangen-Nürnberg

## **Weitere Mitglieder der Prüfungskommission:**

PD Dr. Salvatore R. Manmana  
Institut für Theoretische Physik,  
Georg-August-Universität Göttingen

Prof. Dr. Stefan Mathias  
I. Physikalisches Institut,  
Georg-August-Universität Göttingen

Prof. Dr. Marcus Müller  
Institut für Theoretische Physik,  
Georg-August-Universität Göttingen

Prof. Dr. Claus Ropers  
IV. Physikalisches Institut,  
Georg-August-Universität Göttingen

**Tag der mündlichen Prüfung: 11. Januar 2018**

“ Meine Fragen über die Physik könnten vielleicht  
den Titel bekommen: Vermächtnisse.  
Man vermacht ja auch Kleinigkeiten. ”

(Georg Christoph Lichtenberg, *Sudelbuch L*)



# Contents

<b>1</b>	<b>Introduction</b>	<b>3</b>
1.1	Experimental realization of unitary dynamics in quantum many-body systems	4
1.2	Quenches, transient dynamics, and thermalization . . . . .	8
1.2.1	From quantum dynamics to statistical physics: Ergodicity, integrability, and thermalization . . . . .	9
1.2.2	Transient dynamics: Spreading of information, the approach to equilibrium, and dynamical phase transitions . . . . .	14
1.3	Entanglement: Boon and bane of quantum many-body theory . . . . .	19
1.3.1	Entanglement and the complexity of many-body states . . . . .	19
1.3.2	Methods for many-body theory . . . . .	20
1.4	Scope and main results of this thesis . . . . .	22
<b>2</b>	<b>Phase transitions beyond equilibrium</b>	<b>25</b>
2.1	Dynamical quantum phase transitions . . . . .	25
2.1.1	<i>Publication:</i> Dynamical quantum phase transitions in the Kitaev honeycomb model . . . . .	30
2.2	Phase transitions in non-equilibrium steady states . . . . .	44
2.2.1	<i>Publication:</i> Universal nonanalytic behavior of the Hall conductance in a Chern insulator at the topologically driven nonequilibrium phase transition . . . . .	46
2.2.2	<i>Publication:</i> Universal nonanalytic behavior of the non-equilibrium Hall conductance in Floquet topological insulators . . . . .	61
<b>3</b>	<b>Quantum dynamics from classical networks</b>	<b>76</b>
3.1	State of the art methods in wave-function-based quantum many-body numerics	77
3.1.1	Exact dynamics in the full Hilbert space . . . . .	77
3.1.2	Matrix product states . . . . .	79
3.1.3	Classical networks . . . . .	85
3.2	<i>Preprint:</i> Quantum dynamics in transverse-field Ising models from classical networks . . . . .	87
<b>4</b>	<b>Irreversibility</b>	<b>113</b>
4.1	Emergence of effective irreversibility despite time reversal invariance . . . . .	114

4.2	<i>Publication:</i> Effective time reversal and echo dynamics in the transverse field Ising model . . . . .	119
4.3	Effective time reversal with perturbed Hamiltonian in generic many-body systems . . . . .	132
4.3.1	The effect of adding interactions . . . . .	132
4.3.2	Decay laws . . . . .	133
4.4	<i>Preprint:</i> Irreversible dynamics in quantum many-body systems . . . . .	137
4.5	Relation to out-of-time-order correlators . . . . .	143
4.5.1	Out-of-time-order correlators and scrambling . . . . .	144
4.5.2	Out-of-time-order correlators far from equilibrium . . . . .	147
4.5.3	Double commutators . . . . .	148
4.6	Semiclassical echo dynamics and Lyapunov exponents in the Sachdev-Ye-Kitaev model . . . . .	150
4.6.1	Phase space dynamics with Truncated Wigner Approximation . . . . .	151
4.6.2	Semiclassical dynamics of the Sachdev-Ye-Kitaev model . . . . .	153
<b>5</b>	<b>Summary and outlook</b>	<b>160</b>
	<b>Bibliography</b>	<b>162</b>
	<b>Acknowledgments</b>	<b>187</b>
	<b>Curriculum vitae</b>	<b>188</b>

# Chapter 1

## Introduction

The collective behavior of many degrees of freedom bears a plethora of surprising phenomena in both the classical and the quantum realm. In thermal equilibrium it is understood that the behavior of many-particle systems can be explained by the principles of statistical mechanics. Far from thermal equilibrium, however, the only known principle determining the dynamics a priori are the fundamental laws of motion involving every single degree of freedom. This thesis deals with different aspects of the non-equilibrium dynamics of closed quantum many-body systems.

Non-equilibrium processes and collective phenomena that are governed by classical physics are common everyday experiences. Examples are the mixing of hot coffee with cold milk that was poured into it ([Wettlaufer, 2011](#)) or the dynamics of traffic jams ([Schadschneider, 2006](#)). Ultimately, our whole planet earth is in a non-equilibrium condition since it is subjected to a permanent drive in the form of irradiated sunlight.

The dynamics of quantum many-body systems, instead, naturally elude our everyday experience, primarily due to the extremely short time scales or low temperatures. Natural time and energy scales for human beings are seconds (one heartbeat) and 300 Kelvin (a comfortably warm spring day in central Europe). In the laboratories, however, enormous advances in experimental techniques during the past decades, like the development of quantum simulators of different kinds and ultrafast pump-probe techniques, allow unprecedented control and measurements on extremely short time scales on quantum systems with many degrees of freedom. In these experiments electronic dynamics can be addressed, for which the relevant time scale is femtoseconds ( $10^{-15}$  seconds), as well as dynamics of ultracold atoms, which exhibit fundamental many-body physics at temperatures of some tenths of micro-Kelvins ( $10^{-6}$  Kelvin). Through these new possibilities theoretical studies of quantum many-body systems far from equilibrium, which by themselves raise intriguing fundamental questions, become relevant for real world experiments.

In the first section of this chapter (Section 1.1) a selection of seminal experiments that motivate the theoretical investigation of the dynamics of quantum many-body systems far from equilibrium is discussed. In Section 1.2 cornerstones of the theoretical understanding of the non-equilibrium dynamics are introduced with the intention to give a comprehensive overview of the physical phenomena for readers not familiar with recent developments in the field. Based on entanglement as characteristic phenomenon Section 1.3 sketches the

challenges of theoretical (in particular numerical) treatment of quantum many-body systems. In Section 1.4 the scope of the thesis is outlined and the main results are summarized.

## 1.1 Experimental realization of unitary dynamics in quantum many-body systems

A main motivation to study theoretical aspects of the nonequilibrium dynamics of quantum many-body systems is the recent progress in experimental techniques that facilitate highly controllable analog quantum simulation (Georgescu *et al.*, 2014). These quantum simulators allow to realize simple model Hamiltonians of condensed matter systems and can therefore be understood as special purpose quantum computers (Feynman, 1982). Importantly, these experimental setups do not only allow for a precise manipulation of Hamiltonian parameters but also measurements that resolve the transient dynamics when the system is pushed out of equilibrium.

One class of such quantum simulators is based on cold gases of neutral atoms (bosonic or fermionic) in optical potentials that are produced by off-resonant laser light (Bloch *et al.*, 2008, 2012; Gross and Bloch, 2017). A spatial variation of the light intensity affects the atoms by a position-dependent ac Stark shift through the varying amplitude of the electric field, which results in an effective external potential for the atoms (Grimm *et al.*, 2000). This potential is proportional to the laser intensity and the sign is determined by the detuning, i.e., the difference between laser frequency and the closest resonance frequency of the atoms. Using such optical potentials the atoms can be confined to effectively lower dimensions and with interfering laser beams periodic potentials with a variety of lattice structures can be realized. Since the atoms are neutral their interaction is very short-ranged. In an optical lattice it is a good approximation to assume that only atoms residing on the same lattice site interact. This corresponds to a setting that is theoretically described by the Hubbard model, which is a prominent model for correlated quantum matter (Hubbard, 1963). In second quantization the Hubbard Hamiltonian for fermions with an internal spin-1/2 degree of freedom reads

$$H = -t_h \sum_{\langle i,j \rangle, \sigma} (\hat{c}_{i,\sigma}^\dagger \hat{c}_{j,\sigma} + \hat{c}_{j,\sigma}^\dagger \hat{c}_{i,\sigma}) + U \sum_i \hat{n}_{i,\uparrow} \hat{n}_{i,\downarrow}, \quad (1.1)$$

where  $\langle i, j \rangle$  denotes the set of neighboring lattice sites  $i$  and  $j$ ,  $\sigma = \uparrow, \downarrow$  labels the spin degree of freedom, and  $\hat{n}_{i,\sigma} = \hat{c}_{i,\sigma}^\dagger \hat{c}_{i,\sigma}$  is the site occupation. The parameter  $t_h$  is the tunneling matrix element between adjacent lattice sites, often referred to as hopping amplitude, and  $U$  parametrizes the interaction energy of particles on the same lattice site. Despite its simplicity this model exhibits rich many-body physics, e.g. an interaction driven metal-insulator transition, superconductivity, and magnetism (Tasaki, 1998).

In a cold atom experiment it is not only possible to choose the geometry of the system by adjusting the optical potential accordingly. Also the ratio of the parameters  $t_h$  and  $U$  can be tuned. By changing the depth of the potential, i.e., the laser intensity, the hopping amplitude can be increased or decreased, which effectively corresponds to decreasing or increasing the interaction strength  $U$ . Alternatively, the interaction parameter can be addressed directly



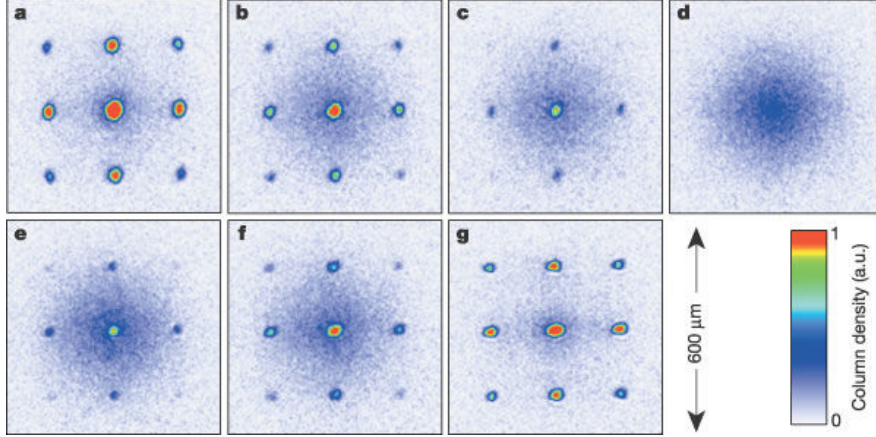


**Fig. 1.1:** Collapse and revival of matter wave coherence in a Bose-Einstein condensate after a sudden increase of the lattice depth. The pictures show the interference pattern observed in time of flight measurements at times between  $0\mu s$  (a) and  $550\mu s$  (g) after the switching of the potential. The initial superfluid state, which exhibits a clear interference pattern, decays until the pattern is completely washed out; however, at time  $550\mu s$  there is an almost perfect revival of the macroscopic matter wave field. [Adapted by permission from Macmillan Publishers Ltd: Nature (Greiner *et al.*, 2002), copyright (2002); <https://www.nature.com/nature/journal/v419/n6902/full/nature00968.html>.]

by means of a Feshbach resonance (Feshbach, 1962; Fano, 1961). In an external magnetic field the different Zeeman shifts of internal states with different magnetic moments allow to tune bound states resonant with scattering channels and in the vicinity of these resonances the scattering length changes drastically. In the Hubbard Hamiltonian (1.1) this translates to the possibility to adjust the value of  $U$  at will, which, remarkably, includes the possibility to change the sign of  $U$ .

A seminal experiment addressing the dynamics of quantum many-body systems was performed on ultracold bosonic atoms in an optical lattice (Greiner *et al.*, 2002) described by the bosonic version of the Hubbard model (1.1). The system was initially prepared in the superfluid ground state before suddenly switching the potential depth to a very large value corresponding to a large interaction strength  $U$  and negligible hopping amplitude  $t_h$ . After varying waiting times  $t$  the optical potential was switched off allowing the atoms to propagate freely for a short period before taking absorption pictures of the resulting atom cloud. The interference patterns resulting from such a *time of flight measurement* reflect the momentum distribution in the system at the time of release. In the experiment of Greiner *et al.* a periodic collapse and revival of the phase coherence of the initial state was revealed in the course of time as depicted in Fig. 1.1. This periodicity of the time-evolution owes to the fact that the Hamiltonian that determines the time evolution is close to an integrable point, where the system does not thermalize.

Another pioneering experiment that aroused a lot of interest in quantum many-body dynamics is the realization of a quantum Newton's cradle (Kinoshita *et al.*, 2006). In this setup an effectively one-dimensional gas of bosonic atoms in the Tonks-Girardeau limit of infinite strength interactions is created in a harmonic trap. It is initially prepared in a superposition of opposite momenta  $k$  and  $-k$ . Time of flight measurements at different times

$t$  reveal that the two momentum groups periodically collide with each other as depicted in Fig. 1.2. Also in this experiment no thermalization is observed, although the whole process amounts to thousands of collisions per atom. The reason for the absence of thermalization is again the integrable nature of the system, which is, though, more subtle than in the previous example. Definitions of integrability and its implication on thermalization are discussed in more detail in Section 1.2.1.

The two experiments described above yield insights into the time evolution of the momentum distribution via time of flight measurements. Cold atom experiments are, however, not restricted to this type of probe. Nowadays, further developments of the experimental techniques allow to take single-site-resolved pictures of the configuration of the atoms in real space and, moreover, to manipulate the initial state with the same precision (Sherson *et al.*, 2010; Weitenberg *et al.*, 2011; Bloch *et al.*, 2012; Choi *et al.*, 2016).

In new experiments so-called Floquet engineering is increasingly exploited to realize new types of systems with cold atoms. In this approach an external field is modulated at a frequency much larger than the typical time scale of the atomic system. Thereby the system properties on the slower time scale can effectively be changed. One important application is the creation of artificial gauge fields allowing to realize the Haldane model, which is a paradigmatic model of a topological insulator (Haldane, 1988), in experiment (Jotzu *et al.*, 2014; Fläschner *et al.*, 2016). This setup is a candidate to observe the nonequilibrium steady state transition addressed in Section 2.2 of this thesis. A synopsis of the theoretical foundations of Floquet engineering can be found in Section 2.2.2.

Besides ultracold neutral atoms in optical lattices there are other experimental setups with a sufficient degree of isolation and control that allow to investigate the dynamics of quantum many-body systems far from equilibrium. For example, ions can be trapped similar to neutral atoms. Being charged such trapped ions experience long range Coulomb interactions in contrast to the short ranged interactions of neutral atoms. This Coulomb coupling leads to collective vibrational modes of the ions in the trapping potential. These can be used in combination with internal degrees of freedom to effectively realize the dynamics of spin models (Porrás and Cirac, 2004; Richerme *et al.*, 2014; Jurcevic *et al.*, 2014, 2017; Zhang *et al.*, 2017), where the system parameters are manipulated by resonantly driving transitions between the different states with lasers. Similar model Hamiltonians were realized using the degrees of freedom of nitrogen-vacancy centers in high-purity diamond samples (Childress

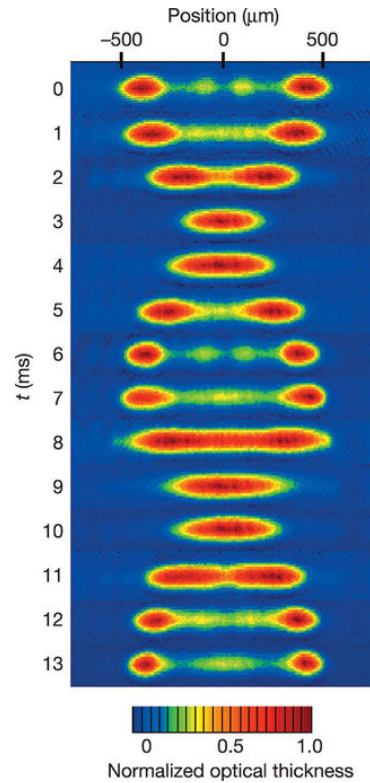


**Fig. 1.2:** A quantum Newton's cradle. The absorption images of time of flight measurements at different times reveal a periodically evolving momentum distribution that remains nonthermal also after many collisions. [Adapted by permission from Macmillan Publishers Ltd: Nature (Kinoshita *et al.*, 2006), copyright (2006); <https://www.nature.com/nature/journal/v440/n7086/full/nature04693.html>.]

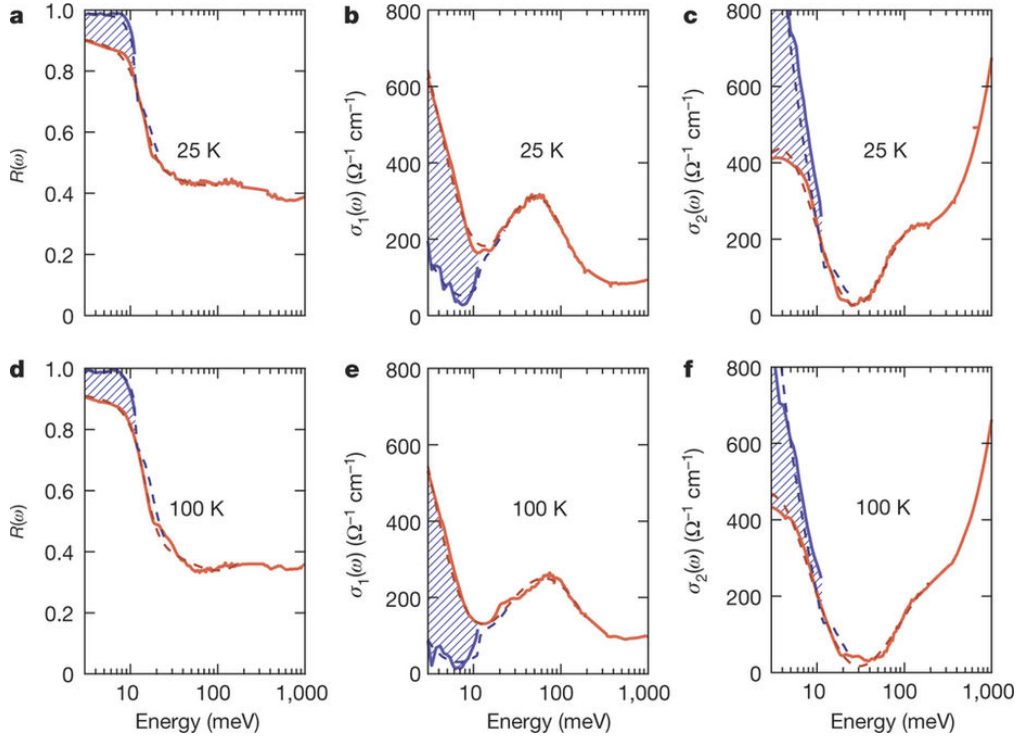


**Fig. 1.3:** Experimental evidence of possible light-induced superconductivity. Reflectivity  $R(\omega)$  and real and imaginary part of the optical conductivity,  $\sigma_1(\omega)$  and  $\sigma_2(\omega)$  measured on  $K_3C_{60}$  in equilibrium (red) and 1ps after excitation with a light pulse. The saturation of the reflectivity at low energies, formation of a gap in  $\sigma_1(\omega)$ , and the divergence of  $\sigma_2(\omega)$  suggest that a transient superconducting state is realized in this experiment. [Reprinted by permission from Macmillan Publishers Ltd: Nature (Mitrano *et al.*, 2016), copyright (2016); <https://www.nature.com/articles/nature16522>]

*et al.*, 2006; Doherty *et al.*, 2013; Choi *et al.*, 2017).

Thanks to recent advances that allow to produce ultrashort laser pulses it has become possible to study also the nonequilibrium dynamics of electrons in solids. In ultrafast pump-probe experiments the electrons are excited by a strong pump pulse before a following weaker probe pulse is applied to track the time evolution of the system. Since this dynamics is much faster than the time scale of relaxation that occurs due to coupling to the lattice, the electrons can be viewed as isolated. Recent experiments on different systems showed that these photo-induced transient states can exhibit the characteristics of phases, which are not stable in equilibrium at the corresponding temperature. One example is the observation of signatures of superconductivity when analyzing the optical properties after a pump pulse was applied to a sample way above the critical temperature (Mitrano *et al.*, 2016); see Fig. 1.3. In other experiments time-resolved photoemission spectroscopy is used to gain insight into the band structure and occupations after a strong excitation. An example application is the recent observation of a photo-induced charge-density-wave to semi-metal phase transition (Mathias *et al.*, 2016).

In another related class of experiments based on short electron pulses time-resolution is introduced to transmission electron microscopy or low energy electron diffraction, for example allowing to observe the ultrafast dynamics of magnetic degrees of freedom (da Silva *et al.*,

2017) or surface structures (Vogelgesang *et al.*, 2017).

## 1.2 Quenches, transient dynamics, and thermalization

The experimental realization of dynamics in closed quantum many-body systems discussed in the previous section can be studied theoretically considering *quench* protocols. In this setting the system is initially, at time  $t = 0$ , prepared in an initial state described by a density matrix  $\hat{\rho}_0$ . This density matrix can be pure,  $\hat{\rho}_0 = |\psi_0\rangle\langle\psi_0|$ , if a prescription to prepare a particular initial state  $|\psi_0\rangle$  exists as is the case for the quantum Newton's cradle experiment. Alternatively it can be an equilibrium density matrix for some temperature  $\beta$  with respect to some Hamiltonian  $\hat{H}_0$ ,  $\hat{\rho}_0 = e^{-\beta\hat{H}_0}$ . This is the case for the collapse and revival experiment described in the previous section. Often, however, temperatures are low enough that it is a good approximation to consider the pure ground state as equilibrium initial state.

For times  $t > 0$  the system is left to evolve according to a Hamiltonian  $\hat{H}$ . In cases where the system is initially prepared in an equilibrium state of  $\hat{H}_0$  a typical situation is that both  $\hat{H}_0$  and  $\hat{H}$  belong to a family of Hamiltonians  $\hat{H}(\lambda)$ , where  $\lambda$  is an external parameter, e.g. an electric or magnetic field, the hopping, or the interaction. In that case the quench protocol is performed by preparing the system in equilibrium with  $\hat{H}_0 = \hat{H}(\lambda_i)$  and then at  $t = 0$  suddenly switching the external parameter to a different value  $\lambda_f$  to induce the dynamics with  $\hat{H} = \hat{H}(\lambda_f)$ .

In the isolated systems under consideration in this thesis the time-dependence of the density matrix is determined by the *von Neumann equation*

$$i\frac{d}{dt}\hat{\rho}(t) = [\hat{H}, \hat{\rho}(t)] . \quad (1.2)$$

This equation yields a nontrivial time evolution if the initial density matrix does not commute with the Hamiltonian  $\hat{H}$ , which is typically the case in the quench protocols described above. If the initial state is pure one can alternatively resort to the dynamics of the plain state  $|\psi(t)\rangle$  instead of the density matrix  $\hat{\rho}(t)$ . In that case the time evolution is determined by the *Schrödinger equation*

$$i\frac{d}{dt}|\psi(t)\rangle = \hat{H}|\psi(t)\rangle . \quad (1.3)$$

A quench as described above constitutes a strong perturbation of the system driving it far from any equilibrium state. This is to be contrasted with weak external perturbations to an equilibrium state, which are considered in linear response theory. Studying linear response yields an insightful description of the effect of weakly coupling a measurement device to the system in order to infer equilibrium properties. A main result is the Fluctuation-Dissipation theorem that relates the measured susceptibilities to thermal fluctuations of the system (Kubo, 1966). The key prerequisite of this formalism is the fact that the external force can be treated perturbatively, meaning that the system always remains close to an equilibrium state. By contrast, the response after quenching a system, of which various aspects will be studied in this thesis, cannot be captured in this framework.

The dynamics following a quench can be largely separated into two regimes, namely the initial transient dynamics and the asymptotic behavior after long times, where typically a new steady state is reached. The following two sections outline important aspects of both regimes that received a lot of interest over the past two decades.

### 1.2.1 From quantum dynamics to statistical physics: Ergodicity, integrability, and thermalization

A fundamental question that arises when considering the behavior of closed quantum many-body systems at long times after a quench is whether a new thermal equilibrium state is eventually established. This question has received a lot of attention from the theoretical perspective in the course of the past years; see Refs. (D’Alessio *et al.*, 2016; Gogolin and Eisert, 2016) for summarizing reviews. Particularly intriguing issues with respect to this question are related to the unitarity of the time evolution in isolated quantum systems. Assuming a system is initially prepared in a pure state, how or in what sense can it evolve to a state that is described by a thermal (i.e., mixed) density matrix at long times? Moreover, a thermal state does not carry any information about initial conditions besides the values of a few conserved quantities. How can this information be lost under unitary dynamics, which is in particular linear, while this loss of information in classical systems is understood to be a consequence of the nonlinearity of the dynamics?

#### Thermalization in generic quantum systems

The reason for thermalization in classical systems is understood in terms of chaotic dynamics, mixing, and ergodicity (Lebowitz and Penrose, 1973). These concepts describe the way the classical phase space is explored under Hamiltonian time evolution. Recent findings, instead, indicate that thermalization in the realm of generic quantum many-body systems is a consequence of the structure of the eigenstates of the system’s Hamiltonian. In seminal works Deutsch and Srednicki (Deutsch, 1991; Srednicki, 1994, 1996, 1999) developed the *Eigenstate Thermalization Hypothesis* (ETH); similar ideas had, however, already been explored before (von Neumann, 1932; Jensen and Shankar, 1985). The ETH states that in terms of physical observables each single eigenstate looks thermal or, more technically, expectation values of physical few-body observables in the thermodynamic limit are smooth functions of the eigenstate energy. The difference of observable expectation values in nearby eigenstates is exponentially suppressed with increasing system size. Since the stationary value of an observable at long times after a quench is determined by the expectation value in the contributing energy eigenstates, the ETH implies that the steady state can be described by a microcanonical ensemble (Rigol *et al.*, 2008). Note that the term “hypothesis” in ETH has to be taken literally because the basic assumptions are to date not formally proven to hold for many-body systems. Nevertheless, there is strong numerical evidence for its validity from studies of a variety of example systems (Steinigeweg *et al.*, 2014; Beugeling *et al.*, 2014; Kim *et al.*, 2014; Mondaini *et al.*, 2016).

When considering physical observables that only probe a finite subsystem  $A$  it becomes evident that a thermalizing system acts as bath for each subsystem. The expectation value of



any observable in  $A$  is fully determined by the reduced density matrix of this subsystem. The reduced density matrix is obtained by tracing out the degrees of freedom in the complement (the “bath”), resulting in a mixed density matrix for the subsystem under consideration. By checking the convergence of the reduced density matrix to a Gibbs state at long times thermalization can be investigated independent of a choice of observables. Using this approach it was revealed that whether a system thermalizes dynamically or not is not independent of the initial state (Bañuls *et al.*, 2011). However, when focussing on the reduced density matrix, restrictions on the energy distribution in the initial state can be identified that imply thermalization without invoking the ETH assumption (Riera *et al.*, 2012; Gogolin and Eisert, 2016). This condition for thermalization limits the set of thermalizing initial states, but it covers most physically relevant situations (Reimann, 2008, 2012).

### Atypical asymptotic states: Integrability and Generalized Gibbs Ensembles

In Section 1.1 two experiments were discussed, where even after very long times the system did not reach a thermal state. The reason for the absence of thermalization in these systems is the fact that they are integrable or almost integrable. Integrable systems make up an interesting exception to generic many-body systems. Although there is no commonly agreed on single definition of integrability (Caux and Mossel, 2011) one defining feature is particularly relevant in the context of thermalization: In integrable quantum systems there exists an extensive set of local operators that commute with the Hamiltonian and with each other, which means that they are conserved under time evolution. In close analogy, a classical integrable system comprises an extensive number of conserved quantities.

Classical billiards are a good example to illustrate the impact of integrability on thermalization. Fig. 1.4 shows two different classical billiards with example trajectories of a ball that bounces off the boundaries elastically. The dynamics in the billiard in Fig. 1.4(a) is ergodic (Bunimovich, 1979), which means that the trajectory shown in the figure will eventually uniformly cover the whole region inside the boundaries. As a result, long time averages can equivalently be computed as averages over the microcanonical ensemble. By contrast, the dynamics of the circular billiard in Fig. 1.4(b) exclude a part of the position space. In this case long time averages generally do not coincide with averages over the microcanonical ensemble, because the dynamics is not ergodic. The reason is the existence of an additional integral of motion besides energy, namely angular momentum. Since the number of integrals of motion coincides with the number of canonical coordinates the dynamics is trivial in terms of action-angle variables and restricted to a torus in phase space. Consequently, integrable classical systems do not thermalize.

In analogy, an important property of integrable quantum systems is the fact that they violate ETH (Rigol *et al.*, 2008); hence, they do not necessarily equilibrate to states that can be described by conventional thermal ensembles. Nevertheless, it has been established over the last years that the steady state reached by an integrable system in the long time limit can be described by a so-called *Generalized Gibbs Ensemble* (GGE). This ensemble can be derived according to Jaynes’s principle (Jaynes, 1957a,b) by maximizing the entropy under the constraint that the expectation value of the extensive set of conserved quantities is known. Thereby the density matrix takes the form of a Gibbs ensemble with one Lagrange multiplier

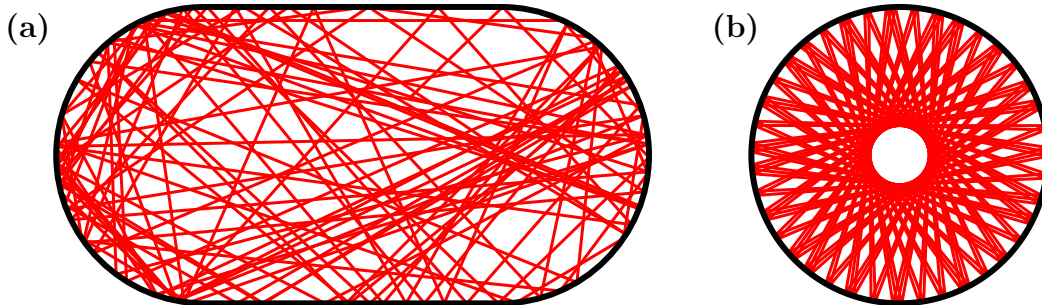


**Fig. 1.4:** Trajectories in billiards with different boundary conditions. **(a)** In the Bunimovich stadium there exist no further symmetries besides time translational symmetry. Hence, the trajectory eventually uniformly covers the whole energy shell in phase space; the system is ergodic. **(b)** In the circular billiard angular momentum is conserved in addition to energy, rendering the system integrable. The dynamics exclude a part of the phase space and the system is not ergodic.

(“generalized temperature”) for each conserved quantity. The applicability of the GGE has been confirmed in many theoretical works; see, e.g., Refs. (Rigol *et al.*, 2006, 2007; Cazalilla, 2006; Kollar and Eckstein, 2008; Barthel and Schollwöck, 2008; Calabrese *et al.*, 2011, 2012; Cassidy *et al.*, 2011; Fagotti and Essler, 2013) for some early works and (Vidmar and Rigol, 2016) for a recent review. Importantly, it was realized that a GGE can only capture the steady state expectation values of local observables (Barthel and Schollwöck, 2008; Gogolin *et al.*, 2011). Moreover, the experimental observation of a stationary state determined by a GGE in a one-dimensional Bose gas has been reported recently (Langen *et al.*, 2015).

The fact that the knowledge of an extensive number of Lagrange multipliers is sufficient to describe the steady state although the dynamics is a priori determined by the overlaps of the initial state with all energy eigenstates, which is exponential in the system size, can be understood by generalizing the ETH. While in integrable systems the expectation values of observables in the energy eigenstates are not smooth functions of the energy, it was found that when labelling eigenstates with the full set of conserved quantities they vary smoothly as the labels are varied slightly (Cassidy *et al.*, 2011). This fact explains the possibility to describe the stationary state reached after long times by a GGE.

Generally, in order to decide whether a specific model is integrable or not it can be hard to identify a suited set of commuting operators. The same holds for exact solvability, which is also commonly used as definition of integrability. An alternative indicator of integrability requiring much less insight into possibly subtle properties of the system of interest is the distribution of energy level spacings, i.e., the statistics of the differences between consecutive eigenenergies. The underlying ideas date back to works of Wigner and Dyson aimed at understanding the complex energy levels of large nuclei (Wigner, 1955, 1957, 1958; Dyson, 1962). The important discovery was the fact that in most bases a Hamiltonian looks essentially like a random matrix, meaning that to understand main properties of the spectrum of a physical Hamiltonian it can be sufficient to understand the spectra of random matrices. Random matrix theory has in the meanwhile become a large field with applications in many different areas (Akemann *et al.*, 2011; Kota, 2014), including the ETH (Srednicki, 1994). The relevant results for the differentiation between integrable and chaotic quantum systems are the

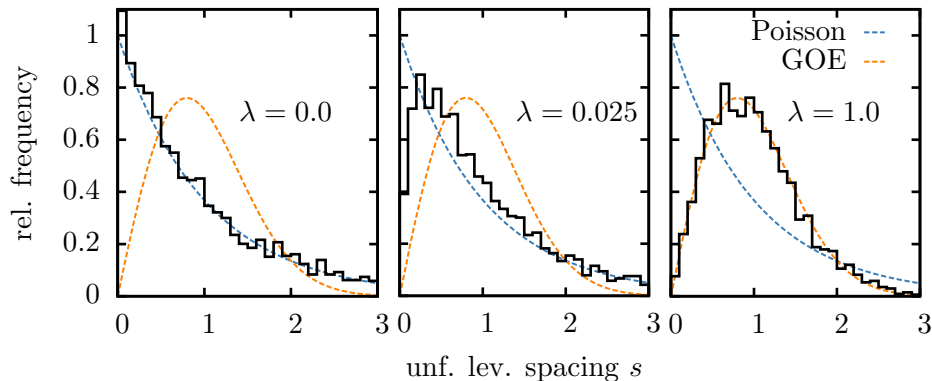


**Fig. 1.5:** Unfolded level spacing histograms of an XXZ chain of  $N = 20$  spins with next-nearest neighbor coupling strength  $\lambda$ . In the integrable case ( $\lambda = 0$ ) the level spacing distribution is Poissonian, whereas the distribution of the Gaussian Orthogonal Ensemble (GOE) is found for the ergodic systems ( $\lambda > 0$ ).

Berry-Tabor conjecture (Berry and Tabor, 1977) and the conjecture formulated by Bohigas, Giannoni, and Schmit (Bohigas *et al.*, 1984) (BGS conjecture). The Berry-Tabor conjecture states that the energy levels of a quantum system with integrable classical counterpart can essentially be viewed as a sequence of independent random variables, meaning that the distribution of the energy level spacings is Poissonian. By contrast, according to the BGS conjecture the level spacings of quantum systems with chaotic classical counterpart follow a Wigner-Dyson distribution. Both conjectures have been confirmed in different settings, e.g. (Bohigas *et al.*, 1984; Wintgen and Friedrich, 1987; Rudnick, 2008), and, therefore, serve in combination as indicator of quantum chaos (although different definitions of quantum chaos are still under debate, see Section 4.1). Importantly, it was found that level spacing statistics also distinguish between integrable and ergodic systems if no classical counterpart exists (Santos and Rigol, 2010; Rigol and Santos, 2010; Kollath *et al.*, 2010; Santos *et al.*, 2012; Atas *et al.*, 2013). The model Hamiltonians considered in this thesis are all of this type. One example, which will be studied in Chapter 4, is a one-dimensional anisotropic Heisenberg antiferromagnet with spin-1/2 degrees of freedom. In the presence of only nearest-neighbor interactions this system is integrable (Doikou *et al.*, 2010), but the integrability is immediately broken by introducing next-nearest-neighbor couplings. Fig. 1.5 shows numerical results for the level spacing distribution in a finite system, where the strength of the next-nearest-neighbor interactions is parametrized by  $\lambda$  ( $\lambda = 0$  is the integrable point). In the extreme cases  $\lambda = 0$  and  $\lambda = 1$  the histograms are clearly compatible with the Poissonian distribution and the Wigner-Dyson distribution, respectively. The center panel demonstrates that already very weak integrability-breaking is sufficient to introduce a distinct feature of generic quantum systems, namely energy level repulsion. In ergodic systems the probability of energy level spacings that equal zero vanishes, whereas energy levels in integrable systems are uncorrelated and can therefore coincide. In the thermodynamic limit the transition from integrable to chaotic is expected to be immediate at arbitrarily small magnitudes of the integrability-breaking term (Modak *et al.*, 2014; Modak and Mukerjee, 2014).



A new kind of integrability that aroused a lot of interest in recent years emerges in the many-body localized phase. Many-body localization (MBL) is the generalization of Anderson localization (Anderson, 1958) to interacting systems. At sufficiently strong disorder many-body systems undergo a transition to a localized phase characterized by the absence of transport similar to an Anderson insulator (Gornyi *et al.*, 2005; Basko *et al.*, 2006; Abanin and Papić, 2017). Another key property of this phase is the emergence of quasi-local integrals of motion, so-called “l-bits” (Serbyn *et al.*, 2013; Huse *et al.*, 2014). These integrals of motion are associated with mutually commuting operators with support mainly around one lattice site and exponentially suppressed contributions away from that. Therefore, the l-bits retain information about the local structure of the initial state for all times, thereby prohibiting thermalization. In virtue of these integrals of motion the impact of integrability on the equilibration process can be observed straightforwardly in real space as has been done in recent experiments (Schreiber *et al.*, 2015; Choi *et al.*, 2016).

In the literature many-body systems that are ergodic in the sense that they exhibit Wigner-Dyson level spacing statistics and obey the ETH are often referred to as “chaotic”. It is, however, to date not clear how classical chaos, whose defining property is the exponential sensitivity of the dynamics to small perturbations, can emerge from quantum dynamics. In classical systems chaos does not only imply ergodicity, but also irreversibility, i.e., the complete loss of information about the initial state in the process of thermalization. The question in what sense quantum dynamics can be exponentially sensitive to perturbations despite its unitary nature is under ongoing debate (Peres, 1984; Gorin *et al.*, 2006; Jacquod and Petitjean, 2009; Kitaev, 2014; Shenker and Stanford, 2014; Maldacena *et al.*, 2016; Hosur *et al.*, 2016; Schmitt and Kehrein, 2016; Bohrdt *et al.*, 2017; Scaffidi and Altman, 2017). Chapter 4 of this thesis contributes to this discussion by exploring the behavior of quantum many-body systems under imperfect effective time reversal, suggesting a definition of irreversibility based on the decay of observable echoes. For a more elaborate introduction to irreversibility see Section 4.1.

## 1.2.2 Transient dynamics: Spreading of information, the approach to equilibrium, and dynamical phase transitions

In the previous section it was discussed how stationary states that are typically approached at long times after the system was pushed out of equilibrium can be described with tools from statistical physics. A priori the only principle that governs the dynamics leading to the stationary state is the fundamental equation of motion, i.e., the Schrödinger equation (1.3), which microscopically describes the interaction of the constituent degrees of freedom. Nevertheless, the transient dynamics can exhibit characteristic features that are largely independent of microscopic details and which can be understood in physical terms. This section outlines a number of quite universal phenomena occurring in typical real time dynamics of many-body systems.

### Buildup of correlations and spreading of information

One remarkable property of quantum many-body systems is the presence of speed limits for the propagation of information despite the clearly nonrelativistic nature of the Schrödinger equation. In a seminal work Lieb and Robinson ([Lieb and Robinson, 1972](#)) demonstrated that in a system with only finite-range interactions and a finite local Hilbert space the information about a local perturbation propagates at a finite velocity, which is an intrinsic feature of the system's Hamiltonian. This speed limit led to the notion of an effective light cone in the spatio-temporal plane in analogy to the light cone known from special relativity. On a technical level Lieb and Robinson derived a bound showing that the operator norm of the commutator of two local operators is exponentially small outside of the light cone. This bound is nowadays known as the *Lieb-Robinson bound*, of which various generalizations and extensions have been worked out; see, e.g., ([B. Nachtergaele and Sims, 2010](#)). The predicted effective light cone has been observed in numerical simulations ([Läuchli and Kollath, 2008](#); [Manmana \*et al.\*, 2009](#)) as well as in experiment ([Cheneau \*et al.\*, 2012](#)). It is important to note that the Lieb-Robinson bounds regard susceptibilities, which are related to commutators of observables, as opposed to correlations, which correspond to anti-commutators. It has been demonstrated that correlations also exhibit an effective light cone structure, but the decay outside the light cone depends on the entanglement present in the initial state and can be slower than exponential ([Medvedyeva \*et al.\*, 2013](#); [Abeling \*et al.\*, 2017](#)).

The Lieb-Robinson velocity, i.e., the ratio of distance and time on the effective light cone, appears as a mathematical parameter in the derivation of the Lieb-Robinson bound depending on the microscopic details of the system under consideration. It turned out that this velocity can be understood physically in a very intuitive way based on a quasiparticle picture. For exactly solvable models, where the quasiparticle dispersion is known, Calabrese and Cardy demonstrated that the Lieb-Robinson velocity is directly related to the maximal group velocity of the quasiparticles ([Calabrese and Cardy, 2006](#)). The underlying physical picture is sketched in Fig. 1.6. A quench that introduces an extensive amount of energy into the system creates quasiparticle excitations at every point in the system. Among these, quasiparticles originating in only minimally separated regions are entangled. After the quench the particles propagate ballistically at their respective group velocity. Being entangled quasiparticles

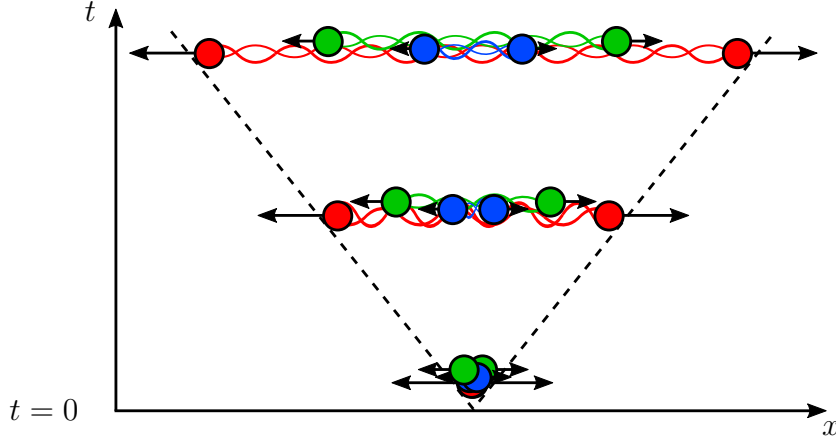


**Fig. 1.6:** Illustration of the quasiparticle picture to explain the spreading of correlations and information after a quench. Quasiparticles that are produced at  $t = 0$  in close vicinity are entangled. As time proceeds counterpropagating quasiparticles cause entanglement and correlations between distant regions in space.

that propagate to different positions spread entanglement and induce correlations between observables measured at these points. The maximal distance that can be bridged at a fixed time after the quench is due to an entangled pair of quasiparticles propagating in opposite directions with the maximal group velocity  $v_{\max}$ , like the red particles depicted in Fig. 1.6. This means, e.g., that equal time correlation functions at a given distance  $d$  do not show any significant signal until time  $t = d/(2v_{\max})$ .

The same picture gives a very conclusive explanation for the typical behavior of entanglement after a quench. The entanglement of any bipartition of a one-dimensional lattice grows linearly after a quench before saturation with a volume law is reached (Calabrese and Cardy, 2005). The reason is that the induced entanglement is proportional to the number of quasiparticles that crossed the border between both subsystems. This picture pertains analogously in higher-dimensional systems (Lemonik and Mitra, 2016). Note that the volume law saturation value of the entanglement entropy of a subsystem is essential for thermalization, because it is formally the same as the thermal entropy of the respective subsystem, which has to be extensive.

A prominent exception to the generic entanglement dynamics described above is the many-body localized phase. Despite the absence of transport in these systems entanglement growth is not completely inhibited. The exponential tails of the l-bits lead to a logarithmic growth of the entanglement entropy with time, which is a characteristic of the MBL phase (Bardarson *et al.*, 2012; Serbyn *et al.*, 2013).

In this thesis the quasiparticle picture will prove beneficial for the interpretation of different results presented in Chapter 4.

## Prethermalization and hydrodynamic tails

In Section 1.2.1 it was discussed how conserved quantities shape the stationary state that is approached by a closed system at long times. In addition, the presence of (almost) conserved

quantities leads to universal features in the transient dynamics and the approach to the final state.

It was first observed in models for early-universe dynamics that near-integrable systems can exhibit a set of very different relaxation time scales, which lead to an emerging intermediate state that appears stationary in some observables, although thermal equilibrium has not yet been reached (Berges *et al.*, 2004). This phenomenon has been dubbed *prethermalization*. Although the cosmological systems are nonintegrable, they can be understood as near-integrable in the sense that the dynamics on the shortest timescale is nearly Gaussian (Langen *et al.*, 2016). This initial dynamics mainly leads to a rapid loss of phase information, which can, e.g., be sufficient to bring the kinetic temperature in terms of the total mean kinetic energy already close to its final equilibrium value. This dephasing time scale determines the beginning of a prethermalization plateau. The redistribution of quasiparticle occupation numbers towards detailed balance, instead, takes much longer. The onset of efficient redistribution of quasiparticles marks the end of the prethermalization regime.

In condensed matter models prethermalization occurs in the dynamics of systems where integrability is weakly broken. The first detailed analysis with this regard was conducted by Moeckel and Kehrein, who studied quenches to a weakly interacting fermionic Hubbard model in high dimensions (Moeckel and Kehrein, 2008, 2009, 2010). Within their analytical approach they could identify the initial dephasing timescale as well as the onset of the long-time dynamics. They found that the prethermalization plateau confined by these two timescales is characterized by an almost stationary quasiparticle distribution that resembles the zero-temperature distribution of a Fermi liquid. The subtle difference to an equilibrium distribution is a discrepancy in the quasiparticle residue, which ultimately leads to thermalization via quasiparticle scattering described by a quantum Boltzmann equation (Stark and Kollar, 2013; Bertini *et al.*, 2015). The analytical predictions for the prethermal state were confirmed numerically by (Eckstein *et al.*, 2009). Subsequent studies refined the picture by showing that observable expectation values on a prethermalization plateau are well described by a GGE (Kollar *et al.*, 2011) or a deformed GGE determined by almost conserved quantities (Essler *et al.*, 2014). Hence, prethermalization continuously connects the statistical theories of the long time asymptotic states in integrable and generic systems.

Prethermalization has been observed experimentally in a cold atom setup (Gring *et al.*, 2012; Langen *et al.*, 2013) in consistency with the theoretical framework discussed above. However, a trapped ion experiment indicates that the picture might have to be extended (Neyenhuis *et al.*, 2016).

As mentioned above the relaxation dynamics towards local equilibrium is generally expected to be described by a quantum Boltzmann equation (Stark and Kollar, 2013; Bertini *et al.*, 2015; Biebl and Kehrein, 2017). This equilibration via scattering of quasiparticles leads to exponential decay of observables towards equilibrium values. The buildup of global equilibrium, however, is even in systems far from any integrable point characterized by the presence of a few conserved quantities such as energy or particle number. These conservation laws constrain the dynamics in that the corresponding densities can only spread diffusively, which leads to an algebraic decay of observables at very late times that is most pronounced in quantities significantly overlapping with some conserved quantity (Lux *et al.*, 2014; Bohrdt *et al.*, 2017; Leviatan *et al.*, 2017). This slow equilibration at late times is referred to as

*hydrodynamic long time tails*. It implies that the time scale for global relaxation is given by  $t_{\text{gl}} \propto L^2/D$ , where  $L$  is the linear extent of the system and  $D$  the diffusion constant, although the Lieb-Robinson bound allows for ballistic propagation of information.

## Dynamical phase transitions

In studies of equilibrium properties of (quantum) many-body systems a focus is on abrupt changes of system properties induced by varying an external parameter, which signal phase transitions. Over the past century a powerful conceptual framework has been developed to understand and classify phase transitions (Stanley, 1971; Fisher, 1974; Sachdev, 2011). Although beyond the equilibrium paradigm, also the dynamics of quantum many-body systems can undergo sudden changes as a function of external control parameters; but in addition, most strikingly, nonanalyticities can occur as a function of time.

Due to the formal resemblance of the time evolution operator  $e^{-it\hat{H}}$  to the statistical operator  $e^{-\beta\hat{H}}$  with the inverse temperature  $\beta$  the return amplitude of a time evolved state,  $\mathcal{G}(t) = \langle \psi_0 | e^{-i\hat{H}t} | \psi_0 \rangle$ , can be interpreted as a boundary partition function (LeClair *et al.*, 1995) at imaginary temperature  $\beta = it$ . Consequently, the notion of a dynamical free energy density  $\lambda(t)$  defined by  $|\langle \psi_0 | e^{-i\hat{H}t} | \psi_0 \rangle|^2 = e^{-N\lambda(t)}$  can be introduced, where  $N$  denotes the system size. A defining feature of equilibrium phase transitions is the nonanalytic behavior of the free energy as function of a control parameter at the critical point. Remarkably, also the dynamical free energy  $\lambda(t)$  can show nonanalyticities as a function of time as was first observed by (Pollmann *et al.*, 2010). Yet, the analogy to equilibrium phase transitions described above was only pointed out by (Heyl *et al.*, 2013), who coined the term *dynamical quantum phase transition* (DQPT) for this phenomenon. As opposed to equilibrium phase transitions DQPTs are not driven by an external control parameter but by progressing time. Fig. 1.7 shows the cartoon picture of a DQPT. The nonanalyticity of the dynamical free energy marks the critical time  $t_c$ , which typically constitutes a short time scale in the dynamics.

Similar to a quantum phase transition that only occurs at zero temperature and therefore eludes direct experimental observation due to the

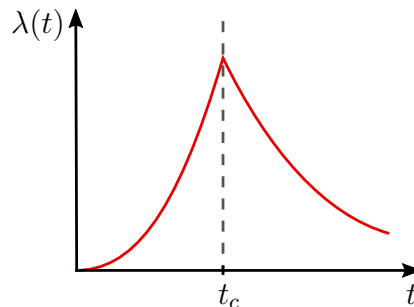


**Fig. 1.7:** Cartoon picture of a dynamical quantum phase transition. The nonanalyticity of the dynamical free energy density  $\lambda(t)$  marks the critical time  $t_c$ .

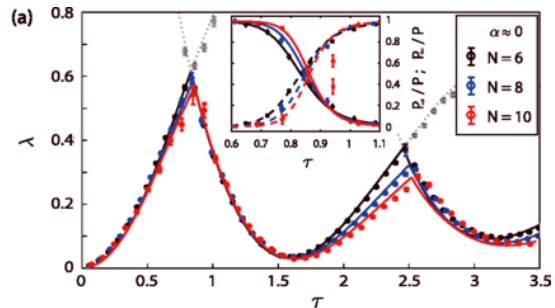


**Fig. 1.8:** Direct observation of a DQPT in an experiment with trapped ions that simulate the dynamics of a long-ranged Ising spin system in a transverse field. The extracted rate function  $\lambda(t)$  shows pronounced kinks at critical times. Reprinted figure with permission from (Jurcevic *et al.*, 2017) Copyright 2017 by the American Physical Society. <https://link.aps.org/doi/10.1103/PhysRevLett.119.080501>

third law of thermodynamics the physical

significance of DQPTs is a priori all but obvious. The scope of this new concept is under ongoing research and the current state of understanding will be outlined in more detail in Section 2.1; see also (Heyl, 2017) for a recent review.

A common condition for the occurrence of DQPTs is a high energy density in the initial state, which is typically induced by quenching across an equilibrium phase transition. Importantly, the term “phase transition” has been justified in theoretical works that demonstrated stability against symmetry-preserving perturbations and universality (Karrasch and Schuricht, 2013; Kriel *et al.*, 2014; Heyl, 2015), and the possibility to identify a dynamical order parameter (Budich and Heyl, 2016; Bhattacharya and Dutta, 2017). Experimental efforts resulted in the recent observation of DQPTs in a trapped ion experiment (Jurcevic *et al.*, 2017) (see also Fig. 1.8) and in a cold atom setup (Fläschner *et al.*, 2016), demonstrating that DQPTs are not just a peculiar mathematical feature. This thesis comprises the study of DQPTs in a two-dimensional model in Section 2.1.1, where a focus is laid on the distribution of zeros of the partition function  $\mathcal{G}(t)$  in the complex time plane.

Additionally, dynamical critical behavior was identified when studying steady states that are reached in the course of the dynamics in systems with symmetry-broken or topological phases. Clearly, the thermal state attained at late times in generic quantum systems can only reflect the equilibrium phase diagram. Long-time asymptotic states in integrable systems, which are described by a GGE, and prethermal states, instead, can exhibit critical effects that are genuinely nonthermal critical effects. Such behavior was found in a fermionic condensate (Yuzbashyan *et al.*, 2006), in fully connected models (Eckstein *et al.*, 2009; Schiró and Fabrizio, 2010; Sciolla and Biroli, 2010; Gambassi and Calabrese, 2011; Tsuji *et al.*, 2013), in a disordered spin chain (Vosk and Altman, 2014), in field theories (Sciolla and Biroli, 2013; Chandran *et al.*, 2013; Smacchia *et al.*, 2015), and in topological insulators (Wang and Kehrein, 2016; Wang *et al.*, 2016; Schmitt and Wang, 2017). General relations to the corresponding equilibrium phase transitions and distinguishing characteristics of the nonequilibrium transitions are to date opaque. On the one hand new nonthermal phases can appear in the dynamical phase diagram (Tsuji *et al.*, 2013). On the other hand the nonequilibrium transition and the equilibrium transition can have closely related scaling exponents, differing only subtly in the statistics of excitations (Chandran *et al.*, 2013; Smacchia *et al.*, 2015).

Section 2.2 of this thesis treats steady state transitions in Chern insulators, showing that nonanalytic behavior occurs in the Hall conductance whenever the system is quenched across an equilibrium phase boundary. The character of the nonanalyticity is solely determined by the typical conic gap closing points and thereby independent of microscopic details of the system.

In two recent works intimate relations between the occurrence of DQPTs and steady state transitions were revealed in long range spin systems and topological insulators (Žunkovič *et al.*, 2016; Wang and Xianlong, 2017). A common aspect of both works is that the timescale set by the occurrence of a DQPT diverges as the phase boundary of the steady state transition is approached. Diverging timescales have also been reported in other studies (Schiró and Fabrizio, 2010; Sciolla and Biroli, 2013), indicating that similar connections might play a role in a broader context.



## 1.3 Entanglement: Boon and bane of quantum many-body theory

A key feature that fundamentally discriminates between quantum and classical theories and essentially enriches the quantum world is the possibility of entangled states in composite quantum systems. The presence of entanglement underlies most counterintuitive phenomena in quantum theory, like the famous Einstein-Podolsky-Rosen (EPR) paradox (Einstein *et al.*, 1935), from which EPR concluded that a “spooky action at a distance” was at work, indicating that quantum theory was incomplete. The suggested way out by introducing classical hidden variables to the theory was ruled out by experimental tests that proved violation of the Bell inequalities (Bell, 1964; Hensen *et al.*, 2015). Instead, entanglement is now understood to be a key phenomenon in composite quantum systems and, moreover, the essential resource for quantum computing (Nielsen and Chuang, 2010; Preskill, 2016). The intention of this section is to give a basic intuition for the properties of entangled states and to outline the strategies applied by different theoretical methods for dealing with complex many-body states.

### 1.3.1 Entanglement and the complexity of many-body states

Entanglement occurs in composite quantum systems. Consider two quantum systems  $A$  and  $B$ , of which the states are elements of Hilbert spaces  $\mathcal{H}_A$  and  $\mathcal{H}_B$ . According to the principles of quantum mechanics the state-space for the description of the combined system, including, e.g., interactions between both subsystems, is the tensor product  $\mathcal{H}_{AB} = \mathcal{H}_A \otimes \mathcal{H}_B$ . Given a basis of subsystem  $A$ ,  $\{|i\rangle_A\}_{i=1\dots D_A}$ , and a basis of subsystem  $B$ ,  $\{|j\rangle_B\}_{j=1\dots D_B}$ , the basis of the composite Hilbert space is given by

$$\{|i\rangle_A \otimes |j\rangle_B\}_{i=1\dots D_A; j=1\dots D_B} . \quad (1.4)$$

Here  $D_A$  and  $D_B$  denote the dimensions of  $\mathcal{H}_A$  and  $\mathcal{H}_B$ , respectively. The dimension of the total Hilbert space  $\mathcal{H}_A \otimes \mathcal{H}_B$  is the product of both.

The simplest possible composite quantum system consists of two spin-1/2 degrees of freedom. Generally, the state of an individual spin can be expanded in the  $\hat{\sigma}^z$  eigenbasis yielding the form  $|\psi\rangle = a|\uparrow\rangle + b|\downarrow\rangle$ . An important property of a single spin state is the fact that it can always be characterized by a corresponding polarization, i.e., there is always a direction  $\vec{n}$  in three-dimensional space such that  $\langle\psi|\vec{n} \cdot \vec{\sigma}|\psi\rangle = 1$ . The same holds for a product state composed of two individually prepared spins,

$$|\Psi\rangle_{AB} = |\psi\rangle_A \otimes |\phi\rangle_B = (a_A|\uparrow\rangle_A + b_A|\downarrow\rangle_A) \otimes (a_B|\uparrow\rangle_B + b_B|\downarrow\rangle_B) . \quad (1.5)$$

Also in this composed state the measurement outcome of the spin polarization in subsystem  $A$  along one specific axis is determined to be +1. The whole many-particle Hilbert space is, however, much larger than the subset of product states. One example for a state that cannot be written as a single product of one state in subspace  $A$  and one state in subspace  $B$  is the singlet state

$$|\mathcal{S}\rangle = \frac{1}{\sqrt{2}} (|\uparrow\rangle_A \otimes |\downarrow\rangle_B - |\downarrow\rangle_A \otimes |\uparrow\rangle_B) . \quad (1.6)$$

Remarkably, in this state the expectation value of the spin polarization in subsystem  $A$  is

$$\langle \mathcal{S} | \vec{n} \cdot \vec{\sigma}_A | \mathcal{S} \rangle = 0 \quad (1.7)$$

for all orientations  $\vec{n}$ . This means that although according to the principles of quantum mechanics the state of the whole system is fully determined by the state vector  $|\mathcal{S}\rangle$  the outcome of a polarization measurement on a subsystem is maximally uncertain. The reason is that  $|\mathcal{S}\rangle$  is an entangled state. Another difference between entangled states and product states is that in a product state the correlation

$$C(\hat{O}_A, \hat{O}_B) = \langle \hat{O}_A \hat{O}_B \rangle - \langle \hat{O}_A \rangle \langle \hat{O}_B \rangle \quad (1.8)$$

vanishes for any choice of observables  $\hat{O}_A$  and  $\hat{O}_B$  in the different subsystems. In entangled states, instead, there can be correlations, the origin of which being genuinely quantal.

The entanglement of a pure state  $|\psi\rangle$  is commonly quantified using the *von Neumann entropy of entanglement*, that is for bipartitions of the system defined as

$$S_A(|\psi\rangle) = -\text{tr}[\hat{\rho}_A^{|\psi\rangle} \log_2 \hat{\rho}_A^{|\psi\rangle}], \quad (1.9)$$

where  $\hat{\rho}_A^{|\psi\rangle} = \text{tr}_B[|\psi\rangle\langle\psi|]$  is the reduced density matrix of subsystem  $A$ . For any bipartition into subsystems  $A$  and  $B$  it holds that  $S_A = S_B$ . The entanglement entropy vanishes for product states, whereas maximally entangled states like the singlet state  $|\mathcal{S}\rangle$  have maximal entanglement entropy. Hence, the entanglement entropy is a key quantity to characterize a many-body wave function.

### 1.3.2 Methods for many-body theory

Any theoretical approach aiming to address genuine quantum effects in many-body systems has to handle entangled many-body states. This is a hard problem as one can imagine considering just the astronomic dimensions that arise already at moderate system sizes when constructing the many-body Hilbert space as prescribed by Eq. (1.4). The dimension increases exponentially as the number of degrees of freedom is increased, yielding, e.g.,  $D = 2^N$  for a system of  $N$  spin-1/2. For a numerical method this means that a full uncompressed encoding of the wave function requires to store an exponentially large number of coefficients in memory. The approach to construct a complete representation of the basis of the many-body Hilbert space and a corresponding matrix representation of the Hamiltonian is called *exact diagonalization* (ED); see for example (Sandvik, 2010). By diagonalizing the Hamiltonian matrix the exact eigenenergies and eigenstates are obtained, which allows to compute all system properties in and out of equilibrium. Symmetries can be exploited to restrict the problem to symmetry sectors of interest, but the largest feasible system sizes are no more than  $N \approx 40$  spin-1/2 degrees of freedom; a recent record is the study of the low energy part of the spectrum of a spin-1/2 system with  $N = 48$  lattice sites employing cutting-edge techniques to exploit the power of a modern supercomputer (Läuchli *et al.*, 2016). In order to address larger system sizes compressed representations of the wave function are required or further approximations have to be employed.



A distinct feature of ground states of gapped systems is the fact that they obey an area law of entanglement, i.e., the entanglement entropy of a subsystem is proportional to the surface of the system (Eisert *et al.*, 2010). This means that ground states in low dimensional systems are only weakly entangled, which is exploited in the *Density Matrix Renormalization Group* (DMRG) (White, 1992; Schollwöck, 2005; Schollwöck, 2011) and related algorithms based on *matrix product states* (MPS). The MPS ansatz allows an efficient representation of compressed many-body states, where the degree of entanglement that is retained in the MPS guides the compression. This allows to restrict ground state searches in low-dimensional systems to a small part of the total Hilbert space. When the initial state is a ground state obeying the area law the time evolution will continuously build up entanglement meaning that the time-evolved state will remain moderately entangled for some time. The evolution of the wave function of one-dimensional systems up to intermediate times can therefore be computed with MPS algorithms; however, the linear growth of entanglement with time (cf. Section 1.2.2) still means an exponential increase of the complexity of the MPS, which eventually renders further evolution unfeasible.

In the case of high dimensions, *Dynamical Mean Field Theory* (DMFT), which becomes exact in the limit of infinite connectivity, is a powerful nonperturbative method to study correlated systems in the thermodynamic limit (Metzner and Vollhardt, 1989; Georges *et al.*, 1996; Vollhardt, 2012). In DMFT the lattice system is self-consistently mapped to a model of a single impurity coupled to a noninteracting bath. This dual problem can be solved efficiently by other methods (see below). In the self-consistency loop usually spatial fluctuations are discarded, which is justified in high dimensions. Therefore, extensions of the scheme have to be employed to study systems without translational invariance or with antiferromagnetic order (Maier *et al.*, 2005). A nonequilibrium extension of DMFT allows to study also nonequilibrium dynamics of high-dimensional systems (Freericks *et al.*, 2006; Aoki *et al.*, 2014).

The impurity problem occurring in DMFT is an interesting setting at its own right, comprising, e.g., the Kondo effect and transport through quantum dots. A generic and numerically exact solver for this problem is *Quantum Monte Carlo* (QMC), which relies on the efficient sampling of the important terms in the series expansion of the partition function, thereby yielding the Green's functions of interest (Gull *et al.*, 2011). A serious obstacle when computing real time dynamics of fermionic systems in this approach is the dynamical sign problem, which restricts real-time QMC to short times; however, recently substantial progress has been reported in this respect (Cohen *et al.*, 2015). Another method to solve the impurity problem in equilibrium is the *Numerical Renormalization Group* (NRG) (Wilson, 1975). An extension, the time-dependent NRG, can be used to simulate nonequilibrium situations (Anders and Schiller, 2005).

An alternative approach, which is in principle independent of the dimensionality of the system of interest, is based on the encoding of the many-body wave function in networks of classical degrees of freedom. Artificial neural networks constitute a very general class of such networks (Carleo and Troyer, 2017) and first studies indicate that they are capable of capturing entanglement with high efficiency (Deng *et al.*, 2016, 2017; Huang and Moore, 2017; Gao and Duan, 2017; Kaubruegger *et al.*, 2017). Therefore, these classical network wave functions are a candidate to bridge the gap between methods suited for low and high

dimensions. In Chapter 3 of this thesis a new method is developed that allows to construct such networks perturbatively.

Besides these approaches, which are mainly based on numerics, there exist various analytical techniques that can be applied to gain insights into the dynamics of systems suited for the respective method. By means of a *Jordan-Wigner-transform* a class of one-dimensional spin Hamiltonians can be mapped to equivalent noninteracting fermions, allowing to derive analytical expressions for all quantities of interest (Lieb *et al.*, 1961; Pfeuty, 1970); see also Section 4.2. The Kitaev honeycomb model studied in Section 2.1.1 of this thesis is an exceptional case, where a Jordan-Wigner-transform yields an exact solution for a spin system in two dimensions. Another class of exactly solvable models can be treated by *Bethe ansatz* techniques (Bethe, 1931; Korepin *et al.*, 1993; Doikou *et al.*, 2010). This applies for example to the anisotropic spin-1/2 Heisenberg chain (XXZ model) and the Lieb-Liniger model of a one-dimensional bosonic gas with delta interactions, which describes the quantum Newton's cradle discussed in Section 1.1 (van den Berg *et al.*, 2016). Both types of models, those treatable with Bethe ansatz and the ones that can be mapped to free fermions, belong to the class of integrable systems introduced in Section 1.2.1.

Moreover, for critical systems analytical insights can be gained by studying the corresponding *conformal field theory* that emerges in the continuum limit (Calabrese and Cardy, 2004, 2006) and *bosonization* allows to study properties of fermions in one dimension with a linear dispersion at the Fermi level (von Delft and Schoeller, 1998; Cazalilla, 2006; Abeling *et al.*, 2017). The dynamics of generic model Hamiltonians can be treated by *unitary perturbation theory*, which is a generalization of canonical perturbation theory known from classical mechanics (Hackl and Kehrein, 2008, 2009). It is based on the flow equation method that can be interpreted as a renormalization group scheme that successively reduces an energy-transfer cutoff imposed on off-diagonal elements of the Hamiltonian instead of an ultraviolet energy cutoff known from equilibrium renormalization group approaches (Kehrein, 2006).

Finally, for systems in the semiclassical limit it is useful to study the dynamics in a phase space approach (Polkovnikov, 2010). For this purpose the *Truncated Wigner Approximation* constitutes an established method to treat systems with large spins or high densities of bosons. A recent extension allows to treat also fermionic systems (Davidson *et al.*, 2017), which will be applied in a study of echo dynamics in Section 4.6 of this thesis.

## 1.4 Scope and main results of this thesis

This thesis deals with different aspects of the dynamics of closed quantum many-body systems far from equilibrium. These aspects can be divided into three categories, namely phase transitions beyond equilibrium, the development of a method to represent time-evolved quantum states as classical networks, and the question how to understand irreversibility in the context of quantum many-body systems. Accordingly, the main body of the thesis is divided into three chapters (Chapters 2-4), each covering one of the aspects. In the following paragraphs the treated issues are briefly motivated and the main results are summarized.

## Phase transitions beyond equilibrium

Chapter 2 treats both types of dynamical critical behavior introduced in Section 1.2.2. The first part addresses the question whether DQPTs, which were in the original work identified in a one-dimensional system (Heyl *et al.*, 2013), occur also in two dimensions and what are the characteristics of the corresponding nonanalyticities. In order to answer these questions the dynamics of the Kitaev model on a honeycomb lattice is studied. This spin system, although two-dimensional, is exactly solvable and therefore suited to yield analytical insights. The study lays a focus on the distribution of Fisher zeros in the complex time plane, which form areas as opposed to lines that occur in one-dimensional systems. These zeros indeed cover the real time axis indicating critical times and it is pointed out how the character of the nonanalyticity can be derived using an analogy to classical electrodynamics.

The second part of this chapter deals with dynamical transitions occurring in the nonequilibrium steady state of Chern insulators after a quench. Since the Chern number that characterizes the topological phases of the system is a ground state property it is a priori unclear whether and how the topological nature of the system is reflected in the time-evolved state. In equilibrium the Hall conductance is at low temperatures in direct correspondence to the topological invariant. In this thesis (Section 2.2.1) the Hall conductance is studied in the asymptotic steady state after a quench, showing that the system undergoes a topologically driven nonequilibrium phase transition whenever the Hamiltonian parameters are quenched across an equilibrium phase boundary. Since far from equilibrium, the Hall conductance after a quench is, however, not quantized and the phase transition is indicated by a continuous nonanalyticity as a function of the quench parameters, which is universal for systems with conic gap closing points. In Section 2.2.2 the analysis is generalized to Floquet topological insulators, which are candidate systems for the experimental observation of the predicted behavior.

## Quantum dynamics from classical networks

As discussed in Section 1.3 the efficient encoding of the many-body wave function is a key challenge of quantum many-body theory. Chapter 3 comprises a discussion of the strengths and shortcomings of methods that are applied later in Chapter 4 before introducing the idea to use classical networks for the compressed representation of quantum states. This approach has been applied successfully in various contexts (Carleo *et al.*, 2012, 2014; Cevolani *et al.*, 2015; Blaß and Rieger, 2016; Hafner *et al.*, 2016). Usually, the chosen network structure is motivated by heuristic considerations and justified a posteriori. In this thesis a new method is introduced to analytically construct classical networks for the description of the quantum dynamics in many-body systems in a controlled way. The perturbative construction encodes time-evolved quantum states of spin-1/2 systems in a network of classical spins with local couplings, such that observable expectation values take the form of thermal averages, which can be sampled efficiently using Monte Carlo algorithms. With this construction the transient dynamics of the transverse-field Ising model in one, two, and three dimensions is studied including local observables, entanglement production, and Loschmidt amplitudes. The derived networks can be mapped to equivalent artificial neural network wave functions as introduced by (Carleo and Troyer, 2017). Thereby a constructive prescription is provided

to design networks suited for numerical time evolution using a time-dependent variational principle (Dirac, 1930; Jackiw and Kerman, 1979; Haegeman *et al.*, 2011; Carleo *et al.*, 2012).

## Irreversibility

While it is understood that classical dynamics is irreversible if it is chaotic, there is to date no commonly accepted explanation of the origin of irreversibility in quantum systems and what “irreversible” actually means in this context. The question of irreversibility is, however, inseparably connected to thermalization, because a genuine thermal state contains no information about initial conditions.

In Chapter 4 the dynamics of observable echoes occurring under imperfect effective time reversal is studied. It is found that in generic quantum many-body systems the echoes decay exponentially as the waiting time is increased. The rate of this decay is largely independent of the magnitude of the imperfection meaning that any effort to improve the precision of the time reversal procedure is ultimately futile. This implies that the dynamics is irreversible for all practical purposes. By contrast, a study of a spin system with quadratic Hamiltonian reveals algebraically decaying echoes and even the possibility of an ever persisting echo for a specific time reversal protocol. Hence, the recovery of the initial state by time reversal can be affordable in the absence of interactions.

The considered echo protocol can be related to the recent discussion of out-of-time-order correlators, which were suggested to probe the butterfly effect and loss of local information in quantum systems, because the prescription for imperfect effective time reversal effectively amounts to measuring an out-of-time-order double commutator. This connection is addressed in Sections 4.5 and 4.6. Section 4.5 comprises a numerical study of out-of-time-order correlators and double commutators as possible indicators of scrambling. In Section 4.6 echo dynamics are analyzed in a semiclassical approach, indicating that said double commutators are responsible for an exponential divergence from perfect echoes, which can be associated with a Lyapunov exponent. In combination, the results indicate that the out-of-time-order double commutators, motivated by echo dynamics, might constitute an alternative probe of the quantum butterfly effect.

# Chapter 2

## Phase transitions beyond equilibrium

The sudden change of system properties as a control parameter is smoothly varied is a primary topic of interest in the study of many-body systems in thermal equilibrium. The theory of phase transitions, which has been developed over the past century, provides a sound conceptual framework for the understanding of these phenomena (Stanley, 1971; Fisher, 1974; Sachdev, 2011). The nonequilibrium dynamics of quantum many-body systems can similarly exhibit sudden changes. However, there is to date no unified framework covering the different nonequilibrium critical phenomena that have been identified in recent years.

In the first part of this chapter (Section 2.1) dynamical quantum phase transitions (DQPTs) are studied, where in analogy to equilibrium phase transitions time occurs as the control parameter that drives the transition indicated by nonanalyticities in the real time dynamics. The second part of this chapter (Section 2.2) deals with phase transitions in nonequilibrium steady states reached after a quench as a function of an external control parameter. Note that recent works suggest that both types of transitions are closely related (Žunkovič *et al.*, 2016; Wang and Xianlong, 2017).

### 2.1 Dynamical quantum phase transitions

The equilibrium properties of a system with Hamiltonian  $\hat{H}$  are determined by the corresponding canonical partition function

$$Z(\beta) = \text{tr}(e^{-\beta\hat{H}}) , \quad (2.1)$$

where  $\beta$  denotes the inverse temperature. All thermodynamic properties of the system can be inferred from the partition function, which is related to the free energy  $F$  by

$$F = -\frac{1}{\beta} \ln Z . \quad (2.2)$$

Equilibrium phase transitions occur when the free energy is nonanalytic as function of some control parameter, e.g. the temperature or an external magnetic field. The nonanalyticity of the free energy implies nonanalytic behavior of the corresponding susceptibilities, which are observed in experiment.

The key quantity for DQPTs is the *Loschmidt amplitude* (Heyl *et al.*, 2013)

$$\mathcal{G}(t) = \langle \psi_0 | e^{-i\hat{H}t} | \psi_0 \rangle , \quad (2.3)$$

which is the overlap of a time-evolved state  $|\psi(t)\rangle = e^{-i\hat{H}t}|\psi_0\rangle$  with the initial state  $|\psi_0\rangle$ . The initial state is usually chosen to be the ground state of an initial Hamiltonian  $\hat{H}_0$ . The corresponding return probability

$$\mathcal{L}(t) = |\langle \psi_0 | e^{-i\hat{H}t} | \psi_0 \rangle|^2 \quad (2.4)$$

is called *Loschmidt echo*. Note that this object received its name in the context of irreversibility (Peres, 1984) as will be further elaborated in Section 4.1.

As the system size  $N$  becomes large the Loschmidt amplitude typically assumes large deviation form (Gambassi and Silva, 2012; Heyl *et al.*, 2013)

$$\mathcal{G}(t) \sim e^{-Ng(t)} , \quad (2.5)$$

which defines the rate function

$$g(t) = - \lim_{N \rightarrow \infty} \frac{1}{N} \ln (\mathcal{G}(t)) . \quad (2.6)$$

Analogously, for the Loschmidt echo

$$\lambda(t) = - \lim_{N \rightarrow \infty} \frac{1}{N} \ln (\mathcal{L}(t)) = 2\text{Re}[g(t)] . \quad (2.7)$$

If the initial Hamiltonian  $\hat{H}_0$  has degenerate ground states  $|\psi_0^{(n)}\rangle$  it is useful to define a generalized Loschmidt echo as the probability to return to the ground state manifold

$$P(t) = \sum_n |\langle \psi_0^{(n)} | \psi(t) \rangle|^2 . \quad (2.8)$$

Formally, the Loschmidt amplitude resembles a boundary partition function (LeClair *et al.*, 1995)

$$Z(z) = \langle \psi_0 | e^{-z\hat{H}} | \psi_0 \rangle \quad (2.9)$$

in the complex plane  $z \in \mathbb{C}$ . For equilibrium partition functions it is understood that the free energy, Eq. (2.2), can become nonanalytic in the thermodynamic limit although  $Z(\beta)$  is a sum of analytic functions, because in the thermodynamic limit *Fisher zeros* in the complex temperature plane coalesce to lines crossing the real temperature axis (Fisher, 1965; Yang and Lee, 1952). Analogously, zeros in the complex time plane can lead to nonanalyticities in the Loschmidt amplitude as will be detailed in Section 2.1.1. In this case the rate function  $\lambda(t)$  can become nonanalytic if zeros in the complex time plane cover the real time axis. Accordingly,  $\lambda(t)$  is sometimes also called *dynamical free energy density*. Nonanalytic behavior of  $\lambda(t)$  was first reported by (Pollmann *et al.*, 2010), but the interpretation as a dynamical critical phenomenon was only worked out by (Heyl *et al.*, 2013), who studied the dynamics after a



quench in the transverse-field Ising model. Heyl et al. define a DQPT as the occurrence of a nonanalyticity in the rate function of the Loschmidt echo as a function of time. In the case of the transverse-field Ising model DQPTs occur as kinks of  $\lambda(t)$  at the critical time  $t_c$ , which can be directly related to zeros of the Loschmidt echo in the complex time plane crossing the real time axis.

Clearly, overlaps like the Loschmidt amplitude (2.3) are hard to measure in experiments. Nevertheless, the direct observation of a DQPT has been reported recently (Jurcevic *et al.*, 2017). The experiment was performed on trapped ions, which effectively realize a transverse-field Ising Hamiltonian with long-range interactions. In that case the generalized Loschmidt echo defined in Eq. (2.8) was considered, based on which further theoretical input and the possibility to measure both contributing overlaps independently allowed to conclude the behavior in the thermodynamic limit from measurements on finite systems. In the experiment the system was prepared in a polarized ground state of the ferromagnetic phase before the magnetic field was quenched across the phase transition. Fig. 2.1(a) shows the result for the rate function of the generalized Loschmidt echo obtained from the measurements in comparison with numerical results. The experimental data clearly reflect the nonanalytic behavior of the rate function in the form of a kink at the critical time; see also Fig. 1.8.

Since the definition of DQPTs regards just the overlap of the time-evolved state with the initial state it is apriori not clear how this can affect the dynamics of experimentally accessible observables. This is similar to quantum phase transitions, which occur at zero temperature and therefore elude direct observation in experiment. However, the effects of both types of transitions beyond initial state overlaps or pure ground states, respectively, can be understood in a similar way. For quantum phase transitions driven by a control parameter  $\kappa$  it is known that the quantum critical point at temperature  $T = 0$  affects the system at temperatures  $T > 0$  in the form of a quantum critical region in the  $T - \kappa$  diagram that extends to nonzero temperatures above the critical point as depicted in Fig. 2.2(a). An analogous picture is obtained for DQPTs when considering time  $t$  as control parameter and energy density  $\epsilon$  with respect to the *initial* Hamiltonian  $\hat{H}_0$  instead of temperature (Heyl, 2014, 2017; Jurcevic *et al.*, 2017), cf. Fig. 2.2(b). In the corresponding diagram the DQPT occurs as a non-analyticity at  $\epsilon = 0$ , but its influence extends to higher energy densities in the form of a critical region, which can be traversed in the dynamics. This relation can be probed explicitly in systems with symmetry breaking like in the trapped ion experiment described above, if the

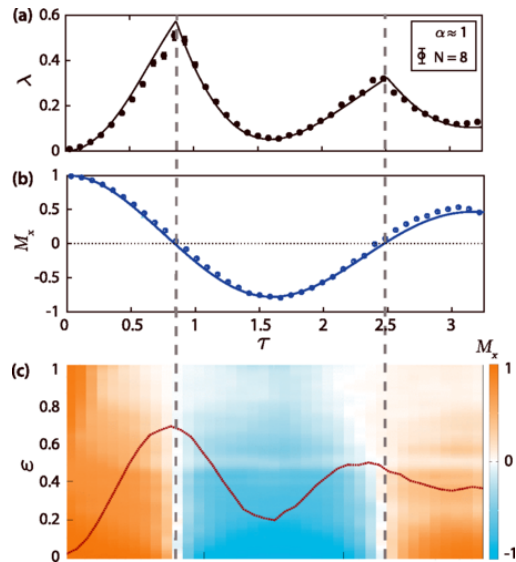


**Fig. 2.1:** Experimental observation of a DQPT. (a) The DQPT is identified by kinks in the rate function  $\lambda(t)$  at the critical time. (b) The measured longitudinal magnetization has roots at the critical times. (c) The energy-time resolved magnetization indicates how the critical point at  $\epsilon = 0$  controls the magnetization dynamics at higher energy densities. Reprinted figure with permission from (Jurcevic *et al.*, 2017) Copyright 2017 by the American Physical Society. <https://link.aps.org/doi/10.1103/PhysRevLett.119.080501>

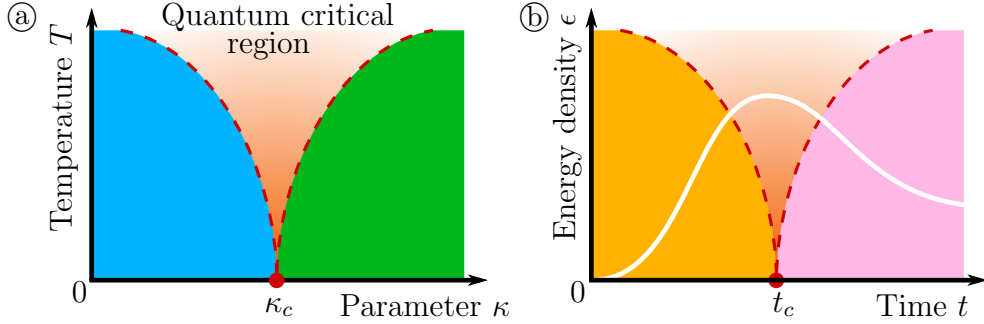


**Fig. 2.2:** Analogy between quantum phase transitions and DQPTs as conceived in (Heyl, 2014; Jurcevic *et al.*, 2017). (a) The quantum critical point at  $T = 0$  affects the system properties at  $T > 0$  in the form of a quantum critical region and two crossover lines. (b) A DQPT occurs as nonanalyticity as function of time at vanishing energy density  $\epsilon$  (measured with the initial Hamiltonian). Dynamics of observables after a quench have their dominant contribution at  $\epsilon > 0$  (indicated by the white line), but there can still be a “critical region” controlled by the critical point.

order parameter commutes with the initial Hamiltonian,  $[\hat{M}, \hat{H}_0] = 0$ . In that case the energy-resolved order parameter  $M(\epsilon, t)$  can be obtained (Heyl, 2014), which is plotted in Fig. 2.1(c) together with the mean energy density  $\epsilon(t) = \langle \psi(t) | \hat{H}_0 | \psi(t) \rangle / N$  indicating how the system traverses the energy-time plane after the quench. At  $\epsilon = 0$  the order parameter exhibits a jump at the critical time. At nonzero energy the time evolution of the order parameter is smooth, but the DQPT still affects the dynamics in the form of roots of the observable at the critical times as shown in Fig. 2.1(b).

DQPTs typically occur when a system is initially prepared in one equilibrium phase and the dynamics is induced by quenching a system parameter across a critical point in the equilibrium phase diagram. There are, however, counterexamples, where either quenching across a phase transition does not lead to DQPTs or DQPTs occur after quenches within one phase (Canovi *et al.*, 2014; Andraschko and Sirker, 2014; Vajna and Dóra, 2015; Schmitt and Kehrein, 2015). Generally, a criterion for the occurrence of DQPTs is that a sufficiently high energy density is added to the system by the quench, such that the initial state is clearly nonthermal; this is usually the case when a system is quenched across an equilibrium critical point. In noninteracting systems the inversion of quasiparticle momentum occupation leads to DQPTs (Heyl *et al.*, 2013; Schmitt and Kehrein, 2015).

A particularly strong connection between DQPTs and the equilibrium phase diagram exists in noninteracting topological systems. For this class of systems it was proven that in one dimension any quench across the underlying topological phase boundary necessarily induces DQPTs in the subsequent dynamics, whereas in two dimensions DQPTs occur if the corresponding ground state Chern numbers differ in their absolute value (Vajna and Dóra, 2015; Huang and Balatsky, 2016). In topological systems it is moreover possible to identify dynamical order parameters, which distinguish between different dynamical phases (Budich and Heyl, 2016; Bhattacharya and Dutta, 2017; Fläschner *et al.*, 2016). One such dynamical order parameter was measured in a recent experiment (Fläschner *et al.*, 2016). Due to the strict relation to DQPTs it is therefore possible to infer information about the ground state



phase diagram from the observed dynamics far from equilibrium.

The following section comprises a study of DQPTs in the Kitaev model on a honeycomb lattice. With regard to DQPTs it is interesting for various aspects. Firstly, it is a two-dimensional spin system, which is nevertheless exactly solvable by Jordan-Wigner transformation. Therefore it is suited to investigate analytically whether DQPTs occur at all also in higher dimensions and how the characteristics change. It turns out that the higher dimensionality affects the structure of the Fisher zeros in the complex time plane in that they form areas instead of lines, which changes the character of the nonanalyticity. Moreover, the Kitaev model has a rich phase diagram including gapless and topological phases, which allows to study the relation of DQPTs to the underlying equilibrium phase diagram.

Note that the presentation of DQPTs above is clearly not exhaustive, although the most relevant conceptual aspects were outlined. The reader is referred to two recent reviews, which give a more detailed account of the current state of understanding of this phenomenon ([Zvyagin, 2016](#); [Heyl, 2017](#)).

### 2.1.1 *Publication:* Dynamical quantum phase transitions in the Kitaev honeycomb model

Reprinted article with permission from

Markus Schmitt and Stefan Kehrein

Physical Review B **92**, 075114 (2015)

<https://doi.org/10.1103/PhysRevB.92.075114>

Copyright (2015) by the American Physical Society.

**Author contributions** M. S. did the analytic and numerical calculations and wrote the article. S. K. suggested to study DQPTs in this model and revised the manuscript. Both authors discussed the results.

# Dynamical quantum phase transitions in the Kitaev honeycomb model

Markus Schmitt\* and Stefan Kehrein

*Institut für Theoretische Physik, Georg-August-Universität Göttingen, D-37077 Göttingen, Germany*

(Received 20 May 2015; published 10 August 2015)

The notion of a dynamical quantum phase transition (DQPT) was recently introduced [Heyl *et al.*, *Phys. Rev. Lett.* **110**, 135704 (2013)] as the nonanalytic behavior of the Loschmidt echo at critical times in the thermodynamic limit. In this work the quench dynamics in the ground state sector of the two-dimensional Kitaev honeycomb model is studied regarding the occurrence of DQPTs. For general two-dimensional systems of BCS type it is demonstrated how the zeros of the Loschmidt echo coalesce to areas in the thermodynamic limit, implying that DQPTs occur as discontinuities in the second derivative. In the Kitaev honeycomb model DQPTs appear after quenches across a phase boundary or within the massless phase. In the 1d limit of the Kitaev honeycomb model it becomes clear that the discontinuity in the higher derivative is intimately related to the higher dimensionality of the nondegenerate model. Moreover, there is a strong connection between the stationary value of the rate function of the Loschmidt echo after long times and the occurrence of DQPTs in this model.

DOI: [10.1103/PhysRevB.92.075114](https://doi.org/10.1103/PhysRevB.92.075114)

PACS number(s): 64.70.Tg, 05.70.Ln, 05.30.Rt

## I. INTRODUCTION

Recent advances in experimental techniques allow us to realize closed quantum systems with cold atomic gases in optical traps [1,2]. These setups are precisely controllable and the unitary time evolution of the systems can be resolved such that the dynamics is experimentally accessible under well-known conditions. Motivated by the new experimental possibilities a lot of theoretical research on the nonequilibrium dynamics of quantum systems has been conducted in the past years. In these theoretical investigations a common protocol for driving a system out of equilibrium is called *quantum quench*. Considering a parametrized Hamiltonian  $H(\alpha)$ , where the parameter typically corresponds to some external field strength in the experimental setup, the system is initially assumed to be in equilibrium with regard to some value  $\alpha_i$  of the parameter. Then, the parameter is suddenly *quenched* to a different final value  $\alpha_f$  driving the system out of equilibrium and inducing a nontrivial time evolution.

Studying the quench dynamics of a quantum many-body system, Heyl *et al.* [3] pointed out the close formal similarity of the canonical partition function of an equilibrium system,  $Z(\beta) = \text{tr}(e^{-\beta H})$ , and the return amplitude

$$\mathcal{G}(t) = \langle \psi_i | e^{-iHt} | \psi_i \rangle \quad (1)$$

of a time-evolved state, suggesting the possibility of critical behavior in the time evolution in analogy to equilibrium phase transitions. It is known that in the thermodynamic limit the zeros of a partition function coalesce to lines in the complex temperature plane and the equilibrium phase transition is marked by the intersection of the zero line with the real temperature axis [4]. Heyl *et al.* found that in the case of the transverse field Ising model the boundary partition function

$$Z(z) = \langle \psi_i | e^{-zH} | \psi_i \rangle \quad (2)$$

has zeros in the complex time plane, which accordingly coalesce to lines in the thermodynamic limit. These lines cross the real time axis after quenching the external field across the

quantum critical point inducing nonanalyticities in the rate function of the Loschmidt echo

$$\begin{aligned} r(t) &= - \lim_{N \rightarrow \infty} \frac{1}{N} \ln |\langle \psi_i | e^{-iHt} | \psi_i \rangle|^2 \\ &= - \lim_{N \rightarrow \infty} \frac{1}{N} \ln \mathcal{L}(t) \end{aligned} \quad (3)$$

at equidistant critical times  $t_n^*$ . Heyl *et al.* denote this nonanalytic behavior at critical times in the thermodynamic limit as a dynamical quantum phase transition (DQPT). They showed that in experiment the DQPT would be observable by measuring the work distribution function of a double quench; in particular, the Loschmidt echo  $\mathcal{L}(t) = |\langle \psi_i | e^{-iHt} | \psi_i \rangle|^2$  is the probability of performing no work.

These findings triggered further work aiming at a better understanding of the phenomenon. By considering an additional integrability-breaking interaction in the transverse field Ising chain it was demonstrated that DQPTs are not a peculiarity specific to integrable models, but are stable against some nonintegrable perturbations [5,6]. Moreover, the signature of DQPTs was found in higher-dimensional systems, namely, in two-dimensional topological insulators [7] and effectively infinite dimensions using DMFT [8]. It was observed in various cases that DQPTs are not necessarily connected to quenching across a quantum critical point [8–11]; however, there seems to be a strong connection to topological phase transitions [7,12]. Canovi *et al.* [8] detected coexisting solutions for so called generalized expectation values in postquench dynamics and, therefore, they introduced the notion of a first-order dynamical phase transition. This could be a way to classify dynamical phase transitions. Furthermore, zeros in the oscillations of the Schmidt gap were related to DQPTs [13] and a close connection between the analytic behavior of  $r(t)$  in the complex plane and its long time limit is conjectured [14].

In this work we study quench dynamics in the Kitaev honeycomb model [15] regarding dynamical quantum phase transitions. The model features a rich phase diagram comprising an extended gapless phase, anyonic excitations, and topological order. Moreover, it is a rare example of a Jordan-Wigner-solvable model in two dimensions [16,17]. As such it has been

\*markus.schmitt@theorie.physik.uni-goettingen.de

studied extensively under various aspects. In this paper we restrict the discussion to the dynamics in the ground state sector.

The dynamics of gapped two-dimensional two-band systems was already studied by Vajna and Dóra with focus on a connection between DQPTs and topological phases [7]. In the presence of a magnetic field the Kitaev model acquires topological order and becomes a system of the same family, albeit being a spin model. In that case we find the behavior in accordance with their results; namely, DQPTs occur after quenches across the boundary between phases with different Chern number. However, the focus of this work lies on quenching between the topologically trivial phases in the absence of a magnetic field. Similarly to their results we find DQPTs as discontinuities in the second derivative, which is inherent to the higher dimensionality of the system, and we elaborate on the relevance of the complex zeros of the dynamical partition function in this context. Moreover, we discuss a remarkable observation regarding the long time behavior of the Loschmidt echo. If no DQPTs occur in the postquench dynamics, then, although the approached stationary state is always an excited state, the long time limit of the Loschmidt echo is given by the fidelity, i.e., the overlap of the initial state with the ground state of the quenched Hamiltonian. This, however, does not hold if the dynamics exhibits DQPTs.

The rest of this paper is organized as follows: In Sec. II the way of solving the model using Jordan-Wigner transformation is sketched and the phase diagram is introduced. Furthermore, the expressions for the dynamical free energy are derived. In Sec. III the zeros of the dynamical partition function in the complex time plane are treated assuming a general BCS-type Hamiltonian, yielding the criteria for the occurrence of DQPTs and the order of the corresponding nonanalyticity. Finally, the zeros of the partition function and the real time evolution are studied explicitly for the Kitaev model in Sec. IV, and two interesting limits are taken into account as well as ramping as an alternative protocol and the quenching with an additional magnetic field.

## II. THE KITAEV HONEYCOMB MODEL

### A. The model

The Kitaev honeycomb model is defined by the Hamiltonian

$$H(\vec{J}) = - \sum_{\alpha \in \{x, y, z\}} \sum_{\alpha\text{-links}} J_{\alpha} \sigma_j^{\alpha} \sigma_k^{\alpha}, \quad (4)$$

which describes a spin-1/2 system with the spins located on the vertices (labeled by  $j, k$ ) of a honeycomb lattice as depicted in Fig. 1 [15]. In this paper we assume the lattice spacing to equal unity. It has been shown [17] that for the above Hamiltonian one can find a Jordan-Wigner contour, which after identifying a conserved  $Z_2$  operator [18] and switching to momentum space yields a BCS-type Hamiltonian

$$H(\vec{J}) = \sum_{\vec{k}} \left[ \frac{\epsilon_{\vec{k}}(\vec{J})}{2} (d_{\vec{k}}^{\dagger} d_{\vec{k}} - d_{-\vec{k}} d_{-\vec{k}}^{\dagger}) + \frac{\Delta_{\vec{k}}(\vec{J})}{2} (d_{\vec{k}}^{\dagger} d_{-\vec{k}}^{\dagger} + d_{-\vec{k}} d_{\vec{k}}) \right] \quad (5)$$

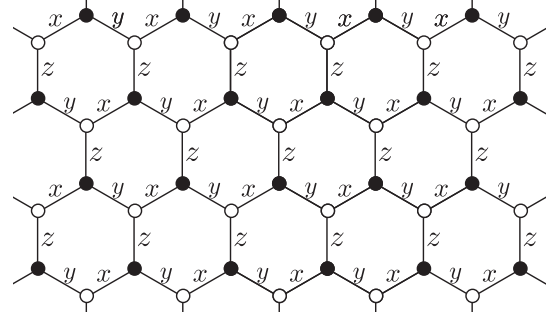


FIG. 1. Lattice of the Kitaev honeycomb model given by Eq. (4). Spin-1/2 degrees of freedom are sitting on the vertices of a honeycomb lattice. The nearest neighbor interaction depends on the link type ( $x, y, \text{ or } z$ ).

with

$$\begin{aligned} \epsilon_{\vec{k}}(\vec{J}) &= 2[J_z + J_x \cos(k_x) + J_y \cos(k_y)], \\ \Delta_{\vec{k}}(\vec{J}) &= 2[J_x \sin(k_x) + J_y \sin(k_y)]. \end{aligned} \quad (6)$$

This Hamiltonian can be diagonalized by a Bogoliubov transformation

$$\begin{pmatrix} a_{\vec{k}}^{\vec{J}} \\ a_{-\vec{k}}^{\vec{J}\dagger} \end{pmatrix} = \begin{pmatrix} u_{\vec{k}}(\vec{J}) & v_{\vec{k}}(\vec{J}) \\ -v_{\vec{k}}(\vec{J})^* & u_{\vec{k}}(\vec{J})^* \end{pmatrix} \begin{pmatrix} d_{\vec{k}} \\ d_{-\vec{k}}^{\dagger} \end{pmatrix}, \quad (7)$$

where

$$\begin{aligned} u_{\vec{k}}(\vec{J}) &= \sqrt{\frac{1}{2} \left( 1 + \frac{\epsilon_{\vec{k}}(\vec{J})}{E_{\vec{k}}(\vec{J})} \right)}, \\ v_{\vec{k}}(\vec{J}) &= \text{sgn}[\Delta_{\vec{k}}(\vec{J})] \sqrt{\frac{1}{2} \left( 1 - \frac{\epsilon_{\vec{k}}(\vec{J})}{E_{\vec{k}}(\vec{J})} \right)} \end{aligned} \quad (8)$$

(see Appendix A for details). Plugging the transformation into Eq. (5) yields the diagonal Hamiltonian

$$H(\vec{J}) = \sum_{\vec{k} \in K} \frac{E_{\vec{k}}(\vec{J})}{2} (a_{\vec{k}}^{\dagger} a_{\vec{k}} - a_{-\vec{k}} a_{-\vec{k}}^{\dagger}) \quad (9)$$

with spectrum

$$E_{\vec{k}}(\vec{J}) = \sqrt{\epsilon_{\vec{k}}(\vec{J})^2 + \Delta_{\vec{k}}(\vec{J})^2}. \quad (10)$$

The Hamiltonian splits into a sum over  $\vec{k}$  sectors, i.e., a sum over  $\vec{k} \in K$ , where  $K$  is a subset of the Brillouin zone such that  $\forall \vec{k} \in K, -\vec{k} \notin K$ . A possible choice is one half of the Brillouin zone, e.g., all  $\vec{k}$  with  $k_x > 0$  [19].

The spectrum has roots at

$$\begin{aligned} k_x &= \pm \arccos \left( \frac{J_y^2 - J_x^2 - J_z^2}{2J_x J_z} \right), \\ k_y &= \mp \arccos \left( \frac{J_x^2 - J_y^2 - J_z^2}{2J_y J_z} \right) \end{aligned} \quad (11)$$

if  $|J_{\alpha}| < |J_{\beta}| + |J_{\gamma}|$ , where  $(\alpha, \beta, \gamma)$  is any permutation of  $(x, y, z)$ . We will in the following only consider nonnegative  $J_{\alpha}$  on the  $J_x + J_y + J_z = 1$  plane. In this section the above result

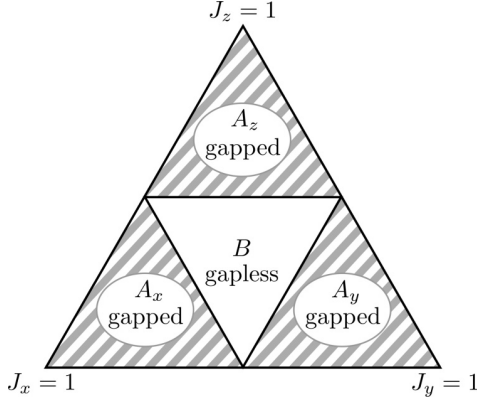


FIG. 2. Phase diagram of the Kitaev model in the  $J_x + J_y + J_z = 1$  plane, where  $J_\alpha \geq 0$ . The gapless phase  $B$  is surrounded by three gapped phases  $A_\alpha$ , where  $J_\alpha > J_\beta + J_\gamma$ .

on the gappedness of the spectrum corresponds to a phase diagram as depicted in Fig. 2. The gapless phase  $B$  at the center of the diagram is surrounded by three distinct gapped phases [15]  $A_x$ ,  $A_y$ , and  $A_z$ , where  $J_x > J_y + J_z$ ,  $J_y > J_x + J_z$ , or  $J_z > J_y + J_x$ , respectively.

In the presence of a magnetic field  $\vec{h}$  the spin Hamiltonian (4) becomes

$$H(\vec{J}, \vec{h}) = - \sum_{\alpha \in \{x, y, z\}} \left( \sum_{\alpha\text{-links}} J_\alpha \sigma_j^\alpha \sigma_k^\alpha + \sum_j h_\alpha \sigma_j^\alpha \right) \quad (12)$$

and the additional term opens a gap also in the  $B$  phase. Moreover, the  $B$  phase becomes topologically nontrivial with Chern number  $\nu = \pm 1$ , whereas the  $A_\alpha$  phases remain trivial with  $\nu = 0$  [15]. At  $J_x = J_y = J_z = J$  there exists a diagonal form of the Hamiltonian even with nonzero magnetic field [15] and the spectrum reads

$$E_{\vec{k}}(J, h) = \sqrt{\tilde{\epsilon}_{\vec{k}}(J, \kappa)^2 + |\tilde{\Delta}_{\vec{k}}(J, \kappa)|^2} \quad (13)$$

with  $\tilde{\epsilon}_{\vec{k}}(J, \kappa) = \epsilon_{\vec{k}}(\vec{J})$ ,  $\vec{J} = (J, J, J)^T$ , and

$$\tilde{\Delta}_{\vec{k}}(J, \kappa) = \Delta_{\vec{k}}(\vec{J}) + 4i\kappa [\sin(k_x) - \sin(k_y) + \sin(k_y - k_x)], \quad (14)$$

where  $\kappa \sim \frac{h_x h_y h_z}{J^2}$ . Through a Bogoliubov transformation (see Appendix A) this maps to

$$H(J, \kappa) = \sum_{\vec{k} \in K} \left[ \frac{\tilde{\epsilon}_{\vec{k}}(J, \kappa)}{2} (d_{\vec{k}}^\dagger d_{\vec{k}} - d_{-\vec{k}} d_{-\vec{k}}^\dagger) + \frac{\tilde{\Delta}_{\vec{k}}(J, \kappa)}{2} d_{\vec{k}}^\dagger d_{-\vec{k}}^\dagger + \frac{\tilde{\Delta}_{\vec{k}}(J, \kappa)^*}{2} d_{-\vec{k}} d_{\vec{k}} \right]. \quad (15)$$

This case will be studied in Sec. IV F. Before, we will stick to the case without magnetic field, i.e., real valued  $\epsilon_{\vec{k}}$  and  $\Delta_{\vec{k}}$ .

### B. Postquench dynamics

In order to study the dynamics in the Kitaev honeycomb model we will consider situations where the system is initially, at  $t < 0$ , prepared in the ground state of  $H(\vec{J}_0)$ , i.e.,

$H(\vec{J}_0)|\psi_i\rangle = E_{GS}|\psi_i\rangle$ . In terms of the free fermion degrees of freedom the initial state is the vacuum:  $a_{\vec{k}}^{\vec{J}_0}|\psi_i\rangle = a_{\vec{k}}^{\vec{J}_0}|0; \vec{J}_0\rangle = 0$ . At  $t = 0$  the parameter is quenched to its final value  $\vec{J}_1$ , such that for  $t > 0$  the time-evolved state is  $|\psi(t)\rangle = e^{-iH(\vec{J}_1)t}|\psi_i\rangle$ . Making use of the Bogoliubov transformation the initial state can be expressed in terms of the final free fermions, which diagonalize  $H(\vec{J}_1)$ :

$$|\psi_i\rangle = \mathcal{N}^{-1} \prod_{\vec{k} \in K} (1 + B_{\vec{k}}(\vec{J}_0, \vec{J}_1) a_{\vec{k}}^{\vec{J}_1 \dagger} a_{-\vec{k}}^{\vec{J}_1}) |0; \vec{J}_1\rangle. \quad (16)$$

Here,

$$B_{\vec{k}}(\vec{J}_0, \vec{J}_1) \equiv \frac{V_{\vec{k}}(\vec{J}_0, \vec{J}_1)}{U_{\vec{k}}(\vec{J}_0, \vec{J}_1)} = \frac{u_{\vec{k}}(\vec{J}_0)v_{\vec{k}}(\vec{J}_1) - u_{\vec{k}}(\vec{J}_1)v_{\vec{k}}(\vec{J}_0)}{u_{\vec{k}}(\vec{J}_1)u_{\vec{k}}(\vec{J}_0) + v_{\vec{k}}(\vec{J}_1)v_{\vec{k}}(\vec{J}_0)} \quad (17)$$

and the normalization constant

$$\mathcal{N}^2 \equiv \prod_{\vec{k} \in K} (1 + B_{\vec{k}}(\vec{J}_0, \vec{J}_1)^2) \quad (18)$$

were introduced and  $|0; \vec{J}_1\rangle$  is the ground state of  $H(\vec{J}_1)$ . A more detailed derivation is given in Appendix A.

For the sake of brevity and lucidity we will in the following refrain from dragging along the dependencies on  $\vec{J}_0$  and  $\vec{J}_1$  explicitly, i.e., identify  $B_{\vec{k}} \equiv B_{\vec{k}}(\vec{J}_0, \vec{J}_1)$  and  $a_{\vec{k}} \equiv a_{\vec{k}}^{\vec{J}_1}$ .

Using (16) to compute the dynamical partition function we obtain

$$Z(z) = \langle \psi_i | e^{-zH} | \psi_i \rangle \quad (19)$$

$$= \prod_{\vec{k} \in K} \frac{1 + B_{\vec{k}}^2 e^{-2E_{\vec{k}}(\vec{J}_1)z}}{1 + B_{\vec{k}}^2}. \quad (20)$$

The dynamical partition function has large deviation form  $Z(z) \sim e^{-Nf(z)}$ , where  $N$  is the system size. Thus, in the thermodynamic limit only the rate function, or dynamical free energy density,

$$f(z) = - \lim_{N \rightarrow \infty} \frac{1}{N} \ln[Z(z)] \quad (21)$$

is well defined.

## III. ZEROS OF THE PARTITION FUNCTION AND CRITICAL TIMES

### A. General aspects

From the study of equilibrium phase transitions it is known that a very insightful approach is to consider the zeros of the partition function in the complex temperature or complex magnetization plane, respectively [4,20,21]. In the thermodynamic limit the zeros of the partition function coalesce to lines or areas in the complex plane, which mark the critical points when approaching the real temperature (magnetization) axis. Analogous reasoning has proven useful in the study of dynamical quantum phase transitions [3,7].

In particular, an interesting analogy to electrodynamics allows us to characterize the dynamical phase transition through the density of zeros of the dynamical partition function in the complex time plane. The starting point is the observation

that the dynamical partition function (19) is an entire function of  $z$  and can as such, according to the Weierstrass factorization theorem, be written as

$$Z(z) = e^{h(z)} \prod_{j \in \mathcal{I}} \left(1 - \frac{z}{z_j}\right), \quad (22)$$

where  $\mathcal{I}$  is some discrete index set,  $z_j \in \mathbb{C}$  are the zeros, and  $h(z)$  is an entire function [3]. With this, the dynamical free energy density reads

$$f(z) = - \lim_{N \rightarrow \infty} \frac{1}{N} \left[ h(z) + \sum_{j \in \mathcal{I}} \ln \left(1 - \frac{z}{z_j}\right) \right]. \quad (23)$$

From this expression it becomes clear that any nonanalytic behavior of the dynamical free energy can only occur at or in the vicinity of the zeros of the dynamical partition function  $z_j$ . Since we are interested in nonanalyticities, we will in the following ignore the contribution of  $h(z)$  and only consider the singular part

$$f^s(z) = - \lim_{N \rightarrow \infty} \frac{1}{N} \sum_{j \in \mathcal{I}} \ln \left(1 - \frac{z}{z_j}\right). \quad (24)$$

In the thermodynamic limit the sum becomes an integral over some continuous variable  $x \in X$ , where  $X \subseteq \mathbb{R}^n$  is a region corresponding to the previously used index set  $\mathcal{I}$ , and the zeros become a function of this variable  $\tilde{z}(x)$ , such that

$$f^s(z) = - \int_X dx \ln \left(1 - \frac{z}{\tilde{z}(x)}\right). \quad (25)$$

A transformation of the integration variable yields

$$f^s(z) = - \int_{z(X)} d\tilde{z} \rho(\tilde{z}) \ln \left(1 - \frac{z}{\tilde{z}}\right), \quad (26)$$

where the Jacobian determinant  $\rho(\tilde{z})$  can be interpreted as the density of zeros in the complex plane [22]. Moreover, setting  $\rho(z) \equiv 0$  for  $z \notin z(X)$  allows us to extend the integration domain to the full complex plane. We will now discuss the real part

$$\phi(z) = \text{Re}[f^s(z)] = - \int_{\mathbb{C}} d\tilde{z} \rho(\tilde{z}) \ln \left|1 - \frac{z}{\tilde{z}}\right|. \quad (27)$$

We will later see that the Loschmidt echo on the real time axis is directly given by  $\phi(t)$ . For  $z = u + iv$  with  $u, v \in \mathbb{R}$   $\ln|z|$  is the Green's function of the Laplacian  $\Delta_{2D} = \frac{\partial^2}{\partial u^2} + \frac{\partial^2}{\partial v^2}$ , i.e.,

$$\Delta_{2D} \phi(z) = -2\pi \rho(z). \quad (28)$$

In other words, the real part of the dynamical free energy density can be interpreted as the electrostatic potential  $\phi(z)$  produced by a charge density  $\rho(z)$  in two dimensions and the question of the behavior of the free energy at critical points becomes the question of the behavior of the electrostatic potential at surfaces. If the zeros form lines in the complex plane, this allows us to deduce the order of the phase transition directly from the density of zeros at or in the vicinity of the physically relevant  $z$  [21].

Although the zeros can form areas in the complex plane these areas do not cover the physical axis in the case of equilibrium phase transitions. This is to be expected, since

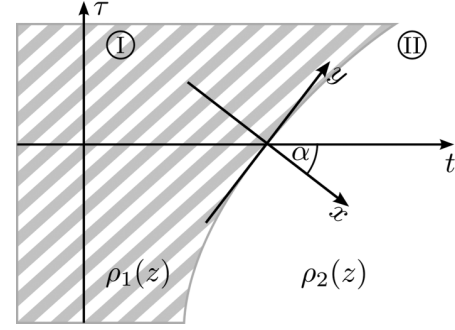


FIG. 3. Schematic picture of the surface separating two densities of zeros in the complex plane and the relevant coordinate frames for determining the behavior of  $\phi(z)$  [Eq. (27)] along the real time axis.

in thermal phase transitions there is typically only one critical point in the physical parameter [22]. However, as we will see in the following section, this is possible in the case of dynamical phase transitions. Thus, consider the situation as depicted in Fig. 3. The density of zeros is given by  $\rho_1(z)$  and  $\rho_2(z)$  in area I and II, respectively, and at the boundary there is a discontinuous change in the density of zeros. Assume the electric potentials  $\phi_i(z)$ ,  $i = 1, 2$ , solve the Laplace equation (28) with the corresponding density  $\rho_i(z)$ . With this a global solution is

$$\phi(z) = \begin{cases} \phi_1(z), & z \in I, \\ \phi_2(z), & z \in II. \end{cases} \quad (29)$$

Let us now focus on the behavior of  $\phi(z)$  at the intersection of the boundary with the real time axis. It is known from electrostatics that the curl of the electric field vanishes. If we choose the  $x$ - $y$ -coordinate frame as indicated in Fig. 3 this implies (through Stokes' theorem) that on the boundary

$$\frac{\partial^2}{\partial y^2} \phi_1(z) - \frac{\partial^2}{\partial y^2} \phi_2(z) = 0. \quad (30)$$

Since we are interested in the behavior of  $\phi(z)$  in the real time axis, we transform to  $t$ - $y'$  coordinates,

$$t = \frac{x}{\cos \alpha} + \frac{y}{\sin \alpha}, \quad (31)$$

$$y' = y.$$

With the Laplace equation (28) this yields

$$(\cos \alpha)^{-2} \frac{\partial^2}{\partial t^2} \phi_i(z) + (1 + \sin^2 \alpha)^{-1} \frac{\partial^2}{\partial y'^2} \phi_i(z) = -2\pi \rho_i(z), \quad (32)$$

and, consequently,

$$\frac{\partial^2}{\partial t^2} [\phi_1(z) - \phi_2(z)] = -2\pi (\cos \alpha)^2 [\rho_1(z) - \rho_2(z)]. \quad (33)$$

This means that if an area of zeros of the partition function overlaps the real time axis, the second derivative of the real part of the free energy is discontinuous.



### B. 2d BCS-type models

In the Kitaev honeycomb model (and general BCS-type models) the partition function is given by (20); i.e., the zeros in the complex plane are given by

$$z_n(\vec{k}) = \frac{1}{2E_{\vec{k}}} [\ln(B_{\vec{k}}^2) + i\pi(2n+1)], \quad n \in \mathbb{Z}. \quad (34)$$

At this point it becomes obvious that in the thermodynamic limit the double product over  $k_x$  and  $k_y$  in Eq. (20) leads to dense areas of zeros in the complex plane, since, generally,  $\partial_{k_x} z_n(\vec{k}) \neq \pm \partial_{k_y} z_n(\vec{k})$ . These areas of zeros cover parts of the real time axis ( $z = it$ ) if  $\text{Re}[z_n(\vec{k})] = 0$ , i.e., if

$$\exists \vec{q} \in K \text{ such that } B_{\vec{q}}^2 = 1. \quad (35)$$

Dubbing the  $B_{\vec{q}}^2 = 1$  isoline  $\mathcal{B}_1 \subset K$ , there are intervals

$$T_n^* = \frac{(2n+1)\pi}{2E_{\mathcal{B}_1}}, \quad n \in \mathbb{Z}, \quad (36)$$

on the real time axis, which are covered by areas of zeros. The beginning  $t_n^b$  and end points  $t_n^e$  of the intervals  $T_n^*$  are determined through Eq. (36) by the maximum and minimum, respectively, of  $E_{\vec{k}}$  on the domain given by  $|B_{\vec{k}}| = 1$ . If the spectrum of the final Hamiltonian is gapped, the beginnings and end points of two consecutive intervals  $T_n^*$  and  $T_{n+1}^*$  are equidistant with  $t_{n+1}^b - t_n^b = \frac{\pi}{2E_{\vec{q}_b}}$  and  $t_{n+1}^e - t_n^e = \frac{\pi}{2E_{\vec{q}_e}}$ , where  $\vec{q}_{b/e}$  are momenta minimizing/maximizing  $E_{\vec{k}}$  on the domain given by  $|B_{\vec{k}}| = 1$ . The length of the single intervals  $T_n^*$  increases linearly with  $n$ . However, if the spectrum is gapless, all those intervals extend to infinity.

The condition (35) allows for a physical interpretation; namely, the occurrence of DQPTs is through a continuity argument related to nonthermal mode occupation [3]. In BCS-type models the mode occupation is given by

$$\langle n_{\vec{k}} \rangle \equiv \langle a_{\vec{k}}^\dagger a_{\vec{k}} \rangle = \sin^2(\arctan B_{\vec{k}}). \quad (37)$$

This means for all modes  $\vec{q}$ , where the condition (35) is satisfied, the mode occupation is  $\langle n_{\vec{q}} \rangle = 1/2$ . Let us assume that for any two points in  $K$  there exists a path connecting both points, along which  $\langle n_{\vec{k}} \rangle$  is continuous [23], and the existence of modes with  $\langle n_{\vec{k}} \rangle < 1/2$ . Both assumptions should be true for physically relevant models and were found to hold in all cases considered in the Kitaev model. In particular, steps in the occupation number would have to be inherited from a spectrum with steps, which is not to be expected in physical systems; small occupation numbers, however, are to be expected at least for UV modes. Then, we can set up the following chain of consequences: through the continuity condition, the existence of nonthermally occupied modes  $\vec{k}^+$  with  $\langle n_{\vec{k}^+} \rangle \geq 1/2$  implies the existence of modes  $\vec{q}$  with  $\langle n_{\vec{q}} \rangle = 1/2$ . This in turn is equivalent to the fulfilling of the condition (35), which implies the occurrence of DQPTs in the time evolution. The mode occupation  $\langle n_{\vec{k}^+} \rangle \geq 1/2$  is nonthermal in the sense that it cannot be realized by Fermi-Dirac statistics with positive temperature.

An equivalent formulation of condition (35) is

$$\exists \vec{q} \in K \text{ such that } \Delta_{\vec{q}}(\alpha_0)\Delta_{\vec{q}}(\alpha_1) + \epsilon_{\vec{q}}(\alpha_0)\epsilon_{\vec{q}}(\alpha_1) = 0, \quad (38)$$

where  $\alpha$  is the quench parameter of the BCS-type Hamiltonian (see Appendix B). From this it becomes clear that after quenching to a gapless phase there are zeros of the dynamical partition function on the real time axis, since  $E_{\vec{q}}(\alpha) = 0 \Leftrightarrow \epsilon_{\vec{q}}(\alpha) = \Delta_{\vec{q}}(\alpha) = 0$ . In the mode occupation picture this can be interpreted as follows: when quenching to a gapless phase, excitations cost no energy; thus, any quench produces inverted mode occupation.

As discussed in the previous section, areas of zeros covering the real time axis result in jumps in the second time derivative of the dynamical free energy density if there is a jump in the density of zeros. Equation (34) gives a ‘‘layer’’ of zeros for every  $n \in \mathbb{Z}$ . Therefore, our total density of zeros is a sum of the densities of the individual ‘‘layers,’’  $\rho_z(z) = \sum_n \rho_z^n(z)$ . The single layer densities are given the Jacobi determinant of the change of variables  $\vec{k} \rightarrow z_n(\vec{k})$  [22],

$$\begin{aligned} \rho_z^n(z) &= \frac{1}{\pi^2} \left| \frac{\partial \text{Re}(z_n)}{\partial k_x} \quad \frac{\partial \text{Re}(z_n)}{\partial k_y} \right|^{-1} \\ &= \frac{1}{\pi^2} \left[ \left( \frac{\partial_{k_x} B_{\vec{k}}^2}{2E_{\vec{k}} B_{\vec{k}}^2} - \frac{\ln(B_{\vec{k}}^2)}{2E_{\vec{k}}^2} \partial_{k_x} E_{\vec{k}} \right) \left( -\frac{(2n+1)\pi}{2E_{\vec{k}}^2} \partial_{k_y} E_{\vec{k}} \right) - \left( \frac{\partial_{k_y} B_{\vec{k}}^2}{2E_{\vec{k}} B_{\vec{k}}^2} - \frac{\ln(B_{\vec{k}}^2)}{2E_{\vec{k}}^2} \partial_{k_y} E_{\vec{k}} \right) \left( -\frac{(2n+1)\pi}{2E_{\vec{k}}^2} \partial_{k_x} E_{\vec{k}} \right) \right]^{-1} \\ &= \frac{4E_{\vec{k}}^3 B_{\vec{k}}^2}{(2n+1)\pi^3} (\partial_{k_x} E_{\vec{k}} \partial_{k_y} B_{\vec{k}}^2 - \partial_{k_y} E_{\vec{k}} \partial_{k_x} B_{\vec{k}}^2)^{-1} = \frac{4E_{\vec{k}}^3 B_{\vec{k}}^2}{(2n+1)\pi^3} \left| \frac{\partial E_{\vec{k}}}{\partial k_x} \quad \frac{\partial E_{\vec{k}}}{\partial k_y} \right|^{-1}, \quad \vec{k} \equiv \vec{k}(z_n). \end{aligned} \quad (39)$$

At this point a more technical view of the zeros of the partition function is useful: the zeros  $z_n(\vec{k})$  correspond to intersections of the isolines

$$B_{\vec{k}}^2 = \exp\left(\frac{(2n+1)\pi \text{Re}[z_n(\vec{k})]}{\text{Im}[z_n(\vec{k})]}\right), \quad E_{\vec{k}} = \frac{(2n+1)\pi}{2\text{Im}[z_n(\vec{k})]} \quad (40)$$

in the momentum plane. This means that the density of zeros  $\rho_z^n(z)$  diverges at the boundary, since there  $\vec{\nabla} E_{\vec{k}} \parallel \vec{\nabla} B_{\vec{k}}^2$ . Thus, when approaching the boundary of an interval  $T_n^*$  from the inside of the interval, the second time derivative of  $\text{Re}[f(t)]$  will diverge.

#### IV. DYNAMICAL PHASE TRANSITIONS IN THE KITAEV HONEYCOMB MODEL

##### A. Zeros of the dynamical partition function in the Kitaev model

In the Kitaev model not only quenches to the massless phase create inverted mode occupation. Also quenches across phase boundaries with final parameter  $\vec{J}_1$  in a massive phase induce critical points in the real time evolution. It is physically reasonable to assume that the mode occupation number  $\langle n_{\vec{k}} \rangle$  is sufficiently well behaved, namely, that for any two  $\vec{k}_0, \vec{k}_1$  there exists a path  $\vec{\gamma}: [0, 1] \rightarrow [-\pi, \pi]^2$  with  $\vec{\gamma}(0) = \vec{k}_0$  and  $\vec{\gamma}(1) = \vec{k}_1$  such that  $\langle n_{\vec{\gamma}(s)} \rangle, s \in [0, 1]$ , is continuous. We found this to be true for all considered cases. Under this prerequisite, the existence of a fully occupied mode  $\vec{k}^+, \langle n_{\vec{k}^+} \rangle = 1$ , implies that  $\langle n_{\vec{q}} \rangle = 1/2$  somewhere, because  $\langle n_{\vec{k}=0} \rangle = 0, \langle n_{\vec{k}^+} \rangle = 1$  corresponds to  $|B_{\vec{k}^+}| = \infty$  and this happens when

$$\begin{aligned} 0 &= u_{\vec{k}^+}(\vec{J}_0)u_{\vec{k}^+}(\vec{J}_1) + v_{\vec{k}^+}(\vec{J}_0)v_{\vec{k}^+}(\vec{J}_1) \\ \wedge 0 &\neq u_{\vec{k}^+}(\vec{J}_0)v_{\vec{k}^+}(\vec{J}_1) - u_{\vec{k}^+}(\vec{J}_1)v_{\vec{k}^+}(\vec{J}_0). \end{aligned} \quad (41)$$

One possibility to fulfill this is

$$\pm 1 = \frac{\epsilon_{\vec{k}^+}(\vec{J}_0)}{E_{\vec{k}^+}(\vec{J}_0)} = -\frac{\epsilon_{\vec{k}^+}(\vec{J}_1)}{E_{\vec{k}^+}(\vec{J}_1)}. \quad (42)$$

Now, consider a quench ending in the  $x$  phase ( $J_1^x \geq J_1^y + J_1^z$ ) and  $\vec{k}^+ = (\pi, 0)$ . Then  $\epsilon_{\vec{k}^+}(\vec{J}_1) = 2(J_1^z - J_1^x + J_1^y)$  and  $\epsilon_{\vec{k}^+}(\vec{J}_1)/E_{\vec{k}^+}(\vec{J}_1) = -1$ . We find that at this point both quenches, starting from another massive phase,

$$J_0^y < J_0^x + J_0^z \Rightarrow \frac{\epsilon_{\vec{k}^+}(\vec{J}_0)}{E_{\vec{k}^+}(\vec{J}_0)} = 1, \quad (43)$$

and from the massless phase,

$$J_0^x < J_0^y + J_0^z \Rightarrow \frac{\epsilon_{\vec{k}^+}(\vec{J}_0)}{E_{\vec{k}^+}(\vec{J}_0)} = 1, \quad (44)$$

lead to nonanalytic behavior because (42) is fulfilled in both cases. The same can be shown for quenches ending in the other massive phases; only  $\vec{k}^+$  needs to be chosen appropriately. This shows that in the Kitaev model occupation inversion is produced by quenches within the massless phase or quenches crossing phase boundaries.

Figure 4 displays locations of the zeros of the Loschmidt echo in the complex plane given by Eq. (34) for two quenches, one within the  $A_x$  phase and one from the  $A_x$  phase to the massless phase. Both panels include a phase diagram with an arrow indicating the quench parameters  $\vec{J}_0 \rightarrow \vec{J}_1$ . The numerical values for the parameters for this figure and all following figures are listed in Table I in Appendix C. The zeros do indeed form areas, which are restricted to the left half plane for the quench within the massive phase but cover parts of the real time (imaginary  $z$ ) axis when  $\vec{J}_0$  and  $\vec{J}_1$  lie in different phases.

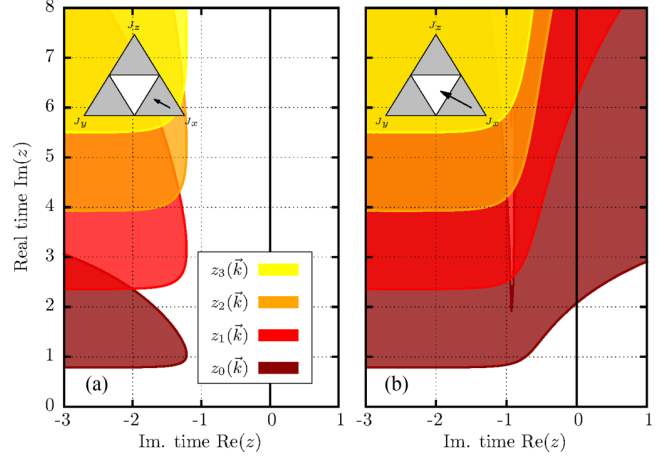


FIG. 4. (Color online) Distribution of zeros of the Loschmidt echo in the complex time plane computed according to Eq. (34) for two different quenches. The zeros form areas in the complex plane. (a) Quench within one phase. The zeros are restricted to the left half plane and no DQPTs occur. (b) Quench to the massless phase. The zero areas overlap the real time axis (i.e., imaginary  $z$  axis) and DQPTs occur at the intersections of the boundaries of the single areas  $z_n(\vec{k})$  with the real time axis. Time is measured in units of  $\sum_{\alpha} J_1^{\alpha}$ .

##### B. Real time evolution

On the real time axis the rate function of the Loschmidt echo  $\mathcal{L}(t) = |Z(it)|^2$  reads

$$\begin{aligned} r(t) &= -\frac{1}{2\pi^2} \int_0^{\pi} \int_{-\pi}^{\pi} dk_x dk_y \\ &\times \ln \left( \frac{\sqrt{1 + 2B_k^2 \cos(2E_{\vec{k}}t) + B_k^4}}{1 + B_k^2} \right) \end{aligned} \quad (45)$$

and the time derivative is

$$\dot{r}(t) = \frac{1}{\pi^2} \int_0^{\pi} \int_{-\pi}^{\pi} dk_x dk_y \frac{B_k^2 E_{\vec{k}} \sin(2E_{\vec{k}}t)}{1 + 2B_k^2 \cos(2E_{\vec{k}}t) + B_k^4}. \quad (46)$$

Figure 5 shows the time evolution of the rate function and its time derivative for various quenches obtained by numerical evaluation of the corresponding integrals. The gray-shaded areas in the plots indicate the intervals  $T_n^*$  [cf. Eq. (36)] of vanishing partition function. The results exhibit the properties expected from the previous considerations. The rate function is smooth for quenches within the gapped phases; however, nonanalyticities occur when phase boundaries are crossed in a quench or after a quench within the gapless phase. The beginning and end points of the critical intervals are equidistant, respectively, and for quenches ending in the massless phase the intervals extend to infinity. As anticipated, nonanalyticities only show up at the boundaries of the critical intervals. Moreover, the nonanalyticities emerge as discontinuities of  $\dot{r}(t)$ , i.e., kinks in  $\dot{r}(t)$ .

Note that the two plots in panels (a) and (c) show the time evolution of the rate function after the two quenches for which Fig. 4 shows the location of the zeros of the partition function.



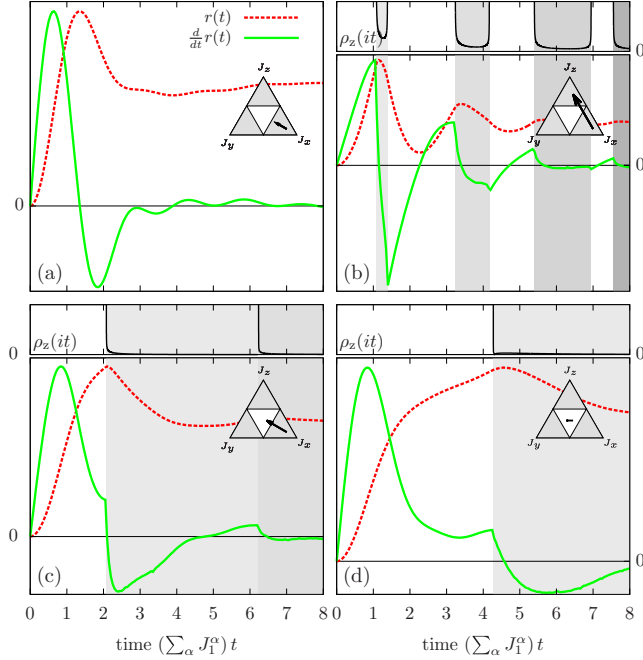


FIG. 5. (Color online) Real time evolution of the rate function of the Loschmidt echo (45) and its time derivative (46) for various quenches. Both were obtained by numerical evaluation of the integrals. The gray-shaded areas indicate sections of the real time axis that are covered by areas of vanishing Loschmidt echo (cf. Fig. 4). If zeros of the Loschmidt echo cover parts of the time axis, also the density of zeros on the time axis,  $\rho_z(it)$ , is included. Kinks in the time derivative of the rate function are observed when quenching across a phase boundary or within the massless phase.

### C. The 1d limit

In the limit  $J_\alpha \rightarrow 0$  for any  $\alpha \in \{x, y, z\}$  the 2d Kitaev model (4) degenerates and becomes a set of separate 1d spin chains. Let us consider the case  $J_z = 0$ . The vanishing of one of the other two parameters will give the same result due to the threefold symmetry. For  $J_z = 0$  the condition for nonanalyticities (35) is fulfilled at  $\vec{q}$  with

$$\cos(q_x - q_y) = \frac{J_0^x J_1^x + J_0^y J_1^y}{J_0^x J_1^y + J_1^x J_0^y}. \quad (47)$$

Along this line also the spectrum is constant,

$$E_{\vec{q}} = \sqrt{J_1^{x2} + J_1^{y2} + 2J_1^x J_1^y \frac{J_0^x J_1^x + J_0^y J_1^y}{J_0^x J_1^y + J_1^x J_0^y}}. \quad (48)$$

Thus, the critical intervals  $T_n^*$  defined in Eq. (36) become critical points

$$t_n^* = \frac{(2n+1)\pi}{2E_{\vec{q}}} \equiv \frac{2n+1}{2} t^* \quad (49)$$

on the real time axis. Figure 6 shows the rate functions for two different quenches with  $J_0^z = J_1^z = 0$ . The quench in Fig. 6(a) does not cross a phase boundary and therefore the rate function is analytic. However, in Fig. 6(b)  $\vec{J}_0 = (\frac{1}{4}, \frac{3}{4}, 0)$  and  $\vec{J}_1 = (\frac{3}{4}, \frac{1}{4}, 0)$  lie in different phases, and according to Eq. (49)

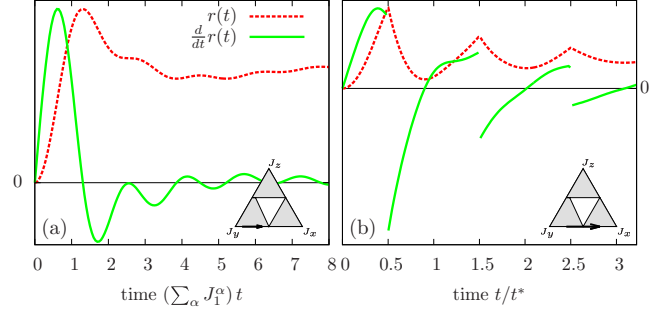


FIG. 6. (Color online) Time evolution of the rate function  $r(t)$  of the Loschmidt echo and its time derivative for two quenches in the effectively one-dimensional Kitaev model with  $J_z = 0$ . The quench in (a) does not cross the phase boundary and the rate function is analytic. In (b) the phase boundary is crossed and discontinuities of  $\dot{r}(t)$  occur at equidistant instances in time  $t_n^*$ .

there are critical times  $t_n^* = \frac{2n+1}{2} \sqrt{\frac{5}{8}} \pi$  at which the rate function becomes singular. In particular, these singularities are discontinuities in the first time derivative of the rate function, not in the second as in the genuinely two-dimensional cases. This observation underlines the fact that the continuity of the first derivative is inherent to the higher dimensionality of the nondegenerate Kitaev model.

### D. The long time limit

In a recent work [14] it was stated that if the Loschmidt echo  $\mathcal{L}(t)$  supports analytic continuation, then the long real time limit  $\lim_{t \rightarrow \infty} \mathcal{L}(t)$  and the long imaginary time limit  $\lim_{\tau \rightarrow \infty} \mathcal{L}(-i\tau)$  coincide. In the context of dynamical phase transitions this gives rise to the conjecture that the occurrence of DQPTs is closely related to the long time behavior of  $\mathcal{L}(t)$ . Dynamical quantum phase transitions occur if the zeros of the dynamical partition function cross the real time axis. This means,  $r(z)$ , the rate function of the Loschmidt echo, is nonanalytic in the  $\tau > 0$  half plane; therefore, the long imaginary time limit and the long real time limit do not necessarily have to coincide.

On the imaginary time axis  $z = \tau$ , with the eigenbasis of the quenched Hamiltonian  $|\phi_n\rangle$ , corresponding energies  $E_n$ , and  $c_n = \langle \phi_n | \psi_i \rangle$ ,

$$\begin{aligned} \mathcal{L}(-i\tau) &= |\langle \psi_i | e^{-H\tau} | \psi_i \rangle|^2 = \left| \sum_{n,n'} c_n^* c_{n'} e^{-E_n \tau} \langle \phi_n | \phi_{n'} \rangle \right|^2 \\ &= \left| \sum_n |c_n|^2 e^{-E_n \tau} \right|^2. \end{aligned} \quad (50)$$

Now, shifting the energy such that  $E_0 = 0$  and assuming the ground state  $|\phi_0\rangle$  to be nondegenerate,

$$\lim_{\tau \rightarrow \infty} \mathcal{L}(-i\tau) = |c_0|^4 = |\langle \phi_0 | \psi_i \rangle|^4 = \mathcal{F}^4, \quad (51)$$

where  $\mathcal{F} \equiv |\langle \phi_0 | \psi_i \rangle|$  is the fidelity. Thereby, the Loschmidt echo is connected to the fidelity in the large imaginary time limit.

As the Loschmidt echo  $\mathcal{L} \propto e^{-Nr(t)}$  equals zero in the thermodynamic limit, one should rather formulate Eq. (51) in terms of the rate function:

$$\begin{aligned} \lim_{\tau \rightarrow \infty} r(-i\tau) &= - \lim_{\tau \rightarrow \infty} \lim_{N \rightarrow \infty} \frac{1}{N} \ln \mathcal{L}(-i\tau) \\ &= - \lim_{N \rightarrow \infty} \frac{1}{N} \ln \mathcal{F}^4. \end{aligned} \quad (52)$$

According to the previous considerations this yields

$$\lim_{t \rightarrow \infty} r(t) = - \lim_{N \rightarrow \infty} \frac{1}{N} \ln \mathcal{F}^4 \quad (53)$$

if  $r(z)$  is analytic in the  $\tau > 0$  half plane. This is a quite remarkable result: In the long time limit the Loschmidt echo approaches a value given solely by the overlap of the initial state with the ground state of the postquench Hamiltonian, although the stationary state will surely never be that ground state. Quenching inevitably produces an excited state. Moreover, some information about the initial state is preserved for all times.

For the Kitaev model the fidelity is

$$\begin{aligned} \mathcal{F} &= |\langle \psi_i | \phi_0 \rangle| = \frac{|\langle 0 | \prod_{\vec{k}} (1 + B_{\vec{k}} a_{-\vec{k}} a_{\vec{k}}) | 0 \rangle|}{\sqrt{\langle \psi_0 | \psi_0 \rangle}} \\ &= \frac{1}{\sqrt{\langle \psi_0 | \psi_0 \rangle}} \stackrel{(18)}{=} \exp \left[ -\frac{N}{2} \int \frac{d^2 k}{4\pi^2} \ln(1 + B_{\vec{k}}^2) \right]. \end{aligned} \quad (54)$$

Thus, if the above conjecture is valid, we should find

$$\lim_{t \rightarrow \infty} r(t) = \frac{1}{2\pi^2} \int d^2 k \ln(1 + B_{\vec{k}}^2) \quad (55)$$

for quenches within the massive phases. Figure 7 shows the long time behavior of the rate function for a quench within the  $A_x$  phase and for a quench crossing phase boundaries; indeed, the rate function converges to the value given by the fidelity after the quench within the massive phase. In the other case, however, the rate function seems to converge, but the value it approaches differs from the one given by the fidelity. Various other cases were checked and the behavior was always consistent with above mentioned conjecture.

One can explain the convergence of the rate function heuristically based on the specific form given in Eq. (45). The expressions for the long time limit of the rate function in Eq. (55) and the definition of the rate function in Eq. (45) only differ in the nominators in the argument of the logarithm, which are 1 and  $1 + B_{\vec{k}}^2 e^{-2iE_{\vec{k}}t}$ , respectively. In the long time limit the factor  $e^{-2iE_{\vec{k}}t}$  oscillates extremely fast as a function of  $\vec{k}$ . If  $B_{\vec{k}}^2$  is slowly changing compared to these oscillations and also small such that

$$\ln(1 + B_{\vec{k}}^2 e^{-2iE_{\vec{k}}t}) \approx B_{\vec{k}}^2 e^{-2iE_{\vec{k}}t}, \quad (56)$$

then the contributions of neighboring points in the momentum plane will cancel in the integral and therefore both integrals Eqs. (45) and (55) become equal. However, if the integrand is singular, there are areas where  $|B_{\vec{k}}| \approx 1$  and therefore the contributions of close-by points do not necessarily cancel. As a result the values of the integrals differ.

In the absence of DQPTs Eq. (53) can also be derived rigorously for BCS-type models by considering the Taylor

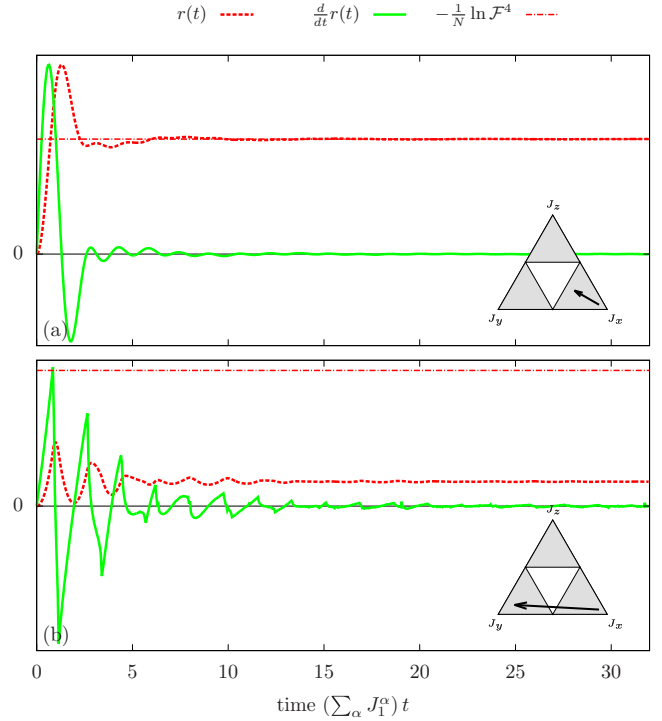


FIG. 7. (Color online) Long-time behavior of the rate function (a) after a quench within the  $A_x$  phase and (b) after a quench crossing phase boundaries. The rate function converges in both cases. For the quench within the massive phase it indeed approaches the value predicted by Heyl's and Vojta's conjecture (52), and in the other case the limit lies well off that value. Note that the derivative of the rate function converges to the zero line in both cases.

expansion of the logarithm in the integrand of Eq. (45) and computing the time averages of the single contributions in the power series.

### E. Ramping

It is known that dynamical quantum phase transitions also occur if the Hamiltonian parameter is continuously ramped across a critical point instead of quenching it [3]. However, it is not clear what happens after ramping the parameter within a gapless phase. In a gapless phase the adiabatic theorem does not apply and it is known that also slow ramping can produce a nonzero defect density [24]. But are these excitations sufficient to induce dynamical quantum phase transitions?

Assume the parameter  $\vec{J}(t)$  of the Hamiltonian is not quenched immediately from  $\vec{J}(t < 0) = J_0$  to  $\vec{J}(t \geq 0) = \vec{J}_1$ , but continuously according to some protocol with  $\vec{J}(t < 0) = \vec{J}_0$  and  $\vec{J}(t > t_r) = \vec{J}_1$ . In this case, the state of the system must at any time still be of the form given in Eq. (16), because at any time  $H(\vec{J}(t))$  can only excite both modes with opposite momenta  $\vec{k}$ ,  $-\vec{k}$  in one  $\vec{k}$  sector. For  $t > t_r$  the dynamics is the same as after a quench; however, the  $B_{\vec{k}}$  will depend on the details of the ramping protocol. As discussed above  $B_{\vec{k}}$  is directly related to the mode occupation number  $\langle n_{\vec{k}} \rangle$ . Thus, in order to determine whether DQPTs occur after ramping from  $\vec{J}_0$  to  $\vec{J}_1$  instead of quenching, it is sufficient to compute the mode occupation at  $t = t_r$ .

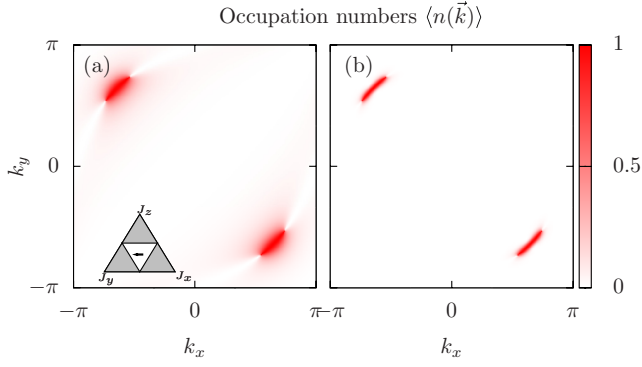


FIG. 8. (Color online) (a) Mode occupation  $\langle n_{\vec{k}} \rangle$  after quenching from  $\vec{J}_0$  to  $\vec{J}_1$  within the gapless phase and (b) mode occupation after linearly ramping from  $\vec{J}_0$  to  $\vec{J}_1$  with ramping time  $t_r = 50$ .

In order to get the mode occupation  $\langle n_{\vec{k}} \rangle$  we make use of the fact that the total time evolution is simply made up by the time evolution of independent two-level systems in the single  $\vec{k}$  sectors and the corresponding Hamiltonians are

$$H_{\vec{k}}(\vec{J}(t)) = \frac{1}{2} \begin{pmatrix} \epsilon_{\vec{k}}(\vec{J}(t)) & \Delta_{\vec{k}}(\vec{J}(t)) \\ \Delta_{\vec{k}}(\vec{J}(t)) & \epsilon_{\vec{k}}(\vec{J}(t)) \end{pmatrix}. \quad (57)$$

In these terms the initial state is the ground state of  $H_{\vec{k}}(\vec{J}_0)$ ,  $H_{\vec{k}}(\vec{J}_0)|\psi_{i,\vec{k}}\rangle = -E_{\vec{k}}(\vec{J}_0)|\psi_{i,\vec{k}}\rangle$ , and the time evolved state  $|\psi_{\vec{k}}(t)\rangle$  can be obtained by numerical integration of the Schrödinger equation. The mode occupation number after the ramping is then given by the overlap

$$\langle n_{\vec{k}} \rangle = |\langle \psi_{\vec{k}}^+ | \psi_{\vec{k}}(t_r) \rangle|^2, \quad (58)$$

where  $H_{\vec{k}}(\vec{J}_1)|\psi_{\vec{k}}^+\rangle = E_{\vec{k}}|\psi_{\vec{k}}^+\rangle$ .

Figure 8 shows the final occupation numbers for a quench within the gapless phase and for linear ramping with

$$\vec{J}(t) = \begin{cases} \vec{J}_0, & t < 0, \\ \vec{J}_0 + (\vec{J}_1 - \vec{J}_0)t/t_r, & 0 \leq t \leq t_r, \\ \vec{J}_1, & t > t_r, \end{cases} \quad (59)$$

and ramping period  $t_r = 50$ . Note that the occupation numbers remain unchanged afterwards. As expected from the previous considerations the quench produces regions of nonthermally occupied modes in the Brillouin zone. Such areas are also present after the ramping. This means that also in the time evolution for times  $t > t_r$  there will be dynamical quantum phase transitions.

### F. Quenching the magnetic field

In the presence of a magnetic field the phase  $B$  (cf. Fig. 2) becomes gapped and at  $J_x = J_y = J_z \equiv J$  there exists a diagonal form of the Hamiltonian [15] with spectrum  $E_{\vec{k}}(J, \kappa)$  as given in Eq. (13) that maps to the general two-band form (see Appendix A for details)

$$H(J, \kappa) = \sum_{\vec{k}} \vec{\gamma}_{\vec{k}}^\dagger (\vec{b}_{\vec{k}}(\alpha) \cdot \vec{\sigma}) \vec{\gamma}_{\vec{k}}, \quad (60)$$

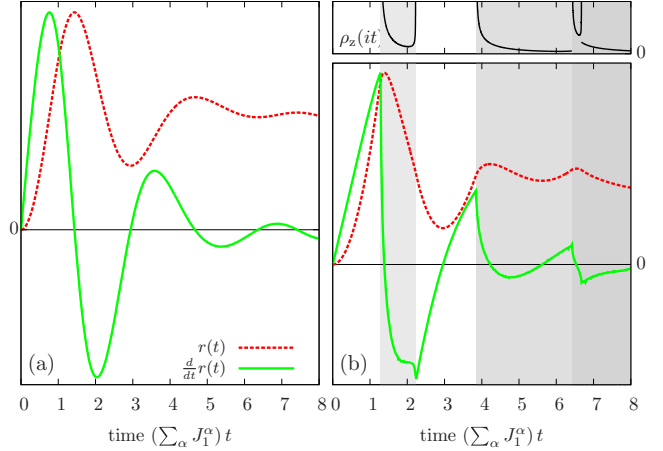


FIG. 9. (Color online) Time evolution of the rate function in the Kitaev model with additional magnetic field after quenching the magnetic field. (a) Quench within one phase,  $\kappa_0 = 0.5 \rightarrow \kappa_1 = 0.1$ . (b) Quench across the phase boundary,  $\kappa_0 = 0.5 \rightarrow \kappa_1 = -0.1$ .

where  $\vec{\sigma} = (\sigma_x, \sigma_y, \sigma_z)^T$  is the vector of Pauli matrices,  $\gamma_{\vec{k}}^\dagger = (d_{\vec{k}}^\dagger, d_{-\vec{k}})$ , and

$$b_{\vec{k}}(J, \kappa) = \frac{1}{2} \begin{pmatrix} \text{Re}[\tilde{\Delta}_{\vec{k}}(J, \kappa)] \\ \text{Im}[\tilde{\Delta}_{\vec{k}}(J, \kappa)] \\ \tilde{\epsilon}_{\vec{k}}(J, \kappa) \end{pmatrix}. \quad (61)$$

The magnetic field  $\vec{h}$  is contained in the parameter  $\kappa \sim \frac{h_x h_y h_z}{J^2}$ . It introduces topological order in the  $B$  phase, characterized by the Chern number

$$\nu(\kappa) = \frac{1}{4\pi} \int_{-\pi}^{\pi} \int_{-\pi}^{\pi} dk_x dk_y \frac{\vec{b}_{\vec{k}} \cdot (\partial_{k_x} \vec{b}_{\vec{k}} \times \partial_{k_y} \vec{b}_{\vec{k}})}{|\vec{b}_{\vec{k}}|^3} = \text{sgn}(\kappa). \quad (62)$$

It was demonstrated that in such systems any quench crossing the boundary between topologically distinct phases induces dynamical quantum phase transitions [7].

Figure 9 shows the time evolution of the rate function after quenching the magnetic field within one phase and between two topologically distinct phases. As expected the signature of dynamical quantum phase transitions shows up after the quench across the phase boundary.

## V. CONCLUSIONS

We demonstrated how the domains of zeros in 2d BCS-type models differ qualitatively compared to 1d systems; namely, in the thermodynamic limit, the zeros coalesce to dense areas of zeros in the complex time plane rather than lines. The covering of intervals of the real time axis by such areas of zeros indicates the existence of critical points in the time evolution. We showed how this leads to dynamical quantum phase transitions as discontinuities in the second time derivative of the dynamical free energy as opposed to discontinuities in the first derivative known from 1d systems.

It was found that in the Kitaev honeycomb model dynamical quantum phase transitions occur after quenches across the

phase boundaries and after quenches within the gapless phase. It is to our knowledge the first time that DQPTs are found in a two-dimensional model after quenching without crossing an equilibrium phase boundary. In accordance with the general considerations regarding the dynamics of BCS-type systems, DQPTs in the Kitaev model show up at the boundaries of the intervals  $T_n^*$  on the time axis which are included in a domain of zeros of the partition function. At these points the DQPTs appear as kinks in the first time derivative of the rate function of the Loschmidt echo. As was shown to hold for any BCS-type model, the curvature of the free energy density diverges when the boundary of such an interval is approached from the inward.

In degenerate versions of the Kitaev model, which effectively constitute one-dimensional spin chains, already the first derivative of the rate function becomes discontinuous after quenching across a phase boundary as known from other 1d models [3]. This underlines the fact that the continuity of the first derivative is inherent to the higher dimensionality of the nondegenerate Kitaev model.

Moreover, we found for the Kitaev model that, in accordance with a conjecture concerning that matter [14], the long time stationary state of the rate function of the Loschmidt echo has a close connection to the occurrence of DQPTs: if no DQPTs occur, i.e., if the rate function is analytic in at least a half of the complex plane, the rate function approaches a value given by the fidelity. If the rate function is, however, nonanalytic, it does in general not converge to this value. The fact that the long time limit in the absence of DQPTs is given by the fidelity deserves particular notice, since the fidelity is the overlap of the initial state with the ground state of the quenched Hamiltonian, but the approached stationary state is surely an excited state.

The examination of the mode occupation numbers after ramping the parameter of the Hamiltonian instead of quenching it implies that the subsequent time evolution also exhibits dynamical quantum phase transitions. Moreover, it was demonstrated that in the presence of a magnetic field quenches between the topologically ordered phases induce dynamical quantum phase transitions, which was previously proven to be a general feature in the dynamics of topologically ordered two-band models in Ref. [7].

DQPTs were to date not observed in experiments. The Loschmidt echo  $\mathcal{L}(t)$ , which shows the nonanalytic behavior, is not directly connected to a quantum mechanical observable. As mentioned above, the work density was suggested as an measurable quantity, which could show the signature of DQPTs. However, the Loschmidt echo becomes exponentially small with increasing system size, whereas, strictly speaking, DQPTs occur only in the thermodynamic limit. Experimentally measuring the signature of DQPTs in work densities will therefore be very challenging. Experimental consequences of DQPTs in other quantities than the work distribution function are currently being investigated. It was shown that DQPTs are connected to time scales of the order parameter dynamics in symmetry broken systems [3]; in particular the occurrence of DQPTs is directly related to the sudden transition from monotonic to oscillatory decay of the order parameter after a quench [25]. Alternatively, the previously mentioned generalized expectation values could

serve as measurable quantities [8]. Moreover, it was shown in a recent work that DQPTs in Ising spin models exhibit scaling and universality and numerical results indicate that signatures of the DQPTs can be found in the dynamics of spin correlations as power-law scaling, which is solely determined by the universality class [26]. This seems to provide a very promising opportunity for measuring DQPTs, since these quantities are accessible with current experimental techniques.

The finding of DQPTs as discontinuities in higher order derivatives in higher dimensional systems raises the question of a classification of dynamical quantum phase transitions. Canovi *et al.* [8] suggested a formalism for such a classification. They related discontinuities in generalized expectation values and coexisting solutions to a first order transition. Here, we found a discontinuity in the second derivative of the dynamical free energy density. In future work it should be investigated how the findings of discontinuities in higher derivatives of the dynamical free energy density tie in with their definition.

## ACKNOWLEDGMENTS

The authors thank N. Abeling, M. Heyl, and B. Blobel for valuable discussions. S.K. acknowledges support through SFB 1073 (project B03) of the Deutsche Forschungsgemeinschaft (DFG).

## APPENDIX A: BOGOLIUBOV TRANSFORMATION AND POSTQUENCH EIGENBASIS

Consider the general Hamiltonian

$$H(\alpha) = \sum_{\vec{k}} \vec{\gamma}_{\vec{k}}^\dagger (\vec{d}_{\vec{k}}(\alpha) \cdot \vec{\sigma}) \vec{\gamma}_{\vec{k}} \quad (\text{A1})$$

with  $\vec{\sigma}$  the vector of Pauli matrices

$$\sigma_x = \begin{pmatrix} 0 & 1 \\ 1 & 0 \end{pmatrix}, \quad \sigma_y = \begin{pmatrix} 0 & -i \\ i & 0 \end{pmatrix}, \quad \sigma_z = \begin{pmatrix} 1 & 0 \\ 0 & -1 \end{pmatrix}, \quad (\text{A2})$$

and  $\vec{\gamma}_{\vec{k}}$  containing the creation and annihilation operators

$$\vec{\gamma}_{\vec{k}} = \begin{pmatrix} f_{\vec{k}} \\ f_{-\vec{k}}^\dagger \end{pmatrix}. \quad (\text{A3})$$

For  $\alpha = \vec{J}$  and  $\vec{b}_{\vec{k}}(\vec{J}) = (\Delta_{\vec{k}}(\vec{J})/2, 0, \epsilon_{\vec{k}}(\vec{J})/2)$  this gives the Hamiltonian of the Kitaev model as in Eq. (5). The unitary transformation

$$\begin{pmatrix} a_{\vec{k}}^\alpha \\ a_{-\vec{k}}^{\alpha\dagger} \end{pmatrix} = W(\alpha) \vec{\gamma}_{\vec{k}} = \begin{pmatrix} u_{\vec{k}}(\alpha) & v_{\vec{k}}(\alpha) \\ -v_{\vec{k}}(\alpha)^* & u_{\vec{k}}(\alpha)^* \end{pmatrix} \begin{pmatrix} f_{\vec{k}} \\ f_{-\vec{k}}^\dagger \end{pmatrix} \quad (\text{A4})$$

that brings the Hamiltonian (A1) into diagonal form is the Bogoliubov transformation. Plugging Eq. (A4) into Eq. (A1) and demanding that all off-diagonal terms vanish yields

$$0 = d_{\vec{k}}^z (u_{\vec{k}} v_{-\vec{k}} - u_{-\vec{k}} v_{\vec{k}}) + (d_{\vec{k}}^x - i d_{\vec{k}}^y) u_{-\vec{k}} u_{\vec{k}} + (d_{\vec{k}}^x + i d_{\vec{k}}^y) v_{-\vec{k}} v_{\vec{k}}, \quad (\text{A5})$$

where all the dependencies on  $\alpha$  have been dropped for the sake of brevity. Since  $W$  is unitary,  $u_{\vec{k}}$  and  $v_{\vec{k}}$  have the general

form

$$u_{\vec{k}} = \cos \theta_{\vec{k}} e^{i\phi_{\vec{k}}}, \quad v_{\vec{k}} = \sin \theta_{\vec{k}} e^{i\psi_{\vec{k}}}. \quad (\text{A6})$$

By choosing

$$\phi_{\vec{k}} = -\psi_{\vec{k}} = -\frac{1}{2} \arctan \left( -\frac{d_{\vec{k}}^y}{d_{\vec{k}}^x} \right) \quad (\text{A7})$$

the equation above becomes real,

$$0 = d_{\vec{k}}^z (\sin \theta_{\vec{k}} \cos \theta_{-\vec{k}} - \cos \theta_{-\vec{k}} \sin \theta_{\vec{k}}) + |d_{\vec{k}}^{xy}| (\cos \theta_{\vec{k}} \cos \theta_{-\vec{k}} - \sin \theta_{\vec{k}} \sin \theta_{-\vec{k}}), \quad (\text{A8})$$

where  $d_{\vec{k}}^{xy} \equiv d_{\vec{k}}^x - i d_{\vec{k}}^y$  was introduced. Then for  $a_{-\vec{k}}^\dagger = (a_{-\vec{k}})^\dagger$  to hold,  $\theta_{\vec{k}}$  must be an odd function of  $\vec{k}$ . Thus,

$$0 = -d_{\vec{k}}^z \sin(2\theta_{\vec{k}}) + |d_{\vec{k}}^{xy}| \cos(2\theta_{\vec{k}}) \Rightarrow \tan(2\theta_{\vec{k}}) = \frac{|d_{\vec{k}}^{xy}|}{d_{\vec{k}}^z} \quad (\text{A9})$$

and this yields

$$|u_{\vec{k}}|^2 = \cos^2 \theta_{\vec{k}} = \frac{1}{2} \left( 1 + \frac{\epsilon_{\vec{k}}}{E_{\vec{k}}} \right), \quad (\text{A10})$$

$$|v_{\vec{k}}|^2 = \sin^2 \theta_{\vec{k}} = \frac{1}{2} \left( 1 - \frac{\epsilon_{\vec{k}}}{E_{\vec{k}}} \right).$$

In the end it is left to choose the signs appropriately such that  $u_{\vec{k}} = u_{-\vec{k}}$  and  $v_{\vec{k}} = -v_{-\vec{k}}$ , e.g.,

$$u_{\vec{k}} = e^{i\phi_{\vec{k}}} \sqrt{\frac{1}{2} \left( 1 + \frac{\epsilon_{\vec{k}}}{E_{\vec{k}}} \right)}, \quad (\text{A11})$$

$$v_{\vec{k}} = \text{sgn}(d_{\vec{k}}^x) e^{-i\phi_{\vec{k}}} \sqrt{\frac{1}{2} \left( 1 - \frac{\epsilon_{\vec{k}}}{E_{\vec{k}}} \right)}.$$

With this transformation the Hamiltonian (A1) becomes diagonal

$$H(\alpha) = \sum_{\vec{k}} \frac{E_{\vec{k}}(\alpha)}{2} (a_{\vec{k}}^{\alpha\dagger} a_{\vec{k}}^\alpha - a_{-\vec{k}}^\alpha a_{-\vec{k}}^{\alpha\dagger}) \quad (\text{A12})$$

with  $E_{\vec{k}}(\alpha) = |\tilde{b}_{\vec{k}}(\alpha)|$ .

To compute the quench dynamics one needs the connection of the degrees of freedom  $a_{\vec{k}}^{\alpha_0}$  that diagonalize the initial Hamiltonian  $H(\alpha_0)$  and the degrees of freedom  $a_{\vec{k}}^{\alpha_1}$  diagonalizing

the final Hamiltonian  $H(\alpha_1)$ . This connection is given by two subsequent Bogoliubov transformations,

$$\begin{pmatrix} a_{\vec{k}}^{\alpha_1} \\ a_{-\vec{k}}^{\alpha_1\dagger} \end{pmatrix} = W(\alpha_1) W(\alpha_0)^\dagger \begin{pmatrix} a_{\vec{k}}^{\alpha_0} \\ a_{-\vec{k}}^{\alpha_0\dagger} \end{pmatrix} = \begin{pmatrix} U_{\vec{k}}(\alpha_0, \alpha_1) & V_{\vec{k}}(\alpha_0, \alpha_1) \\ -V_{\vec{k}}(\alpha_0, \alpha_1)^* & U_{\vec{k}}(\alpha_0, \alpha_1)^* \end{pmatrix} \begin{pmatrix} a_{\vec{k}}^{\alpha_0} \\ a_{-\vec{k}}^{\alpha_0\dagger} \end{pmatrix} \quad (\text{A13})$$

with

$$U_{\vec{k}}(\alpha_0, \alpha_1) = u_{\vec{k}}(\alpha_1) u_{\vec{k}}(\alpha_0)^* + v_{\vec{k}}(\vec{J}_1) v_{\vec{k}}(\alpha_0)^*, \quad (\text{A14})$$

$$V_{\vec{k}}(\alpha_0, \alpha_1) = u_{\vec{k}}(\alpha_0) v_{\vec{k}}(\alpha_1) - u_{\vec{k}}(\alpha_1) v_{\vec{k}}(\alpha_0).$$

Since  $|\psi_i\rangle$  is the ground state of  $H(\vec{J}_0)$

$$a_{\vec{k}}^{\alpha_0} |\psi_i\rangle = (U_{\vec{k}}(\alpha_0, \alpha_1) a_{\vec{k}}^{\vec{J}_1} - V_{\vec{k}}(\alpha_0, \alpha_1) a_{-\vec{k}}^{\alpha_1\dagger}) |\psi_i\rangle = 0 \quad (\text{A15})$$

must hold. Moreover, the ground state of a BCS-type Hamiltonian has vanishing total momentum; thus,

$$|\psi_i\rangle = \frac{1}{\mathcal{N}} \prod_{\vec{k}} (1 + B_{\vec{k}}(\alpha_0, \alpha_1) a_{\vec{k}}^{\alpha_1\dagger} a_{-\vec{k}}^{\alpha_1\dagger}) |0; \alpha_1\rangle = \frac{1}{\mathcal{N}} \exp \left( \sum_{\vec{k}} B_{\vec{k}}(\alpha_0, \alpha_1) a_{\vec{k}}^{\alpha_1\dagger} a_{-\vec{k}}^{\alpha_1\dagger} \right) |0; \alpha_1\rangle, \quad (\text{A16})$$

where the coefficients  $B_{\vec{k}}(\alpha_0, \alpha_1)$  are to be determined,  $\mathcal{N}$  is a normalization constant, and  $|0; \alpha_1\rangle$  denotes the vacuum of the postquench fermions:  $a_{\vec{k}}^{\alpha_1} |0; \alpha_1\rangle = 0$ . Plugging Eq. (A16) into Eq. (A15) yields

$$\begin{aligned} & (U_{\vec{k}}(\alpha_0, \alpha_1) a_{\vec{k}}^{\alpha_1} - V_{\vec{k}}(\alpha_0, \alpha_1) a_{-\vec{k}}^{\alpha_1\dagger}) \\ & \times \prod_{\vec{k}'} (1 + B_{\vec{k}'}(\alpha_0, \alpha_1) a_{\vec{k}'}^{\alpha_1\dagger} a_{-\vec{k}'}^{\alpha_1\dagger}) |0\rangle_{\alpha_1} \\ & = [U_{\vec{k}}(\alpha_0, \alpha_1) B_{\vec{k}}(\alpha_0, \alpha_1) - V_{\vec{k}}(\alpha_0, \alpha_1)] a_{-\vec{k}}^{\alpha_1\dagger} \\ & \times \prod_{\vec{k}' \neq \vec{k}} (1 + B_{\vec{k}'}(\alpha_0, \alpha_1) a_{\vec{k}'}^{\alpha_1\dagger} a_{-\vec{k}'}^{\alpha_1\dagger}) |0; \alpha_1\rangle \\ & = 0, \end{aligned} \quad (\text{A17})$$

which holds for

$$B_{\vec{k}}(\alpha_0, \alpha_1) = \frac{V_{\vec{k}}(\alpha_0, \alpha_1)}{U_{\vec{k}}(\alpha_0, \alpha_1)} = \frac{u_{\vec{k}}(\alpha_0) v_{\vec{k}}(\alpha_1) - u_{\vec{k}}(\alpha_1) v_{\vec{k}}(\alpha_0)}{u_{\vec{k}}(\alpha_0) u_{\vec{k}}(\alpha_1) + v_{\vec{k}}(\alpha_0) v_{\vec{k}}(\alpha_1)}. \quad (\text{A18})$$

## APPENDIX B: CONDITION FOR REAL TIME ZEROS OF THE PARTITION FUNCTION

The condition  $B_{\vec{k}}^2 = 1$  [cf. Eq. (35)] can be rearranged as follows: We have

$$\begin{aligned} 1 = |B_{\vec{k}}| & \Leftrightarrow \left| \sqrt{1 + \frac{\epsilon_{\vec{k}}(\vec{J}_0)}{E_{\vec{k}}(\vec{J}_0)}} \sqrt{1 + \frac{\epsilon_{\vec{k}}(\vec{J}_1)}{E_{\vec{k}}(\vec{J}_1)}} + \text{sgn}[\Delta_{\vec{k}}(\vec{J}_0) \Delta_{\vec{k}}(\vec{J}_1)] \sqrt{1 - \frac{\epsilon_{\vec{k}}(\vec{J}_0)}{E_{\vec{k}}(\vec{J}_0)}} \sqrt{1 - \frac{\epsilon_{\vec{k}}(\vec{J}_1)}{E_{\vec{k}}(\vec{J}_1)}} \right| \\ & = \left| \text{sgn}[\Delta_{\vec{k}}(\vec{J}_1)] \sqrt{1 + \frac{\epsilon_{\vec{k}}(\vec{J}_0)}{E_{\vec{k}}(\vec{J}_0)}} \sqrt{1 - \frac{\epsilon_{\vec{k}}(\vec{J}_1)}{E_{\vec{k}}(\vec{J}_1)}} - \text{sgn}[\Delta_{\vec{k}}(\vec{J}_0)] \sqrt{1 - \frac{\epsilon_{\vec{k}}(\vec{J}_0)}{E_{\vec{k}}(\vec{J}_0)}} \sqrt{1 + \frac{\epsilon_{\vec{k}}(\vec{J}_1)}{E_{\vec{k}}(\vec{J}_1)}} \right| \end{aligned}$$

$$\begin{aligned}
&\Leftrightarrow \left(1 + \frac{\epsilon_{\bar{k}}(\vec{J}_0)}{E_{\bar{k}}(\vec{J}_0)}\right) \left(1 + \frac{\epsilon_{\bar{k}}(\vec{J}_1)}{E_{\bar{k}}(\vec{J}_1)}\right) + \left(1 - \frac{\epsilon_{\bar{k}}(\vec{J}_0)}{E_{\bar{k}}(\vec{J}_0)}\right) \left(1 - \frac{\epsilon_{\bar{k}}(\vec{J}_1)}{E_{\bar{k}}(\vec{J}_1)}\right) \\
&\quad + 2\text{sgn}[\Delta_{\bar{k}}(\vec{J}_0)\Delta_{\bar{k}}(\vec{J}_1)] \sqrt{\left[1 - \left(\frac{\epsilon_{\bar{k}}(\vec{J}_0)}{E_{\bar{k}}(\vec{J}_0)}\right)^2\right] \left[1 - \left(\frac{\epsilon_{\bar{k}}(\vec{J}_1)}{E_{\bar{k}}(\vec{J}_1)}\right)^2\right]} \\
&= \left(1 + \frac{\epsilon_{\bar{k}}(\vec{J}_0)}{E_{\bar{k}}(\vec{J}_0)}\right) \left(1 - \frac{\epsilon_{\bar{k}}(\vec{J}_1)}{E_{\bar{k}}(\vec{J}_1)}\right) + \left(1 - \frac{\epsilon_{\bar{k}}(\vec{J}_0)}{E_{\bar{k}}(\vec{J}_0)}\right) \left(1 + \frac{\epsilon_{\bar{k}}(\vec{J}_1)}{E_{\bar{k}}(\vec{J}_1)}\right) \\
&\quad - 2\text{sgn}[\Delta_{\bar{k}}(\vec{J}_0)\Delta_{\bar{k}}(\vec{J}_1)] \sqrt{\left[1 - \left(\frac{\epsilon_{\bar{k}}(\vec{J}_0)}{E_{\bar{k}}(\vec{J}_0)}\right)^2\right] \left[1 - \left(\frac{\epsilon_{\bar{k}}(\vec{J}_1)}{E_{\bar{k}}(\vec{J}_1)}\right)^2\right]} \\
&\Leftrightarrow \frac{\epsilon_{\bar{k}}(\vec{J}_0)\epsilon_{\bar{k}}(\vec{J}_1)}{E_{\bar{k}}(\vec{J}_0)E_{\bar{k}}(\vec{J}_1)} = -\text{sgn}[\Delta_{\bar{k}}(\vec{J}_0)\Delta_{\bar{k}}(\vec{J}_1)] \sqrt{\left[1 - \left(\frac{\epsilon_{\bar{k}}(\vec{J}_0)}{E_{\bar{k}}(\vec{J}_0)}\right)^2\right] \left[1 - \left(\frac{\epsilon_{\bar{k}}(\vec{J}_1)}{E_{\bar{k}}(\vec{J}_1)}\right)^2\right]} \\
&\Rightarrow 1 = \left(\frac{\epsilon_{\bar{k}}(\vec{J}_0)}{E_{\bar{k}}(\vec{J}_0)}\right)^2 + \left(\frac{\epsilon_{\bar{k}}(\vec{J}_1)}{E_{\bar{k}}(\vec{J}_1)}\right)^2. \tag{B1}
\end{aligned}$$

Plugging this into the second last line we find the additional condition

$$\text{sgn}[\Delta_{\bar{k}}(\vec{J}_0)\epsilon_{\bar{k}}(\vec{J}_0)] = -\text{sgn}[\Delta_{\bar{k}}(\vec{J}_1)\epsilon_{\bar{k}}(\vec{J}_1)], \tag{B2}$$

which allows us to write

$$1 = |B_{\bar{k}}| \Leftrightarrow \left[1 + \left(\frac{\epsilon_{\bar{k}}(\vec{J}_0)}{E_{\bar{k}}(\vec{J}_0)}\right)^2 + \left(\frac{\epsilon_{\bar{k}}(\vec{J}_1)}{E_{\bar{k}}(\vec{J}_1)}\right)^2 \wedge -1 = \frac{\text{sgn}[\epsilon_{\bar{k}}(\vec{J}_1)\Delta_{\bar{k}}(\vec{J}_1)]}{\text{sgn}[\epsilon_{\bar{k}}(\vec{J}_0)\Delta_{\bar{k}}(\vec{J}_0)]}\right]. \tag{B3}$$

Plugging in  $E_{\bar{k}}(J)^2 = \epsilon_{\bar{k}}(J)^2 + \Delta_{\bar{k}}(J)^2$  yields

$$1 = |B_{\bar{k}}(J_0, J_1)| \Leftrightarrow \Delta_{\bar{k}}(\vec{J}_0)\Delta_{\bar{k}}(\vec{J}_1) + \epsilon_{\bar{k}}(\vec{J}_0)\epsilon_{\bar{k}}(\vec{J}_1) = 0. \tag{B4}$$

So, for the emergence of a nonanalyticity at a given time  $t = t^*$  we get two (simplified) conditions:

$$E_{\bar{k}}(\vec{J}_1) = \frac{(2n+1)\pi}{2t^*} \equiv C_{t^*}^n, \tag{B5}$$

$$0 = \Delta_{\bar{k}}(\vec{J}_0)\Delta_{\bar{k}}(\vec{J}_1) + \epsilon_{\bar{k}}(\vec{J}_0)\epsilon_{\bar{k}}(\vec{J}_1). \tag{B6}$$

### APPENDIX C: QUENCH/RAMPING PARAMETERS

In Table I we give a summary of the quench parameters used for the figures in the main text.

TABLE I. Quench parameters.

Figure	$J_0^x$	$J_0^y$	$J_0^z$	$J_1^x$	$J_1^y$	$J_1^z$	$\kappa_0$	$\kappa_1$
4(a)	0.8	0.1	0.1	0.6	0.2	0.2	0	0
4(b)	0.8	0.1	0.1	0.4	0.3	0.3	0	0
5(a)	0.8	0.1	0.1	0.6	0.2	0.2	0	0
5(b)	0.8	0.1	0.1	0.2	0.1	0.7	0	0
5(c)	0.8	0.1	0.1	0.4	0.3	0.3	0	0
5(d)	0.4	0.3	0.3	0.3	0.4	0.3	0	0
6(a)	0.1	0.9	0.0	0.4	0.6	0.0	0	0



TABLE I. (*Continued.*)

Figure	$J_0^x$	$J_0^y$	$J_0^z$	$J_1^x$	$J_1^y$	$J_1^z$	$\kappa_0$	$\kappa_1$
6(b)	0.25	0.75	0.0	0.75	0.25	0.0	0	0
7(a)	0.9	0.05	0.05	0.6	0.2	0.2	0	0
7(b)	0.9	0.05	0.05	0.1	0.8	0.1	0	0
8(a)	0.8	0.1	0.1	0.6	0.2	0.2	0	0
8(b)	0.8	0.1	0.1	0.4	0.3	0.3	0	0
9(a)	1/3	1/3	1/3	1/3	1/3	1/3	0.5	0.1
9(b)	1/3	1/3	1/3	1/3	1/3	1/3	0.5	-0.1

- [1] M. Greiner, O. Mandel, T. Esslinger, T. Hänsch, and I. Bloch, *Nature (London)* **415**, 39 (2002).
- [2] T. Kinoshita, T. Wenger, and D. Weiss, *Nature (London)* **440**, 900 (2006).
- [3] M. Heyl, A. Polkovnikov, and S. Kehrein, *Phys. Rev. Lett.* **110**, 135704 (2013).
- [4] G. E. Fisher, *Lectures in Theoretical Physics*, Lectures Delivered at the Summer Institute for Theoretical Physics, Vol. 7 (University of Colorado Press, Boulder, 1965).
- [5] C. Karrasch and D. Schuricht, *Phys. Rev. B* **87**, 195104 (2013).
- [6] J. N. Kriel, C. Karrasch, and S. Kehrein, *Phys. Rev. B* **90**, 125106 (2014).
- [7] S. Vajna and B. Dóra, *Phys. Rev. B* **91**, 155127 (2015).
- [8] E. Canovi, P. Werner, and M. Eckstein, *Phys. Rev. Lett.* **113**, 265702 (2014).
- [9] M. Fagotti, [arXiv:1308.0277](https://arxiv.org/abs/1308.0277).
- [10] S. Vajna and B. Dóra, *Phys. Rev. B* **89**, 161105 (2014).
- [11] F. Andraschko and J. Sirker, *Phys. Rev. B* **89**, 125120 (2014).
- [12] J. Budich and M. Heyl, [arXiv:1504.05599](https://arxiv.org/abs/1504.05599).
- [13] G. Torlai, L. Tagliacozzo, and G. De Chiara, *J. Stat. Mech.* (2014) P06001.
- [14] M. Heyl and M. Vojta, [arXiv:1310.6226](https://arxiv.org/abs/1310.6226).
- [15] A. Kitaev, *Ann. Phys.* **321**, 2 (2006).
- [16] H.-D. Chen and J. Hu, *Phys. Rev. B* **76**, 193101 (2007).
- [17] H.-D. Chen and Z. Nussinov, *J. Phys. A: Math. Theor.* **41**, 075001 (2008).
- [18] Here, we choose  $\alpha_r = -1$  (cf. Ref. [17]), such that the result for the spectrum agrees with the result in Ref. [15].
- [19] To be precise one would have to decide how to deal with the  $k_x = 0$  axis; however, this will not play any role in the later calculations.
- [20] C. N. Yang and T. D. Lee, *Phys. Rev.* **87**, 404 (1952).
- [21] I. Bena, M. Droz, and A. Lipowski, *Int. J. Mod. Phys. B* **19**, 4269 (2005).
- [22] W. van Saarloos and D. Kurtze, *J. Phys. A: Math. Gen.* **17**, 1301 (1984).
- [23] Assuming conventional continuity is too strong in this case, since in the Kitaev model the mode occupation number is not necessarily continuous after quenching (see Fig. 8).
- [24] S. Mondal, D. Sen, and K. Sengupta, *Phys. Rev. B* **78**, 045101 (2008).
- [25] M. Heyl, *Phys. Rev. Lett.* **113**, 205701 (2014).
- [26] M. Heyl, [arXiv:1505.02352](https://arxiv.org/abs/1505.02352).



## 2.2 Phase transitions in non-equilibrium steady states

Topological order allows to characterize phases beyond the Landau paradigm (Wen, 2013). This section addresses the question whether and how topological order is reflected in the nonequilibrium dynamics of Chern insulators.

A key experiment that elucidated the necessity to understand phase transitions in the absence of a local order parameter was the discovery of the integer quantum Hall effect (von Klitzing *et al.*, 1980). In this experiment on a two-dimensional electron gas subjected to an external magnetic field it was observed that with very high precision the Hall conductance takes only values

$$\sigma_{xy} = C \frac{e^2}{h}, \quad (2.10)$$

where  $e$  is the elementary charge,  $h$  is Planck’s constant, and  $C \in \mathbb{Z}$  is an integer. As the magnetic field amplitude was tuned the Hall conductance exhibited jumps between different values, but no local order parameter could be identified to explain this as a phase transition within the Landau framework. Instead, it was found in a seminal work (Thouless *et al.*, 1982) that the integer  $C$  was a topological invariant associated with the ground state of the corresponding Hamiltonian, namely the Chern number, which serves as a topological order parameter. This relation of the observable to topological properties of the ground state explains the extraordinary precision of the experimental results, because the value of  $C$  is robust against local perturbations and can only be affected by global changes in the system. Consequently, the conductance quantum  $e^2/h$  is nowadays the natural constant that is determined with the highest precision.

It turned out that a quantized Hall conductance can also occur without an external magnetic field. This fact was pointed out by (Haldane, 1988) using a simplistic model Hamiltonian as example, which became known as the Haldane model. This system is a *topological insulator*, i.e., the bulk is a band insulator but the surface hosts gapless excitations. Such edge states exist at the boundary to “ordinary” insulators, because the topological invariant of the wave function cannot change without a gap closing. These edge states are robust against local perturbations of the Hamiltonian, because they are topologically protected. Considering more realistic model Hamiltonians it was later suggested that topological insulators can occur as real materials (Kane and Mele, 2005; Bernevig *et al.*, 2006) and their existence was indeed verified experimentally soon after that (König *et al.*, 2007).

In cold atom experiments Floquet engineering allows to realize effective gauge fields. In this way the Haldane model was recently implemented in experiment despite its unnatural simplicity (Jotzu *et al.*, 2014). The observation of DQPTs in another cold atom realization of the Haldane model (Fläschner *et al.*, 2016) demonstrates how the quench dynamics of Chern insulators become experimentally accessible using such quantum simulators.

These experimental possibilities motivate theoretical studies of topological insulators far from equilibrium. The topological invariant characterizing the different phases of a Chern insulator, however, is a property of the ground state wave function. Since a quench induces large excitations it is not clear whether the topological properties of the Hamiltonian play a role in the dynamics far from equilibrium. This question has been addressed in different

works. A key insight is that when quenching from a ground state of the Hamiltonian the Chern number of the time-evolved state always remains unchanged (D'Alessio and Rigol, 2015). Nevertheless, it was found that the topological properties of the post-quench Hamiltonian can leave an imprint on the observables of the time-evolved system, in particular the Hall response (Dehghani *et al.*, 2015; Wang and Kehrein, 2016; Hu *et al.*, 2016; Caio *et al.*, 2016).

As will be shown in what follows, the steady state reached a long time after quenching a Chern insulator exhibits a topologically driven nonequilibrium phase transition, indicated by a universal nonanalyticity of the Hall conductance as a function of the quench parameters. In Section 2.2.1 this behavior is derived and its universal character is demonstrated using different example systems. In Section 2.2.2 the analysis is generalized to Floquet topological insulators, which are candidate systems for the experimental observation of the predicted behavior.

### 2.2.1 *Publication:* Universal nonanalytic behavior of the Hall conductance in a Chern insulator at the topologically driven nonequilibrium phase transition

Reprinted article with permission from

Pei Wang, Markus Schmitt, and Stefan Kehrein

Physical Review B **93**, 085134 (2016)

<https://doi.org/10.1103/PhysRevB.93.085134>

Copyright (2016) by the American Physical Society.

**Author contributions** P. W. conceived to study the Hall conductance in the steady state of the quenched Chern insulator and performed the analysis of the Dirac model and the Haldane model. M. S. worked out the details for the Kitaev honeycomb model. P. W. wrote the main part of the manuscript with contributions from M. S.. All authors discussed the results and the interpretation.

# Universal nonanalytic behavior of the Hall conductance in a Chern insulator at the topologically driven nonequilibrium phase transition

Pei Wang,<sup>1,2,\*</sup> Markus Schmitt,<sup>2</sup> and Stefan Kehrein<sup>2</sup>

<sup>1</sup>*Department of Physics, Zhejiang Normal University, Jinhua 321004, China*

<sup>2</sup>*Institute for Theoretical Physics, Georg-August-Universität Göttingen, Friedrich-Hund-Platz 1, Göttingen 37077, Germany*

(Received 15 December 2015; published 24 February 2016)

We study the Hall conductance of a Chern insulator after a global quench of the Hamiltonian. The Hall conductance in the long time limit is obtained by applying the linear response theory to the diagonal ensemble. It is expressed as the integral of the Berry curvature weighted by the occupation number over the Brillouin zone. We identify a topologically driven nonequilibrium phase transition, which is indicated by the nonanalyticity of the Hall conductance as a function of the energy gap  $m_f$  in the post-quench Hamiltonian  $\hat{H}_f$ . The topological invariant for the quenched state is the winding number of the Green's function  $W$ , which equals the Chern number for the ground state of  $\hat{H}_f$ . In the limit  $m_f \rightarrow 0$ , the derivative of the Hall conductance with respect to  $m_f$  is proportional to  $\ln|m_f|$ , with the constant of proportionality being the ratio of the change of  $W$  at  $m_f = 0$  to the energy gap in the initial state. This nonanalytic behavior is universal in two-band Chern insulators such as the Dirac model, the Haldane model, or the Kitaev honeycomb model in the fermionic basis.

DOI: [10.1103/PhysRevB.93.085134](https://doi.org/10.1103/PhysRevB.93.085134)

## I. INTRODUCTION

The notions of topological order and topological invariant were introduced into condensed matter physics for classifying certain states of matter that cannot be classified by broken symmetries. Their change in the ground state of a system is accompanied by a topological phase transition. It is well known that the topological order or the topological invariant are robust against local perturbations to the Hamiltonian. But it is not clear whether they are also robust against a global quench of the Hamiltonian, and what is the proper way of defining them in a quenched state far from equilibrium. Recently, these questions drew attention [1–19] due to their relevance with the implementation of topological quantum computing.

Suppose that the system is initially in the ground state of the Hamiltonian  $\hat{H}_i$ . At the time  $t = 0$ , the Hamiltonian is suddenly changed from  $\hat{H}_i$  to  $\hat{H}_f$ . The system is then driven out of equilibrium, and the wave function evolves unitarily. In the toric code model, the topological entropy of the unitarily evolving wave function is found to keep invariant [1–3] after a quench. In general, the long-range entanglement in a wave function cannot be changed by local unitary transformations [20]. Therefore, the topological entropy of the unitarily evolving wave function keeps a constant if  $\hat{H}_f$  has no long-range interaction. Similarly, the Chern number of the unitarily evolving wave function in a Chern insulator [4–6] is found to be independent of  $\hat{H}_f$ . If one chose it as the topological order parameter of the quenched state, the topological order would be always robust against a quench of the Hamiltonian.

However, in the  $p$ -wave superfluid or the  $s$ -wave superfluid with spin-orbit coupling, the winding number of the Green's function depends on both  $\hat{H}_i$  and  $\hat{H}_f$  [7–10]. And in the topological superconductor with proximity-induced superconductivity, the topological properties of the quenched state were argued to be  $\hat{H}_f$  dependent [11–13]. When the initial state is in a topologically nontrivial phase, the quenched state in the long

time limit is in the trivial (nontrivial) phase if the ground state of  $\hat{H}_f$  is in the trivial (nontrivial) phase. This conclusion is supported by the study of the Majorana order parameter [11], the entanglement spectrum [12], and the dynamics of edge states [13]. Especially, in the thermodynamic limit, the survival probability of the Majorana edge modes decays to a finite value if the quench is within the same topological phase. But it decays to zero if the quench is across the phase boundary [13].

Up to now, the definition of the topological order parameter in a quenched state is ambiguous. Different topological invariants which are equivalent in a ground state might be dramatically different in a quenched state. This is clearly demonstrated in the  $p$ -wave superfluid [8], in which the winding number of the Anderson pseudospin texture is independent of  $\hat{H}_f$  but that of the Green's function is  $\hat{H}_f$  dependent. It is then necessary to study which topological invariant is experimentally relevant.

The order parameter is defined to distinguish different phases at a phase transition. A phase transition can be indicated in an experimentally relevant way by the nonanalyticity of the observables. And the topological invariant was introduced to explain phase transitions that are beyond the conventional framework of symmetry breaking. For example, the Chern number [21] was introduced in the quantum Hall effect [22] to explain the jump of the Hall conductance at some magnetic fields. Following this logic, we study the phase transitions in the quenched states, which are indicated by the nonanalyticity of a measurable observable as a function of the parameters of the quenched state, i.e., the parameters in  $\hat{H}_i$  or  $\hat{H}_f$ . The experimentally relevant topological invariant for the quenched state is defined in such a way that its change accompanies the phase transition.

A topologically driven phase transition in the quenched state has been argued to exist in the one-dimensional superfluid with spin-orbit coupling, in which the superfluid order parameter and the tunneling conductance at the edge were calculated numerically [10]. However, unambiguous evidence for the nonanalyticity of observables cannot be obtained from the numerics. In this paper we study the quenched state of a Chern insulator. We argue that the Hall conductance in the long

\*wangpei@zjut.edu.cn

time limit after the quench can be expressed as the integral of the Berry curvature weighted by the occupation number over the Brillouin zone. In a generic two-band Chern insulator, the Hall conductance is not quantized, but is a continuous function of the energy gap  $m_f$  in the post-quench Hamiltonian  $\hat{H}_f$ . However, the derivative of the Hall conductance with respect to  $m_f$  is logarithmically divergent in the limit  $m_f \rightarrow 0$  if the Chern number for the ground state of  $\hat{H}_f$  changes at  $m_f = 0$ . And the prefactor of the logarithm is the ratio of the change of the Chern number to the energy gap in the initial state. We strictly prove this statement by relating the nonanalyticity of the Hall conductance to the spectrum of  $\hat{H}_f$  nearby the gap closing point in the Brillouin zone. The experimentally relevant topological invariant for the quenched state is the winding number of the Green's function, which is equal to the Chern number for the ground state of  $\hat{H}_f$  but is generally different from the Chern number of the unitarily evolving wave function. We then identify a nonequilibrium phase transition in the quenched state, which has a topological nature in the sense that the nonanalyticity is determined by the change of the topological invariant at the transition. The nonanalytic behavior of the Hall conductance is universal, being independent of the symmetry of the model or local perturbations to  $\hat{H}_i$  and  $\hat{H}_f$ . Our findings serve as a benchmark in the future study of the topologically driven phase transitions in the quenched states.

The contents of the paper are arranged as follows. We derive the formula for the quench-state Hall conductance in a  $N$ -band Chern insulator in Sec. II, and show its form in a two-band Chern insulator in Sec. III. In Sec. IV we study a general two-band Chern insulator and prove the universal nonanalytic behavior of the Hall conductance. Subsequently, in Sec. V we apply our formalism to three models, namely the Dirac model, the Haldane model, and the Kitaev honeycomb model and demonstrate that numerical results for the Hall conductance close to critical points do in fact show the expected universal behavior. We discuss the topological invariant for the quenched state in Sec. VI. At last, a concluding section summarizes our results.

## II. HALL CONDUCTANCE OF THE QUENCHED STATE

Let us consider a  $N$ -component Fermi gas in two dimensions. Its Hamiltonian in momentum space is written as

$$\hat{H} = \sum_{\vec{k}} \hat{c}_{\vec{k}}^\dagger \mathcal{H}_{\vec{k}} \hat{c}_{\vec{k}}, \quad (1)$$

where  $\hat{c}_{\vec{k}} = (\hat{c}_{\vec{k}1}, \hat{c}_{\vec{k}2}, \dots, \hat{c}_{\vec{k}N})^T$  is the fermionic operator.  $i = 1, 2, \dots, N$  might denote the spin of electrons, the sublattice index in the case of a honeycomb lattice, or the internal state of atoms. The single-particle Hamiltonian  $\mathcal{H}_{\vec{k}}$  has  $N$  eigenvalues, which form  $N$  energy bands, respectively. If the Fermi energy lies within the band gap, the bands lower than the Fermi energy are fully occupied in the ground state, but those above the Fermi energy are empty. The Chern number of the ground-state wave function is defined as (see an introduction of the Chern number in Ref. [23])

$$C = \frac{i}{2\pi} \sum_{\alpha \in \text{occ}} \int d\vec{k}^2 \left( \left\langle \frac{\partial u_{\vec{k}\alpha}}{\partial k_x} \middle| \frac{\partial u_{\vec{k}\alpha}}{\partial k_y} \right\rangle - \text{H.c.} \right), \quad (2)$$

where  $|u_{\vec{k}\alpha}\rangle$  is the eigenvector of  $\mathcal{H}_{\vec{k}}$  with  $\alpha = 1, 2, \dots, N$  denoting the different bands. The sum of  $\alpha$  is over all the occupied bands, and the integral with respect to  $\vec{k}$  is over the Brillouin zone. The Chern number is a topological invariant, which is robust against a local deformation of the Hamiltonian and can only take an integer value.

The Chern number describes the topological property of the ground-state wave function. In the celebrated paper by Thouless *et al.* [21], the Chern number is related to the Hall conductance  $\sigma_H^G$  as

$$\sigma_H^G = C e^2 / h. \quad (3)$$

The Chern number for the ground state is then a measurable physical quantity. Or one can say that the Hall conductance is the topological order parameter of the ground state. When the Chern number is nonzero, the Fermi gas displays a quantum Hall effect even if there is no net magnetic field [24]. The system is then called a Chern insulator.

Suppose that the system is initially in the ground state of  $\hat{H}_i$ , before the Hamiltonian is quenched into  $\hat{H}_f$ . The system is then driven out of equilibrium, and the wave function follows a unitary time evolution  $|\Psi(t)\rangle = e^{-i\hat{H}_f t} |\Psi(0)\rangle$ , where  $|\Psi(0)\rangle$  denotes the ground state of  $\hat{H}_i$ . In a few paradigmatic models [4–6], the Chern number of the unitarily evolving wave function is shown to be a constant, being independent of the post-quench Hamiltonian  $\hat{H}_f$ . If one chooses it as the topological order parameter of the quenched state, the topological order is always robust against a quench of the Hamiltonian. However, the Chern number of the unitarily evolving wave function cannot be directly measured. To address the topological order parameter of the quenched state in an experimentally relevant way, we study a measurable quantity—the Hall conductance. In the quenched state, the Hall conductance must be distinguished from the Chern number.

We notice that the Hall conductance cannot be expressed as the expectation value of a local operator with respect to the unitarily evolving wave function  $|\Psi(t)\rangle$ . Instead, it is the long-time response of the system to an external electric field in linear response theory [25]. This fact is related to the observation that measuring the Hall conductance unavoidably introduces decoherence and therefore in the long time limit the system cannot be described by the unitarily evolving wave function any more. Instead, the system should be described by the diagonal ensemble [26]. If the expectation value of an observable  $\hat{O}$  after the quench relaxes to some steady value, it must be equal to its time average:

$$\lim_{t \rightarrow \infty} O(t) = \lim_{T \rightarrow \infty} \frac{1}{T} \int_0^T dt \langle \Psi(t) | \hat{O} | \Psi(t) \rangle. \quad (4)$$

We insert the eigenbasis of  $\hat{H}_f$  in the right-hand side. In the limit  $T \rightarrow \infty$ , the off-diagonal terms of  $\hat{O}$  are averaged out [26], we then have

$$\begin{aligned} \lim_{t \rightarrow \infty} O(t) &= \sum_E |\langle E | \Psi(0) \rangle|^2 \langle E | \hat{O} | E \rangle \\ &= \text{Tr}[\hat{O} \hat{\rho}], \end{aligned} \quad (5)$$

where  $|E\rangle$  is the eigenstate of  $\hat{H}_f$  and  $\hat{\rho}$  is diagonal in the basis  $|E\rangle$  with the diagonal elements  $|\langle E | \Psi(0) \rangle|^2$ . The diagonal

ensemble  $\hat{\rho}$  is obtained by dropping the off-diagonal terms in the initial density matrix. This is equivalent to considering the decoherence effect. Even though Eq. (5) is based on the hypothesis of nondegenerate eigenenergies, the diagonal ensemble is also applicable in many integrable quantum systems [27,28].

Based on the above argument, the Hall conductance of the quenched state should be calculated in the diagonal ensemble. Let us represent an arbitrary many-body eigenstate of  $\hat{H}_f$  by  $|\{z_{\bar{k}\alpha}\}\rangle$ , where  $z_{\bar{k}\alpha} = 1, 0$  denotes whether the single-particle state  $|u_{\bar{k}\alpha}^f\rangle$  is occupied or not, respectively. Note that  $|u_{\bar{k}\alpha}^f\rangle$  is the eigenvector of the post-quench single particle Hamiltonian  $\mathcal{H}_{\bar{k}}^f$ . The diagonal ensemble can be written as

$$\hat{\rho} = \sum_{\{z_{\bar{k}\alpha}\}} p(\{z_{\bar{k}\alpha}\}) |\{z_{\bar{k}\alpha}\}\rangle \langle\{z_{\bar{k}\alpha}\}|, \quad (6)$$

where  $p(\{z_{\bar{k}\alpha}\}) = |\langle\{z_{\bar{k}\alpha}\}|\Psi(0)\rangle|^2$  and the sum is over all the possible occupation configurations.

Now let us suppose a system located in the  $x - y$  plane with its density matrix being  $\hat{\rho}$ .  $\hat{\rho}$  is stationary in the sense that  $[\hat{\rho}, \hat{H}_f] = 0$ . Therefore, we can use the linear response theory to calculate the Hall conductance by simply replacing the thermal ensemble by  $\hat{\rho}$ . In the linear response theory [25] we suppose that an infinitesimal electric field is switched on in the  $x$  direction, and then the current in the  $y$  direction is measured after an infinitely long time. The current is proportional to the electric field strength with the constant of proportionality defined as the Hall conductance. The Hall conductance can be expressed by the current-current correlation as

$$\sigma_H = \lim_{\omega \rightarrow 0} \frac{1}{S\omega} \int_0^\infty dt e^{i\omega t} \text{Tr}[\hat{\rho}[\hat{J}_y, \hat{J}_x(t)]], \quad (7)$$

where  $\omega$  denotes the frequency of the electric field and the limit  $\omega \rightarrow 0$  corresponds to the dc conductance, and  $S$  denotes the area of the system.  $\hat{J}_x$  and  $\hat{J}_y$  are the current operators in the  $x$  and  $y$  directions, respectively. They are written as

$$\hat{J}_{x/y} = e \sum_{\bar{k}} \hat{c}_{\bar{k}}^\dagger \frac{\partial \mathcal{H}_{\bar{k}}^f}{\partial k_{x/y}} \hat{c}_{\bar{k}}. \quad (8)$$

Since both the Hamiltonian and the current operator are quadratic, we can reexpress the Hall conductance by using the single-particle states as

$$\sigma_H = \lim_{\omega \rightarrow 0} \frac{1}{S\omega} \int_0^\infty dt e^{i\omega t} \sum_{\bar{k}, \alpha} n_{\bar{k}\alpha} \langle u_{\bar{k}\alpha}^f | [\hat{J}_k^y, \hat{J}_k^x(t)] | u_{\bar{k}\alpha}^f \rangle, \quad (9)$$

where the momentum-resolved current operator is a  $N$ -by- $N$  matrix, defined as  $\hat{J}_{\bar{k}}^{x/y} = e \frac{\partial \mathcal{H}_{\bar{k}}^f}{\partial k_{x/y}}$ . The occupation number  $n_{\bar{k}\alpha}$  is related to the probability function  $p(\{z_{\bar{k}\alpha}\})$  by  $n_{\bar{k}\alpha} = \sum_{\{z_{\bar{k}'\alpha'}\}} p(\{z_{\bar{k}'\alpha'}\}) \delta_{z_{\bar{k}\alpha}, 1}$ . In Eq. (9) the sum of  $\alpha$  is over all the energy bands.

When calculating the integral with respect to  $t$  in Eq. (9), one can insert a factor  $e^{-\eta|t|}$  into the integrand with  $\eta$  being an infinitesimal number. The integral then becomes convergent. Because the dc Hall conductance must be a real number, we keep the real part of  $\sigma_H$ , but neglect the imaginary part. The

Hall conductance becomes

$$\sigma_H = \frac{-ie^2}{S} \sum_{\bar{k}, \alpha, \beta} \frac{n_{\bar{k}\alpha}}{(\epsilon_{\bar{k}\alpha} - \epsilon_{\bar{k}\beta})^2} \times \left[ \langle u_{\bar{k}\alpha}^f | \frac{\partial \mathcal{H}_{\bar{k}}^f}{\partial k_y} | u_{\bar{k}\beta}^f \rangle \langle u_{\bar{k}\beta}^f | \frac{\partial \mathcal{H}_{\bar{k}}^f}{\partial k_x} | u_{\bar{k}\alpha}^f \rangle - \text{H.c.} \right] \quad (10)$$

where  $\epsilon_{\bar{k}\alpha}$  denotes the eigenvalue of  $\mathcal{H}_{\bar{k}}^f$  in the band  $\alpha$ . In thermodynamic limit,  $\sum_{\bar{k}}$  is replaced by  $\frac{S}{(2\pi)^2} \int d\bar{k}^2$ . By using the relation  $\mathcal{H}_{\bar{k}}^f = \sum_{\alpha} \epsilon_{\bar{k}\alpha} |u_{\bar{k}\alpha}^f\rangle \langle u_{\bar{k}\alpha}^f|$ , we finally express the Hall conductance as

$$\sigma_H = \frac{e^2}{h} \frac{i}{2\pi} \sum_{\alpha} \int d\bar{k}^2 n_{\bar{k}\alpha} \left( \left\langle \frac{\partial u_{\bar{k}\alpha}^f}{\partial k_x} \middle| \frac{\partial u_{\bar{k}\alpha}^f}{\partial k_y} \right\rangle - \text{H.c.} \right). \quad (11)$$

We choose  $e^2/h$  as the unit of conductance. The dimensionless Hall conductance  $C_{\text{neq}} = \sigma_H/(e^2/h)$  is expressed as

$$C_{\text{neq}} = \frac{i}{2\pi} \sum_{\alpha} \int d\bar{k}^2 n_{\bar{k}\alpha} \left( \left\langle \frac{\partial u_{\bar{k}\alpha}^f}{\partial k_x} \middle| \frac{\partial u_{\bar{k}\alpha}^f}{\partial k_y} \right\rangle - \text{H.c.} \right). \quad (12)$$

This formula of Hall conductance stands for the quenched states in general Fermi gases, in which the interaction between fermions is neglected. We notice that a Kubo formula calculation by Deghani, Oka, and Mitra [29] derived the similar formula in a different way for Floquet topological states. Comparing Eq. (12) with Eq. (2), we see the difference between the quench-state Hall conductance and the ground-state Chern number. In the integrand of Eq. (12), the Berry curvature is weighted by the occupation number  $n_{\bar{k}\alpha}$ , and the sum of  $\alpha$  is over all the bands. In the special case of  $\hat{H}_i = \hat{H}_f$  (no quench), the occupation is either 0 for an empty band or 1 for a fully occupied band, and then the Hall conductance reduces to the Chern number. But for  $\hat{H}_i \neq \hat{H}_f$ , no bands are fully occupied or completely empty.  $n_{\bar{k}\alpha}$  changes continuously with the momentum  $\bar{k}$ . The integrand of Eq. (12) cannot be expressed as the curl of some function in the Brillouin zone, so that  $C_{\text{neq}}$  is not quantized, but can take an arbitrary value. This is different from the Chern number  $C$ , which must be an integer.

### III. QUENCH-STATE HALL CONDUCTANCE IN A TWO-BAND CHERN INSULATOR

Equation (12) gives the Hall conductance of the quenched states in  $N$ -component Fermi gases. Next we discuss the case of  $N = 2$ , in which the Hall conductance can be conveniently expressed as a function of the parameters in  $\hat{H}_i$  and  $\hat{H}_f$  by utilizing the properties of the SU(2) algebra.

In a two-component Fermi gas, the single-particle Hamiltonian can always be decomposed into

$$\mathcal{H}_{\bar{k}} = \vec{d}_{\bar{k}} \cdot \vec{\sigma}, \quad (13)$$

where  $\vec{\sigma} = (\sigma_x, \sigma_y, \sigma_z)$  denote the Pauli matrices. There might be an additional constant in the expression of  $\mathcal{H}_{\bar{k}}$ ; however, the constant term has no effect on the eigenvectors, and, thus, does not contribute to the Hall conductance. The Hall conductance is only determined by the coefficient vectors  $\vec{d}_{\bar{k}} = (d_{1\bar{k}}, d_{2\bar{k}}, d_{3\bar{k}})$  in the initial and post-quench Hamiltonians.



The two eigenvalues of  $\mathcal{H}_{\vec{k}}$  are  $\pm d_{\vec{k}}$  with

$$d_{\vec{k}} = \sqrt{(d_{1\vec{k}})^2 + (d_{2\vec{k}})^2 + (d_{3\vec{k}})^2}. \quad (14)$$

The system has two bands, namely the lower band corresponding to the negative eigenvalue and the upper band corresponding to the positive eigenvalue. There is a gap between the two bands if we have  $d_{\vec{k}} \neq 0$  everywhere in the Brillouin zone.

We set the chemical potential to zero, in which case the lower band is fully occupied but the upper band is empty. The Chern number of the ground state is written as

$$C = \frac{i}{2\pi} \int d\vec{k}^2 \left( \left\langle \frac{\partial u_{\vec{k}-}}{\partial k_x} \middle| \frac{\partial u_{\vec{k}-}}{\partial k_y} \right\rangle - \text{H.c.} \right), \quad (15)$$

where  $|u_{\vec{k}-}\rangle$  denotes the eigenvector of  $\mathcal{H}_{\vec{k}}$  with the negative eigenvalue. The Chern number can be expressed by using the coefficient vector as [23]

$$C = \int d\vec{k}^2 \frac{\left( \frac{\partial \vec{d}_{\vec{k}}}{\partial k_x} \times \frac{\partial \vec{d}_{\vec{k}}}{\partial k_y} \right) \cdot \vec{d}_{\vec{k}}}{4\pi d_{\vec{k}}^3}. \quad (16)$$

The Chern number usually keeps invariant as the Hamiltonian changes. But at some special points of the parameter space, the energy gap closes ( $d_{\vec{k}} = 0$ ) somewhere in the Brillouin zone. The Chern number then has a jump, which indicates a topological phase transition in the ground state.

We quench the Hamiltonian from  $\mathcal{H}_{\vec{k}}^i = \vec{d}_{\vec{k}}^i \cdot \vec{\sigma}$  to  $\mathcal{H}_{\vec{k}}^f = \vec{d}_{\vec{k}}^f \cdot \vec{\sigma}$ , and then calculate the Hall conductance in the quenched state. The eigenvectors of  $\mathcal{H}_{\vec{k}}^{i/f}$  with the positive and negative eigenvalues are denoted by  $|u_{\vec{k}\alpha}^{i/f}\rangle$  with  $\alpha = \pm$ , respectively. The momentum  $\vec{k}$  is a good quantum number in both the initial and the post-quench Hamiltonians. Therefore, the occupation number is simply expressed as

$$n_{\vec{k}\alpha} = \left| \langle u_{\vec{k}\alpha}^f | u_{\vec{k}-}^i \rangle \right|^2, \quad (17)$$

where  $|u_{\vec{k}-}^i\rangle$  is the initial state according to our protocol. The total occupation at each  $\vec{k}$  is conserved, satisfying

$$n_{\vec{k}+} + n_{\vec{k}-} \equiv 1. \quad (18)$$

In fact, the occupation number can be written as

$$n_{\vec{k}\pm} = \frac{1}{2} \mp \frac{1}{2} \frac{\vec{d}_{\vec{k}}^f \cdot \vec{d}_{\vec{k}}^i}{d_{\vec{k}}^f d_{\vec{k}}^i}, \quad (19)$$

where  $d_{\vec{k}}^{i/f}$  is the length of the coefficient vector  $\vec{d}_{\vec{k}}^{i/f}$ .  $\frac{\vec{d}_{\vec{k}}^f \cdot \vec{d}_{\vec{k}}^i}{d_{\vec{k}}^f d_{\vec{k}}^i}$  is called the occupation factor, which is just the cosine of the angle between the initial and the post-quench coefficient vectors.

In the two-band Chern insulator, the Berry curvatures in the lower and upper bands are opposite to each other everywhere in the Brillouin zone [23]. We have

$$\frac{i}{2\pi} \left( \left\langle \frac{\partial u_{\vec{k}\pm}^f}{\partial k_x} \middle| \frac{\partial u_{\vec{k}\pm}^f}{\partial k_y} \right\rangle - \text{H.c.} \right) = \mp C_{\vec{k}}, \quad (20)$$

where

$$C_{\vec{k}} = \frac{\left( \frac{\partial \vec{d}_{\vec{k}}^f}{\partial k_x} \times \frac{\partial \vec{d}_{\vec{k}}^f}{\partial k_y} \right) \cdot \vec{d}_{\vec{k}}^f}{4\pi (d_{\vec{k}}^f)^3}. \quad (21)$$

Substituting Eqs. (19) and (21) into Eq. (12), we determine the Hall conductance as

$$C_{\text{neq}} = \int d\vec{k}^2 \frac{(\vec{d}_{\vec{k}}^f \cdot \vec{d}_{\vec{k}}^i) \left( \frac{\partial \vec{d}_{\vec{k}}^f}{\partial k_x} \times \frac{\partial \vec{d}_{\vec{k}}^f}{\partial k_y} \right) \cdot \vec{d}_{\vec{k}}^f}{4\pi d_{\vec{k}}^i (d_{\vec{k}}^f)^4}, \quad (22)$$

where the integral is over the Brillouin zone.

In the next section we analyze the behavior of  $C_{\text{neq}}$  close to critical points at which the gap of the spectrum closes and  $C$  changes.

#### IV. UNIVERSAL NONANALYTIC BEHAVIOR OF THE HALL CONDUCTANCE IN TWO-BAND CHERN INSULATORS

Suppose that there is a tunable parameter in the Hamiltonian (13), namely  $M$  without loss of generality. The vector  $\vec{d}_{\vec{k}}$  is a function of  $M$ . We use  $M_i$  to denote the free parameter in the initial Hamiltonian, and  $M_f$  to denote that in the post-quench Hamiltonian. Every pair  $(M_i, M_f)$  determines a quenched state. We further suppose that the initial state (or  $M_i$ ) is fixed. The quench-state Hall conductance  $C_{\text{neq}}$  is then a function of  $M_f$ . If the function  $C_{\text{neq}}(M_f)$  is nonanalytic at some point, namely at  $M_f = M_f^c$ , we say that there is a nonequilibrium phase transition at  $M_f = M_f^c$ . The term ‘‘nonequilibrium phase transition’’ comes from the fact that this phase transition happens in the quenched state which is far from equilibrium.

Let us discuss why  $C_{\text{neq}}(M_f)$  can be nonanalytic. In a generic model,  $\vec{d}_{\vec{k}}^{i/f}$  is an analytic function of  $\vec{k}$  and  $M_{i/f}$ . According to Eq. (22), both numerator and denominator of the integrand are analytic functions. The denominator is the product of  $d_{\vec{k}}^i$  and  $(d_{\vec{k}}^f)^4$ . The former is nonzero everywhere in the Brillouin zone, since the initial state is usually chosen to be a gapped state. But  $M_f$  is a variable. We use  $M_f^c$  to denote the point at which the energy gap in the post-quench Hamiltonian closes. At  $M_f \neq M_f^c$ ,  $d_{\vec{k}}^f$  is nonzero at each  $\vec{k}$ . Therefore, the integrand in Eq. (22) is an analytic function of  $\vec{k}$  and is bounded everywhere in the Brillouin zone.  $C_{\text{neq}}$  is then analytic at  $M_f \neq M_f^c$ . However, at  $M_f = M_f^c$ , the energy gap of  $\hat{H}_f$  closes somewhere in the Brillouin zone, namely at  $\vec{k} = \vec{q}$  without loss of generality. We then have  $d_{\vec{q}}^f = 0$ . The integrand in Eq. (22) is divergent at  $\vec{k} = \vec{q}$ . We expect  $C_{\text{neq}}(M_f)$  to be nonanalytic at  $M_f = M_f^c$ . It is worth emphasizing that the nonanalyticity of  $C_{\text{neq}}(M_f)$  can only be found at the gap closing points of the post-quench Hamiltonian, at which the Chern number for the ground state of  $\hat{H}_f$  changes.

Let us first see how the Chern number given by Eq. (16) is related to the expansion of the coefficient vector  $\vec{d}_{\vec{k}} = (d_{1\vec{k}}, d_{2\vec{k}}, d_{3\vec{k}})$  around  $\vec{k} = \vec{q}$ . One can easily see the topological



nature of the Chern number by reexpressing it as

$$C = \frac{-1}{2\pi} \int d\vec{S} \cdot (\nabla_{\vec{k}} \times \vec{A}), \quad (23)$$

where

$$\vec{A} = \frac{d_{1\vec{k}} \nabla_{\vec{k}} d_{2\vec{k}} - d_{2\vec{k}} \nabla_{\vec{k}} d_{1\vec{k}}}{2d_{\vec{k}}(d_{\vec{k}} - d_{3\vec{k}})} \quad (24)$$

is the so-called Berry connection and  $\vec{S}$  denotes the Brillouin zone oriented in the direction perpendicular to the momentum plane. According to the Kelvin-Stokes theorem, the Chern number equals the line integral of  $\vec{A}$  along the boundary of the Brillouin zone, plus the line integrals of  $\vec{A}$  around all the singularities of  $\vec{A}$  within the Brillouin zone. The former integral must be zero due to the periodicity of  $\vec{A}$ . Supposing that the singularities of  $\vec{A}$  are  $\vec{q}_1, \vec{q}_2, \dots, \vec{q}_N$ , we then have

$$C = \sum_{j=1}^N C^{(\vec{q}_j)}, \quad (25)$$

with

$$C^{(\vec{q}_j)} = \frac{1}{2\pi} \lim_{\eta \rightarrow 0} \oint_{\partial B_\eta(\vec{q}_j)} \vec{A} \cdot d\vec{k}, \quad (26)$$

where  $\partial B_\eta(\vec{q}_j)$  denotes the boundary of a circle of radius  $\sqrt{\eta}$  centered at  $\vec{q}_j$ , and the integral is along the anticlockwise direction.

According to Eq. (24), a singularity of  $\vec{A}$  is a momentum  $\vec{q}$  satisfying  $d_{3\vec{q}} = d_{\vec{q}}$ . Note that  $d_{\vec{k}}$  in the expression of  $\vec{A}$  cannot be zero in a gapped state. We then have  $d_{1\vec{q}} = d_{2\vec{q}} = 0$  at the singularity. In fact, the three components of the coefficient vector are on an equal footing in the expression of the Chern number. One can permute the three components in the expression of  $\vec{A}$ . Therefore, a singularity of  $\vec{A}$  in general refers to a momentum at which two components of the coefficient vector vanish. Here we choose  $d_{1\vec{q}}$  and  $d_{2\vec{q}}$  as the vanishing components without loss of generality. For convenience of discussion, we call  $\vec{q}$  a singularity of  $\vec{A}$  whether  $d_{3\vec{q}} = d_{\vec{q}}$  or  $d_{3\vec{q}} = -d_{\vec{q}}$ .  $d_{3\vec{q}}$  is a free parameter of the model. We will denote it as  $m$  in the following. In fact,  $m$  is nothing but  $(M - M_c)$  in the Dirac model, the Haldane model, or the Kitaev model, which will be discussed in Sec. V. Since  $m = 0$  indicates the closing of the energy gap, we call  $m$  the gap parameter.

In the case of multiple singularities in one Brillouin zone,  $m$  at different singularities might refer to different parameters in the model. An example is the Haldane model, where a single Brillouin zone contains two singularities  $\vec{q}_1$  and  $\vec{q}_2$  with  $d_{\vec{q}_1} \neq d_{\vec{q}_2}$ . In a generic model,  $d_{\vec{k}}$  must have a global minimum point at one of the singularities, when the system is close to the gap closing point. In other words, the energy gap must be  $2|m|$  at one of the singularities. In fact, the minimum point of  $d_{\vec{k}}$  is always related to the symmetry of the model, so are the singularities. On the other hand, if the energy gap closes simultaneously at multiple singularities due to the symmetry of the model, the gap parameter at these singularities must be the same one. In this case, we say that  $m$  is the corresponding gap parameter for these singularities. An example is the Kitaev honeycomb model in a magnetic field.

According to Eqs. (25) and (26), the Chern number is determined only by the coefficient vector in the infinitesimal neighborhoods of the singularities. Therefore, at each singularity  $\vec{q}$ , we expand  $d_{\vec{k}}$  into a power series. For this purpose we assume that the expansion of  $d_{1\vec{k}}$  and  $d_{2\vec{k}}$  does not vary with  $m$ . Then we have

$$\begin{aligned} d_{1\vec{k}} &= a_{1x} \Delta k_x + a_{1y} \Delta k_y + O(\Delta k^2), \\ d_{2\vec{k}} &= a_{2x} \Delta k_x + a_{2y} \Delta k_y + O(\Delta k^2), \\ d_{3\vec{k}} &= m + O(\Delta k^2), \end{aligned} \quad (27)$$

where  $\Delta \vec{k} := \vec{k} - \vec{q}$  and  $a_{jx}$  and  $a_{jy}$  depend on the singularity and the model. A linear term is absent in the expression of  $d_{3\vec{k}}$ . Otherwise, the minimum point of  $d_{\vec{k}}$  would not be at  $\Delta \vec{k} = 0$ , which contradicts our assumption. We also assume that  $d_{\vec{k}}$  has an isolated minimum point at the singularity  $\Delta \vec{k} = 0$ . At  $m = 0$  the spectrum has then a conic structure nearby the singularity. This assumption puts constraints on  $a_{jx}$  and  $a_{jy}$ .

The Berry connection can be reexpressed as

$$\vec{A} = \left( \frac{d_{\vec{k}} + d_{3\vec{k}}}{2d_{\vec{k}}} \right) \left( \frac{d_{1\vec{k}} \nabla_{\vec{k}} d_{2\vec{k}} - d_{2\vec{k}} \nabla_{\vec{k}} d_{1\vec{k}}}{(d_{1\vec{k}})^2 + (d_{2\vec{k}})^2} \right). \quad (28)$$

$C^{(\vec{q})}$  is an integral of  $\vec{A}$  over the boundary of an infinitesimal neighborhood of  $\vec{q}$ . When calculating  $C^{(\vec{q})}$ , we can replace the term inside the first bracket of Eq. (28) by its value at  $\Delta \vec{k} = 0$ , i.e.,  $[1 + \text{sgn}(m)]/2$ . The higher-order terms in the expansion of  $d_{3\vec{k}}$  have no relevant contribution to  $C^{(\vec{q})}$ . Regarding numerator and denominator inside the second bracket of Eq. (28), the terms  $O(\Delta k^2)$  in  $d_{1\vec{k}}$  or  $d_{2\vec{k}}$  contribute to the numerator a correction  $O(\Delta k^2)$  and to the denominator a correction  $O(\Delta k^3)$ , which can both be neglected when calculating  $\oint_{\partial B_\eta(\vec{q}_j)} \vec{A} \cdot d\vec{k}$  in the limit  $\eta \rightarrow 0$ . Therefore,  $C^{(\vec{q})}$  is only determined by the lowest order expansion of the coefficient vector given by Eq. (27). It is straightforward to determine  $C^{(\vec{q})}$  as

$$C^{(\vec{q})} = \frac{1}{2} [1 + \text{sgn}(m)] \text{sgn}(a_{1x} a_{2y} - a_{2x} a_{1y}). \quad (29)$$

At the gap closing point  $m = 0$ , the change of  $C^{(\vec{q})}$  is  $\text{sgn}(a_{1x} a_{2y} - a_{2x} a_{1y})$ .

Next we discuss the nonanalyticity of the quench-state Hall conductance, which can be expressed by using the initial and post-quench coefficient vectors as given in Eq. (22). The integral in the expression of  $C_{\text{neq}}$  is over the Brillouin zone which is finite in general. If the integrand is an analytic function of  $\vec{k}$  and the other parameters in the Hamiltonians and is bounded in the Brillouin zone,  $C_{\text{neq}}$  must be analytic. In a generic model, the coefficient vectors  $\vec{d}_{\vec{k}}^i$  and  $\vec{d}_{\vec{k}}^f$  are analytic functions and are bounded. Therefore,  $C_{\text{neq}}$  is nonanalytic only if  $d_{\vec{k}}^f$  vanishes somewhere in the Brillouin zone, that is the energy gap of the post-quench Hamiltonian closes. Notice that the initial state is chosen to be a gapped state so that  $d_{\vec{k}}^i$  cannot be zero.

As mentioned above, the energy gap closes only at the singularities. Without loss of generality, we suppose that  $m$  is the corresponding gap parameter for the singularities  $\vec{q}_1, \vec{q}_2, \dots, \vec{q}_{N'}$  with  $N' \leq N$ . The Hall conductance  $C_{\text{neq}}$  as a function of  $m_f$  (the gap parameter for the post-quench

Hamiltonian) is nonanalytic at  $m_f = 0$ . We divide the domain of integration in the expression of  $C_{\text{neq}}$  into the infinitesimal neighborhoods of  $\vec{q}_1, \vec{q}_2, \dots, \vec{q}_{N'}$  and the left area. The nonanalytic part of the Hall conductance is expressed as

$$C_{\text{neq}}^\eta = \sum_{j=1}^{N'} C_{\text{neq}}^{(\vec{q}_j)}, \quad (30)$$

with

$$C_{\text{neq}}^{(\vec{q}_j)} = \int_{\mathcal{B}_\eta(\vec{q}_j)} d\vec{k}^2 \frac{(\vec{d}_k^f \cdot \vec{d}_k^i) \left( \frac{\partial \vec{d}_k^f}{\partial k_x} \times \frac{\partial \vec{d}_k^f}{\partial k_y} \right) \cdot \vec{d}_k^f}{4\pi d_k^i (d_k^f)^4}, \quad (31)$$

where  $\mathcal{B}_\eta(\vec{q}_j)$  is a circle of radius  $\sqrt{\eta}$  centered at  $\vec{q}_j$ .  $\eta$  can be arbitrarily small. Note that  $(C_{\text{neq}} - C_{\text{neq}}^\eta)$  is an analytic function of  $m_f$ , since  $d_k^f$  has a positive lower limit in the corresponding domain of integration.

$C_{\text{neq}}^{(\vec{q}_j)}$  is an integral over the infinitesimal neighborhood of  $\vec{q}$ . For calculating  $C_{\text{neq}}^{(\vec{q}_j)}$  we expand the coefficient vectors  $\vec{d}_k^i$  and  $\vec{d}_k^f$  around  $\vec{q}$ . Let us first consider the lowest order expansion given by Eq. (27).  $d_k^i$  can be replaced by its value at  $\vec{k} = \vec{q}$ , i.e.,  $d_k^i = |m_i|$ , with  $m_i$  denoting the gap parameter in the initial Hamiltonian. The energy gap in the initial state is  $2|m_i|$ . Substituting Eq. (27) into Eq. (31), for the denominator we obtain

$$(d_k^f)^4 = \left( m_f^2 + \sum_{j=1}^2 (a_{jx} \Delta k_x + a_{jy} \Delta k_y)^2 \right)^2. \quad (32)$$

We already assumed that  $d_k^f$  has a conic structure at  $m_f = 0$ . For  $a_{jx}$  and  $a_{jy}$  that meet this constraint, we can always perform a linear transformation of coordinates to get

$$\sum_{j=1}^2 (a_{jx} \Delta k_x + a_{jy} \Delta k_y)^2 = \Delta k^2. \quad (33)$$

In the new coordinates, for the numerator of the integrand in Eq. (31) we obtain

$$\mathcal{N} = (a_{1x} a_{2y} - a_{2x} a_{1y}) [m_i m_f^2 + m_f \Delta k^2]. \quad (34)$$

It is then straightforward to work out  $C_{\text{neq}}^{(\vec{q}_j)}$ , which is

$$C_{\text{neq}}^{(\vec{q}_j)} \sim \frac{-\text{sgn}(a_{1x} a_{2y} - a_{2x} a_{1y})}{2|m_i|} m_f \ln |m_f|. \quad (35)$$

Here we only show the nonanalytic part of  $C_{\text{neq}}^{(\vec{q}_j)}$ , which is independent of the shape of the neighborhood or the choice of  $\eta$ .

Clearly  $C_{\text{neq}}^{(\vec{q}_j)}$  is a continuous function of  $m_f$  even at  $m_f = 0$ . The asymptotic behavior of its derivative in the limit  $m_f \rightarrow 0$  is

$$\lim_{m_f \rightarrow 0} \frac{dC_{\text{neq}}^{(\vec{q}_j)}}{dm_f} \sim \frac{-\text{sgn}(a_{1x} a_{2y} - a_{2x} a_{1y})}{2|m_i|} \ln |m_f|. \quad (36)$$

Recall that  $\text{sgn}(a_{1x} a_{2y} - a_{2x} a_{1y})$  equals the change of  $C^{(\vec{q}_j)}$  at the gap closing point.  $C^{(\vec{q}_j)}$  is the contribution to the Chern number from the singularity  $\vec{q}$ . For distinguishing  $C^{(\vec{q}_j)}$  for the ground state of  $\hat{H}_f$  from that for the ground state of  $\hat{H}_i$ , the

former is specifically denoted by the symbol  $C_f^{(\vec{q}_j)}$ .  $C_f^{(\vec{q}_j)}$  is given by Eq. (29) in which  $m$  is replaced by  $m_f$ . We can then express Eq. (36) by using the change of  $C_f^{(\vec{q}_j)}$  at  $m_f = 0$  as

$$\lim_{m_f \rightarrow 0} \frac{dC_{\text{neq}}^{(\vec{q}_j)}}{dm_f} \sim \frac{\lim_{m_f \rightarrow 0^-} C_f^{(\vec{q}_j)}(m_f) - \lim_{m_f \rightarrow 0^+} C_f^{(\vec{q}_j)}(m_f)}{2|m_i|} \times \ln |m_f|. \quad (37)$$

The nonanalytic part of the Hall conductance at  $m_f = 0$  is a sum of  $C_{\text{neq}}^{(\vec{q}_j)}$  at the singularities  $\vec{q}_1, \vec{q}_2, \dots, \vec{q}_{N'}$  that corresponds to  $m_f$ . While the Chern number  $C_f$  is a sum of  $C_f^{(\vec{q}_j)}$  at all the singularities  $\vec{q}_1, \vec{q}_2, \dots, \vec{q}_N$  in the Brillouin zone. The singularity  $\vec{q}_j$  with  $j > N'$  does not correspond to  $m_f$ , and then has no contribution to the nonanalyticity of  $C_{\text{neq}}$ . But  $C_f^{(\vec{q}_j)}$  also keeps invariant at  $m_f = 0$ , since  $C_f^{(\vec{q}_j)}$  changes only if its corresponding gap parameter becomes zero. Therefore, the asymptotic behavior in the derivative of the Hall conductance can be expressed as

$$\lim_{m_f \rightarrow 0} \frac{dC_{\text{neq}}}{dm_f} \sim \frac{\lim_{m_f \rightarrow 0^-} C_f(m_f) - \lim_{m_f \rightarrow 0^+} C_f(m_f)}{2|m_i|} \times \ln |m_f|. \quad (38)$$

We thus proved that the nonanalytic behavior of the Hall conductance is universal in a generic two-band Chern insulator. The quench-state Hall conductance is a continuous function of the gap parameter in the post-quench Hamiltonian. Its derivative is logarithmically divergent as the gap parameter becomes zero. The prefactor of the logarithm is the ratio of the change of the Chern number for the ground state of the post-quench Hamiltonian to the energy gap in the initial state. The Hall conductance is nonanalytic only at the gap closing points where the Chern number changes.

Up to now, we only considered the lowest order expansion of the coefficient vector in the calculation of  $C_{\text{neq}}^{(\vec{q}_j)}$ . To finish our proof, we will show that the higher-order terms in the expansion do not affect the continuity of  $C_{\text{neq}}^{(\vec{q}_j)}$  and have no contribution to the asymptotic behavior of  $dC_{\text{neq}}^{(\vec{q}_j)}/dm_f$  in the limit  $m_f \rightarrow 0$ .

Let us consider the second order term in the expansion of  $d_{3\vec{k}}^f$  [see Eq. (27)]. Without loss of generality, we suppose it to be  $\Omega = b_{3x} \Delta k_x^2 + b_{3y} \Delta k_y^2 + b_{3m} \Delta k_x \Delta k_y$ , with  $b_{3x}, b_{3y}$ , and  $b_{3m}$  denoting the free parameters. We recalculate the integrand in the expression of  $C_{\text{neq}}^{(\vec{q}_j)}$  [see Eq. (31)]. For the denominator we obtain

$$(d_k^f)^4 = \left[ m_f^2 + \sum_{j=1}^2 (a_{jx} \Delta k_x + a_{jy} \Delta k_y)^2 + 2m_f \times (b_{3x} \Delta k_x^2 + b_{3y} \Delta k_y^2 + b_{3m} \Delta k_x \Delta k_y) + O(\Delta k^4) \right]^2. \quad (39)$$

For the numerator we obtain

$$\begin{aligned} \mathcal{N} = & (a_{1x}a_{2y} - a_{2x}a_{1y}) \left[ m_i m_f^2 + m_f \sum_{j=1}^2 (a_{jx} \Delta k_x + a_{jy} \Delta k_y)^2 \right. \\ & \left. + m_f^2 (b_{3x} \Delta k_x^2 + b_{3y} \Delta k_y^2 + b_{3m} \Delta k_x \Delta k_y) + O(\Delta k^4) \right]. \end{aligned} \quad (40)$$

Since the integral is over an infinitesimal neighborhood of  $\vec{q}$ , the fourth order terms  $O(\Delta k^4)$  in numerator and denominator of the integrand can be neglected. The additional second order term in  $(d_k^f)^4$  that comes from  $\Omega$  is proportional to  $m_f$ . Therefore, it is much smaller than the other second order terms in the limit  $m_f \rightarrow 0$  and can be neglected in the study of the nonanalyticity at  $m_f = 0$ . For the numerator, the additional second order term coming from  $\Omega$  is proportional to  $m_f^2$  and then can be neglected, since the other second order terms in the numerator is proportional to  $m_f$ . A more precise argument can be obtained by replacing  $\sum_{j=1}^2 (a_{jx} \Delta k_x + a_{jy} \Delta k_y)^2$  by  $\Delta k'^2$  and replacing  $\Omega$  by  $b \Delta k'^2$  both in the numerator and denominator of the integrand. After this replacement, the integral can be worked out. It is then straightforward to verify that  $\Omega$  does not change the continuity of  $C_{\text{neq}}^{(\vec{q})}$  or the asymptotic behavior of  $dC_{\text{neq}}^{(\vec{q})}/dm_f$ . Furthermore, in the power series of  $d_{3\vec{k}}$ , the terms of order higher than two contribute to the numerator or denominator of the integrand the corrections which are at least of order three. These corrections can be neglected for an infinitesimal domain of integration.

Next we consider the higher-order terms in  $d_{1\vec{k}}$  or  $d_{2\vec{k}}$ . The terms of order higher than one contribute to the denominator of the integrand a correction  $O(\Delta k^3)$ . At the same time, the terms of order higher than three contribute to the numerator a correction  $O(\Delta k^3)$ . Therefore, the terms of order higher than three in  $d_{1\vec{k}}$  or  $d_{2\vec{k}}$  can be neglected. The second and third order terms in  $d_{1\vec{k}}$  or  $d_{2\vec{k}}$  contribute to the numerator a linear term and a second order term that is proportional to  $m_f^2$ . The latter can be neglected due to the same reason mentioned above. Finally, the linear term in the numerator is antisymmetric under  $\Delta k_\alpha \rightarrow -\Delta k_\alpha$ . The integral of an antisymmetric function over a circle must be zero. Hence, the terms of order higher than one in  $d_{1\vec{k}}$  or  $d_{2\vec{k}}$  can be neglected. Thereby, we finished our proof. Both the Chern number for the ground state and the nonanalyticity of the Hall conductance for the quenched state are only determined by the lowest order expansion of the coefficient vector at the singularities.

Finally, it is worth emphasizing that the asymptotic behavior of  $dC_{\text{neq}}/dm_f$  depends only upon the change of the Chern number at  $m_f = 0$  and the energy gap in the initial state. The universal nonanalytic behavior of the Hall conductance is related to the conic structure of the spectrum at the singularities. It is topologically protected in the sense that it is independent of the detail of the model. Therefore, even if we only consider the noninteracting model in the absence of disorder in the above argument, the nonanalytic behavior of the Hall conductance should not be changed by weak interaction or weak disorder. But the Chern number in Eq. (38) is not well defined in the presence of the interaction between particles. It is then necessary to find a more generic topological invariant

instead of  $C_f$ . This generic topological invariant is argued to be the winding number of the Green's function in Sec. VI. In the next section we demonstrate how the previous considerations and results for the quench-state Hall conductance apply to three selected models differing in various properties.

## V. NONANALYTIC BEHAVIOR OF THE HALL CONDUCTANCE IN THE DIRAC MODEL, THE HALDANE MODEL, AND THE KITAEV HONEYCOMB MODEL

In this section we will show for some specific models at hand that  $C_{\text{neq}}$  is in fact nonanalytic and the asymptotic behavior agrees with the results from the previous section. We will discuss three models with different symmetries and dispersion relations, which are the Dirac model, the Haldane model, and the Kitaev model on a honeycomb lattice.

### A. The Dirac model

In the Dirac model [23] the coefficient vector is expressed as

$$\vec{d}_{\vec{k}} = (k_x, k_y, M - Bk^2), \quad (41)$$

where  $k^2 = k_x^2 + k_y^2$ . The Dirac model has continuous translational symmetry in real space. The range of  $\vec{k}$  is over the whole momentum plane, which is treated as the Brillouin zone in our formalism. Regarding our previous discussion of the Chern number and the Hall conductance, the Dirac model includes a little pitfall we need to overcome due to an infinite Brillouin zone. There are two singularities which are  $q = 0$  and  $q = \infty$  [6]. The contribution of  $q = 0$  to the Chern number is  $[1 + \text{sgn}(M)]/2$  according to Eq. (29). But the singularity at infinity also contributes to the Chern number by  $[\text{sgn}(B) - 1]/2$ . Therefore, the total Chern number is in fact

$$C = \frac{1}{2}[\text{sgn}(M) + \text{sgn}(B)]. \quad (42)$$

This means that the Dirac model is an example of a system with two distinct parameters that can drive a topological transition. A topological phase transition happens in the ground state at  $M = 0$  or  $B = 0$ . For  $M = 0$ , the energy gap closes at  $q = 0$  which is the unique singularity that corresponds to the nonanalyticity of  $C$  and  $C_{\text{neq}}$ . However, to analyze the nonanalyticity of  $C_{\text{neq}}$  at  $B_f = 0$  we need a little trick. We substitute Eq. (41) into Eq. (22) and obtain the expression of the quench-state Hall conductance. It is

$$C_{\text{neq}} = \int d\vec{k}^2 \frac{[k^2 + (B_i k^2 - M_i)(B_f k^2 - M_f)](B_f k^2 + M_f)}{4\pi d_k^i (d_k^f)^4}, \quad (43)$$

with

$$d_k^i = \sqrt{k^2 + (B_i k^2 - M_i)^2} \quad (44)$$

and

$$(d_k^f)^4 = [k^2 + (B_f k^2 - M_f)^2]^2. \quad (45)$$

At this point it becomes clear that the transition at  $B_f = 0$  is related to the singularity at infinity. Here we cannot directly apply the argument from the previous section, which was based

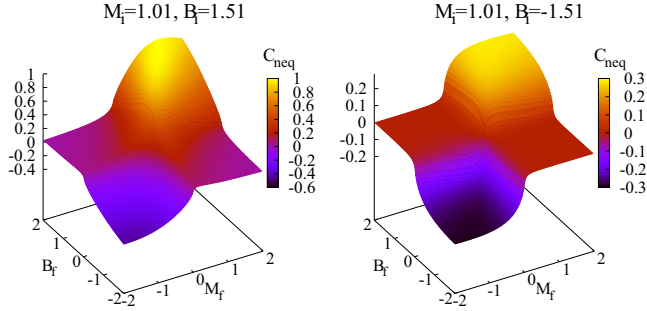


FIG. 1. The Hall conductance  $C_{\text{neq}}$  as a function of  $(M_f, B_f)$  for different  $(M_i, B_i)$ . (Left panel) The initial state has a nonzero Chern number with  $M_i, B_i > 0$ . (Right panel) The Chern number of the initial state is zero with  $M_i > 0$  but  $B_i < 0$ .

on an expansion of  $\vec{d}_k$  at the finite singularity. However, the Dirac model features rotational symmetry, which is reflected in the fact that the integrand in Eq. (43) is a function of  $k^2$ . It is convenient to calculate this integral in polar coordinates. Integrating with respect to the azimuth angle, we obtain

$$C_{\text{neq}} = \int_0^\infty d(k^2) \times \frac{[k^2 + (B_i k^2 - M_i)(B_f k^2 - M_f)](B_f k^2 + M_f)}{4d_k^i (d_k^f)^4}. \quad (46)$$

Thereby it becomes clear that the integrand in Eq. (46) is invariant as we simultaneously change the variable  $k \rightarrow 1/k$  and exchange the parameters  $M_{i/f} \leftrightarrow B_{i/f}$ . Consequently, the Hall conductance is symmetric under an exchange of  $M_{i/f}$  and  $B_{i/f}$  in the sense that

$$C_{\text{neq}}(M_i, B_i, M_f, B_f) = C_{\text{neq}}(B_i, M_i, B_f, M_f). \quad (47)$$

The same argument applies for the Chern number, i.e.,  $C(M, B) = C(B, M)$ . Thus, the nonanalytic behavior of  $C_{\text{neq}}$  at  $B_f = 0$  is as same as that at  $M_f = 0$ .

Figure 1 shows the result of the Hall conductance obtained by numerical integration of Eq. (46).  $C_{\text{neq}}$  is plotted as a function of the parameters  $(M_f, B_f)$  in the post-quench Hamiltonian. The left and right panels are for different initial states. Different from the ground-state Hall conductance (42), the quench-state Hall conductance changes continuously.  $C_{\text{neq}}$  is close to zero as  $M_f$  and  $B_f$  have different signs, being positive as  $M_f, B_f \gg 0$  but negative as  $M_f, B_f \ll 0$ .

To analyze the behavior of the Hall conductance close to the transition  $M_f = 0$  we expand  $\vec{d}_k$  around  $\vec{q} = 0$  and obtain

$$\begin{aligned} a_{1x}^{\vec{q}} &= 1, & a_{1y}^{\vec{q}} &= 0, & a_{2x}^{\vec{q}} &= 0, & a_{2y}^{\vec{q}} &= 1, \\ d_{3\vec{q}} &= M. \end{aligned} \quad (48)$$

Employing Eq. (36) we directly obtain the asymptotic behavior of the quench-state Hall conductance:

$$\lim_{M_f \rightarrow M_f^c} \frac{\partial C_{\text{neq}}}{\partial M_f} \sim -\frac{1 \ln |M_f - M_f^c|}{2 |M_i - M_i^c|}. \quad (49)$$

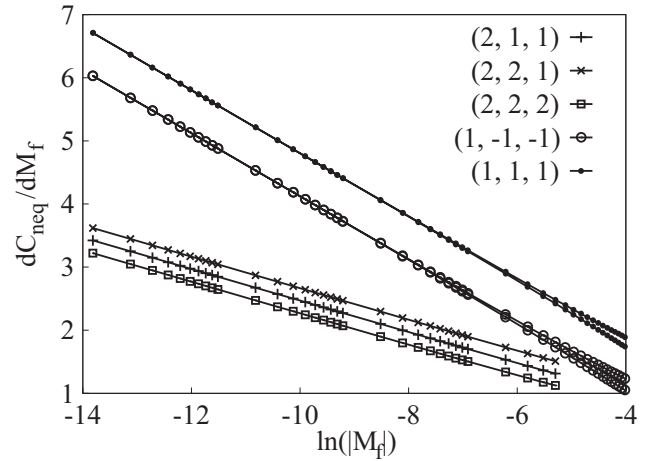


FIG. 2.  $\partial C_{\text{neq}}/\partial M_f$  as a function of  $\ln |M_f|$ . The different types of lines and points represent  $\partial C_{\text{neq}}/\partial M_f$  for different  $(M_i, B_i, B_f)$ . We simultaneously plot  $\partial C_{\text{neq}}/\partial M_f$  in the limit  $M_f \rightarrow 0^+$  and  $M_f \rightarrow 0^-$ , which are undistinguishable at small  $|M_f|$ .

In Fig. 2 we show the numerical result of  $\frac{\partial C_{\text{neq}}}{\partial M_f}$  as a function of  $\ln |M_f|$  in the vicinity of  $M_f = 0$ . In the range  $|M_f| < e^{-6}$ , this function is approximately linear with the slope  $-1/2|M_i|$ . Thereby, the numerical results verify our analysis.

According to Eq. (47),  $C_{\text{neq}}$  is symmetric to  $M_f$  and  $B_f$ . By replacing  $M_{i/f}$  by  $B_{i/f}$  in Eq. (49), we obtain

$$\lim_{B_f \rightarrow B_f^c} \frac{\partial C_{\text{neq}}}{\partial B_f} \sim -\frac{1 \ln |B_f - B_f^c|}{2 |B_i - B_i^c|}, \quad (50)$$

where  $B_f^c = B_i^c = 0$ . It is worth emphasizing again that the energy gap of the post-quench Hamiltonian does not close at  $B_f = 0$ . The Hall conductance is nonanalytic at  $B_f = 0$  because  $k \rightarrow \infty$  becomes a singularity of the integrand in Eq. (46). However, in a generic model, the Brillouin zone is finite so that a singularity at infinity does not exist. Therefore, we can say that for a generic lattice system the Hall conductance can only be nonanalytic at the gap closing point of the post-quench Hamiltonian.

As expected from the general argument in the previous section, the Hall conductance is continuous everywhere in the parameter space of the quenched state. But its derivative is logarithmically divergent at  $M_f = 0$  or  $B_f = 0$ . The nonanalyticity of the Hall conductance reveals a nonequilibrium phase transition at  $M_f = 0$  or  $B_f = 0$ . This phase transition can be addressed by a change of the Chern number for the ground state of the post-quench Hamiltonian which is a topological invariant. The nonanalytic behavior of the Hall conductance at the nonequilibrium phase transition is quite different from that at the ground-state phase transition. In the latter case, the Hall conductance is discontinuous at the transition but its derivative keeps zero almost everywhere in the parameter space.

This phase transition cannot be explained under the broken symmetry picture, since the quenched states in different phases share the common symmetries of the Dirac model. In fact, this phase transition is topologically driven. And the Chern number for the ground state of the post-quench Hamiltonian serves as a suitable order parameter, which can be used to distinguish



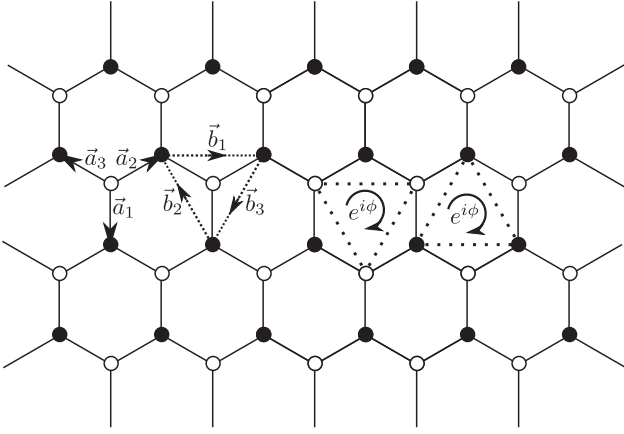


FIG. 3. Schematic diagram of the Haldane model. The black and empty circles denote the “A” and “B” sites, respectively. The circle arrow at the center of the dotted lines connecting three A sites or three B sites shows the direction of hopping with the matrix element  $t_2 e^{i\phi}$ . The six vectors  $\vec{a}_s$  and  $\vec{b}_s$  with  $s = 1, 2, 3$  are marked, which are used for expressing the Hamiltonian in momentum space.

the quenched states in different phases (see Sec. VI for more discussion).

### B. The Haldane model

Next we study the quench-state Hall conductance in the Haldane model. The model was first proposed by Haldane [24] in 1988. Due to the recent progress in manipulating cold atoms, the Haldane model was realized in an optical lattice [30]. The study of the nonequilibrium phase transition in the Haldane model provides an opportunity for testing our theory.

The Haldane model describes a Fermi gas on a honeycomb lattice with each site at most being occupied by a single fermion. Figure 3 is the schematic diagram. There are two interpenetrating sublattices, which are the sublattice “A” denoted by the black circles and the sublattice “B” denoted by the empty circles. For simplicity we set the lattice constant (the edge length of the hexagon) to unity. In the Haldane model, the Hamiltonian contains three terms:

$$\hat{H} = \hat{H}_1 + \hat{H}_2 + \hat{H}_3. \quad (51)$$

The first term describes the hopping between the nearest neighbors, i.e., between one A site and one B site, with the hopping matrix element set to unity.  $\hat{H}_1$  is expressed as

$$\hat{H}_1 = \sum_{\langle \vec{A}_i, \vec{B}_j \rangle} (\hat{c}_{\vec{A}_i}^\dagger \hat{c}_{\vec{B}_j} + \text{H.c.}), \quad (52)$$

where  $\hat{c}_{\vec{A}_i}^\dagger$  and  $\hat{c}_{\vec{B}_j}$  are the fermionic operators,  $\vec{A}_i$  and  $\vec{B}_j$  denote different A and B sites, respectively, and  $\langle \vec{A}_i, \vec{B}_j \rangle$  denotes the nearest-neighbor relation. The second term describes the hopping between the next-nearest neighbors, i.e., between two A sites or between two B sites. The hopping matrix elements are complex numbers. And inside each hexagon, it is  $(t_2 e^{i\phi})$  if the hopping is in the clockwise direction (see the circle arrow in Fig. 3), but  $(t_2 e^{-i\phi})$  if the hopping is in the anticlockwise

direction.  $\hat{H}_2$  is expressed as

$$\begin{aligned} \hat{H}_2 = & \sum_{\langle\langle \vec{A}_i, \vec{A}_j \rangle\rangle} (t_2 e^{i\phi} \hat{c}_{\vec{A}_i}^\dagger \hat{c}_{\vec{A}_j} + \text{H.c.}) \\ & + \sum_{\langle\langle \vec{B}_i, \vec{B}_j \rangle\rangle} (t_2 e^{i\phi} \hat{c}_{\vec{B}_i}^\dagger \hat{c}_{\vec{B}_j} + \text{H.c.}), \end{aligned} \quad (53)$$

where  $t_2$  and  $\phi$  are real numbers, and  $\langle\langle \vec{A}_i, \vec{A}_j \rangle\rangle$  denotes that the sites  $\vec{A}_i$  and  $\vec{A}_j$  are the next-nearest neighbors to each other and the hopping from  $\vec{A}_j$  to  $\vec{A}_i$  is in the clockwise direction. The third term of the Hamiltonian describes an on-site potential which breaks the inversion symmetry.  $\hat{H}_3$  is expressed as

$$\hat{H}_3 = M \sum_{\vec{A}_i} \hat{c}_{\vec{A}_i}^\dagger \hat{c}_{\vec{A}_i} - M \sum_{\vec{B}_i} \hat{c}_{\vec{B}_i}^\dagger \hat{c}_{\vec{B}_i}. \quad (54)$$

The Haldane model is a two-band model. We express the Hamiltonian in momentum space. In the basis  $(\hat{c}_{\vec{k}_1}, \hat{c}_{\vec{k}_2})^T$  where  $\hat{c}_{\vec{k}_1} = \sum_{\vec{A}_j} \frac{e^{-i\vec{k} \cdot \vec{A}_j}}{\sqrt{L}} \hat{c}_{\vec{A}_j}$  and  $\hat{c}_{\vec{k}_2} = \sum_{\vec{B}_j} \frac{e^{-i\vec{k} \cdot \vec{B}_j}}{\sqrt{L}} \hat{c}_{\vec{B}_j}$  ( $L$  is the total number of sites), the single-particle Hamiltonian is in the form of Eq. (13) with the components of  $\vec{d}_{\vec{k}}$  expressed as

$$\begin{aligned} d_{1\vec{k}} &= \sum_{s=1,2,3} \cos(\vec{k} \cdot \vec{a}_s), \\ d_{2\vec{k}} &= \sum_{s=1,2,3} \sin(\vec{k} \cdot \vec{a}_s), \\ d_{3\vec{k}} &= M - 2t_2 \sin \phi \sum_{s=1,2,3} \sin(\vec{k} \cdot \vec{b}_s). \end{aligned} \quad (55)$$

Here we employ six constant vectors

$$\begin{aligned} \vec{a}_1 &= \begin{pmatrix} 0 \\ -1 \end{pmatrix}, \quad \vec{a}_2 = \frac{1}{2} \begin{pmatrix} \sqrt{3} \\ 1 \end{pmatrix}, \quad \vec{a}_3 = \frac{1}{2} \begin{pmatrix} -\sqrt{3} \\ 1 \end{pmatrix}, \\ \vec{b}_1 &= \begin{pmatrix} \sqrt{3} \\ 0 \end{pmatrix}, \quad \vec{b}_2 = \frac{1}{2} \begin{pmatrix} -\sqrt{3} \\ 3 \end{pmatrix}, \quad \vec{b}_3 = -\frac{1}{2} \begin{pmatrix} \sqrt{3} \\ 3 \end{pmatrix}, \end{aligned} \quad (56)$$

which are shown in Fig. 3.

In order to investigate the gappedness of the spectrum we fix  $t_2$  and  $\phi$ , while changing  $M$ . Up to lattice translations we find two distinct solutions for  $d_{\vec{q}} = 0$ , namely

$$\vec{q}_+ = \left( \frac{8\pi}{3\sqrt{3}}, 0 \right) \quad \text{for} \quad M = M_c^+ = 3\sqrt{3}t_2 \sin \phi \quad (57)$$

and

$$\vec{q}_- = \left( \frac{4\pi}{3\sqrt{3}}, 0 \right) \quad \text{for} \quad M = M_c^- = -3\sqrt{3}t_2 \sin \phi. \quad (58)$$

Thereby we find that the Haldane model is an example of a system with different gap closing points  $\vec{q}_{\pm}$  depending on the external parameters. Figure 4 schematically shows these gap closing points and their lattice translations in the  $\vec{k}$  plane. For  $M = M_c^+$  the energy gap closes at each empty circle, while for  $M = M_c^-$  the gap closes at each black circle. We notice that in the first Brillouin zone which is the hexagon centered at  $\Gamma$  in Fig. 4, the singularities are located at the vertices of the boundary. In order to avoid problems when evaluating Eq. (22) we choose a different Brillouin zone, which is the rhomboid area surrounded by the dashed lines in Fig. 4. With this choice, the singularity is located inside the Brillouin zone.

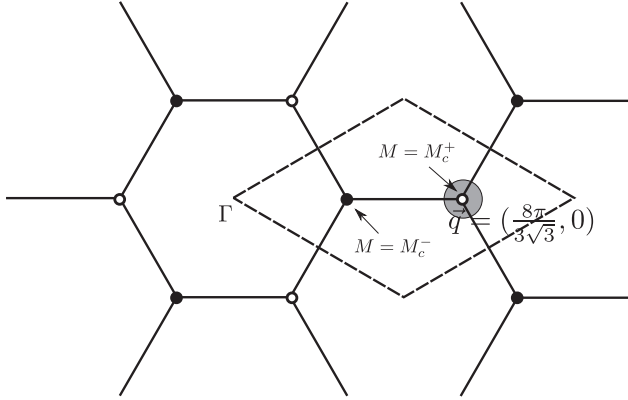


FIG. 4. The reciprocal lattice of the Haldane model.  $\Gamma = (0,0)$  denotes the origin. The hexagon surrounding  $\Gamma$  point is the first Brillouin zone. The black (empty) circles denote the singularities at which the energy gap closes for  $M = M_c^-$  ( $M = M_c^+$ ). We choose the Brillouin zone surrounded by the dashed lines to calculate the Hall conductance.  $\vec{q}$  is the singularity inside this Brillouin zone as  $M = M_c^+$ , and the shadow around  $\vec{q}$  represents the region contributing to the nonanalyticity of the Hall conductance.

In order to obtain the Chern number and the asymptotic behavior of the quench-state Hall conductance we expand  $\vec{d}_{\vec{k}}$  [Eq. (55)] at the gap closing points, yielding the coefficients

$$\begin{aligned} a_{1x}^{\vec{q}_+} &= \frac{3}{2}, & a_{1y}^{\vec{q}_+} &= 0, & a_{2x}^{\vec{q}_+} &= 0, & a_{2y}^{\vec{q}_+} &= -\frac{3}{2}, \\ d_{3\vec{q}_+} &= M - 3\sqrt{3}t_2 \sin \phi \end{aligned} \quad (59)$$

and

$$\begin{aligned} a_{1x}^{\vec{q}_-} &= -\frac{3}{2}, & a_{1y}^{\vec{q}_-} &= 0, & a_{2x}^{\vec{q}_-} &= 0, & a_{2y}^{\vec{q}_-} &= -\frac{3}{2}, \\ d_{3\vec{q}_-} &= M + 3\sqrt{3}t_2 \sin \phi, \end{aligned} \quad (60)$$

respectively. Plugging this into Eq. (29), the Chern number of the ground state is found to be

$$C = \frac{1}{2} [\text{sgn}(M + 3\sqrt{3}t_2 \sin \phi) - \text{sgn}(M - 3\sqrt{3}t_2 \sin \phi)]. \quad (61)$$

Let us now study the quench-state Hall conductance as a function of  $M_f$  while fixing the initial parameters  $M_i$ ,  $t_{2i}$ , and  $\phi_i$  and the post-quench parameters  $t_{2f}$  and  $\phi_f$ . The Hall conductance is nonanalytic at  $M_f = M_f^c$  with

$$M_f^c := +3\sqrt{3}t_{2f} \sin \phi_f, \quad (62)$$

where the gap of the post-quench Hamiltonian closes at the momentum  $\vec{q}_+$ . The Hall conductance is also nonanalytic at  $M_f = -3\sqrt{3}t_{2f} \sin \phi_f$ . But the nonanalytic behavior of the Hall conductance is the same at the two different gap closing points. We will then only discuss the case of  $M_f = M_f^c$ .

Since  $\vec{q}_+$  is the unique singularity at  $M_f = M_f^c$  the quench-state Hall conductance is according to Eq. (30) determined by  $C_{\text{neq}}^{\vec{q}_+}$  and plugging the expansion (59) into Eq. (36) yields

$$\frac{dC_{\text{neq}}}{dM_f} \sim \frac{1}{2} \frac{\ln |M_f - M_f^c|}{|M_i - M_i^c|}. \quad (63)$$

This result is verified by the numerical evaluation of the Hall conductance (22). Figure 5 shows the Hall conductance and

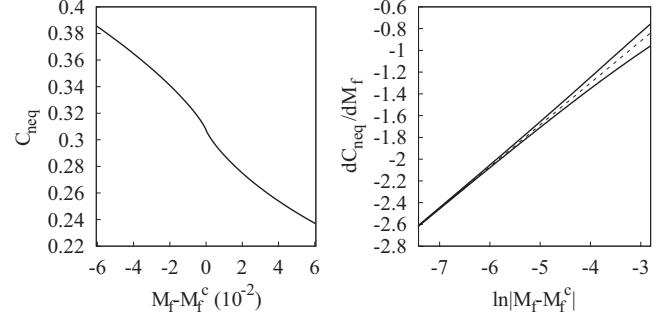


FIG. 5. The Hall conductance and its derivative in the vicinity of  $M_f = M_f^c$ . The former is plotted in the left panel, while the latter is plotted in the right panel. In the right panel, the solid lines denote  $\frac{dC_{\text{neq}}}{dM_f}$  obtained from numerical integration, while the dashed one is a straight line with slope  $\frac{1}{2|M_i - M_i^c|}$ . The parameters are set to  $M_i = 0$ ,  $\phi_i = \phi_f = \pi/6$ ,  $t_{2i} = 0.5$ , and  $t_{2f} = 1$ .

its derivative. We see clearly that  $C_{\text{neq}}$  is a continuous function and  $dC_{\text{neq}}/dM_f$  is a linear function of  $\ln |M_f - M_f^c|$  in the limit  $M_f \rightarrow M_f^c$ . The slope of  $dC_{\text{neq}}/dM_f$  coincides with our prediction.

### C. The Kitaev honeycomb model

Finally, we study the Kitaev honeycomb model in a magnetic field. Different from the Dirac model or the Haldane model, the Kitaev honeycomb model [31] is not a fermionic model, but a spin-1/2 model defined on a honeycomb lattice with generally anisotropic nearest-neighbor interactions (see Fig. 6). The Hamiltonian of the isotropic Kitaev honeycomb model in a magnetic field  $\vec{h}$  is

$$\hat{H}(\vec{h}) = - \sum_{\alpha \in \{x,y,z\}} \left[ J \sum_{\alpha \text{ links}} \hat{\sigma}_i^\alpha \hat{\sigma}_j^\alpha - \sum_j h_\alpha \hat{\sigma}_j^\alpha \right], \quad (64)$$

where the sum over the  $x$ ,  $y$ , or  $z$  links means the sum over pairs of lattice sites  $\langle i, j \rangle$  that are linked by a bond labeled by

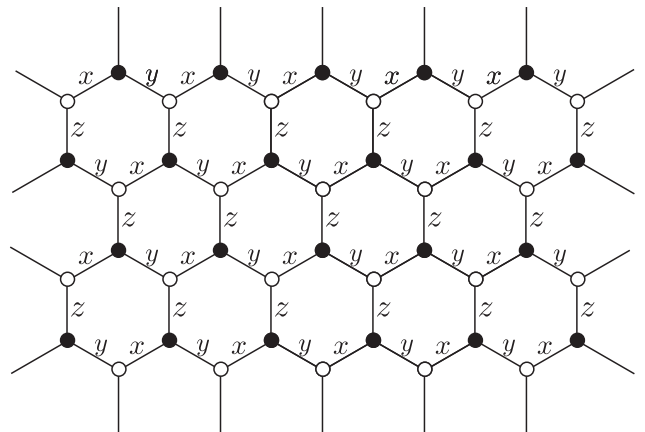


FIG. 6. Lattice of the Kitaev honeycomb model. Spin-1/2 degrees of freedom reside on the vertices of a honeycomb lattice. The anisotropic nearest-neighbor interaction depends on the link type ( $x$ ,  $y$ , or  $z$ ).

$x$ ,  $y$ , or  $z$  in Fig. 6, respectively, and  $\hat{\sigma}^\alpha$  denotes the three Pauli matrices. We set the bond length and  $J$  to unity. It has been shown [32] that in the absence of a magnetic field ( $\vec{h} = 0$ ) for the above Hamiltonian one can find a Jordan-Wigner contour, which after identifying a conserved  $Z_2$  operator [31] and switching to momentum space yields a two-band Hamiltonian as defined in Eq. (13) with coefficient vector

$$\vec{d}_{\vec{k}} = (d_{1\vec{k}}, 0, d_{3\vec{k}}), \quad (65)$$

where

$$\begin{aligned} d_{1\vec{k}} &= \sin(\vec{Q}_1 \cdot \vec{k}) + \sin(\vec{Q}_2 \cdot \vec{k}), \\ d_{3\vec{k}} &= 1 + \cos(\vec{Q}_1 \cdot \vec{k}) + \cos(\vec{Q}_2 \cdot \vec{k}). \end{aligned} \quad (66)$$

Here  $\vec{Q}_1 = (\frac{\sqrt{3}}{2}, \frac{3}{2})$  and  $\vec{Q}_2 = (-\frac{\sqrt{3}}{2}, \frac{3}{2})$  are the lattice vectors. This Hamiltonian can be diagonalized by a Bogoliubov transformation yielding a gapless spectrum  $\sqrt{d_{1\vec{k}}^2 + d_{3\vec{k}}^2}$ .

Switching on an external field  $\vec{h}$  opens a gap in the spectrum. For isotropic spin-spin couplings there exists a diagonal form of the Hamiltonian also with nonzero magnetic field [31] and the spectrum becomes  $\sqrt{d_{1\vec{k}}^2 + d_{2\vec{k}}^2 + d_{3\vec{k}}^2}$  with

$$d_{2\vec{k}} = 2M[\sin(\vec{Q}_1 \cdot \vec{k}) - \sin(\vec{Q}_2 \cdot \vec{k}) - \sin(\sqrt{3}k_x)], \quad (67)$$

where  $M \sim \frac{h_x h_y h_z}{J^2}$ . The diagonal Hamiltonian can be transformed to the two-band form in Eq. (13) via a Bogoliubov transformation [33], yielding

$$\vec{d}_{\vec{k}} = (d_{1\vec{k}}, d_{2\vec{k}}, d_{3\vec{k}}). \quad (68)$$

The spin-1/2 model with the Hamiltonian  $\hat{H}(\vec{h}) \equiv \hat{H}(M)$  is thereby transformed into a gapped two-band model of fermions. We can then define the Chern number. The Chern number of the ground state is

$$C = \text{sgn}(M). \quad (69)$$

A topological phase transition in the ground state happens at  $M = 0$ , i.e., at zero magnetic field, at which the energy gap closes with the roots of  $d_{\vec{k}}$  sitting on the corners of the hexagonal Brillouin zone (see Fig. 7). These roots are the singularities of the Berry curvature. There are two types of conic singularities, denoted by the black and the empty circles in Fig. 7. As in the Haldane model, we choose a rhomboid unit cell as the Brillouin zone. We then have to consider the singularities at

$$\vec{q}_1 = \left( \frac{8\pi}{3\sqrt{3}}, 0 \right), \quad \vec{q}_2 = \left( \frac{4\pi}{3\sqrt{3}}, 0 \right). \quad (70)$$

As opposed to the previous examples the Kitaev model exhibits two simultaneous gap closing points in the spectrum. The expansion for the components of the coefficient vector  $\vec{d}_{\vec{k}}$  as in Eq. (27) reveals that both gap closing points differ, since

$$\begin{aligned} d_{1\vec{k}}^{(\vec{q}_1)} &= -\frac{3}{2}\Delta k_y, & d_{2\vec{k}}^{(\vec{q}_1)} &= -3\sqrt{3}M, & d_{3\vec{k}}^{(\vec{q}_1)} &= \frac{3}{2}\Delta k_x, \\ d_{1\vec{k}}^{(\vec{q}_2)} &= -\frac{3}{2}\Delta k_y, & d_{2\vec{k}}^{(\vec{q}_2)} &= 3\sqrt{3}M, & d_{3\vec{k}}^{(\vec{q}_2)} &= -\frac{3}{2}\Delta k_x. \end{aligned} \quad (71)$$

Notice that in this model it is the first and third components of  $\vec{d}_{\vec{k}}$  vanishing at the singularities. According to the properties of the SU(2) algebra, we can permute the three components of  $\vec{d}_{\vec{k}}$

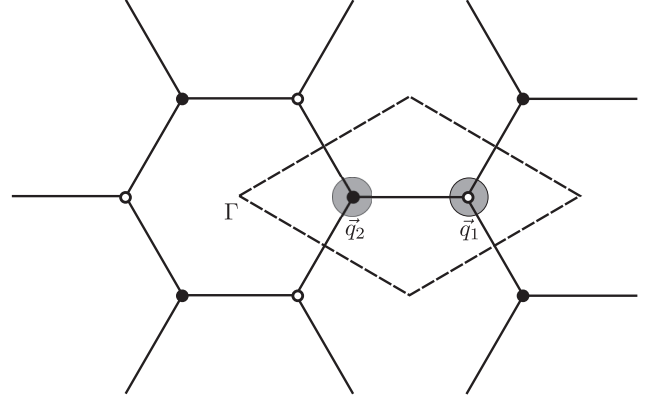


FIG. 7. The reciprocal lattice of the Kitaev honeycomb model.  $\Gamma = (0,0)$  denotes the origin. The black and the empty circles denote the singularities at which the energy gap closes as there is no magnetic field. The dashed lines surround the Brillouin zone that we choose to calculate the Chern number and the Hall conductance.  $\vec{q}_1$  and  $\vec{q}_2$  are two singularities inside this Brillouin zone. The shadows around them represent the regions contributing to the nonanalyticity of the Hall conductance.

without changing the results for  $C$  and  $C_{\text{neq}}$ . One of the possible permutations is  $(d_{1\vec{k}}, d_{2\vec{k}}, d_{3\vec{k}}) \rightarrow (d_{3\vec{k}}, d_{1\vec{k}}, d_{2\vec{k}})$ . With Eq. (29) it then becomes clear how the Chern number in Eq. (69) comes about.

Next we study the quench-state Hall conductance in the two-component Fermi gas with the coefficient vector given by Eq. (68). It is worth mentioning that the value of the  $Z_2$  operator defined in the transformation from the Kitaev model to the fermionic model is conserved in a quench of the parameter  $M$ . Therefore, a quench in the Kitaev model can be mapped into a quench in the corresponding two-component Fermi gas and vice versa. However, the observable in the Kitaev model that corresponds to the Hall conductance is difficult to write down, which will not be discussed in this paper.

Since there are two singularities in the Brillouin zone, the nonanalytic part of the Hall conductance can be expressed as

$$C_{\text{neq}} \sim C_{\text{neq}}^{(\vec{q}_1)} + C_{\text{neq}}^{(\vec{q}_2)}. \quad (72)$$

Plugging the expansion coefficients from Eq. (71) after the permutation into Eqs. (35) and (30) yields

$$C_{\text{neq}} \sim \frac{-(M_f - M_f^c)}{|M_i - M_i^c|} \ln |M_f - M_f^c|, \quad (73)$$

where  $M_i^c = 0$  and  $M_f^c = 0$  denote the gap closing point in the initial and post-quench Hamiltonians, respectively. Accordingly, the asymptotic behavior of the derivative at the gap closing point  $M_f^c = 0$  can be expressed as

$$\lim_{M_f \rightarrow M_f^c} \frac{dC_{\text{neq}}}{dM_f} \sim \frac{-\ln |M_f - M_f^c|}{|M_i - M_i^c|}. \quad (74)$$

Figure 8 shows the Hall conductance and its derivative obtained by numerical integration of Eq. (22) for a quench starting from different  $M_i$ . As expected, if no quench is performed,  $C_{\text{neq}}$  equals the Chern number of the initial state. When  $M_f$  approaches the gap closing point  $M_f^c = 0$ , the



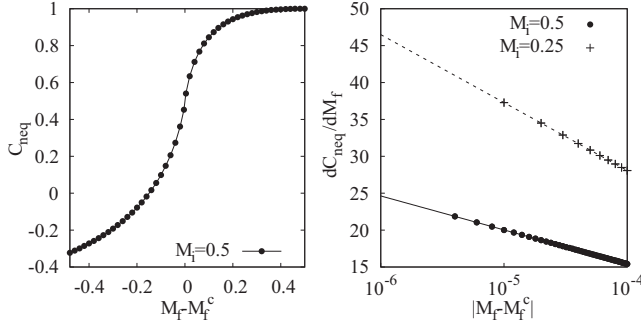


FIG. 8. (Left panel) The function  $C_{\text{neq}}(M_f)$  for a quench starting from  $M_i = 1/2$  obtained by numerical integration (adaptive Simpson's) of Eq. (22) over a half unit cell and doubling the result. (Right panel) Derivative of  $C_{\text{neq}}$  with respect to  $M_f$  for a quench from  $M_i = 1/2$  and one quench from  $M_i = 1/4$ . The dots denote the numerical results, while the lines are fits of the form  $(-|M_i - M_i^c|^{-1} \ln |M_f - M_f^c| + \text{const.})$ .

curve becomes infinitely steep, before it flattens again for smaller  $M_f$ . The derivative  $dC_{\text{neq}}/dM_f$  is displayed together with fits of the form  $(-|M_i - M_i^c|^{-1} \ln |M_f - M_f^c| + \text{const.})$ . The numerical results form a perfect line as a function of  $\ln |M_f - M_f^c|$  and thereby confirm the validity of above considerations regarding the asymptotic behavior of  $C_{\text{neq}}(M_f)$  nearby  $M_f^c$ .

Having verified the validity of our assertions from Sec. IV regarding the universal critical behavior of the quench-state Hall conductance by testing it for three different example systems we will in the next section discuss what is the underlying topological invariant for the quenched state that changes at the critical points.

## VI. TOPOLOGICAL INVARIANT FOR THE QUENCHED STATE

Now we are prepared to discuss which is the experimentally relevant topological invariant for the quenched state of a Chern insulator. A naive idea of defining the topological invariant for a quenched state is to use the Chern number of the unitarily evolving wave function. It is defined as

$$C(t) = \frac{i}{2\pi} \sum_{\alpha \in \text{oc}} \int d\vec{k}^2 \left( \left\langle \frac{\partial u_{\vec{k}\alpha}(t)}{\partial k_x} \middle| \frac{\partial u_{\vec{k}\alpha}(t)}{\partial k_y} \right\rangle - \text{H.c.} \right). \quad (75)$$

$C(t)$  is a straightforward extension of the Chern number for the ground state given by Eq. (2) in which the eigenstate  $|u_{\vec{k}\alpha}\rangle$  is replaced by the evolving single-particle state  $|u_{\vec{k}\alpha}(t)\rangle$ . The sum of  $\alpha$  is over the occupied bands in the initial state.  $C(t)$  is well defined for a noninteracting model in which the evolution of different single-particle states is independent of each other. But  $C(t)$  keeps invariant after a quench, being independent of the post-quench Hamiltonian  $\hat{H}_f$  [4–6]. Therefore, one cannot use  $C(t)$  to explain the nonequilibrium phase transition discovered in this paper, which is indicated by the nonanalyticity of the Hall conductance as  $\hat{H}_f$  changes.

It has been shown in previous sections that the Chern number  $C_f$  for the ground state of the post-quench Hamiltonian can be used as the topological invariant for the quenched

state. It is experimentally relevant in the sense that the nonequilibrium phase transition is always accompanied by the change of  $C_f$  and vice versa. The change of  $C_f$  also determines the asymptotic behavior of the derivative of the Hall conductance at the transition. But  $C_f$  is not well defined in the presence of interaction. On the other hand, it is well known that the winding number of the Green's function  $W$  is equal to the Chern number for the ground states [34]. Next we will show that, for the quenched states in a noninteracting model,  $W$  in fact equals the Chern number  $C_f$ , being independent of the initial state. Since  $W$  is also well defined in the presence of interaction, it serves as a more generic topological invariant for the quenched state. We notice that  $W$  was already employed to describe the topological property of the quenched state in a topological superfluid [8].

The textbook definition of the retarded Green's function after a quench is

$$G_{j,j'}^r(\vec{k}, t, t') = -i\theta(t - t') \langle \Psi(0) | \{ \hat{c}_{\vec{k}j}(t), \hat{c}_{\vec{k}j'}^\dagger(t') \}_+ | \Psi(0) \rangle, \quad (76)$$

where  $|\Psi(0)\rangle$  denotes the initial state,  $\hat{c}_{\vec{k}j}$  with  $j = 1, 2, \dots, N$  denotes the fermionic operator in the original basis of the Hamiltonian (1), and  $\{ \}_+$  denotes the anticommutator. The Green's function in frequency-momentum space is obtained by a Fourier transformation as

$$G_{j,j'}^r(\omega, \vec{k}) = \int_{-\infty}^{\infty} d(t - t') e^{i\omega(t-t')} G_{j,j'}^r(\vec{k}, t, t'). \quad (77)$$

Note that  $t, t' > 0$  must be larger than the time when the quench is performed. The domain of the Green's function can be extended to imaginary frequency by analytic continuation. Let us use  $G^r$  to denote the  $N$ -by- $N$  Green's function matrix with the elements  $G_{j,j'}^r(i\omega, \vec{k})$ . The winding number is then defined as [34,35]

$$W = \frac{1}{24\pi^2} \int_{-\infty}^{\infty} d\omega \int d\vec{k}^2 \epsilon^{\alpha\beta\gamma} \text{Tr} \times \left[ G^{r-1} \frac{\partial G^r}{\partial k_\alpha} G^{r-1} \frac{\partial G^r}{\partial k_\beta} G^{r-1} \frac{\partial G^r}{\partial k_\gamma} \right], \quad (78)$$

where  $\epsilon^{\alpha\beta\gamma}$  is the Levi-Civita symbol with  $\alpha, \beta, \gamma = 0, 1, 2$ , and  $k_0 = \omega$ ,  $k_1 = k_x$ , and  $k_2 = k_y$ .  $G^{r-1}$  is the inverse of  $G^r$ .

In Eq. (76) the time-dependent operators are defined as  $\hat{c}_{\vec{k}j}(t) = e^{i\hat{H}_f t} \hat{c}_{\vec{k}j} e^{-i\hat{H}_f t}$ . In the absence of interaction, the post-quench Hamiltonian  $\hat{H}_f$  is quadratic.  $\hat{c}_{\vec{k}j}(t)$  must be a linear combination of  $\hat{c}_{\vec{k}j'}$  with  $j' = 1, 2, \dots, N$ . Therefore,  $\{ \hat{c}_{\vec{k}j}(t), \hat{c}_{\vec{k}j'}^\dagger(t') \}_+$  is in fact a number instead of an operator. The Green's function is then independent of the initial state  $|\Psi(0)\rangle$ , so is the winding number  $W$ .  $W$  depends only upon the post-quench Hamiltonian  $\hat{H}_f$ .  $W$  keeps invariant even if we replace  $|\Psi(0)\rangle$  by the ground state of  $\hat{H}_f$ . Therefore,  $W$  must equal the Chern number  $C_f$  for the ground state of  $\hat{H}_f$  [34].

We reexpress the asymptotic behavior of the derivative of the Hall conductance by using  $W$  as

$$\lim_{m_f \rightarrow 0} \frac{dC_{\text{neq}}}{dm_f} \sim \frac{\lim_{m_f \rightarrow 0^-} W(m_f) - \lim_{m_f \rightarrow 0^+} W(m_f)}{2|m_i|} \ln |m_f|. \quad (79)$$

We expect that Eq. (79) also stands in the presence of weak interaction. Moreover,  $2|m_i|$  and  $2|m_f|$  in the formula denote the energy gap of  $\hat{H}_i$  and  $\hat{H}_f$ , respectively, which are well defined even in the presence of interaction. The change of the winding number determines the nonanalyticity of the Hall conductance at the gap closing point of  $\hat{H}_f$ . Whether there is a nonequilibrium phase transition in the quenched state is uniquely determined by whether the winding number changes. In this sense, the nonequilibrium phase transition is topologically driven. And the winding number is the experimentally relevant topological invariant for the quenched state.

## VII. CONCLUSIONS

In summary, the Hall conductance of a quenched state in the long time limit is calculated by applying the linear response theory to the diagonal ensemble. In the eigenbasis of the post-quench Hamiltonian, the diagonal ensemble is obtained by neglecting all the off-diagonal elements in the initial density matrix. The quench-state Hall conductance can be expressed as the integral of the Berry curvature weighted by the nonequilibrium distribution of particles [see Eq. (12)]. It is not quantized in general, but can take an arbitrary value.

The Hall conductance as a function of the gap parameter  $m_f$  in the post-quench Hamiltonian  $\hat{H}_f$  displays a universal nonanalytic behavior in a generic two-band Chern insulator. The examples discussed in this work include the Dirac model, the Haldane model, and the Kitaev honeycomb model in the fermionic basis. The Hall conductance is continuous everywhere. But its derivative with respect to  $m_f$  is logarithmically divergent in the limit  $m_f \rightarrow 0$  (the energy gap of  $\hat{H}_f$  is  $2|m_f|$ ), if the winding number of the Green's function for the quenched state  $W$  changes at  $m_f = 0$ . The prefactor of the logarithm is the ratio of the change of  $W$  to the energy gap in the initial state [see Eq. (79)]. The nonanalyticity of the Hall

conductance indicates a topologically driven nonequilibrium phase transition. The topological invariant for the quenched state is the winding number  $W$ .

The Hamiltonian of a two-band Chern insulator in momentum space can be decomposed into the linear combination of Pauli matrices. The nonanalyticity of the Hall conductance depends only upon the lowest order expansion of the coefficients of Pauli matrices at the singularities in the Brillouin zone. Singularities are defined as momenta where the energy gap closes at  $m_f = 0$ .

The Haldane model has been realized in an optical lattice recently [30]. A system of cold atoms is well isolated from the environment. The nonequilibrium distribution of atoms in a quenched state survives for a long time. Our prediction can therefore be checked in a system of cold atoms. It is difficult to measure the Hall conductance directly in cold atoms. But the Hall conductance can also be obtained from the Faraday rotation angle [36], which is correspondingly easier to measure in cold atoms. On the other hand, in solid-state materials where the measurement of Hall conductance is a standard technique, the nonequilibrium distribution of electrons is difficult to realize due to the fast relaxation process. A possible solution is to periodically drive the system for keeping it out of equilibrium. The time evolution of a periodically driven system is governed by a time-independent Floquet Hamiltonian [37]. It was suggested that a Floquet Chern insulator can be realized in graphene ribbons [38,39]. Due to the similarity between the dynamics of a periodically driven quantum state and a quenched state [40], we expect that the techniques developed in this paper can also be used to analyze the nonanalyticity of the Hall conductance in a Floquet Chern insulator.

## ACKNOWLEDGMENTS

This work is supported by NSFC under Grant No. 11304280 and China Scholarship Council. M.S. acknowledges support by the German National Academic Foundation.

- 
- [1] D. I. Tsomokos, A. Hamma, W. Zhang, S. Haas, and R. Fazio, *Phys. Rev. A* **80**, 060302(R) (2009).
  - [2] G. B. Halász and A. Hamma, *Phys. Rev. Lett.* **110**, 170605 (2013).
  - [3] A. Rahmani and C. Chamon, *Phys. Rev. B* **82**, 134303 (2010).
  - [4] L. D'Alessio and M. Rigol, *Nat. Commun.* **6**, 8336 (2015).
  - [5] M. D. Caio, N. R. Cooper, and M. J. Bhaseen, *Phys. Rev. Lett.* **115**, 236403 (2015).
  - [6] P. Wang and S. Kehrein, [arXiv:1504.05689](https://arxiv.org/abs/1504.05689).
  - [7] M. S. Foster, V. Gurarie, M. Dzero, and E. A. Yuzbashyan, *Phys. Rev. Lett.* **113**, 076403 (2014).
  - [8] M. S. Foster, M. Dzero, V. Gurarie, and E. A. Yuzbashyan, *Phys. Rev. B* **88**, 104511 (2013).
  - [9] Y. Dong, L. Dong, M. Gong, and H. Pu, *Nat. Commun.* **6**, 6103 (2015).
  - [10] P. Wang, W. Yi, and G. Xianlong, *New J. Phys.* **17**, 013029 (2015).
  - [11] E. Perfetto, *Phys. Rev. Lett.* **110**, 087001 (2013).
  - [12] M.-C. Chung, Y.-H. Jhu, P. Chen, C.-Y. Mou, and X. Wan, [arXiv:1401.0433](https://arxiv.org/abs/1401.0433).
  - [13] P. D. Sacramento, *Phys. Rev. E* **90**, 032138 (2014).
  - [14] A. Bermudez, D. Patanè, L. Amico, and M. A. Martin-Delgado, *Phys. Rev. Lett.* **102**, 135702 (2009).
  - [15] A. Bermudez, L. Amico, and M. A. Martin-Delgado, *New J. Phys.* **12**, 055014 (2010).
  - [16] W. DeGottardi, D. Sen, and S. Vishveshwara, *New J. Phys.* **13**, 065028 (2011).
  - [17] A. A. Patel, S. Sharma, and A. Dutta, *Eur. Phys. J. B* **86**, 367 (2013).
  - [18] A. Rajak and A. Dutta, *Phys. Rev. E* **89**, 042125 (2014).
  - [19] A. Rajak, T. Nag, and A. Dutta, *Phys. Rev. E* **90**, 042107 (2014).
  - [20] X. Chen, Z.-C. Gu, and X.-G. Wen, *Phys. Rev. B* **82**, 155138 (2010).
  - [21] D. J. Thouless, M. Kohmoto, M. P. Nightingale, and M. den Nijs, *Phys. Rev. Lett.* **49**, 405 (1982).
  - [22] K. von Klitzing, G. Dorda, and M. Pepper, *Phys. Rev. Lett.* **45**, 494 (1980).

- [23] S.-Q. Shen, *Topological Insulators: Dirac Equation in Condensed Matters* (Springer, Berlin, 2012).
- [24] F. D. M. Haldane, *Phys. Rev. Lett.* **61**, 2015 (1988).
- [25] G. D. Mahan, *Many-Particle Physics*, 3rd ed. (Kluwer Academic/Plenum, New York, 2000).
- [26] M. Rigol, V. Dunjko, and M. Olshanii, *Nature (London)* **452**, 854 (2008).
- [27] M. Rigol, *Phys. Rev. Lett.* **103**, 100403 (2009).
- [28] S. Ziraldo, A. Silva, and G. E. Santoro, *Phys. Rev. Lett.* **109**, 247205 (2012).
- [29] H. Dehghani, T. Oka, and A. Mitra, *Phys. Rev. B* **91**, 155422 (2015).
- [30] G. Jotzu, M. Messer, R. Desbuquois, M. Lebrat, T. Uehlinger, D. Greif, and T. Esslinger, *Nature (London)* **515**, 237 (2014).
- [31] A. Kitaev, *Ann. Phys.* **321**, 2 (2006).
- [32] H.-D. Chen and Z. Nussinov, *J. Phys. A* **41**, 075001 (2008).
- [33] M. Schmitt and S. Kehrein, *Phys. Rev. B* **92**, 075114 (2015).
- [34] Q. Niu, D. J. Thouless, and Y.-S. Wu, *Phys. Rev. B* **31**, 3372 (1985).
- [35] V. Gurarie, *Phys. Rev. B* **83**, 085426 (2011).
- [36] X.-L. Qi and S.-C. Zhang, *Rev. Mod. Phys.* **83**, 1057 (2011).
- [37] T. Kitagawa, E. Berg, M. Rudner, and E. Demler, *Phys. Rev. B* **82**, 235114 (2010).
- [38] T. Oka and H. Aoki, *Phys. Rev. B* **79**, 081406(R) (2009).
- [39] Z. Gu, H. A. Fertig, D. P. Arovas, and A. Auerbach, *Phys. Rev. Lett.* **107**, 216601 (2011).
- [40] A. Lazarides, A. Das, and R. Moessner, *Phys. Rev. E* **90**, 012110 (2014).

## 2.2.2 *Publication:* Universal nonanalytic behavior of the non-equilibrium Hall conductance in Floquet topological insulators

Reprinted article with permission from

Markus Schmitt and Pei Wang

Physical Review B **96**, 054306 (2017)

<https://doi.org/10.1103/PhysRevB.96.054306>

Copyright (2017) by the American Physical Society.

**Author contributions** M. S. did most analytic and all numerical calculations and wrote the article. P. W. suggested to study non-equilibrium phase transitions in driven systems, derived the jump height when quenching from a gapless initial state, and revised the manuscript. Both authors discussed the results and the interpretation.

# Universal nonanalytic behavior of the nonequilibrium Hall conductance in Floquet topological insulators

Markus Schmitt<sup>1,\*</sup> and Pei Wang<sup>2</sup>

<sup>1</sup>*Institute for Theoretical Physics, Georg-August-Universität Göttingen - Friedrich-Hund-Platz 1, Göttingen 37077, Germany*

<sup>2</sup>*Department of Physics, Zhejiang Normal University - Jinhua 321004, China*

(Received 13 March 2017; published 28 August 2017)

We study the Hall conductance in a Floquet topological insulator in the long time limit after sudden switches of the driving amplitude. Based on a high frequency expansion of the effective Hamiltonian and the micromotion operator we demonstrate that the Hall conductance as a function of the driving amplitude follows universal nonanalytic laws close to phase transitions that are related to conic gap closing points, namely a logarithmic divergence for gapped initial states and jumps of a definite height for gapless initial states. This constitutes a generalization of the results known for the static systems to the driven case.

DOI: [10.1103/PhysRevB.96.054306](https://doi.org/10.1103/PhysRevB.96.054306)

## I. INTRODUCTION

Since the experimental discovery and theoretical explanation of the quantum Hall effect [1,2] the concept of topological order has gained great importance in condensed matter physics for the understanding of phase transitions that cannot be associated with symmetry breaking. The astonishingly robust integer quantization of the Hall conductance in units of the conductance quantum,  $\sigma_{xy} = Ce^2/h$ , is due to the fact that  $C \in \mathbb{Z}$  can be identified as a topological invariant of the underlying band structure, namely the Chern number. After Haldane's seminal proposal of a model system featuring a quantized Hall conductance in the absence of an external magnetic field [3] enormous experimental and theoretical efforts led to the discovery of a large variety of systems with similar topologically protected transport properties, which are today referred to as topological insulators (TIs) [4].

Following theoretical proposals [5,6] a topological insulator was recently realized experimentally with ultracold fermions in a periodically shaken optical lattice [7]. Despite the absence of energy conservation such *Floquet* topological insulators (FTIs) can be characterized by the Chern number of an effective Hamiltonian and support edge modes [8]. This allows us to tune the topological properties of the system by adjusting the external driving force and opens possibilities to investigate nonequilibrium signatures of topological insulators, which gained increasing theoretical attention lately [9–13]. Note, however, that in some aspects the behavior of FTIs can significantly differ from the known behavior of TIs, e.g., when considering the bulk-edge correspondence [14].

A situation that was studied recently by Deghani *et al.* [10] is the measurement of the Hall conductance a long time after suddenly switching on the external driving force. The system is initially prepared in the ground state of the undriven Hamiltonian  $H_0$ . Then the driving is suddenly switched on at time  $t = 0$  and for  $t > 0$  the system evolves under a time-periodic Hamiltonian  $H_A(t)$ , where  $A$  is the driving amplitude. The Hall conductance in the limit  $t \rightarrow \infty$  is finally obtained using linear response theory and a dephasing argument. As a result they numerically find for an electronic system that the post-quench Hall conductance, which is not any more an

integer multiple of the conductance quantum, exhibits sudden changes whenever the post-quench Hamiltonian  $H_A(t)$  crosses a topological phase boundary as a function of the driving amplitude  $A$ . This behavior is very similar to the behavior of closed TIs after a quench, which exhibit a universal nonanalytic behavior at the ground state transition of the final Hamiltonian as shown in Refs. [15,16].

In this paper we extend the analysis of closed TIs given in Refs. [15,16] to FTIs. We analytically investigate the behavior of the Hall conductance after sudden switches of the driving amplitude for a tight binding Hamiltonian with a time periodic external potential. The analysis is based on high frequency expansions of the effective Hamiltonian and the micromotion operator. We focus on phase transitions that are associated with a closing of the quasienergy gap at the  $K$  points in the Brillouin zone. These already appear when only the first order contribution in the high frequency expansion of the effective Hamiltonian is considered. We find that suddenly switching on the driving amplitude from  $A_i = 0$  to  $A_f \neq 0$  with a gapless initial Hamiltonian leads to jumps of the Hall conductance by multiples of  $\frac{\pi e^2}{2h}$  whenever  $A_f$  crosses a phase boundary, which agrees with the numerical results of Ref. [10] reproduced in Fig. 1(a). If, instead, the system is initially prepared in a quasistationary Floquet mode of the initial Hamiltonian  $H_{A_i}(t)$  before suddenly switching the driving amplitude to  $A_f$  the Hall conductance is continuous at critical values of  $A$ . Nevertheless, it is nonanalytic with a logarithmically diverging derivative as a function of the driving amplitude  $A_f$  as shown in Fig. 1(b).

A distinct feature of FTIs is the possible presence of so-called  $\pi$ -edge modes [8,14,17,18]. Note that our results do not apply to gap closings that affect these edge modes as discussed in Sec. IV A.

The rest of the paper is divided into two parts. In Sec. II we introduce the model system under consideration and briefly summarize the methods used and previous results, which are relevant for the further analysis. In Sec. III we present our analysis resulting in the identification of the abovementioned nonanalytic behavior of the Hall conductance, which is universal for conic gap-closing points in two-band FTIs.

## II. BACKGROUND

In this section we introduce the model Hamiltonian under consideration and briefly review the Floquet formalism and the

\*markus.schmitt@theorie.physik.uni-goettingen.de

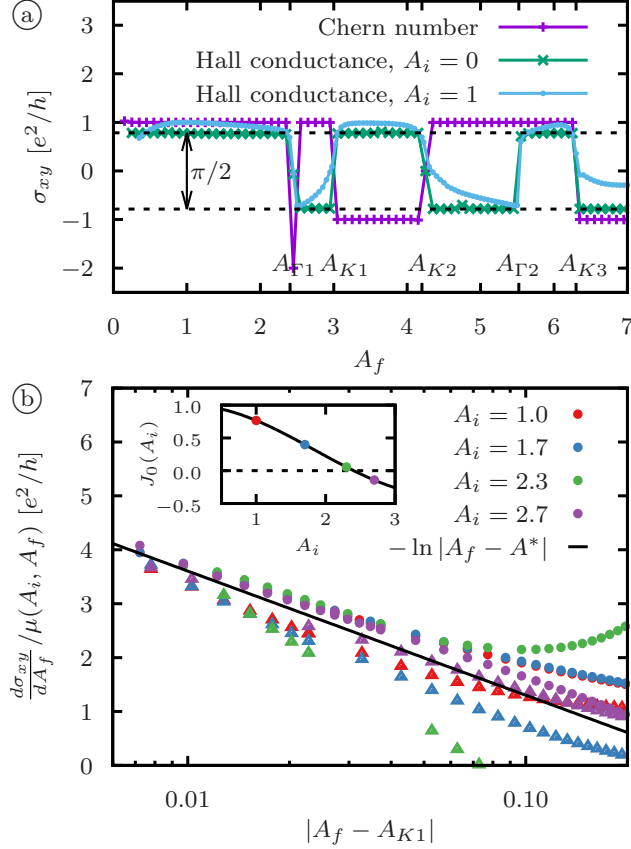


FIG. 1. (a) Floquet Chern number  $C$  and nonequilibrium Hall conductance  $\sigma_{xy}$  for quenches with  $A_i = 0$  and  $A_i = 1$  as function of  $A_f$  for driving frequency  $\omega = 10$ . (b) Derivative of the nonequilibrium Hall conductance rescaled by the prefactor  $\mu(A_i, A_f) = J_0(A_f)|m_i|/J_0(A_i)m'_f$  determined in Eq. (77) close to the transition at  $A_{K1}$ . As  $A_f$  approaches  $A_{K1}$  the slopes agree increasingly well with the predicted  $\ln |A_f - A_{K1}|$  (black line) in all cases even if the value  $J_0(A_i)$  shown in the inset is small. Circles/triangles denote points to the left/right of  $K_1$ .

high frequency expansion used for our analysis. Moreover, we give a short summary of previous results on the nonequilibrium Hall conductance relevant for this work.

### A. Model Hamiltonian

We consider a simple model Hamiltonian, namely a tight binding model on a hexagonal lattice subject to a time-periodic external potential,

$$\tilde{H}(t) = -t_h \sum_{\langle i,j \rangle} (c_i^\dagger c_j + \text{H.c.}) + \sum_i V(\vec{r}_i, t) c_i^\dagger c_i, \quad (1)$$

where  $V(\vec{r}, t) = V_0 \vec{r} \cdot [-\cos(\omega t) \hat{e}_x + \sin(\omega t) \hat{e}_y]$  and  $\langle i, j \rangle$  denotes the set of pairs of neighboring lattice sites. This Hamiltonian constitutes a simple description of graphene illuminated by a circularly polarized laser [19] or ultracold atoms in a circularly shaken optical lattice [7].

A time-dependent gauge transformation restores translational invariance and allows us to write the Hamiltonian in

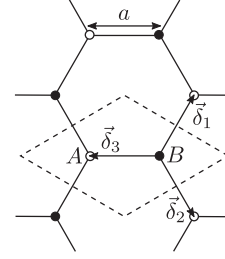


FIG. 2. We consider a hexagonal lattice structure. The dashed line marks a possible choice of the unit cell with two basis sites  $A$  and  $B$ . Depicted is moreover the unit of distance  $a$  and the nearest-neighbor vectors  $\vec{\delta}_i$ .

momentum space as

$$H(t) = \sum_{\vec{k}} \vec{c}_{\vec{k}}^\dagger [\vec{d}_{\vec{k}}(t) \cdot \vec{\sigma}] \vec{c}_{\vec{k}} \quad (2)$$

(cf. Appendix A). In this expression for the Hamiltonian we introduced

$$\vec{c}_{\vec{k}} = \begin{pmatrix} c_{\vec{k}A} \\ c_{\vec{k}B} \end{pmatrix} \quad (3)$$

and the coefficient vector  $\vec{d}_{\vec{k}}(t) = (d_{\vec{k}x}(t), d_{\vec{k}y}(t), d_{\vec{k}z}(t))^T$  with

$$d_{\vec{k}x}(t) = -t_h \sum_{j=1}^3 \cos((\vec{k} - \vec{A}(t)) \cdot \vec{\delta}_j), \quad (4)$$

$$d_{\vec{k}y}(t) = -t_h \sum_{j=1}^3 \sin((\vec{k} - \vec{A}(t)) \cdot \vec{\delta}_j), \quad (5)$$

$$d_{\vec{k}z}(t) = 0 \quad (6)$$

as well as the vector of Pauli matrices  $\vec{\sigma} = (\sigma^x, \sigma^y, \sigma^z)^T$ . The vectors

$$\vec{\delta}_1 = \frac{a}{2} \begin{pmatrix} 1 \\ \sqrt{3} \end{pmatrix}, \quad \vec{\delta}_2 = \frac{a}{2} \begin{pmatrix} 1 \\ -\sqrt{3} \end{pmatrix}, \quad \vec{\delta}_3 = a \begin{pmatrix} -1 \\ 0 \end{pmatrix} \quad (7)$$

are given by the differences of the positions of neighboring lattice sites (cf. Fig. 2). Moreover,

$$\vec{A}(t) = \frac{V_0 a}{\omega} \begin{pmatrix} \sin(\omega t) \\ \cos(\omega t) \end{pmatrix}, \quad (8)$$

where  $a$  denotes the lattice spacing. In the following we will use the dimensionless driving amplitude  $A = |\vec{A}(t)| = V_0 a \omega^{-1}$  to quantify the driving strength and, moreover, set  $a \equiv 1$ .

### B. Periodic driving and Floquet formalism

In this section we recapitulate the Floquet formalism for the treatment of time-periodic Hamiltonians and thereby introduce the notation for the subsequent discussion. We closely follow the presentation and notation of Refs. [20,21].

#### 1. Effective Hamiltonian and micromotion operator

For a time-periodic Hamiltonian  $H(t+T) = H(t)$  acting on a Hilbert space  $\mathcal{H}$  the Floquet theorem states that the



Schrödinger equation

$$i \frac{d}{dt} |\psi(t)\rangle = H(t) |\psi(t)\rangle \quad (9)$$

is solved by *Floquet states* of the form

$$|\psi_n(t)\rangle = e^{-i\epsilon_n t} |\phi_n(t)\rangle \quad (10)$$

with *quasienergies*  $\epsilon_n$  and periodic *Floquet modes*  $|\phi_n(t + T)\rangle = |\phi_n(t)\rangle$  [22,23]. Note that  $\epsilon_n$  and  $|\phi_n(t)\rangle$  are not defined uniquely. Instead, given a solution  $\epsilon_n$  and  $|\phi_n(t)\rangle$ , alternative choices are given by  $\epsilon_{nm} = \epsilon_n + m\omega$  and  $|\phi_{nm}(t)\rangle = e^{im\omega t} |\phi_n(t)\rangle$  with  $\omega = 2\pi/T$  and  $m \in \mathbb{Z}$ , resulting in the same Floquet state

$$|\psi_n(t)\rangle = e^{-i\epsilon_n t} |\phi_n(t)\rangle = e^{-i\epsilon_{nm} t} |\phi_{nm}(t)\rangle. \quad (11)$$

Plugging Eq. (11) into the Schrödinger equation (9) yields the Floquet equation

$$\left( H(t) - i \frac{d}{dt} \right) |\phi_{nm}(t)\rangle = \epsilon_{nm} |\phi_{nm}(t)\rangle, \quad (12)$$

which determines the Floquet modes and quasienergies.

The Floquet states are eigenstates of the time evolution operator over one period, i.e.,

$$U(t_0 + T, t_0) |\psi_n(t_0)\rangle = e^{-i\epsilon_n T} |\psi_n(t_0)\rangle, \quad (13)$$

and can therefore be regarded as eigenstates of a *Floquet Hamiltonian*  $H_{t_0}^F$  defined by

$$U(t_0 + nT, t_0) = e^{-iH_{t_0}^F nT}. \quad (14)$$

The parameter  $t_0$  is an arbitrary gauge choice for the Hamiltonian with the property that  $H_{t_0+T}^F = H_{t_0}^F$ . Introducing the corresponding gauge-dependent fast-motion operator

$$U_{t_0}^F(t) \equiv U(t, t_0) e^{iH_{t_0}^F(t-t_0)}, \quad (15)$$

which is time periodic,  $U_{t_0}^F(t + T) = U_{t_0}^F(t)$ , the full time evolution operator can be expressed as

$$U(t_2, t_1) = U_{t_0}^F(t_2) e^{-iH_{t_0}^F(t_2-t_1)} U_{t_0}^F(t_1)^\dagger. \quad (16)$$

Since the quasienergies  $\epsilon_{nm}$  have no  $t_0$  dependence, the family of Floquet Hamiltonians,  $H_{t_0}^F$ , is moreover gauge equivalent to an *effective Hamiltonian*  $H_F$ , which has no explicit dependence on the driving phase  $t_0$  [24]. The corresponding gauge transformation is determined by a Hermitian *kick operator*  $\mathcal{K}(t)$  such that

$$H_F = e^{i\mathcal{K}(t_0)} H_{t_0}^F e^{-i\mathcal{K}(t_0)}. \quad (17)$$

Note that in general  $H_F$  alone does not generate the dynamics over one period. Nevertheless, the time evolution operator is still split as

$$U(t_2, t_1) = U_F(t_2) e^{-iH_F(t_2-t_1)} U_F(t_1)^\dagger, \quad (18)$$

where the *micromotion operator*

$$U_F(t) = e^{-i\mathcal{K}(t)} = U_F(t + T) \quad (19)$$

was introduced, and the eigenvalue problem

$$H_F |u_{nm}\rangle = \epsilon_{nm} |u_{nm}\rangle \quad (20)$$

determines the Floquet modes

$$|\phi_{nm}(t)\rangle = e^{im\omega t} U_F(t) |u_{nm}\rangle. \quad (21)$$

## 2. High frequency expansion of the effective Hamiltonian

Since they are periodic in time it is beneficial to view the Floquet modes  $|\phi_{nm}(t)\rangle$  as elements of the composed *Sambe space*  $\mathcal{S} = \mathcal{H} \otimes \mathcal{L}_T$ , where  $\mathcal{L}_T$  is the space of  $T$ -periodic square integrable functions [25]. Given  $\{|\alpha\rangle\}$  is a basis of  $\mathcal{H}$ , the vectors

$$|\alpha m\rangle = e^{im\omega t} |\alpha\rangle \quad (22)$$

constitute a basis of  $\mathcal{S}$ . Here we introduced the notation  $|\cdot\rangle$  for vectors which are explicitly considered as elements of  $\mathcal{S}$ . With the natural scalar product in Sambe space we obtain

$$\langle\langle \alpha m | \alpha' m' \rangle\rangle = \langle \alpha | \alpha' \rangle \frac{1}{T} \int_0^T dt e^{-i\omega(m-m')t} = \delta_{\alpha\alpha'} \delta_{mm'}. \quad (23)$$

In these terms the operator

$$Q = H(t) - i \frac{d}{dt} \quad (24)$$

acts on  $\mathcal{S}$  and Eq. (12) is an eigenvalue problem

$$Q |\phi_{nm}\rangle = \epsilon_{nm} |\phi_{nm}\rangle. \quad (25)$$

The matrix elements of  $Q$  are

$$\langle\langle \alpha' m' | Q | \alpha m \rangle\rangle = \langle \alpha' | H_{m'-m} | \alpha \rangle + \delta_{m'm} \delta_{\alpha'\alpha} m\omega \quad (26)$$

with the Fourier components of  $H(t)$ ,

$$H_m = \frac{1}{T} \int_0^T dt e^{-im\omega t} H(t). \quad (27)$$

Equation (26) reveals the block structure of  $Q$  with block indices  $m, m'$ . Eckardt and Anisimovas [20] identified the micromotion operator (19) as the operator, which block diagonalizes (26), thereby yielding the time-independent effective Hamiltonian

$$H_F = U_F^\dagger(t) H(t) U_F(t) - i U_F^\dagger(t) \frac{d}{dt} U_F(t). \quad (28)$$

Making use of the large separation of diagonal matrix elements for large frequencies  $\omega$  in Eq. (26) they apply degenerate perturbation theory to derive expansions for the effective Hamiltonian as well as the micromotion operator in powers of  $1/\omega$ . As a result they find a way to express the effective Hamiltonian as a series

$$H_F = \sum_{n=0}^{\infty} \frac{1}{\omega^n} H_F^{(n)}, \quad (29)$$

which can be used to systematically approximate  $H_F$  at high frequencies. The same holds for the kick operator, which takes the form

$$\mathcal{K}(t) = \sum_{n=1}^{\infty} \frac{1}{\omega^n} \mathcal{K}^{(n)}(t). \quad (30)$$

In our analysis we consider contributions to these series up to first order, which are

$$H_F^{(0)} = H_0, \quad H_F^{(1)} = \sum_{m=1}^{\infty} \frac{[H_m, H_{-m}]}{m} \quad (31)$$



and

$$\mathcal{K}^{(1)}(t) = -i \sum_{m=1}^{\infty} \frac{e^{im\omega t} H_m - e^{-im\omega t} H_{-m}}{m}. \quad (32)$$

### C. Nonequilibrium Hall conductance

In the following we will study the Hall conductance of the stationary state that is reached after a quench of the driving amplitude at time  $t^*$ . We assume the system is prepared in an initial state  $|\psi_0(t)\rangle$ , which is the ground state of the Hamiltonian with driving amplitude  $A_0 = 0$  or a quasistationary Floquet mode of the driven Hamiltonian with  $A_0 \neq 0$ . At time  $t_0$  the driving amplitude is suddenly switched from  $A_0$  to  $A_1$  and a nontrivial time evolution is induced. We study the Hall conductance of the state the system reaches a long time after the quench. Based on linear response theory and using a dephasing argument Dehghani *et al.* [10] derived an expression for the Hall conductance of a periodically driven electronic two-band system for this protocol obtaining

$$\sigma_{xy} = \frac{e^2}{2\pi h} \int_{BZ} d^2k \bar{F}_{\bar{k}d}(\rho_{\bar{k}d}(t^*) - \rho_{\bar{k}u}(t^*)) \quad (33)$$

with the time-averaged Berry curvature

$$\bar{F}_{\bar{k}d} = \frac{2}{T} \int_0^T dt \text{Im}[\langle \partial_{k_y} \phi_{\bar{k}d}(t) | \partial_{k_x} \phi_{\bar{k}d}(t) \rangle] \quad (34)$$

and the occupation numbers of the Floquet modes,

$$\rho_{\bar{k}\alpha}(t^*) = |\langle \psi_0(t^*) | \phi_{\bar{k}\alpha}(t^*) \rangle|^2. \quad (35)$$

Here we introduced the indices  $\alpha = u, d$  labeling the upper/lower band. In a cold atom setup with neutral atoms the electron charge  $e$  would be replaced by unity.

Dehghani *et al.* [10] considered quenches from the undriven ground state of the graphene Hamiltonian (2) to nonzero driving amplitudes  $A$ . They demonstrated that the Hall conductance as a function of the final driving amplitude changes rapidly whenever the Chern number

$$C = \frac{1}{2\pi} \int_{BZ} d^2k \bar{F}_{\bar{k}d} \quad (36)$$

jumps. We reproduced these numerical results as shown in Figs. 1(a) and 3 using the method described in Appendix B of this paper. Our results presented in Sec. III provide an analytical understanding of the behavior of the nonequilibrium Hall conductance occurring under this protocol when quenching close to the transition points.

### D. Nonanalytic behavior of the Hall conductance of the quenched state for closed systems

For the case of closed systems Wang *et al.* [15,16] studied an analogous situation to the one described above, considering quenches of a parameter  $M$  that allows us to tune the Hamiltonian  $H(M)$  between different topological phases. In a closed two-band system the Hall conductance of the stationary state after a quench is

$$\sigma_{xy} = \frac{e^2}{\pi h} \int_{BZ} d^2k \text{Im}[\langle \partial_{k_y} \varphi_{\bar{k}d} | \partial_{k_x} \varphi_{\bar{k}d} \rangle](\rho_{\bar{k}d} - \rho_{\bar{k}u}), \quad (37)$$

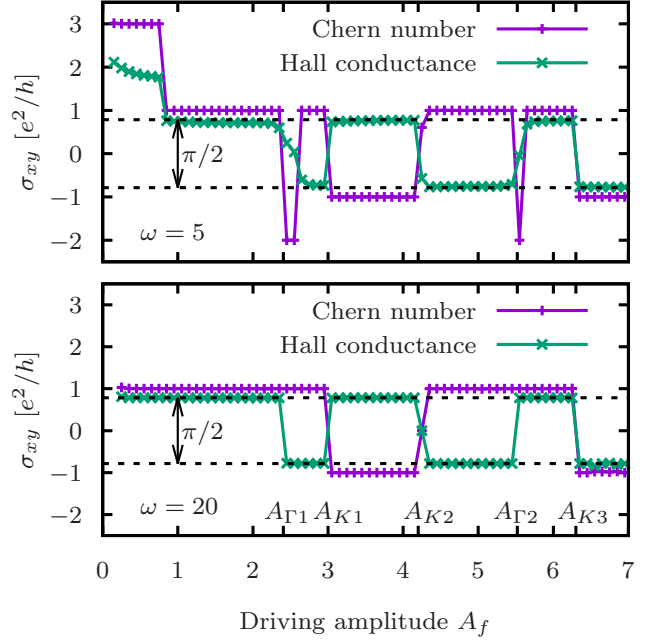


FIG. 3. Numerical results for the nonequilibrium Hall conductance after suddenly switching on the driving with amplitude  $A_f$  with the ground state of the undriven system as initial state for  $\omega = 5$  (top) and  $\omega = 20$  (bottom). The Chern number is computed according to Eq. (36).

where  $|\varphi_{\bar{k}\alpha}\rangle$  are the eigenstates of the post-quench Hamiltonian  $H(M_f)$  and  $\rho_{\bar{k}\alpha} = |\langle \psi_0 | \varphi_{\bar{k}\alpha} \rangle|^2$  are the occupation numbers of these eigenstates after the quench. The expressions for the Hall conductance in Eqs. (33) and (37) have very similar structure and, in fact, also in the case of the closed system the Hall conductance of the quenched state changes significantly when the quench parameter approaches an equilibrium phase boundary. In particular, considering the nonequilibrium Hall conductance close to a phase boundary  $M_c$  one finds that the behavior close to critical points is dominated by the nonanalytic part

$$\sigma_{xy}^{\text{div.}} = \frac{e^2}{h} \sum_{\bar{q}} C_{\eta}^{(\bar{q})}(M_i, M_f) \quad (38)$$

with

$$C_{\eta}^{(\bar{q}_j)} = \int_{\mathcal{B}_{\eta}(\bar{q}_j)} \frac{d^2k}{\pi} \text{Im}[\langle \partial_{k_y} \varphi_{\bar{k}d} | \partial_{k_x} \varphi_{\bar{k}d} \rangle](\rho_{\bar{k}d} - \rho_{\bar{k}u}), \quad (39)$$

where  $\mathcal{B}_{\eta}(\bar{q}_j)$  is a circle of radius  $\eta$  centered at  $\bar{q}_j$ , the gap-closing points of the energy spectrum in the Brillouin zone. If the parameter  $M - M_c$  is chosen proportional to the gap size the derivative of these contributions diverges as

$$\frac{d\sigma_{xy}^{\text{div.}}}{dM_f} \sim \frac{e^2}{h} \frac{C_f^- - C_f^+}{2|M_i - M_c|} \ln|M_f - M_c|, \quad (40)$$

where  $C_f^{\pm}$  are the Chern numbers on the right hand side (+,  $M_f > M_c$ ) and left hand side (-) of the transition, respectively. This constitutes a universal nonanalytic behavior of the nonequilibrium Hall conductance  $\sigma_{xy}$ . The result above is obtained by expanding the coefficient vector  $\vec{d}_{\bar{k}}$ , which is for

any two-band system defined analogously to Eq. (2), around the gap closing points  $\vec{q}$ ,

$$\vec{d}_{\vec{k}} = \vec{d}_{\vec{q}} + \hat{J}_{\vec{q}}^{\vec{d}} \Delta \vec{k} + \mathcal{O}(\Delta \vec{k}^2), \quad (41)$$

where  $\hat{J}_{\vec{q}}^{\vec{d}}$  is the Jacobian matrix of  $\vec{d}_{\vec{k}}$  and  $\Delta \vec{k} = \vec{k} - \vec{q}$ . The integral over the Brillouin zone in Eq. (37) is for  $M_f$  close to  $M_c$  dominated by contributions from the vicinity of gap closing points. The remaining part  $\sigma_{xy} - \sigma_{xy}^{\text{div}}$  is an analytic function which is in particular continuous. Any nonanalyticity of the Hall conductance is contributed by  $\sigma_{xy}^{\text{div}}$ . Note that the terms of  $\mathcal{O}(\Delta \vec{k}^2)$  do not contribute to the nonanalytic behavior, as discussed in Ref. [16]. The nonanalyticity can therefore be analyzed based on the expansion to linear order in Eq. (41) yielding the result in Eq. (40).

Note that, remarkably, the Dirac cones also lead to universal behavior of the Hall conductance away from the critical points as shown in Ref. [26]. In the following we will extend the analysis of the nonanalytic behavior to the case of driven systems based on a high frequency expansion of the effective Hamiltonian and the micromotion operator.

### III. RESULTS

#### A. Time-averaged Berry curvature and Berry connection

An important property of the Berry curvature  $\Omega_{\vec{k}}$  in undriven systems is the fact that it can be related to a local gauge potential, namely the Berry connection  $\vec{A}_{\vec{k}}$ , via

$$\Omega_{\vec{k}} = \vec{\nabla} \times \vec{A}_{\vec{k}}. \quad (42)$$

This property implies through the Kelvin-Stokes theorem that the Chern number is an integer [27].

It should be noted that it is a priori not clear whether a corresponding time-averaged Berry connection can be attributed to the time-averaged Berry curvature  $\bar{F}_{\vec{k}d}$  defined in Eq. (34), because for a nonvanishing Chern number the Berry connection must exhibit singularities, which could prohibit exchanging integrals and derivatives unheedingly. Nevertheless, we argue in this section that the time-averaged Berry curvature is at least up to corrections of second order in  $\omega^{-1}$  given by the Berry curvature of the effective Hamiltonian, which is related to a Berry connection.

Applying the product rule for the derivatives the time-averaged Berry curvature (34) can be split into two parts when plugging in Eq. (21) for the Floquet modes, yielding

$$\begin{aligned} \bar{F}_{\vec{k}d} = & \Omega_{\vec{k}}^F \\ & + \frac{2}{T} \int_0^T dt \text{Im} \left[ \langle u_{\vec{k}}^d | (\partial_{k_y} U_F(t)^\dagger) U_F(t) | \partial_{k_x} u_{\vec{k}}^d \rangle \right. \\ & + \langle \partial_{k_y} u_{\vec{k}}^d | U_F(t)^\dagger (\partial_{k_x} U_F(t)) | u_{\vec{k}}^d \rangle \\ & \left. + \langle u_{\vec{k}}^d | (\partial_{k_y} U_F(t)^\dagger) (\partial_{k_x} U_F(t)) | u_{\vec{k}}^d \rangle \right] \end{aligned} \quad (43)$$

with  $\Omega_{\vec{k}}^F = 2 \text{Im} \langle \partial_{k_y} u_{\vec{k}}^d | \partial_{k_x} u_{\vec{k}}^d \rangle$  the Berry curvature of the effective Hamiltonian  $H_F$ . For the derivatives of the operator exponentials  $U_F(t) = \exp(-i\mathcal{K}(t))$  we employ the identity

$$\frac{d}{d\lambda} e^{-i\mathcal{K}(t)} = \int_0^1 ds e^{-(1-s)i\mathcal{K}(t)} \frac{d\mathcal{K}(t)}{d\lambda} e^{-si\mathcal{K}(t)} \quad (44)$$

given in Ref. [28]. This reveals that the last term in Eq. (43) is of  $\mathcal{O}(\omega^{-2})$ , because  $\mathcal{K}(t) \sim \mathcal{O}(\omega^{-1})$ . For the remaining terms the Baker-Campbell-Hausdorff formula yields

$$\begin{aligned} (\partial_{k_y} U_F(t)^\dagger) U_F(t) &= \int_0^1 ds e^{i(1-s)\mathcal{K}(t)} \frac{\partial \mathcal{K}(t)}{\partial k_y} e^{-i(1-s)\mathcal{K}(t)} \\ &= \frac{d\mathcal{K}(t)}{dk_y} + \frac{i}{2} [\mathcal{K}(t), \partial_{k_y} \mathcal{K}(t)] + \dots \\ &= \frac{d\mathcal{K}(t)}{dk_y} + \mathcal{O}(\omega^{-2}). \end{aligned} \quad (45)$$

The ellipsis after the second equality stands for higher nested commutators with  $\mathcal{K}(t)$ , which are all of higher order in  $\omega^{-1}$ . The analogous argument yields  $U_F(t)^\dagger (\partial_{k_y} U_F(t)) = \frac{d\mathcal{K}(t)}{dk_y} + \mathcal{O}(\omega^{-2})$ . Now, according to Eq. (32), the time dependence of the first order contribution to the kick operator,  $\mathcal{K}^{(1)}(t)$ , is given as a sum of  $e^{im\omega t}$  with  $m \neq 0$ . Hence,  $\int_0^T dt \partial_{k_{x/y}} \mathcal{K}^{(1)}(t) = 0$  and we obtain

$$\bar{F}_{\vec{k}d} = \Omega_{\vec{k}}^F + \mathcal{O}(\omega^{-2}). \quad (46)$$

Note moreover, that if despite the singularities in  $\bar{F}_{\vec{k}d}$  the time integral and derivatives with respect to  $\vec{k}$  can be exchanged the time-averaged Berry curvature can be written as the curl of a time-averaged Berry connection

$$\vec{A}_{\vec{k}d}^{\alpha} = \frac{1}{T} \int_0^T dt \langle \phi_{\vec{k}d}(t) | \partial_{k_{\alpha}} | \phi_{\vec{k}d}(t) \rangle \quad (47)$$

meaning that due to the usual arguments the Chern number  $C = \frac{1}{2\pi} \int_{BZ} d^2k \vec{\nabla} \times \vec{A}_{\vec{k}d}$  is an integer. That is, however, only possible if all higher order terms in Eq. (46) vanish and  $C$  is identically the Chern number of the effective Hamiltonian  $H_F$ .

#### B. High frequency expansion

For the subsequent analysis it is useful to formulate both the high frequency expansion of the effective Hamiltonian and the expansion of the kick operator in terms of coefficient vectors  $\vec{h}_{\vec{k}}$  and  $\vec{g}_{\vec{k}}(t)$  such that in the single momentum sectors

$$H_{\vec{k}F} = \vec{h}_{\vec{k}} \cdot \vec{\sigma} \quad (48)$$

and

$$\mathcal{K}_{\vec{k}}(t) = -\vec{g}_{\vec{k}}(t) \cdot \vec{\sigma}. \quad (49)$$

In this section we present expressions for the time averaged Berry curvature and the Floquet mode occupation based on expansions of the respective coefficient vectors.

We will from now on set the hopping  $t_h \equiv 1$ . This means that the high frequency expansion is valid for  $\omega/t_h = \omega \gg 1$ .

##### 1. Effective Hamiltonian and Berry curvature

For the high frequency expansion of the effective Hamiltonian given in Eq. (31) we need the Fourier components of the time-dependent Hamiltonian  $H_{\vec{k}}(t) = \vec{d}_{\vec{k}}(t) \cdot \vec{\sigma}$ . These are

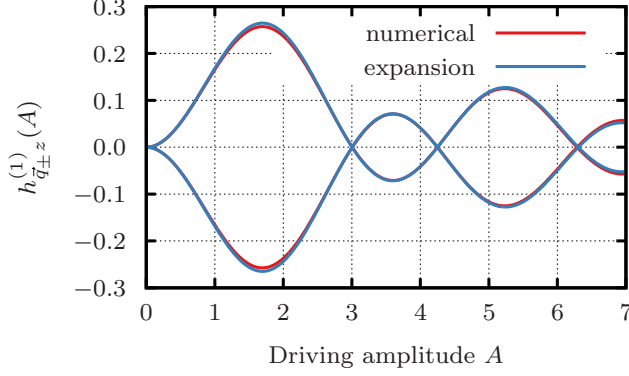


FIG. 4. Values of the first order contribution to the  $z$  component of the coefficient vector at the Dirac points,  $h_{\vec{q}_{\pm z}}^{(1)}(A)/\omega$ , for  $\omega = 10$  as a function of the driving amplitude  $A$  in comparison with the numerical result for  $h_{\vec{q}_{\pm z}}(A)$ .

determined by

$$\begin{aligned} d_{kx}^m &= \frac{1}{T} \int_0^T dt e^{im\omega t} d_{\vec{k}x}(t) \\ &= -J_m(A) \sum_{j=1}^3 \frac{1}{2} e^{-im\psi_j} [e^{i\vec{k}\cdot\vec{\delta}_j} + (-1)^m e^{-i\vec{k}\cdot\vec{\delta}_j}] \\ d_{ky}^m &= -J_m(A) \sum_{j=1}^3 \frac{-i}{2} e^{-im\psi_j} [e^{i\vec{k}\cdot\vec{\delta}_j} + (-1)^{m+1} e^{-i\vec{k}\cdot\vec{\delta}_j}], \end{aligned} \quad (50)$$

where  $J_m(x)$  denotes the  $m$ th Bessel function and  $\psi_j = \arctan(\delta_j^y/\delta_j^x)$  was introduced. This yields as the zeroth order term of the effective Hamiltonian just the undriven Hamiltonian rescaled by the zeroth Bessel function,

$$\vec{h}_{\vec{k}}^{(0)}(A) = -J_0(A) \sum_{j=1}^3 \begin{pmatrix} \cos(\vec{k}\cdot\vec{\delta}_j) \\ \sin(\vec{k}\cdot\vec{\delta}_j) \\ 0 \end{pmatrix}. \quad (51)$$

As the first order term is the commutator of only the Pauli matrices  $\sigma_x$  and  $\sigma_y$ , there is only a contribution to the  $z$  component of the coefficient vector, namely

$$h_{kz}^{(1)}(A) = 4 \sum_{n=1}^{\infty} \frac{J_n(A)^2 \sin\left(\frac{2n\pi}{3}\right)}{n} \sum_{j=1}^3 \sin(\vec{k}\cdot\vec{\gamma}_j), \quad (52)$$

where the next-nearest-neighbor vectors

$$\vec{\gamma}_1 = \vec{\delta}_1 - \vec{\delta}_3, \quad \vec{\gamma}_2 = \vec{\delta}_2 - \vec{\delta}_1, \quad \vec{\gamma}_3 = \vec{\delta}_3 - \vec{\delta}_2 \quad (53)$$

were introduced. Note that since  $J_n(A)^2/n$  decreases with increasing  $n$  the infinite sum in Eq. (52) can for practical purposes safely be approximated by a truncation restricted to the first few terms. Figure 4 shows the analytical result for  $h_{\vec{q}_{\pm z}}^{(1)}(A)$  for  $\omega = 10$  in comparison with the numerical result at the Dirac points ( $K$  points)

$$\vec{q}_{\pm} = \left( \pm \frac{0}{\pm \frac{4\pi}{3\sqrt{3}a}} \right). \quad (54)$$

Both show good agreement, in particular in the vicinity of the roots.

The appearance of the n.n.n. vectors in the effective Hamiltonian reflects the fact that in real space the first order contribution to the effective Hamiltonian adds a hopping between next-nearest neighbors. The resulting effective Hamiltonian corresponds to the famous Haldane model where in this case the external driving opens a gap in the quasienergy spectrum leading to a nonvanishing Chern number [3,7,20].

Omitting possible second order contributions to the time-averaged Berry curvature as discussed in Sec. III A the Chern number (36) is solely determined by the effective Hamiltonian  $H_F$  and can be expressed in terms of the coefficient vector  $\vec{h}_{\vec{k}}$  as

$$C = \int_{BZ} d^2k \frac{\left( \frac{\partial \vec{h}_{\vec{k}}}{\partial k_x} \times \frac{\partial \vec{h}_{\vec{k}}}{\partial k_y} \right) \cdot \vec{h}_{\vec{k}}}{4\pi (h_{\vec{k}})^3} \quad (55)$$

(cf. [27]).

Note that there are different possibilities for gap closing points in the quasienergy spectrum of the effective Hamiltonian, which reads to first order

$$H_{F\vec{k}} = h_{kx}^{(0)} \sigma^x + h_{ky}^{(0)} \sigma^y + \frac{1}{\omega} h_{kz}^{(1)} \sigma^z + \mathcal{O}(\omega^{-2}). \quad (56)$$

Independent of the driving amplitude the zeroth-order terms have roots at the Dirac points  $\vec{q}_{\pm}$ . Therefore, roots of  $h_{\vec{q}_{\pm z}}^{(1)}(A)$  as a function of the driving amplitude mark gap-closing points. Moreover,  $h_{kz}^{(1)}(A)$  has a root at the  $\Gamma$  point  $\vec{k}_{\Gamma} = (0,0)$  independent of driving amplitude. This means that the quasienergy spectrum closes at this point at roots of  $J_0(A)$ , because there the zeroth order terms vanish on the whole Brillouin zone. We marked the transitions that can be attributed to gap closing points at  $K$  or  $\Gamma$  points with labels  $A_{Ki}$  and  $A_{\Gamma i}$ , respectively, in Fig. 3. In the following analysis we will focus on the transitions with gap closing at the  $K$  points.

## 2. Micromotion operator and occupation numbers

The second ingredient for the Hall conductance of the quenched state is the mode occupation difference

$$\begin{aligned} \rho_{\vec{k}d}(t^*) - \rho_{\vec{k}u}(t^*) \\ = |\langle \psi_0(t^*) | \phi_{\vec{k}d}(t^*) \rangle|^2 - |\langle \psi_0(t^*) | \phi_{\vec{k}u}(t^*) \rangle|^2, \end{aligned} \quad (57)$$

which depends on the quench time  $t^*$ . Figure 5(a) shows the mode occupation in the Brillouin zone for a quench from  $A_0 = 0.1$  to  $A_1 = 2.8$  at  $t_0 = 0$ . Quenching the amplitude leads to a smearing of the occupation numbers along the direction of the driving field. Since we consider quasistationary Floquet modes as initial states, the time dependence is fully determined by the pre- and post-quench micromotion operators.

As given by Eq. (32) the first order term of the high frequency expansion of the kick operator is

$$\mathcal{K}_{\vec{k}}^{(1)}(t) = -i \sum_{m=1}^{\infty} \frac{1}{m} [e^{im\omega t} \vec{d}_{\vec{k}}^m - e^{-im\omega t} \vec{d}_{\vec{k}}^m] \cdot \vec{\sigma} \quad (58)$$

with  $\vec{d}_{\vec{k}}^m$  given in Eq. (50). We approximate the micromotion operator with

$$U_{\vec{k}}^F(t) = \exp(-i\mathcal{K}_{\vec{k}}^{(1)}(t)/\omega) + \mathcal{O}(\omega^{-2}) \quad (59)$$

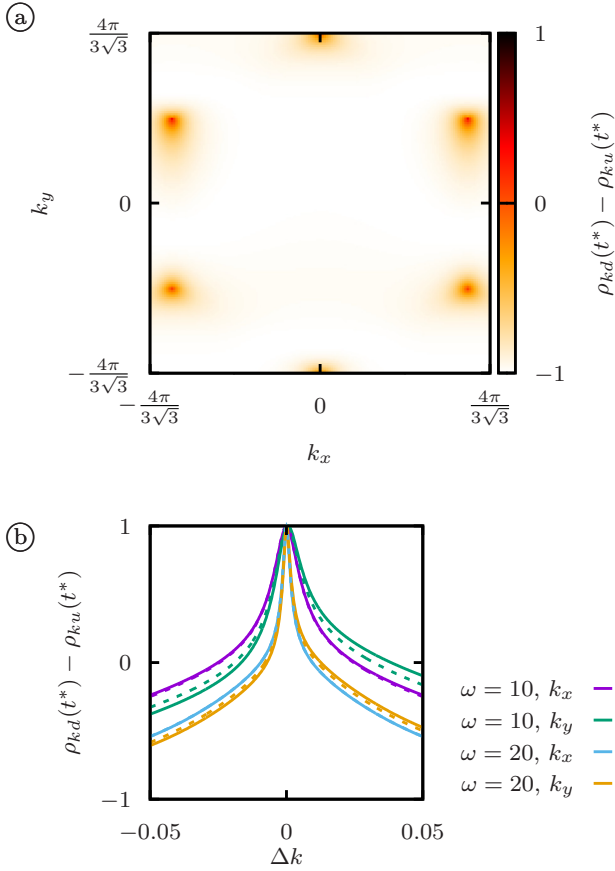


FIG. 5. (a) Numerical result for the mode occupation after quenching the driving amplitude from  $A_0 = 0.1$  to  $A_1 = 2.8$  at  $t^* = 0$ . (b) Comparison between numerical results (solid lines) and the high frequency expansion (61) (dashed lines) along cuts with constant  $k_x$  or  $k_y$ , respectively, through the  $K$  point  $\vec{q} = (0, -4\pi/3\sqrt{3})$  for two different frequencies.

and define  $\vec{g}_{\vec{k}}(t) = (g_{\vec{k}x}(t), g_{\vec{k}y}(t), g_{\vec{k}z}(t))$  via

$$-\mathcal{K}_{\vec{k}}^{(1)}(t) = \vec{g}_{\vec{k}}(t) \cdot \vec{\sigma}. \quad (60)$$

This approximation of the micromotion operator and the first order result for the eigenvectors of the effective Hamiltonian yields via Eq. (21) the  $t_0$ -dependent occupation numbers

$$\begin{aligned} \rho_{\vec{k}d}(t^*) - \rho_{\vec{k}u}(t^*) \\ = \frac{\vec{h}_{\vec{k}}^i \cdot \vec{h}_{\vec{k}}^f}{|\vec{h}_{\vec{k}}^i| |\vec{h}_{\vec{k}}^f|} + \frac{(\vec{h}_{\vec{k}}^i \times \vec{h}_{\vec{k}}^f) \cdot \Delta \vec{g}_{\vec{k}}(t^*)}{|\vec{h}_{\vec{k}}^i| |\vec{h}_{\vec{k}}^f|} + \mathcal{O}(\omega^{-2}). \end{aligned} \quad (61)$$

Here  $\Delta \vec{g}_{\vec{k}}(t^*) = \vec{g}_{\vec{k}}^{A_f}(t^*) - \vec{g}_{\vec{k}}^{A_i}(t^*)$  denotes the difference of the Kick operator coefficients before and after switching the driving amplitude. A detailed derivation of this result is given in Appendix C.

Figure 5(b) shows a comparison between the analytical result in Eq. (61) and the numerical result on cuts through a  $K$  point with constant  $k_x$  and  $k_y$ , respectively, for two different driving frequencies. The truncated high frequency expansion clearly captures the anisotropy introduced by the external field

and the agreement with numerics improves as the driving frequency is increased.

In order to analyze the nonanalytic part of the Hall conductance (39) it is crucial that the occupation numbers contribute a factor  $|h_{\vec{k}}^f|^{-1}$ , because thereby the denominator becomes a polynomial and it is possible to find the antiderivative of the integrand. The result in Eq. (61) shows that the correction is proportional to  $|h_{\vec{k}}^f|^{-1}$ . Moreover, the first order contribution to the occupation numbers is an odd function of  $\Delta \vec{k} = \vec{k} - \vec{q}_{\pm}$ . Therefore, as discussed in Ref. [16], the corresponding part of the integrand will not contribute to the nonanalytic behavior of the Hall conductance (34). This means that close to the phase boundaries any dependence of the Hall conductance on the quench time is a second order contribution in powers of the inverse frequency. We will therefore ignore it in the further analysis.

Experimental setups with finite ramping times will usually not be able to prepare initial states with a completely filled lower band and an empty upper band. Nevertheless, we will focus on this situation in the following analysis and discuss the effect of partially filled bands as initial states later in Sec. III D.

### C. Universal behavior at the phase transition

Putting together Eqs. (34), (46), and (61) the nonequilibrium Hall conductance is determined by

$$\sigma_{xy} = \frac{e^2}{h} \int d\vec{k}^2 \frac{(\vec{h}_{\vec{k}}^f \cdot \vec{h}_{\vec{k}}^i) \left( \frac{\partial \vec{h}_{\vec{k}}^f}{\partial k_x} \times \frac{\partial \vec{h}_{\vec{k}}^f}{\partial k_y} \right) \cdot \vec{h}_{\vec{k}}^f}{4\pi h_{\vec{k}}^i (h_{\vec{k}}^f)^4}, \quad (62)$$

where the integral is over the Brillouin zone.

We will analyze the nonanalytic behavior of (62) based on expansions of the integrand around the gap closing points as summarized in Sec. II D and discussed more extensively in Ref. [16]. According to the high frequency expansion to first order in powers of  $\omega^{-1}$ , we can suppose the coefficient vectors  $\vec{h}_{\vec{k}}^{i/f}$  of the initial and final Hamiltonian, respectively, around some singularity  $\vec{q}$  to be

$$h_{\vec{k}x}^{i/f} = J_0(A_{i/f})(a_{1x} \Delta k_x + a_{1y} \Delta k_y) + \mathcal{O}(\Delta k^2) \quad (63)$$

$$h_{\vec{k}y}^{i/f} = J_0(A_{i/f})(a_{2x} \Delta k_x + a_{2y} \Delta k_y) + \mathcal{O}(\Delta k^2) \quad (64)$$

$$h_{\vec{k}z}^{i/f} = m(A_{i/f}) + \mathcal{O}(\Delta k^2), \quad (65)$$

where  $\Delta k_{x/y} = k_{x/y} - q_{x/y}$ . Note that  $A_i$  and  $A_f$  are the free parameters and  $m(A_{i/f}) = h_{\vec{q}_z}^{(1)}(A_{i/f})$  is also a function of  $A_{i/f}$ . In contrast to the closed system analyzed in Refs. [15,16] for the driven system the expansion coefficients of all components depend on the external parameter, namely the driving amplitude  $A$ . However, by introducing the expansion

$$h_{\vec{k}x}^{*i/f} = a_{1x} \Delta k_x + a_{1y} \Delta k_y + \mathcal{O}(\Delta k^2) \quad (66)$$

$$h_{\vec{k}y}^{*i/f} = a_{2x} \Delta k_x + a_{2y} \Delta k_y + \mathcal{O}(\Delta k^2) \quad (67)$$

$$h_{\vec{k}z}^{*i/f} = \frac{m(A_{i/f})}{J_0(A_{i/f})} + \mathcal{O}(\Delta k^2) \equiv \tilde{m}_{i/f} + \mathcal{O}(\Delta k^2), \quad (68)$$

the structure of the integrand in Eq. (62) remains the same and we obtain the nonanalytic contributions defined in Eq. (39), which read

$$\mathcal{C}_\eta^{(\bar{q})} = \text{sgn}(J_0(A_i)) \times \int_{\mathcal{B}_\eta(\bar{q}_i)} d\bar{k}^2 \frac{(\vec{h}_k^{*f} \cdot \vec{h}_k^{*i}) \left( \frac{\partial \vec{h}_k^{*f}}{\partial k_x} \times \frac{\partial \vec{h}_k^{*f}}{\partial k_y} \right) \cdot \vec{h}_k^{*f}}{4\pi h_k^{*i} (h_k^{*f})^4}. \quad (69)$$

Therefore, the analysis of the behavior of the Hall conductance close to a transition can be done based on the expansion (66)–(68) with constant coefficients in the first two components given that  $J_0(A_{i/f}) \neq 0$ . As mentioned above, it is sufficient to consider the expansion to linear order. In the vicinity of roots of  $J_0(A_{i/f})$ , however, the corresponding expansions of the first two components of the coefficient vectors are potentially dominated by higher order contributions.

### 1. Quenching from the undriven initial state

We first focus on the quenches with the ground state of the undriven system as initial state, i.e.,  $A_i = 0$  and  $A_f \neq 0$ . The gaplessness of the initial Hamiltonian is reflected by  $\tilde{m}_i = 0$  in Eq. (68), whereas  $\tilde{m}_f \neq 0$ . The linear transformation of coordinates

$$\begin{pmatrix} \Delta k'_x \\ \Delta k'_y \end{pmatrix} = \begin{pmatrix} a_{1x} & a_{1y} \\ a_{2x} & a_{2y} \end{pmatrix} \begin{pmatrix} \Delta k_x \\ \Delta k_y \end{pmatrix} \quad (70)$$

allows us to make use of the rotational symmetry around the singularity, yielding

$$\mathcal{C}_\eta^{(\bar{q})} = \text{sgn}(J_0(A_i)) \frac{\tilde{m}_f \text{sgn}(a_{1x}a_{2y} - a_{2x}a_{1y})}{2} \times \int_0^\eta d\Delta k' \frac{\Delta k'^2}{(\tilde{m}_f^2 + \Delta k'^2)^2}. \quad (71)$$

The nonvanishing part of this integral in the limit  $m_f \rightarrow 0$  is

$$\frac{\tilde{m}_f \text{sgn}(a_{1x}a_{2y} - a_{2x}a_{1y})}{4} \int_0^\eta d\Delta k' \frac{1}{\tilde{m}_f^2 + \Delta k'^2}. \quad (72)$$

$$= \frac{\text{sgn}(a_{1x}a_{2y} - a_{2x}a_{1y})}{4} \arctan(\eta/\tilde{m}_f). \quad (73)$$

For arbitrary  $\eta > 0$ , we have  $\lim_{m_f \rightarrow 0} \arctan(\eta/\tilde{m}_f) = \text{sgn}(\tilde{m}_f)\pi/2$ . Thus, the discontinuity of  $\mathcal{C}_\eta^{(\bar{q})}$  at  $m_f = 0$  must be

$$\mathcal{C}_\eta^{(\bar{q})}(m_f \rightarrow 0^+) - \mathcal{C}_\eta^{(\bar{q})}(m_f \rightarrow 0^-) = \frac{\pi}{4} \text{sgn}[J_0(A_i)J_0(A_f)(a_{1x}a_{2y} - a_{2x}a_{1y})]. \quad (74)$$

Summing up the contributions of both  $K$  points according to Eq. (38) yields the discontinuity of the total Hall conductance, which is

$$\begin{aligned} & \sigma_{xy}(A_f - A_c \rightarrow 0^+) - \sigma_{xy}(A_f - A_c \rightarrow 0^-) \\ &= \frac{\pi}{4} \text{sgn}\left(\frac{J_0(A_i)}{J_0(A_f)}\right) \left[ \lim_{m_f \rightarrow 0^+} C - \lim_{m_f \rightarrow 0^-} C \right] \\ &= \pm \frac{\pi e^2}{2h}. \end{aligned} \quad (75)$$

The sign depends on the particular choice of the gap closing point  $A_c$ . For critical points which are related to a closing of the gap at the  $K$  points in the Brillouin zone the comparison with the numerical results in Figs. 1(a) and 3 shows that the dimensionless Hall conductance indeed jumps by  $\pi/2$ .

### 2. Quenching from a driven initial state

We now turn to the case where the system is initially prepared in a quasistationary Floquet mode of the driven Hamiltonian with  $A_i \neq 0$ . When the initial state is a Floquet mode of the driven Hamiltonian, the analysis is completely analogous to the case of the closed system in Refs. [15,16]. Plugging Eqs. (66)–(68) into Eq. (69) yields the nonanalytic part of the integral, which is

$$\mathcal{C}_\eta^{(\bar{q})} \sim - \frac{J_0(A_i) \text{sgn}(a_{1x}a_{2y} - a_{2x}a_{1y})}{J_0(A_f)} \frac{1}{2|m_i|} \times m_f(A_f) \ln \left| \frac{m_f(A_f)}{J_0(A_f)} \right|. \quad (76)$$

Note first of all that by contrast to quenching from the undriven ground state the Hall conductance is continuous at the transition points if the initial state is a Floquet mode of the driven Hamiltonian, which is also evident in Fig. 1(a). Nevertheless, the derivative with respect to  $A_f$  in the limit  $A_f \rightarrow A_f^c$  is nonanalytic and diverges like

$$\begin{aligned} \frac{d\mathcal{C}_\eta^{(\bar{q})}}{dA_f} &\sim - \frac{J_0(A_i) \text{sgn}(a_{1x}a_{2y} - a_{2x}a_{1y})}{J_0(A_f^c)} \frac{1}{2|m_i|} \\ &\times \left. \frac{dm_f}{dA_f} \right|_{A_f=A_f^c} \ln |m_f(A_f)|. \end{aligned} \quad (77)$$

Summing up the contributions from both gap closing points in the Brillouin zone yields the divergent part of the derivative of the Hall conductance

$$\begin{aligned} \frac{d\sigma_{xy}^{\text{div.}}}{dA_f} &\sim \frac{J_0(A_i)}{J_0(A_f^c)} \frac{\lim_{m_f \rightarrow 0^+} C - \lim_{m_f \rightarrow 0^-} C}{2|m_i|} \\ &\times \left. \frac{dm_f}{dA_f} \right|_{A_f=A_f^c} \ln |m_f(A_f)|. \end{aligned} \quad (78)$$

Figure 1(b) shows the derivative of the Hall conductance for quenches with different  $A_i$  and  $A_f$  close to the transition  $K_1$ . The derivatives have been rescaled by the respective prefactors  $\mu(A_i, A_f) = J_0(A_f)|m_i|/J_0(A_i)m'_f$  such that according to Eq. (77) the slopes of all results coincide. Moreover, the results for different  $A_i$  have been shifted in order to compare them despite the different regular contributions to the Hall conductance. The numerical data agree with the analytically predicted slope and the agreement improves as  $A_f$  approaches the transition point  $A_{K_1}$ . Note that after a quench starting with  $A_i = 2.3$  the agreement is good although this is very close to a root of  $J_0(A_i)$  as can be seen in the inset of Fig. 1(b).

The presented data were obtained using a grid with  $6000 \times 6000$  points in the numerical scheme described in Appendix B. This grid resolution determines the computational cost and has to be increased as  $A_f$  approaches  $A_{K_1}$ . Thereby our computational resources limit the numerical results to the regime presented in Fig. 1(b).



#### D. The effect of partially filled Floquet bands as initial state

As mentioned before the completely filled lower Floquet band we considered above cannot necessarily be prepared with high fidelity in practice [9,29]. In particular, ramping across a gap closing point prohibits adiabatic preparation of the initial state. Therefore, the initial state will typically be given by partially filled Floquet bands in experiments.

Considering partially filled bands produced using some ramping protocol the single particle initial states will be a superposition of the pre-quench Floquet modes  $|\phi_{0\bar{k}}^\alpha(t)\rangle$ ,

$$|\psi_{\bar{k}}^0(t)\rangle = \cos\theta_{\bar{k}}|\phi_{0\bar{k}}^d(t)\rangle + \sin\theta_{\bar{k}}e^{i\varphi_{\bar{k}}(t)}|\phi_{0\bar{k}}^u(t)\rangle. \quad (79)$$

In this expression  $\theta_{\bar{k}}$  parametrizes the single particle occupation number and it will depend on the details of the ramping protocol. The phase is given by  $\varphi_{\bar{k}}(t) = \varphi_{\bar{k}}^0 + (\epsilon_{\bar{k}}^d - \epsilon_{\bar{k}}^u)t = \varphi_{\bar{k}}^0 - 2|\vec{h}_{\bar{k}}^i|t$ , where  $\vec{h}_{0\bar{k}}$  is the coefficient vector of the initial effective Hamiltonian. Plugging this into Eq. (57) yields

$$\begin{aligned} & \rho_{\bar{k}}^d(t^*) - \rho_{\bar{k}}^u(t^*) \\ &= \cos(2\theta_{\bar{k}}) \left( |\langle \phi_{0\bar{k}}^d(t^*) | \phi_{\bar{k}}^d(t^*) \rangle|^2 - |\langle \phi_{0\bar{k}}^d(t^*) | \phi_{\bar{k}}^u(t^*) \rangle|^2 \right) \\ &+ \sin(2\theta_{\bar{k}}) \operatorname{Re} \left[ e^{i\varphi_{\bar{k}}(t^*)} \left( \langle \phi_{0\bar{k}}^d(t^*) | \phi_{\bar{k}}^d(t^*) \rangle \langle \phi_{\bar{k}}^d(t^*) | \phi_{0\bar{k}}^u(t^*) \rangle \right. \right. \\ &\left. \left. - \langle \phi_{0\bar{k}}^d(t^*) | \phi_{\bar{k}}^u(t^*) \rangle \langle \phi_{\bar{k}}^u(t^*) | \phi_{0\bar{k}}^d(t^*) \rangle \right) \right] \end{aligned} \quad (80)$$

Thereby, the Hall conductance after a quench can be split into two parts,  $\sigma_{xy} = \sigma_{xy}^{(1)} + \sigma_{xy}^{(2)}$ , corresponding to the first and the second contribution to the occupation difference.

The first term of the occupation difference above equals the occupation difference one obtains when the system is initialized in the lower Floquet band weighted by the prefactor  $\cos(2\theta_{\bar{k}})$ . The specific form of the occupation after preparation, which is parametrized by  $\theta_{\bar{k}}$ , will depend on the preparation protocol. If  $\theta_{\bar{k}}$  can be approximated by a constant in the vicinity of the gap closing points  $\vec{q}_j$  it will not affect the nonanalytic behavior and  $\sigma_{xy}^{(1)}$  will contribute a logarithmic divergence to the derivative of the Hall conductance at the critical time. In the case of the driven hexagonal system considered above the nonanalyticity in Eq. (77) acquires an additional prefactor  $\cos(\theta_{\vec{q}})$  with  $\vec{q}$  given in Eq. (54).

Under the assumption that both  $\theta_{\bar{k}}$  and  $\varphi_{\bar{k}}^0$  are well behaved in the vicinity of the gap closing points the second term yields a contribution to the nonequilibrium Hall conductance that is independent of the driving frequency and behaves like the Hall conductance after quenching from a critical state, as discussed in Sec. III C 1, but is weighted with  $\sin(\theta_{\vec{q}})$  and oscillates with frequency  $2|\vec{h}_{\vec{q}}^i|$ , i.e., the initial gap width. For our specific model and the class of critical points we considered above the contribution is

$$\pm \sin(2\theta_{\vec{k}_0}) \cos(\varphi_{\vec{k}_0}^0(t^*)) \frac{\pi e^2}{2h}. \quad (81)$$

A detailed derivation of this result is given in Appendix D. This contribution is nonuniversal as it depends on the quench time  $t^*$ . However, it can in practice be eliminated by averaging over a range of quench times  $t^*$ .

Altogether the results obtained for the completely filled lower Floquet band will pertain when allowing partially filled Floquet bands as initial states if the occupation numbers

in the vicinity of gap closing points are well behaved. Nonanalyticities in the occupation difference, however, could potentially lead to different behavior of the nonequilibrium Hall conductance.

Any kind of occupation that reflects the spectral properties of a gapped system will be smooth in the vicinity of the gap closing points  $\vec{q}$ . For example, thermal occupation numbers corresponding to an inverse temperature  $\beta$  are obtained from the pure state (79) if  $\cos\theta_{\bar{k}} = e^{-\beta\epsilon_{\bar{k}}^d/2} (2 \cosh(\beta\epsilon_{\bar{k}}^d))^{-1/2}$ , where the (quasi)energies  $\epsilon_{\bar{k}}$  are smooth everywhere. Nevertheless, ramping across gap closing points could possibly leave an imprint of the nonanalyticity in the resulting occupation numbers. Moreover, it might be possible that the characteristics of the occupation depend on the choice of the ramping protocol. Such effects, since beyond the scope of this work, should be investigated in the future.

## IV. DISCUSSION

### A. Universality

The nonanalytic behavior of the Hall conductance at the critical points studied in this work is universal in the same sense as discussed in Ref. [16]. The key feature that determines the nonanalytic behavior is the conic structure of the quasienergy spectrum close to the gap closing point. Thereby, the nonanalytic behavior does not depend on the details of the model.

Both expressions characterizing the nonanalytic behavior, Eq. (75) and Eq. (78), depend only on the band gap  $m(A)$ , the band width ratio  $J_0(A_i)/J_0(A_f)$ , and the jump of the Chern number at the transition. The Chern number is, however, only defined in translationally invariant systems. Nevertheless, we expect our results to hold also for systems with weak disorder as we argue in the following. Note that this argument regards transitions that occur as a function of the parameter  $A$  in the presence of weak disorder. Disorder-driven topological transitions at intermediate or strong disorder as reported in Refs. [30,31] are of different nature and, hence, not in the class of transitions we consider in this paper.

Other than in undriven topological insulators edge modes of Floquet topological insulators do not only occur in the energy gap around  $\epsilon_{\bar{k}} = 0$ . Due to the periodicity of the quasienergy spectrum they can also lie in the gap at  $\epsilon_{\bar{k}} = \omega/2 = \pi/T$  that separates the quasienergies of neighboring quasienergy “Brillouin zones.” The Chern number corresponds to the difference between the number of edge modes at  $\epsilon = 0$ , denoted by  $\nu_0$ , and the number of edge modes at  $\epsilon = \pi/T$ , denoted by  $\nu_\pi$ , i.e.,  $C = \nu_0 - \nu_\pi$ . In Ref. [14] a bulk invariant was introduced that directly corresponds to the number of edge states in a particular gap for systems with translational invariance. This was generalized to disordered systems in Ref. [32]. For the disordered system one adds additional time-independent fluxes  $\vec{\Theta} = (\theta_x, \theta_y)$  threaded through the lattice to the time-periodic Hamiltonian of interest leading to a time evolution operator  $U(\vec{\Theta}, t) = \mathcal{T}_t \exp(-i \int_0^t dt' H(\vec{\Theta}, t'))$ . The number of edge states in a gap around a given quasienergy  $\epsilon$ ,  $\nu_\epsilon$ , is then determined by

$$\nu_\epsilon = W[U_\epsilon], \quad (82)$$



where

$$W[U_T] = \frac{1}{8\pi^2} \int_0^T dt \int d^2\theta \times \text{tr} \left( U_T^{-1} \partial_t U_T [U_T^{-1} \partial_{\theta_x} U_T, U_T^{-1} \partial_{\theta_y} U_T] \right) \quad (83)$$

is a winding number of the map  $U_T(\vec{\Theta}, t)$  from  $(\vec{\Theta}, t) \in S^1 \times S^1 \times S^1$  to the space of time evolution operators  $U_T(\theta, t)$  periodic in  $\theta_x, \theta_y$ , and  $t$ .  $U_\epsilon(\vec{\Theta}, t)$  is related to the time evolution operator of the driven system  $U(\vec{\Theta}, t)$  via

$$U_\epsilon(\vec{k}, t) = \begin{cases} U(\vec{\Theta}, 2t) & \text{if } 0 \leq t \leq T/2 \\ e^{-iH_{\text{eff}}^\epsilon(\vec{\Theta})t} & \text{if } T/2 \leq t \leq T. \end{cases} \quad (84)$$

In this expression  $\epsilon$  determines the direction  $e^{-i\epsilon T}$  of the branch cut of the logarithm in the definition of the effective Hamiltonian

$$H_{\text{eff}}^\epsilon(\vec{\Theta}) = \frac{i}{T} \log_\epsilon U(\vec{\Theta}, T). \quad (85)$$

With these results the characteristic nonanalytic behavior given by Eqs. (75) and (78) can be reexpressed in terms of the winding number  $W$  as

$$\sigma_{xy}^{\text{div.}} \sim \frac{\pi}{4} \text{sgn} \left( \frac{J_0(A_i)}{J_0(A_f)} \right) \left[ \lim_{m_f \rightarrow 0^+} \Delta W - \lim_{m_f \rightarrow 0^-} \Delta W \right] \quad (86)$$

for quenches from the gapless initial state and as

$$\sigma_{xy}^{\text{div.}} \sim \frac{J_0(A_i)}{J_0(A_f^c)} \frac{\lim_{m_f \rightarrow 0^+} \Delta W - \lim_{m_f \rightarrow 0^-} \Delta W}{2|m_i|} \times \left. \frac{dm_f}{dA_f} \right|_{A_f=A_f^c} \ln |m_f| \quad (87)$$

for the gapped initial state. Here we introduced  $\Delta W = W[U_0] - W[U_{\pi/T}]$ . This form of the nonanalytic behavior is expected to pertain also in the presence of weak disorder. Since it is beyond the scope of this paper, it is left for the future to demonstrate this anticipated behavior explicitly using specific examples.

Note, however, that these results for the nonanalytic behavior apply only to transitions with conic gap closing points at  $\epsilon = 0$ , which corresponds to points  $\vec{q}$  in the Brillouin zone where the coefficient vector of the effective Hamiltonian vanishes,  $|\vec{h}_{\vec{q}}| = 0$ . A unique feature of Floquet systems is the possibility of gap closing points at  $\epsilon = \pi/T$ , which were for example studied in Refs. [8,14,17,18,31]. These transitions correspond to the presence of points  $\vec{q}$  in the Brillouin zone where  $|\vec{h}_{\vec{q}}| = \pi/T$ . In that case any nonanalyticity in the Hall conductance that is determined by the integral in Eq. (62) must originate in nonanalytic behavior of the numerator instead of roots of the denominator. Therefore, our analysis does not apply in these cases.

## B. Conclusion

Based on a high frequency expansion of the effective Hamiltonian and the micromotion operator we studied the nonequilibrium Hall conductance after sudden switches of the driving amplitude. Considering a tight binding Hamiltonian on a hexagonal lattice with periodically modulated potential we found two kinds of nonanalytic behavior after quenches close

to critical driving amplitudes at which the ground state Chern number exhibits a jump. When the system is initially prepared in the undriven ground state of the gapless Hamiltonian  $H_0$  the nonequilibrium Hall conductance jumps by  $\pm \frac{\pi e^2}{2h}$  whenever the final driving amplitude  $A_f$  crosses a phase boundary  $A_c$  of the effective Hamiltonian with a gap closing at the  $K$  points. Considering neutral atoms in an optical lattice instead of an electronic system the electron charge  $e$  is to be replaced by unity. If the system is instead initially prepared in a Floquet mode of the driven Hamiltonian  $H_{A_i}(t)$  the nonequilibrium Hall conductance after switching to  $A_f$  is continuous at  $A_f = A_c$ , but the derivative  $\frac{d\sigma_{xy}}{dA_f}$  diverges logarithmically.

This nonanalytic behavior is universal in the same sense as discussed in Ref. [16]. The characteristics of the nonanalyticity only depend on the conic structure of the quasienergy spectrum in the vicinity of the gap closing points and are therefore independent of other details of the model. In particular, it is expected that the behavior remains the same in the presence of weak disorder, where the winding number of the time evolution operator serves as topological invariant instead of the Chern number.

Nevertheless, at the additional frequency dependent transition points visible in Fig. 3(a) one might find different behavior if the gap-closing points have different character. This question should be addressed in future research.

Our results show that the universal nonanalytic behavior of the nonequilibrium Hall conductance carries over from closed TIs discussed in Refs. [15,16] to FTIs, which can be realized experimentally in ultracold atom setups in optical lattices with the necessary control of external parameters [7,33]. Moreover, small electric fields required to probe the Hall response can be generated in ultracold atom experiments [34]. These experiments naturally encounter a situation similar to the one considered in this paper, because in the preparation process the external driving force is usually ramped up at some point in order to bring the system from the initial topologically trivial state into the topologically nontrivial state of the driven Hamiltonian. It is, however, understood that the Chern number of a state is invariant under unitary evolution [9]. In a recent work [12] it was demonstrated how topological properties of the final Hamiltonian can nevertheless be inferred from the time-averaged nonequilibrium Hall conductance after slow but nonadiabatic ramps. Our results show that in the opposite limit of infinitely fast ramps the topological invariant determines the behavior close to transition points. In particular the jump height or the prefactor of the logarithmic divergence, respectively, are determined by the jump of the topological invariant at the transition. In future work it should be investigated, whether the behavior at infinitely long times investigated here can be found in the time-averaged Hall conductance at finite times similar to Ref. [12]. Moreover, the effect of ramping could be studied based on a high frequency expansion as presented in Ref. [35].

## ACKNOWLEDGMENTS

The authors acknowledge helpful discussions with H. Dehghani, S. Kehrein, and D. Huse and thank L. Cevolani and N. Abeling for proofreading the manuscript. M.S. acknowledges support by the Studienstiftung des Deutschen Volkes.

P.W. is supported by NSFC under Grant No. 11304280. For the numerical computations the Armadillo library [36] was used.

### APPENDIX A: RESTORING TRANSLATIONAL INVARIANCE BY A TIME-DEPENDENT GAUGE TRANSFORMATION

In order to restore translational invariance we perform a time-dependent gauge transformation with

$$W(t) = \prod_i \exp\left( i c_i^\dagger c_i \int dt V(\vec{r}_i, t) \right) \quad (\text{A1})$$

yielding

$$\begin{aligned} H(t) &= W(t) \tilde{H}(t) W^\dagger(t) - i W(t) \partial_t W^\dagger(t) \\ &= -J \sum_{\langle i,j \rangle} (e^{-i\theta_{ij}(t)} c_i^\dagger c_j + \text{H.c.}), \end{aligned} \quad (\text{A2})$$

where

$$\theta_{ij}(t) = (\vec{r}_i - \vec{r}_j) \cdot \vec{A}(t) \quad (\text{A3})$$

was introduced with

$$\vec{A}(t) = \frac{V_0 a}{\omega} \begin{pmatrix} \sin(\omega t) \\ \cos(\omega t) \end{pmatrix}, \quad (\text{A4})$$

where  $a$  denotes the lattice spacing.

Introducing explicit labels  $A$  and  $B$  for the sublattices and the Fourier transform of the operators,

$$c_{i,A/B} = \frac{1}{\sqrt{N}} \sum_{\vec{k}} e^{-i\vec{k} \cdot \vec{r}_{i,A/B}} c_{\vec{k},A/B} \quad (\text{A5})$$

yields the Hamiltonian in momentum space,

$$H(t) = -J \sum_{\vec{k}} \vec{c}_{\vec{k}}^\dagger [\vec{d}_{\vec{k}}(t) \cdot \vec{\sigma}] \vec{c}_{\vec{k}}. \quad (\text{A6})$$

In this expression for the Hamiltonian we introduced

$$\vec{c}_{\vec{k}} = \begin{pmatrix} c_{\vec{k}A} \\ c_{\vec{k}B} \end{pmatrix}, \quad (\text{A7})$$

and the coefficient vector  $\vec{d}_{\vec{k}}(t)$  is given in Eqs. (4)–(6) in the main text.

### APPENDIX B: NUMERICAL COMPUTATION OF FLOQUET MODES AND HALL CONDUCTANCE

In order to solve Eq. (25) numerically we set up the matrix  $Q$  as given in Eq. (26) truncating it at some maximal  $|m| = M$ . The diagonalization of the truncated matrix yields Floquet modes  $|\phi_{nm}\rangle$  for  $-M \leq m \leq M$  and corresponding quasienergies with the property  $\epsilon_{nm} = \epsilon_{n0} + m\omega$  for small  $|m|$ . The best approximation for the eigenvector of the infinite matrix is obtained in the middle of the spectrum, i.e., for  $m = 0$ .

For the two-band system under consideration we obtain a solution at every  $\vec{k}$  point and the solutions can be written as

vectors with  $2(2M + 1)$  components

$$\vec{\phi}_{\vec{k},M}^{\alpha m} \equiv |\phi_{\vec{k}}^{\alpha m}\rangle = \begin{pmatrix} \phi_{\vec{k},(u,M)}^{\alpha m} \\ \phi_{\vec{k},(d,M)}^{\alpha m} \\ \phi_{\vec{k},(u,M-1)}^{\alpha m} \\ \vdots \\ \phi_{\vec{k},(d,-M)}^{\alpha m} \end{pmatrix}. \quad (\text{B1})$$

The best approximation to the time-dependent Floquet mode  $|u_{\vec{k}}^\alpha(t)\rangle \in \mathbb{C}^2$  is then given by

$$|\phi_{\vec{k}}^\alpha(t)\rangle = \sum_{\beta \in \{u,d\}} \sum_{n=-M}^M e^{in\omega t} \phi_{\vec{k},(\beta,n)}^{\alpha 0} |\beta\rangle. \quad (\text{B2})$$

Plugging Eq. (B2) into Eq. (34) yields

$$\begin{aligned} \bar{F}_{\vec{k}} &= \int_0^T \frac{dt}{T} \sum_{\alpha,\alpha'} \sum_{n,n'} \langle \alpha | e^{-in\omega t} \partial_x (\phi_{\vec{k},(\alpha,n)}^{d0})^* \partial_y (\phi_{\vec{k},(\alpha',n')}^{d0}) e^{in'\omega t} | \alpha' \rangle \\ &= \sum_{\alpha,\alpha'} \sum_{n,n'} \partial_x (\phi_{\vec{k},(\alpha,n)}^{d0})^* \partial_y (\phi_{\vec{k},(\alpha',n')}^{d0}) \underbrace{\langle \alpha | \alpha' \rangle}_{\delta_{\alpha\alpha'}} \underbrace{\int_0^T c_0^T \frac{dt}{T} e^{i(n'-n)\omega t}}_{\delta_{nn'}} \\ &= \sum_{\alpha} \sum_n \partial_x (\phi_{\vec{k},(\alpha,n)}^{d0})^* \partial_y (\phi_{\vec{k},(\alpha,n)}^{d0}) = (\partial_x \vec{\phi}_{\vec{k},M}^{d0}) \cdot (\partial_y \vec{\phi}_{\vec{k},M}^{d0}). \end{aligned} \quad (\text{B3})$$

This means it is not necessary to perform the time averaging for the averaged Berry curvature explicitly. The derivatives can be approximated as difference quotients. This procedure yields a numerical approximation for  $\bar{F}_{\vec{k}}$  on a grid of  $\vec{k}$  points. Choosing this grid appropriately the Hall conductance (33) can be computed efficiently using the method introduced in Ref. [37] as already established by Dehghani *et al.* [10].

### APPENDIX C: DERIVATION OF TIME DEPENDENT MODE OCCUPATION NUMBERS

The first order term of the high frequency expansion of the kick operator is

$$\mathcal{K}^{(1)}(t) = -i \sum_{m=1}^{\infty} \frac{e^{im\omega t} H_m - e^{-im\omega t} H_{-m}}{m}. \quad (\text{C1})$$

Note that in this formula we dropped the explicit  $\vec{k}$  dependence in the notation, which we will do also in the rest of this section wherever it is not relevant in order to keep the notation clear.

We approximate the micromotion operator with

$$U_F(t) = \exp(-i\mathcal{K}^{(1)}(t)/\omega) + \mathcal{O}(\omega^{-2}) \quad (\text{C2})$$

and define  $\vec{g}(t) = (g_x(t), g_y(t), g_z(t))$  via

$$-\mathcal{K}^{(1)}(t) = g_x(t)\sigma^x + g_y(t)\sigma^y + g_z(t)\sigma^z. \quad (\text{C3})$$

Note that according to Eq. (C1)  $g_z(t) = 0$  to first order in  $1/\omega$ . The expression for  $\mathcal{K}^{(1)}(t)$  as a sum of Pauli matrices allows us to rewrite the micromotion operator as

$$\begin{aligned} \exp(-i\mathcal{K}^{(1)}(t)) &= \exp[ig(t)(\vec{n}(t) \cdot \vec{\sigma})] \\ &= \cos(g(t)) + i \sin(g(t))(\vec{n}(t) \cdot \vec{\sigma}) \end{aligned} \quad (\text{C4})$$

with

$$\vec{n}(t) = \frac{\vec{g}(t)}{g(t)}, \quad g(t) = |\vec{g}(t)|. \quad (\text{C5})$$

Plugging this expression for the micromotion operator into Eq. (21) we obtain the overlaps of Floquet modes,

$$\langle \phi_0^d(t) | \phi^\alpha(t) \rangle = \langle u_0^d | [\cos(g_0(t)) - i \sin(g_0(t))(\vec{n}_0 \cdot \vec{\sigma})] \times [\cos(g(t)) + i \sin(g(t))(\vec{n} \cdot \vec{\sigma})] | u^\alpha \rangle \quad (\text{C6})$$

$$\begin{aligned} &= \langle u_0^d | u^\alpha \rangle \cos(g_0(t)) \cos(g(t)) \\ &+ \sin(g_0(t)) \sin(g(t)) \langle u_0^d | (\vec{n}_0 \cdot \vec{\sigma})(\vec{n} \cdot \vec{\sigma}) | u^\alpha \rangle \\ &- i \sin(g_0(t)) \cos(g(t)) \langle u_0^d | \vec{n}_0 \cdot \vec{\sigma} | u^\alpha \rangle \\ &+ i \cos(g_0(t)) \sin(g(t)) \langle u_0^d | \vec{n} \cdot \vec{\sigma} | u^\alpha \rangle, \quad (\text{C7}) \end{aligned}$$

where the index 0 indicates Floquet modes/micromotion operator of the initial Hamiltonian with driving amplitude  $A_0$ . To evaluate this we need the eigenstates of the effective Hamiltonian  $H_{F\vec{k}} = \vec{h}_{\vec{k}} \cdot \vec{\sigma}$ , which read

$$|u_{\vec{k}}^{u/d}\rangle = \sqrt{\frac{h_{xz}^2 + h_{ky}^2}{2|\vec{h}_{\vec{k}}|(|\vec{h}_{\vec{k}}| \pm h_{kz})}} \begin{pmatrix} \frac{h_{kx} \pm i h_{ky}}{1} \\ 1 \end{pmatrix}. \quad (\text{C8})$$

These yield the overlaps

$$\Gamma_1^\alpha \equiv \langle u_0^d | u^\alpha \rangle = \frac{1 + \frac{h_z^0 - |\vec{h}_0|}{h_x^0 - i h_y^0} \frac{h_z \pm |\vec{h}|}{h_x + i h_y}}{\mathcal{N}_\alpha} \quad (\text{C9})$$

$$\Gamma_x^\alpha \equiv \langle u_0^d | \sigma^x | u^\alpha \rangle = \frac{\frac{h_z^0 - |\vec{h}_0|}{h_x^0 - i h_y^0} + \frac{h_z \pm |\vec{h}|}{h_x + i h_y}}{\mathcal{N}_\alpha} \quad (\text{C10})$$

$$\Gamma_y^\alpha \equiv \langle u_0^d | \sigma^y | u^\alpha \rangle = -i \frac{\frac{h_z^0 - |\vec{h}_0|}{h_x^0 - i h_y^0} - \frac{h_z \pm |\vec{h}|}{h_x + i h_y}}{\mathcal{N}_\alpha}, \quad (\text{C11})$$

where

$$\mathcal{N}_\alpha^{-1} = \sqrt{\frac{(h_x^2 + h_y^2)(h_x^2 + h_y^2)}{4|\vec{h}_0| |\vec{h}| (|\vec{h}_0| - h_z^0) (|\vec{h}| \pm h_z)}}. \quad (\text{C12})$$

Then

$$\begin{aligned} &\langle \phi_0^d(t) | \phi^\alpha(t) \rangle \\ &= \Gamma_1^\alpha [\cos(g_0) \cos(g) + \sin(g_0) \sin(g) (n_0^x n^x + n_0^y n^y)] \\ &+ i \Gamma_z^\alpha \sin(g_0) \sin(g) (n_0^x n^y - n_0^y n^x) \\ &- i \sin(g_0) \cos(g) (n_0^x \Gamma_x^\alpha + n_0^y \Gamma_y^\alpha) \\ &+ i \cos(g_0) \sin(g) (n^x \Gamma_x^\alpha + n^y \Gamma_y^\alpha) \\ &= \Gamma_1^\alpha [\cos(g_0) \cos(g) + \sin(g_0) \sin(g) (n_0^x n^x + n_0^y n^y)] \\ &+ i \Gamma_y^\alpha (\cos(g_0) \sin(g) n^y - \sin(g_0) \cos(g) n_0^y) \\ &+ i \Gamma_x^\alpha (\cos(g_0) \sin(g) n^x - \sin(g_0) \cos(g) n_0^x) \\ &+ i \Gamma_z^\alpha \sin(g_0) \sin(g) (n_0^x n^y - n_0^y n^x). \quad (\text{C13}) \end{aligned}$$

Since  $g, g_0 \sim \mathcal{O}(\omega^{-1})$ , we approximate  $\cos(g) \approx 1$  and  $\sin(g) \approx g$  and drop all terms of  $\mathcal{O}(\omega^{-2})$ , which yields

$$\begin{aligned} &\langle \phi_0^d(t) | \phi^\alpha(t) \rangle \\ &= \Gamma_1^\alpha + i \Gamma_y^\alpha (g(t) n^y(t) - g_0(t) n_0^y(t)) \\ &+ i \Gamma_x^\alpha (g(t) n^x(t) - g_0(t) n_0^x(t)) \\ &= \Gamma_1^\alpha + i \Gamma_y^\alpha \underbrace{(g_y(t) - g_y^0(t))}_{\equiv \Delta g_y(t)} + i \Gamma_x^\alpha \underbrace{(g_x(t) - g_x^0(t))}_{\equiv \Delta g_x(t)}. \quad (\text{C14}) \end{aligned}$$

Then, again omitting terms quadratic in  $1/\omega$ ,

$$\begin{aligned} &|\langle \phi_0^d(t) | \phi^\alpha(t) \rangle|^2 \\ &= (\Gamma_1^\alpha + i \Gamma_y^\alpha \Delta g_y(t) + i \Gamma_x^\alpha \Delta g_x(t)) \\ &\times (\Gamma_1^{\alpha*} - i \Gamma_y^{\alpha*} \Delta g_y(t) - i \Gamma_x^{\alpha*} \Delta g_x(t)) \\ &= |\Gamma_1^\alpha|^2 - \text{Im} [\Gamma_1^{\alpha*} \Gamma_x^\alpha] \Delta g_x(t) - \text{Im} [\Gamma_1^{\alpha*} \Gamma_y^\alpha] \Delta g_y(t). \quad (\text{C15}) \end{aligned}$$

In the end we are interested in

$$\begin{aligned} &|\langle \phi_0^d(t) | \phi^d(t) \rangle|^2 - |\langle \phi_0^d(t) | \phi^u(t) \rangle|^2 \\ &= (|\Gamma_1^d|^2 - |\Gamma_1^u|^2) - (\text{Im} [\Gamma_1^{d*} \Gamma_x^d] - \text{Im} [\Gamma_1^{u*} \Gamma_x^u]) \Delta g_x(t) \\ &- (\text{Im} [\Gamma_1^{d*} \Gamma_y^d] - \text{Im} [\Gamma_1^{u*} \Gamma_y^u]) \Delta g_y(t). \quad (\text{C16}) \end{aligned}$$

The different contributions to the overlaps are

$$|\Gamma_1^d|^2 - |\Gamma_1^u|^2 = \frac{\vec{d}_0 \cdot \vec{d}}{|d| |d_0|} \quad (\text{C17})$$

$$\text{Im} [\Gamma_1^{d*} \Gamma_x^d] - \text{Im} [\Gamma_1^{u*} \Gamma_x^u] = \frac{d_y d_z^0 - d_y^0 d_z}{|d| |d_0|} \quad (\text{C18})$$

$$\text{Im} [\Gamma_1^{d*} \Gamma_y^d] - \text{Im} [\Gamma_1^{u*} \Gamma_y^u] = \frac{d_x^0 d_z - d_x d_z^0}{|d| |d_0|}. \quad (\text{C19})$$

Since  $\Delta g_z(t) = 0$ , we can finally write

$$\begin{aligned} &|\langle \phi_0^d(t) | \phi^d(t) \rangle|^2 - |\langle \phi_0^d(t) | \phi^u(t) \rangle|^2 \\ &= \frac{\vec{h}_0 \cdot \vec{h}}{|\vec{h}| |h_0|} + \frac{(\vec{h}_0 \times \vec{h}) \cdot \Delta \vec{g}(t)}{|\vec{h}| |h_0|} + \mathcal{O}(\omega^{-2}). \quad (\text{C20}) \end{aligned}$$

#### APPENDIX D: PARTIALLY FILLED BANDS

In this section we derive the leading contribution to

$$\begin{aligned} &\sin(2\theta_{\vec{k}}) \text{Re} [e^{i\varphi_{\vec{k}}(t)} (\langle \phi_{0\vec{k}}^d(t) | \phi_{\vec{k}}^d(t) \rangle \langle \phi_{\vec{k}}^d(t) | \phi_{0\vec{k}}^u(t) \rangle) \\ &- \langle \phi_{0\vec{k}}^d(t) | \phi_{\vec{k}}^u(t) \rangle \langle \phi_{\vec{k}}^u(t) | \phi_{0\vec{k}}^d(t) \rangle] \quad (\text{D1}) \end{aligned}$$

which is a part of the occupation difference when quenching from partially filled Floquet bands given in Eq. (80) in the main text. For the sake of brevity we will drop the explicit  $\vec{k}$  dependence in the notation wherever it is not relevant in the following.

The derivation is analogous to the one given in Appendix C. We generalize the expressions for the overlaps (C9)–(C11) to

$$\Gamma_1^{\alpha\beta} = \langle u_0^\alpha | u^\beta \rangle = \frac{1}{\mathcal{N}_{\alpha\beta}} \left( 1 + \frac{h_z^0 \pm h_0}{h_x^0 - i h_y^0} \frac{h_z \pm h}{h_x + i h_y} \right) \quad (\text{D2})$$

$$\Gamma_x^{\alpha\beta} = \langle u_0^\alpha | \sigma^x | u^\beta \rangle = \frac{1}{\mathcal{N}_{\alpha\beta}} \left( \frac{h_z^0 \pm h_0}{h_x^0 - ih_y^0} + \frac{h_z \pm h}{h_x + ih_y} \right) \quad (\text{D3})$$

$$\Gamma_y^{\alpha\beta} = \langle u_0^\alpha | \sigma^y | u^\beta \rangle = -i \frac{1}{\mathcal{N}_{\alpha\beta}} \left( \frac{h_z^0 \pm h_0}{h_x^0 - ih_y^0} - \frac{h_z \pm h}{h_x + ih_y} \right) \quad (\text{D4})$$

with

$$\mathcal{N}_{\alpha\beta} = \sqrt{\frac{(h_x^2 + h_y^2)(h_x^{02} + h_y^{02})}{4hh_0(h_0 \pm h_z^0)(h \pm h_z)}}. \quad (\text{D5})$$

In the expressions above  $\alpha$  is always associated with the first  $\pm$  and  $\beta$  with the second. For the overlaps in Eq. (D1) this yields

$$\begin{aligned} & \langle \phi_{0\bar{k}}^d(t) | \phi_{\bar{k}}^d(t) \rangle \langle \phi_{\bar{k}}^d(t) | \phi_{0\bar{k}}^u(t) \rangle - \langle \phi_{0\bar{k}}^d(t) | \phi_{\bar{k}}^u(t) \rangle \langle \phi_{\bar{k}}^u(t) | \phi_{0\bar{k}}^d(t) \rangle \\ &= (\Gamma_1^{dd} + i\Gamma_x^{dd} \Delta g_x(t) + i\Gamma_y^{dd} \Delta g_y(t)) \\ & \quad \times (\Gamma_1^{ud*} - i\Gamma_x^{ud*} \Delta g_x(t) - i\Gamma_y^{ud*} \Delta g_y(t)) \\ & \quad - (\Gamma_1^{du} + i\Gamma_x^{du} \Delta g_x(t) + i\Gamma_y^{du} \Delta g_y(t)) \\ & \quad \times (\Gamma_1^{uu*} - i\Gamma_x^{uu*} \Delta g_x(t) - i\Gamma_y^{uu*} \Delta g_y(t)) \\ &= \frac{h_z^0(h_x^0 h_x + h_y^0 h_y) + ih_0(h_x^0 h_y - h_y^0 h_x)}{hh_0 \sqrt{h_x^{02} + h_y^{02}}} \\ & \quad - \frac{4h_z}{hh_0 \sqrt{h_x^{02} + h_y^{02}}} [h_z^0 h_y^0 + ih_0 h_x^0] \Delta g_x(t) \\ & \quad + \frac{4h_z}{hh_0 \sqrt{h_x^{02} + h_y^{02}}} [h_z^0 h_x^0 - ih_0 h_y^0] \Delta g_y(t) + \mathcal{O}(\omega^{-2}), \end{aligned} \quad (\text{D6})$$

where second order terms were omitted.

We consider the first term, which is frequency independent. When the linearization around the gap closing point given in Eqs. (63)–(65) is plugged in, the imaginary part vanishes. For the real part we can approximate  $h_0 \approx h_0^z$  close to the gap closing point. Thereby we obtain

$$\frac{h_x^0 h_x + h_y^0 h_y}{h \sqrt{h_x^{02} + h_y^{02}}}. \quad (\text{D7})$$

The contribution of this part of the occupation to the Hall conductance is

$$\begin{aligned} \sigma_{xy}^{(2)} &= \int \frac{d^2 k}{4\pi} \sin(2\theta_{\bar{k}}) \cos(\varphi_{\bar{k}}(t)) \\ & \quad \times \frac{h_{kx}^0 h_{kx} + h_{ky}^0 h_{ky}}{\sqrt{h_{kx}^{02} + h_{ky}^{02}}} \frac{(\partial_x \vec{h}_{\bar{k}} \times \partial_y \vec{h}_{\bar{k}}) \vec{h}_{\bar{k}}}{h_{\bar{k}}^4}. \end{aligned} \quad (\text{D8})$$

Assuming  $\sin(2\theta_{\bar{k}}) \cos(\varphi_{\bar{k}}(t))$  well behaved in the vicinity of the gap closing point  $\vec{k}_0$ , we can approximate

$$\begin{aligned} \sigma_{xy}^{(2)} &= \sin(2\theta_{\vec{k}_0}) \cos(\varphi_{\vec{k}_0}(t)) \\ & \quad \times \int \frac{d^2 k}{4\pi} \frac{h_{kx}^0 h_{kx} + h_{ky}^0 h_{ky}}{\sqrt{h_{kx}^{02} + h_{ky}^{02}}} \frac{(\partial_x \vec{h}_{\bar{k}} \times \partial_y \vec{h}_{\bar{k}}) \vec{h}_{\bar{k}}}{h_{\bar{k}}^4} \end{aligned} \quad (\text{D9})$$

and then the integral is the same one gets when quenching from a gapless initial state, which is discussed in Sec. III C 1 of the main text. This means that partially filled initial states add a jump to the Hall conductance at the transition. But through the  $\cos(\varphi_{\vec{k}_0}(t))$  factor the jump oscillates as a function of the quench time with frequency equal to the initial gap  $2m(A_i)$ .

- 
- [1] K. V. Klitzing, G. Dorda, and M. Pepper, *Phys. Rev. Lett.* **45**, 494 (1980).
- [2] D. J. Thouless, M. Kohmoto, M. P. Nightingale, and M. den Nijs, *Phys. Rev. Lett.* **49**, 405 (1982).
- [3] F. D. M. Haldane, *Phys. Rev. Lett.* **61**, 2015 (1988).
- [4] M. Z. Hasan and C. L. Kane, *Rev. Mod. Phys.* **82**, 3045 (2010).
- [5] T. Oka and H. Aoki, *Phys. Rev. B* **79**, 081406 (2009).
- [6] T. Kitagawa, T. Oka, A. Brataas, L. Fu, and E. Demler, *Phys. Rev. B* **84**, 235108 (2011).
- [7] G. Jotzu, M. Messer, R. Desbuquois, M. Lebrat, T. Uehlinger, D. Greif, and T. Esslinger, *Nature (London)* **515**, 237 (2014).
- [8] T. Kitagawa, E. Berg, M. Rudner, and E. Demler, *Phys. Rev. B* **82**, 235114 (2010).
- [9] L. D'Alessio and M. Rigol, *Nat. Commun.* **6**, 8336 (2015).
- [10] H. Dehghani, T. Oka, and A. Mitra, *Phys. Rev. B* **91**, 155422 (2015).
- [11] J. C. Budich and M. Heyl, *Phys. Rev. B* **93**, 085416 (2016).
- [12] Y. Hu, P. Zoller, and J. C. Budich, *Phys. Rev. Lett.* **117**, 126803 (2016).
- [13] M. D. Caio, N. R. Cooper, and M. J. Bhaseen, *Phys. Rev. B* **94**, 155104 (2016).
- [14] M. S. Rudner, N. H. Lindner, E. Berg, and M. Levin, *Phys. Rev. X* **3**, 031005 (2013).
- [15] P. Wang and S. Kehrein, *New J. Phys.* **18**, 053003 (2016).
- [16] P. Wang, M. Schmitt, and S. Kehrein, *Phys. Rev. B* **93**, 085134 (2016).
- [17] L. Jiang, T. Kitagawa, J. Alicea, A. R. Akhmerov, D. Pekker, G. Refael, J. I. Cirac, E. Demler, M. D. Lukin, and P. Zoller, *Phys. Rev. Lett.* **106**, 220402 (2011).
- [18] T. Kitagawa, M. A. Broome, A. Fedrizzi, M. S. Rudner, E. Berg, I. Kassel, A. Aspuru-Guzik, E. Demler, and A. G. White, *Nat. Commun.* **3**, 882 (2012).
- [19] J. Karch, P. Olbrich, M. Schmalzbauer, C. Zoth, C. Brinsteiner, M. Fehrenbacher, U. Wurstbauer, M. M. Glazov, S. A. Tarasenko, E. L. Ivchenko, D. Weiss, J. Eroms, R. Yakimova, S. Lara-Avila, S. Kubatkin, and S. D. Ganichev, *Phys. Rev. Lett.* **105**, 227402 (2010).
- [20] A. Eckardt and E. Anisimovas, *New J. Phys.* **17**, 093039 (2015).
- [21] M. Bukov, L. D'Alessio, and A. Polkovnikov, *Adv. Phys.* **64**, 139 (2015).
- [22] G. Floquet, *Ann. Scient. Ec. Norm. Sup.* **12**, 47 (1883).
- [23] J. H. Shirley, *Phys. Rev.* **138**, B979 (1965).
- [24] N. Goldman and J. Dalibard, *Phys. Rev. X* **4**, 031027 (2014).

- [25] H. Sambe, *Phys. Rev. A* **7**, 2203 (1973).
- [26] F. N. Ünal, E. J. Mueller, and M. O. Oktel, *Phys. Rev. A* **94**, 053604 (2016).
- [27] S.-Q. Shen, *Topological Insulators* (Springer, Berlin, 2012).
- [28] R. M. Wilcox, *J. Math. Phys.* **8**, 962 (1967).
- [29] P. Weinberg, M. Bukov, L. D'Alessio, A. Polkovnikov, S. Vajna, and M. Kolodrubetz, *Phys. Rep.* **688**, 1 (2017).
- [30] P. Titum, N. H. Lindner, M. C. Rechtsman, and G. Refael, *Phys. Rev. Lett.* **114**, 056801 (2015).
- [31] S. Roy and G. J. Sreejith, *Phys. Rev. B* **94**, 214203 (2016).
- [32] P. Titum, E. Berg, M. S. Rudner, G. Refael, and N. H. Lindner, *Phys. Rev. X* **6**, 021013 (2016).
- [33] N. Fläschner, B. S. Rem, M. Tarnowski, D. Vogel, D.-S. Lühmann, K. Sengstock, and C. Weitenberg, *Science* **352**, 1091 (2016).
- [34] M. Aidelsburger, M. Lohse, C. Schweizer, M. Atala, J. T. Barreiro, S. Nascimbene, N. R. Cooper, I. Bloch, and N. Goldman, *Nat. Phys.* **11**, 162 (2015).
- [35] V. Novičenko, E. Anisimovas, and G. Juzeliūnas, *Phys. Rev. A* **95**, 023615 (2017).
- [36] C. Sanderson and R. Curtin, *J. Open Source Softw.* **1**, 26 (2016).
- [37] T. Fukui, Y. Hatsugai, and H. Suzuki, *J. Phys. Soc. Jpn.* **74**, 1674 (2005).

# Chapter 3

## Quantum dynamics from classical networks

As it was outlined in Section 1.3 the efficient numerical treatment of quantum many-body systems is a great challenge – beyond equilibrium even more than in equilibrium. Due to the exponential growth of the Hilbert space dimension the exact treatment based on a full uncompressed representation of the wave function becomes prohibitively expensive already at small system sizes. Over the past decades two particularly notable versatile approaches have been developed, which facilitate the treatment of large classes of many-body systems within their respective frameworks, namely the Density Matrix Renormalization Group (DMRG) including related algorithms based on matrix product states (MPS) and Dynamical Mean Field Theory (DMFT). The nonequilibrium extensions of these methods are reliable tools to compute real time dynamics in one dimension (DMRG) or three and more dimensions (DMFT). In two dimensions, however, DMRG quickly becomes very expensive due to the exponential cost of encoding entanglement and the applicability of DMFT is questionable, because it relies on a high connectivity. In this chapter an alternative approach for the efficient representation of many-body wave functions is explored, namely the encoding in networks of classical degrees of freedom, which could potentially bridge the gap between low and high dimensions.

In the first part of this chapter (Section 3.1) the two numerical methods that will be used in Chapter 4, namely exact diagonalization and infinite Time Evolving Block Decimation (iTEBD)<sup>1</sup>, are introduced. The intention is to illustrate the strengths and limitations of these methods and to sketch their way of functioning for technical nonexperts. Moreover, in Section 3.1.3 recent developments regarding classical network wave functions, which are relevant for this work, are summarized. In Section 3.2 a new way to construct classical networks to encode quantum dynamics based on a perturbative approach is introduced and applied to study the dynamics of transverse-field Ising models in one, two, and three dimensions as a benchmark.

---

<sup>1</sup>iTEBD is an algorithm for (imaginary) time evolution based on Matrix Product States.



## 3.1 State of the art methods in wave-function-based quantum many-body numerics

This section comprises minimal introductions to exact diagonalization and iTEBD, a MPS-based time-evolution algorithm. For more detailed descriptions the reader is referred to the literature, e.g. (Sandvik, 2010) for exact diagonalization and (Schollwöck, 2011; Kjäll *et al.*, 2013) for DMRG in general and the iTEBD algorithm. For the sake of simplicity the focus is in the following on spin-1/2 systems, but in all cases the generalization to larger dimensions of the local Hilbert spaces is possible.

### 3.1.1 Exact dynamics in the full Hilbert space

In the following we will consider the XXZ Hamiltonian on two lattice sites,

$$\hat{H} = \frac{J}{2}(\hat{S}_1^+ \hat{S}_2^- + \hat{S}_1^- \hat{S}_2^+) + J_z \hat{S}_1^z \hat{S}_2^z, \quad (3.1)$$

to exemplify the key ingredients of an exact diagonalization algorithm.

#### The computational representation and exact diagonalization

The footing of exact diagonalization algorithms is a suited representation of the computational basis. In a spin-1/2 system a common choice is to construct the basis from the local eigenbasis of the  $\hat{S}_z$  operators. These basis states can be encoded very efficiently in a computer using the bit representation of integer variables and identifying  $|\downarrow\rangle \equiv 0$  and  $|\uparrow\rangle \equiv 1$ . A central benefit of this representation is that any physical representation is in a very simple manner related to an index, e.g.  $|\uparrow\downarrow\rangle \equiv 10 \equiv 2$ , which allows for efficient searches in the basis list. The following table displays the basis representation of the Hilbert space of two spins,  $\mathcal{H} = \mathbb{C}^2$ :

Basis state	Physical configuration	Integer (index)	Bit representation	Column vector
$ b_0\rangle$	$ \downarrow\rangle \otimes  \downarrow\rangle$	0	00	$(1, 0, 0, 0)^t$
$ b_1\rangle$	$ \downarrow\rangle \otimes  \uparrow\rangle$	1	01	$(0, 1, 0, 0)^t$
$ b_2\rangle$	$ \uparrow\rangle \otimes  \downarrow\rangle$	2	10	$(0, 0, 1, 0)^t$
$ b_3\rangle$	$ \uparrow\rangle \otimes  \uparrow\rangle$	3	11	$(0, 0, 0, 1)^t$

Once a basis list is set up the matrix elements  $\langle b_i | \hat{H} | b_j \rangle$  can be figured out by considering the action of the constituents of the Hamiltonian on the basis representation. This yields a matrix representation of the Hamiltonian, which in the case of our example system is

$$\hat{H} \equiv \mathbf{H} = \begin{pmatrix} J_z/4 & 0 & 0 & 0 \\ 0 & -J_z/4 & J/2 & 0 \\ 0 & J/2 & -J_z/4 & 0 \\ 0 & 0 & 0 & J_z/4 \end{pmatrix}. \quad (3.2)$$

The resulting matrix is readily diagonalized by standard numerical algorithms yielding the eigenbasis  $\{|E_i\rangle\}$  with corresponding eigenenergies  $\{E_i\}$ . On that basis it is straightforward to compute the time evolution of a state  $|\psi_0\rangle$ ,

$$|\psi(t)\rangle = e^{-i\hat{H}t} |\psi_0\rangle = \sum_i e^{-iE_i t} \langle E_i | \psi_0 \rangle |E_i\rangle . \quad (3.3)$$

The result for  $|\psi(t)\rangle$  obtained in this way is exact for all times. Moreover, it is possible to extract the expectation values of arbitrary observables by considering representations of the corresponding operators in the computational basis.

Clearly, the maximal system size that can be treated in this way is, however, limited by the available computational resources. The dimension of the Hilbert space to describe a system of size  $N$  is  $D = d^N$ , where  $d$  is the dimension of the local Hilbert space. Hence, storing a matrix representation of a Hamiltonian naively means storing  $D^2 = d^{2N}$  numbers in memory. Assuming the matrix elements are all real and stored with double precision the Hamiltonian matrix of a spin-1/2 system with  $N = 14$  lattice sites already requires almost 2.2 Gigabytes of memory. Also the computational cost to diagonalize the matrix grows exponentially, because it is polynomial in the matrix dimensions.

The numerical expense can be diminished by taking symmetries of the Hamiltonian into account. A symmetry that leads to an obvious signature in the Hamiltonian matrix (3.2) is the  $U(1)$  symmetry that implies the conservation of total magnetization,  $[\hat{H}, \hat{S}_1^z + \hat{S}_2^z] = 0$ . Accordingly, the Hamiltonian has block form and the Hilbert space can be split into a direct sum of symmetry sectors  $\mathcal{H} = \mathcal{H}_{S=1} \oplus \mathcal{H}_{S=0} \oplus \mathcal{H}_{S=-1}$ . As a consequence the single blocks can be treated separately, which reduces the computational cost.

Note that in our example the Hamiltonian on the  $S = 0$  sector is moreover symmetric under global spin flip. This can be accounted for by choosing alternative basis states  $|\tilde{b}_{1/2}\rangle = (|b_1\rangle \pm |b_2\rangle)/\sqrt{2}$ , which are eigenstates of the spin flip operator  $\hat{\sigma}_1^x \otimes \hat{\sigma}_2^x$ . Thereby, an additional block structure is revealed in the  $S = 0$  sector; in fact, a full diagonalization of the Hamiltonian is obtained based just on symmetry considerations. Other symmetries that can lead to a simplification of the problem are lattice inversion symmetry and translational invariance in the presence of periodic boundary conditions; see (Sandvik, 2010) for details.

## Krylow space methods

A family of algorithms based on exact representations of the many-body Hilbert space that allow to reduce both the memory demand and the computational complexity are so-called Krylow space methods. In particular, Lanczos algorithms allow to compute the low energy part of the spectrum or time evolution (Lanczos, 1950; Park and Light, 1986). In the following the iterative Lanczos method is sketched, which is applied within this thesis to compute echo dynamics in Chapter 4.

For a given Hamiltonian  $\hat{H}$  the evolution of a state  $|\psi\rangle$  for a time  $\delta t$  can be written in a series expansion, for which at small  $\delta t$  a truncation at the  $M$ -th power is a good approxima-

tion,

$$e^{-i\hat{H}\delta t} |\psi\rangle = \sum_{n=0}^{\infty} \frac{(-i\delta t)^n}{n!} \hat{H}^n |\psi\rangle \approx \sum_{n=0}^M \frac{(-i\delta t)^n}{n!} \hat{H}^n |\psi\rangle . \quad (3.4)$$

This shows that up to corrections of  $\mathcal{O}(\delta t^{N+1})$  the time-evolved state is contained in the Krylow subspace  $\mathcal{K}_M = \text{span}\{|\psi\rangle, \hat{H}|\psi\rangle, \hat{H}^2|\psi\rangle, \dots, \hat{H}^M|\psi\rangle\}$ . In the Lanczos algorithm an orthonormal basis  $\{|l_1\rangle, \dots, |l_M\rangle\}$  of this subspace is constructed such that

$$(\mathbf{H}_M)_{ij} \equiv \langle l_i | \hat{H} | l_j \rangle \quad (3.5)$$

is a tridiagonal matrix of dimensions  $M \times M$ . Diagonalization of this matrix yields the spectrum  $\epsilon_n$  and the corresponding eigenvectors  $|n\rangle\rangle$ . Here the notation  $|\cdot\rangle\rangle$  was introduced for vectors that are regarded as elements of the Krylow space. With this the time evolution operator is approximated as

$$e^{-i\hat{H}\delta t} \approx \sum_{i,j,n} e^{-i\epsilon_n \delta t} \langle\langle l_i | n \rangle\rangle \langle\langle n | l_j \rangle\rangle |l_i\rangle \langle l_j| , \quad (3.6)$$

which conserves the unitarity of the time evolution.

In order to compute the dynamics the desired time interval is split into small time steps  $\delta t$  and the Lanczos procedure is iteratively applied. Control parameters of the approximation are the time step  $\delta t$  and the Krylow space dimension  $M$ ; it is important to check the convergence of the results to ensure accuracy. For the problems treated with this approach later in this thesis the required Krylow space dimension lay between five and ten meaning that the computational cost for the diagonalization of  $(\mathbf{H}_M)_{ij}$  is negligible. Instead the iterated application of the Hamiltonian in order to construct the subspace constitutes the computationally most intense part of this algorithm. In contrast to exact diagonalization, which requires dense storage of the Hamiltonian matrix, this can be implemented quite memory efficiently by using a sparse matrix format or computing the matrix elements on the fly.

### 3.1.2 Matrix product states

The matrix product state (MPS) formulation of many-body wave-functions constitutes an efficient parametrization for states with weak and moderate entanglement. Due to the area law of entanglement the MPS representation is well suited to treat ground states in one-dimensional systems. Moreover, the dynamics starting from a weakly entangled state can be captured with MPS as long as the entanglement remains moderate. In the following the basics of the MPS formalism are outlined before the iTEBD algorithm for time evolution in an infinite translationally invariant system is introduced.

#### Schmidt decomposition

A fundamental ingredient for the MPS formalism is the *Schmidt decomposition*. For a vector  $|\psi\rangle$ , which is an element of a composite Hilbert space  $\mathcal{H} = \mathcal{H}_1 \otimes \mathcal{H}_2$ , and Hilbert space

dimensions  $\dim(\mathcal{H}_1) = m$  and  $\dim(\mathcal{H}_2) = n$  with  $m \leq n$  there exist vectors  $\{|u_1\rangle, \dots, |u_m\rangle\} \in \mathcal{H}_1$  and  $\{|v_1\rangle, \dots, |v_m\rangle\} \in \mathcal{H}_2$ , which are pairwise orthonormal,  $\langle u_i | u_j \rangle = \delta_{ij}$  and  $\langle v_i | v_j \rangle = \delta_{ij}$ , and a nonnegative set of real numbers  $\Lambda_1 \geq \Lambda_2 \geq \dots \geq \Lambda_m \geq 0$  such that

$$|\psi\rangle = \sum_{i=1}^m \Lambda_i |u_i\rangle \otimes |v_i\rangle . \quad (3.7)$$

The  $\Lambda_i$  are commonly referred to as Schmidt coefficients. A proof of this statement as well as any practical implementation on a computer rely on the singular value decomposition: For any  $m \times n$ -matrix  $M$  there is a decomposition

$$M = U \Sigma V \quad (3.8)$$

with  $U$  a unitary  $m \times m$ -matrix,  $V$  a unitary  $n \times n$  matrix, and  $\Sigma$  a diagonal  $m \times n$ -matrix.

The Schmidt decomposition has a close connection to entanglement entropy. Assuming  $\mathcal{H}_1$  is the Hilbert space of subsystem  $A$  and  $\mathcal{H}_2$  the Hilbert space of subsystem  $B$  the reduced density matrix of subsystem  $A$  is

$$\hat{\rho}_A = \text{tr}_B (|\psi\rangle\langle\psi|) = \sum_{i=1}^m \Lambda_i^2 |u_i\rangle\langle u_i| \quad (3.9)$$

and, therefore, the von Neumann entropy of entanglement is directly given by the Schmidt coefficients,

$$S_A = - \sum_{i=1}^m \Lambda_i^2 \log_2 \Lambda_i^2 . \quad (3.10)$$

This property plays a crucial role for the controlled compression of the MPS representation of a state  $|\psi\rangle$ .

## Matrix product states

For any state

$$|\psi\rangle = \sum_{i_1, \dots, i_N=1}^p C_{i_1, \dots, i_N} |i_1\rangle \otimes \dots \otimes |i_N\rangle . \quad (3.11)$$

of a one-dimensional system with local Hilbert space dimension  $p$  and local basis  $\{|i\rangle\}_{i=1}^p$  the wave function coefficients can by successive Schmidt decompositions be written as

$$C_{i_1, \dots, i_N} = \sum_{\alpha_1=1}^p \sum_{\alpha_2=1}^{p^2} \dots \sum_{\alpha_n=1}^{\min(p^n, p^{N-n})} \dots \sum_{\alpha_N=1}^p \Gamma_{1, \alpha_1}^{[1]i_1} \Lambda_{\alpha_1}^{[1]} \Gamma_{\alpha_1, \alpha_2}^{[2]i_2} \Lambda_{\alpha_2}^{[2]} \Gamma_{\alpha_2, \alpha_3}^{[3]i_3} \Lambda_{\alpha_3}^{[2]} \dots \Lambda_{\alpha_{N-1}}^{[N-1]} \Gamma_{\alpha_{N-1}, 1}^{[N]i_N} . \quad (3.12)$$

In this expression the  $\Gamma_{\alpha_l, \alpha_{l+1}}^{[l]i_l}$  essentially correspond to the basis transformation between the computational basis and the Schmidt basis. At first this expression seems to be a particularly

inefficient encoding of the  $p^N$  coefficients of the wave function, because the largest matrix appearing in the expression above,  $\Gamma^{[N/2]i}$ , alone has the same number of entries. However, for ground states of gapped systems the Schmidt coefficients  $\Lambda_\alpha^{[n]}$  decay exponentially, which means that the matrix sizes can be truncated in a controlled way to some maximal feasible *bond dimension*  $D$ . The deviation of the compressed wave function  $|\psi_c\rangle$  obtained in this way is at worst

$$\| |\psi_c\rangle - |\psi\rangle \| \leq 2 \sum_{n=1}^N \epsilon_n(D) , \quad (3.13)$$

where  $\epsilon_n(D) = \sum_{\alpha > D} (\Lambda_\alpha^{[n]})^2$  (Verstraete and Cirac, 2006). Hence, the state can in good approximation be represented using  $pN$  matrices of maximal dimension  $D$ , i.e.,  $\mathcal{O}(pND^2)$  coefficients. In practice it is often sufficient to work with  $D \sim \mathcal{O}(10^3)$ , which means a tremendous reduction of the required memory in comparison to uncompressed storage of the wave function. Typically, a maximal discarded weight is introduced as control parameter, based on which the bond dimension is adjusted dynamically such that it is minimal with the constraint that the allowed discarded weight is not exceeded.

In Eq. (3.12) the Schmidt coefficients can be interpreted as entries of a diagonal matrix  $\Lambda_{\alpha_n, \alpha'_n}^{[n]} = \Lambda_{\alpha_n}^{[n]} \delta_{\alpha_n, \alpha'_n}$ . With this the wave function coefficient is expressed as a product of rank 2 and rank 3 tensors, which are associated with single lattice sites,

$$C_{i_1, \dots, i_n} = \sum_{\{\alpha_n, \alpha'_n\}} \Gamma_{\alpha_1}^{[1]i_1} \Lambda_{\alpha_1, \alpha'_1}^{[1]} \Gamma_{\alpha_1 \alpha_2}^{[2]i_2} \Lambda_{\alpha_2, \alpha'_2}^{[2]} \Gamma_{\alpha_2 \alpha_3}^{[3]i_3} \Lambda_{\alpha_3, \alpha'_3}^{[2]} \dots \Lambda_{\alpha_{N-1}, \alpha'_{N-1}}^{[N-1]} \Gamma_{\alpha_N}^{[N]i_N} . \quad (3.14)$$

Alternatively, the tensors  $\Gamma_{\alpha_{n-1} \alpha_n}^{[n]i_n}$  can be understood as a set of  $p$  matrices labeled by  $i_n$ . Then the coefficient  $C_{i_1, \dots, i_n}$  is in the form above expressed as a product of  $2N - 1$  matrices. Therefore the name *matrix product state*.

## Graphical representation

Explicit formulas containing matrix products or tensor products, as for example eq. (3.14), are typically very cumbersome and inconvenient to work with. However, the actual operations that are described by the formulas are very simple, namely contractions of indices, i.e., sums over common indices of multiple tensors. In order to avoid the bulky notation it is useful to resort to Penrose graphical notation of tensors (Penrose, 1971). In that notation a tensor corresponds to a node and each index of the tensor corresponds to a leg of that node, for example,

$$\Gamma_{\alpha_1, \alpha_2}^{[1]i_1} = \begin{array}{c} \Gamma^{[1]} \\ \alpha_1 \text{---} \bullet \text{---} \alpha_2 \\ | \\ i_1 \end{array}$$

If common indices of two tensors are contracted this is represented by joining the corresponding legs of the tensors to an edge, for example

$$\sum_{\alpha_2} \Gamma_{\alpha_1, \alpha_2}^{[1]i_1} \Gamma_{\alpha_2, \alpha_3}^{[2]i_2} = \begin{array}{c} \Gamma^{[1]} \quad \Gamma^{[2]} \\ \alpha_1 \text{---} \text{---} \alpha_2 \text{---} \text{---} \alpha_3 \\ | \quad | \\ i_1 \quad i_2 \end{array} = \begin{array}{c} \text{---} \text{---} \text{---} \text{---} \text{---} \\ | \quad | \\ i_1 \quad i_2 \end{array}$$

Note that, as desired, the graphical representation directly allows to interpret the result as a tensor with four external indices as shown after the second equality. Accordingly, the coefficient tensor is represented by

$$C_{i_1, \dots, i_N} = \begin{array}{c} \Gamma^{[1]} \quad \Lambda^{[1]} \quad \Gamma^{[2]} \quad \Lambda^{[2]} \quad \Gamma^{[3]} \quad \dots \quad \Gamma^{[N]} \\ \text{---} \text{---} \text{---} \text{---} \text{---} \text{---} \text{---} \text{---} \text{---} \text{---} \\ | \quad | \quad | \quad | \quad | \quad \dots \quad | \\ i_1 \quad i_2 \quad i_3 \quad \dots \quad i_N \end{array}$$

An operator  $\hat{O}$  acting on the Hilbert space can be written as

$$\hat{O} = \sum_{\substack{i_1, \dots, i_N \\ i'_1, \dots, i'_N}} O_{i_1, \dots, i_N}^{i'_1, \dots, i'_N} |i'_1\rangle \otimes \dots \otimes |i'_N\rangle \langle i_1| \otimes \dots \otimes \langle i_N|, \quad (3.15)$$

i.e., it is defined by a rank  $2N$  tensor with entries  $O_{i_1, \dots, i_N}^{i'_1, \dots, i'_N}$ . A graphical representation is

$$O_{i_1, \dots, i_N}^{i'_1, \dots, i'_N} = \begin{array}{c} |i_1| \quad |i_2| \quad \dots \quad |i_N| \\ \text{---} \text{---} \text{---} \text{---} \text{---} \\ \hat{O} \\ \text{---} \text{---} \text{---} \text{---} \text{---} \\ |i'_1| \quad |i'_2| \quad \dots \quad |i'_N| \end{array}$$

The product  $\hat{O}|\psi\rangle$  is represented by

$$\begin{array}{c} \text{---} \text{---} \text{---} \text{---} \text{---} \\ \hat{O}|\psi\rangle \\ |i'_1| \quad |i'_2| \quad \dots \quad |i'_N| \end{array} = \begin{array}{c} |\psi\rangle \\ |i_1| \quad |i_2| \quad \dots \quad |i_N| \\ \text{---} \text{---} \text{---} \text{---} \text{---} \\ \hat{O} \\ \text{---} \text{---} \text{---} \text{---} \text{---} \\ |i'_1| \quad |i'_2| \quad \dots \quad |i'_N| \end{array}$$

In analogy to the coefficient tensor  $C_{i_1, \dots, i_n}$  of a state the coefficient tensor  $O_{i_1, \dots, i_N}^{i'_1, \dots, i'_N}$  can be decomposed into a product of lower rank tensors, leading to a *matrix product operator* (MPO). This is, however, beyond the scope of this discussion.

### Time evolution in a translationally invariant system (iTEBD)

Since the MPS formulation of the wave function explicitly reflects how the notion of real space shapes the space of physically relevant states it is within this framework possible to deal with translationally invariant states of an infinite system. The basic idea is that translational invariance implies that in the MPS representation (Eq. (3.12)) all  $\Gamma_{\alpha_{n-1}, \alpha_n}^{[n]i_n}$  are the same as well as all  $\Lambda_{\alpha_n}^{[n]}$ . In combination with the fact that time evolution with a local Hamiltonian involves only a couple of neighboring lattice sites this effective simplicity of the



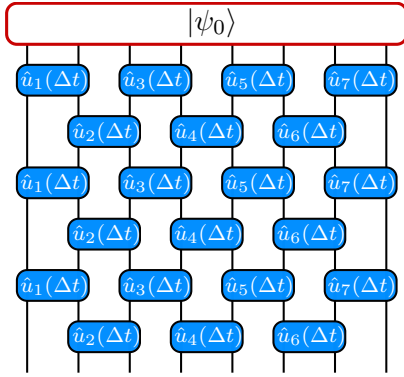


**Fig. 3.1:** Graphical representation of Trotter time evolution. The initial state  $|\psi_0\rangle$  is evolved for three time steps  $\Delta t$ .

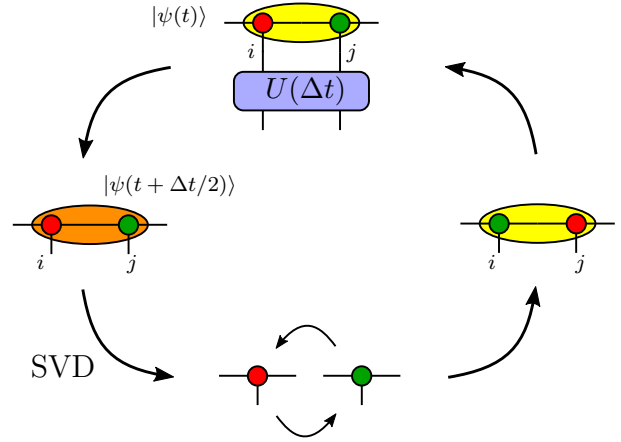


**Fig. 3.2:** Schematic depiction of the iTEBD cycle. Iteration of this loop amounts to time evolution in an infinite translationally invariant system.

infinite MPS is exploited for the efficient computation of dynamics in an algorithm called *infinite Time Evolving Block Decimation* (iTEBD).

For a local Hamiltonian that can be expressed as  $\hat{H} = \sum_{i=1}^N \hat{h}_{i,i+1}$  with  $\hat{h}_{i,i+1}$  acting only on lattice sites  $i$  and  $i + 1$  a Suzuki-Trotter expansion of the time evolution operator for a short time  $\Delta t$  yields

$$\hat{U}(\Delta t) = e^{-i\hat{H}\Delta t} = \prod_{i \text{ odd}} e^{-i\hat{h}_{i,i+1}\Delta t} \prod_{i \text{ even}} e^{-i\hat{h}_{i,i+1}\Delta t} + \mathcal{O}(\Delta t^2), \quad (3.16)$$

Thereby, the action of the time evolution operator can be approximated by subsequent evolutions on the even and odd bonds of the lattice. The time evolution for longer time intervals  $T = n\Delta t$  is then obtained by iterative application of  $U(\Delta t)$ ,

$$\hat{U}(n\Delta t) = \hat{U}(\Delta t)^n \approx \left( \prod_{i \text{ odd}} \hat{u}_i(\Delta t) \prod_{i \text{ even}} \hat{u}_i(\Delta t) \right)^n, \quad (3.17)$$

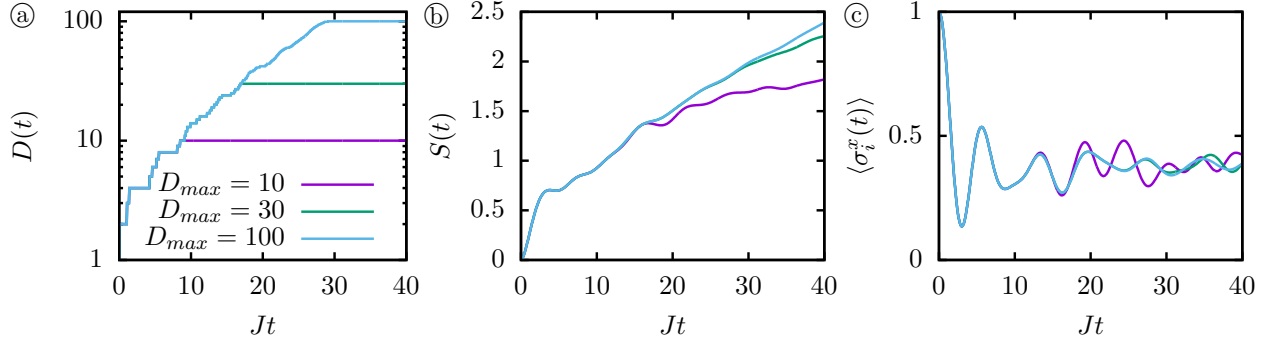
where  $\hat{u}_i(\Delta t) = e^{-i\hat{h}_{i,i+1}\Delta t}$ .

Fig. 3.1 shows a graphical representation of the Trotter time evolution of an initial state  $|\psi_0\rangle$ . As is evident from this depiction the time evolution on even and odd bonds, respectively, can be performed independently on the single bonds. Together with translational invariance this allows to compute the time evolution with high efficiency using the iTEBD algorithm. The idea is sketched in a simplified version in Fig. 3.2. A detailed description can, e.g., be found in (Pollmann, 2016). The algorithm requires two pairs of tensors,  $\Gamma_{\alpha_1, \alpha'_1}^{[1]i_1}$ ,  $\Lambda_{\alpha_1}^{[1]}$  and  $\Gamma_{\alpha_2, \alpha'_2}^{[2]i_2}$ ,  $\Lambda_{\alpha_2}^{[2]}$ . The contraction of each pair is depicted by the red and green node, respectively, in Fig. 3.2. In the following we refer to the corresponding tensors as  $\tilde{\Gamma}_{\alpha, \alpha'}^{[1]i_1}$  and  $\tilde{\Gamma}_{\alpha', \alpha''}^{[2]i_2}$ . The algorithm is a loop and each iteration corresponds to evolving the wave function by a half time step. The steps are the following:

1. Apply the time evolution operator to  $|\psi(t)\rangle$  to obtain  $|\psi(t + \Delta t/2)\rangle$ .
2. Decompose  $|\psi(t + \Delta t/2)\rangle$  into its constituent tensors  $\tilde{\Gamma}_{\alpha, \alpha'}^{[1]i_1}$  and  $\tilde{\Gamma}_{\alpha', \alpha''}^{[2]i_2}$ .
3. Swap both tensors by relabelling their indices to  $\tilde{\Gamma}_{\alpha', \alpha''}^{[1]i_2}$  and  $\tilde{\Gamma}_{\alpha, \alpha'}^{[2]i_1}$  and contract along  $\alpha'$ .
4. Continue with step 1.

The idea of this algorithm is that due to translational invariance after performing the time evolution, e.g., on an even bond (step 1) the next time step will couple the green tensor (cf. Fig. 3.2) to another red tensor to its right, which is, however, identical to the red tensor to its left after the time evolution. Hence, it suffices to simply swap the red and green tensors and perform the next time step on the resulting tensor after contraction. The loop has to be iterated twice in order to perform one time step  $\Delta t$ . Note that although the state after one iteration is above denoted by  $|\psi(t + \Delta t/2)\rangle$  this does not correspond to  $\hat{U}(\Delta t/2) |\psi(t)\rangle$ .

Fig. 3.3 displays data from an example time evolution with iTEBD for different maximal bond dimensions  $D_{\max}$ . The entanglement entropy shows the typical linear growth with time (cf. Section 1.2.2), which means an exponential growth of the required bond dimension for a fixed maximal discarded weight. Some time after the maximal allowed bond dimension is reached discrepancies between the different results become evident.



**Fig. 3.3:** Exemplary data from time evolution computed with the iTEBD algorithm for a quench in the Ising model with magnetic field defined in Eq. (4.6) ( $|\psi_0\rangle = \bigotimes_l |\rightarrow\rangle_l$ ,  $h_x/J = 0.3$ ,  $h_z/J = 0.1$ ) with different restrictions on the bond dimension,  $D \leq D_{\max}$ . **(a)** Dynamically adjusted bond dimension  $D$  (maximal discarded weight  $\epsilon_{\max} = 10^{-10}$ ), **(b)** Entanglement entropy  $S(t)$ , **(c)** transverse magnetization  $\langle \hat{\sigma}_i^x \rangle$ .

### 3.1.3 Classical networks

An alternative approach to represent many-body wave functions is to encode the state in a network of classical degrees of freedom. Considering for simplicity a spin-1/2 system with computational basis  $|\vec{s}\rangle = |s_1\rangle \otimes \dots \otimes |s_N\rangle$ , where  $s_i = \uparrow, \downarrow$ , the idea is to write the wave function coefficients in the form

$$\psi(\vec{s}) = \langle \vec{s} | \psi \rangle = e^{\mathcal{H}(\vec{s})} . \quad (3.18)$$

In this expression  $\mathcal{H}(\vec{s})$  is a Hamilton function describing interactions between classical degrees of freedom  $\vec{s}$ , thereby defining a *network* of classical spins. Since the wave function coefficients can be complex, the coupling constants appearing in  $\mathcal{H}(\vec{s})$  are in general complex numbers. This approach allows to represent the wave function in compressed form if it is possible to find a Hamilton function that accurately reproduces the wave function coefficients  $\psi(\vec{s})$  for all basis states  $|\vec{s}\rangle$  requiring only a small number of coupling constants.

Considering an observable  $\hat{O}$  with matrix elements  $\langle \vec{s} | \hat{O} | \vec{s}' \rangle = O_{\vec{s}, \vec{s}'}$ , the expectation value is readily written as

$$\langle \psi | \hat{O} | \psi \rangle = \sum_{\vec{s}} e^{\tilde{\mathcal{H}}(\vec{s})} \tilde{O}_{\vec{s}} \quad (3.19)$$

with

$$\tilde{O}_{\vec{s}} = \sum_{\vec{s}'} \text{Re} \left[ O_{\vec{s}, \vec{s}'} e^{\mathcal{H}(\vec{s}') - \mathcal{H}(\vec{s})} \right] . \quad (3.20)$$

This corresponds to a thermal expectation value of the observable  $\tilde{O}_{\vec{s}}$  in the classical spin system defined by  $\tilde{\mathcal{H}}(\vec{s}) = 2\text{Re}(\mathcal{H}(\vec{s}))$ . Considering an observable that is diagonal in the computational basis,  $\langle \vec{s} | \hat{O} | \vec{s}' \rangle = O_{\vec{s}} \delta_{\vec{s}, \vec{s}'}$ , this expectation value simplifies to

$$\langle \psi | \hat{O} | \psi \rangle = \sum_{\vec{s}} e^{\tilde{\mathcal{H}}(\vec{s})} O_{\vec{s}} . \quad (3.21)$$

With a wave function given in this form expectation values can be computed efficiently by Metropolis Monte Carlo ([Metropolis \*et al.\*, 1953](#)).

Classical network wave functions are commonly used in *variational Monte Carlo* algorithms for ground state searches ([McMillan, 1965](#); [Sorella, 2005](#); [Capello \*et al.\*, 2007](#)) or time evolution ([Carleo \*et al.\*, 2012, 2014](#); [Cevolani \*et al.\*, 2015](#); [Blaß and Rieger, 2016](#); [Hafner \*et al.\*, 2016](#); [Carleo \*et al.\*, 2017](#)). The Jastrow wave function ([Jastrow, 1955](#)) corresponding to a classical network of the form

$$\mathcal{H}_J(\vec{s}) = \sum_{i,j} C_{ij} s_i s_j \quad (3.22)$$

turned out to be a suited ansatz for many problems. Moreover, a new class of networks has been proposed recently as versatile ansatz, namely artificial neural networks. The first proposal by ([Carleo and Troyer, 2017](#)) suggests to consider classical networks in the form

of a *Restricted Boltzmann Machine* (RBM) to represent the many-body wave function. In this approach the classical system consists of the *visible* spins  $\vec{s}$  supplemented with additional *hidden* spins  $\vec{h}$ . As depicted exemplarily in Fig. 3.4 the RBM network contains only two-spin-couplings involving one visible and one hidden spin and possibly local fields for each spin; therefore the term “restricted”. The coefficient of a configuration  $\vec{s}$  is obtained by integrating out the hidden spins, which can be done analytically due to the restriction of the couplings,

$$\psi(\vec{s}) = \sum_{\vec{h}} \exp \left( \sum_{i=1}^N v_i s_i + \sum_{j=1}^{N_h} w_j h_j + \sum_{i,j} W_{ij} s_i h_j \right) \quad (3.23)$$

$$= 2^{N_h} \exp \left( \sum_{i=1}^N v_i s_i \right) \prod_{j=1}^{N_h} \cosh \left( w_j + \sum_{i=1}^N W_{ij} s_i \right). \quad (3.24)$$

This class of networks encloses the Jastrow-type networks (3.22), but it is much more general, because (3.24) can in addition comprise all kinds of higher order couplings. This flexibility is essentially guaranteed by representability theorems, on which machine learning with artificial neural networks is based (Hornik, 1991; Le Roux and Bengio, 2008).

In (Carleo and Troyer, 2017) it was shown that RBMs allow to find ground state wave functions in two-dimensional systems, which are competitive with other state of the art methods. Moreover, the principled possibility to compute time-evolution after a quench was demonstrated. Subsequently, a series of works investigated the capabilities of artificial neural networks to represent many-body wave functions. It was found that various prototypical ground states of exotic phases of matter, including ones that show long-range topological order, can be represented efficiently by an RBM (Deng *et al.*, 2016; Huang and Moore, 2017; Kaubruegger *et al.*, 2017). Moreover, a study of the entanglement properties implies that strong entanglement is not the restricting factor impeding the efficiency of RBMs (Deng *et al.*, 2017).

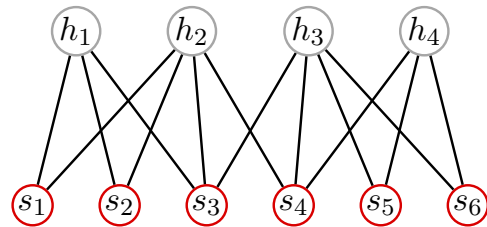


**Fig. 3.4:** Exemplary structure of a Restricted Boltzmann Machine. Visible degrees of freedom  $s_i$  are coupled to hidden degrees of freedom  $h_i$  through couplings  $W_{ij}$  indicated by black lines.

In the second part of this chapter (Section 3.2) a classical network representation of a time-evolved wave function after a quench is derived perturbatively via a cumulant expansion. It is found that the derived classical networks capture the quantum dynamics at short and intermediate times quite accurately. Hence, the approach provides a constructive prescription to design classical networks suited for time evolution going beyond the Jastrow ansatz (3.22). Moreover, the results show how locality can be exploited in a controlled way to simplify general RBM architectures.

## 3.2 *Preprint:* Quantum dynamics in transverse-field Ising models from classical networks

Markus Schmitt and Markus Heyl

arXiv:1707.06656; submitted.

<https://arxiv.org/abs/1707.06656>

**Author contributions** M. H. devised to exploit the classical network structure emerging from the cumulant expansion by Monte Carlo sampling. The details of the study were conceived jointly by both authors. M. S. carried out the analytical and numerical calculations and developed the sampling scheme for the Loschmidt amplitude as well as the mapping to artificial neural networks. Both authors contributed equally to the writing of the manuscript.

# Quantum dynamics in transverse-field Ising models from classical networks

Markus Schmitt<sup>1\*</sup> and Markus Heyl<sup>2</sup>

<sup>1</sup> Institute for Theoretical Physics, Georg-August-Universität Göttingen,  
Friedrich-Hund-Platz 1 - 37077 Göttingen, Germany

<sup>2</sup> Max-Planck-Institute for the Physics of Complex Systems, Nöthnitzer Str. 38 - 01187  
Dresden, Germany

\* markus.schmitt@theorie.physik.uni-goettingen.de

January 16, 2018

## Abstract

The efficient representation of quantum many-body states with classical resources is a key challenge in quantum many-body theory. In this work we analytically construct classical networks for the description of the quantum dynamics in transverse-field Ising models that can be solved efficiently using Monte Carlo techniques. Our perturbative construction encodes time-evolved quantum states of spin-1/2 systems in a network of classical spins with local couplings and can be directly generalized to other spin systems and higher spins. Using this construction we compute the transient dynamics in one, two, and three dimensions including local observables, entanglement production, and Loschmidt amplitudes using Monte Carlo algorithms and demonstrate the accuracy of this approach by comparisons to exact results. We include a mapping to equivalent artificial neural networks, which were recently introduced to provide a universal structure for classical network wave functions.

---

## Contents

<b>1</b>	<b>Introduction</b>	<b>2</b>
<b>2</b>	<b>Results</b>	<b>3</b>
2.1	Classical network via cumulant expansion	3
2.2	Observables	5
2.3	Entanglement	6
2.4	Loschmidt amplitude	7
2.5	Construction of equivalent ANNs	8
<b>3</b>	<b>Conclusions</b>	<b>9</b>
<b>A</b>	<b>Perturbative classical networks</b>	<b>10</b>
<b>B</b>	<b>Loschmidt amplitude as classical partition function</b>	<b>15</b>
<b>C</b>	<b>Exemplary derivation of ANN couplings from the cumulant expansion</b>	<b>19</b>
	<b>References</b>	<b>21</b>

---



## 1 Introduction

A key challenge in quantum many-body theory is the efficient representation of quantum many-body states using classical compute resources. The full information contained in such a many-body state in principle requires resources that grow exponentially with the number of degrees of freedom. Therefore, reliable schemes for the compression and efficient encoding of the essential information are vital for the numerical treatment of correlated systems with many degrees of freedom. This is of particular relevance for dynamics far from equilibrium, where large parts of the spectrum of the Hamiltonian play an important role.

For low-dimensional systems matrix product states [1, 2] and more general tensor network states [3] constitute a powerful ansatz for the compressed representation of physically relevant many-body wave functions. These allow for the efficient computation of ground states and real time evolution. In high dimensions properties of quantum many-body systems in and out of equilibrium can be obtained by dynamical mean field theory [4–7], which yields exact results in infinite dimensions. This leaves a gap at intermediate dimensions, where exciting physics far from equilibrium has recently been observed experimentally [8–13].

An alternative approach, which received increased attention lately, is the representation of the wave function based on networks of classical degrees of freedom. Given the basis vectors  $|\vec{s}\rangle = |s_1\rangle \otimes |s_2\rangle \otimes \dots \otimes |s_N\rangle$  of a many-body Hilbert space, where the  $s_l$  label the local basis, the coefficients of the wave function  $|\psi\rangle$  are expressed as

$$\psi(\vec{s}) = \langle \vec{s} | \psi \rangle = e^{\mathcal{H}(\vec{s})} \quad (1)$$

where  $\mathcal{H}(\vec{s})$  is an effective Hamilton function defining the classical network. Wave functions of this form were used in combination with Monte Carlo algorithms for variational ground state searches [14–16] and time evolution [17–23]. Recently, it was suggested that the wave function (1) can generally be encoded in an artificial neural network (ANN) trained to resemble the desired state [23]. This idea was seized in a series of subsequent works exploring the capabilities of this and related representations [24–31]. Importantly, there are no principled restrictions on dimensionality.

In this work we present a scheme to perturbatively derive analytical expressions for perturbative classical networks (pCNs) as representation of time-evolved wave functions for transverse-field Ising models (TFIMs) which can be extended directly also to other models.

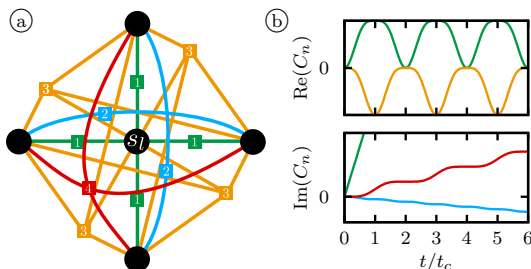


Figure 1: (a) Structure of the perturbative classical network for the TFIM in  $d = 2$  and (b) dynamics of the couplings (color coded as in (a)). The black dots in the network structure represent a classical spin  $s_l$  and its four neighbors in a translationally invariant square lattice. Each square with number  $n$  corresponds to a coupling of the connected classical spins with coupling constant  $C_n(t)$ . The resulting time-dependent classical Hamiltonian function  $\mathcal{H}(\vec{s}, t)$  encodes quantum dynamics via Eq. (1).

The resulting networks consist of the same number of classical spins as the corresponding quantum system and exhibit only local couplings making the encoding particularly efficient. We compute the transient dynamics of the TFIM in one, two, and three dimensions ( $d = 1, 2, 3$ ) including local observables, correlation functions, entanglement production, and Loschmidt amplitudes. By comparing to exact solutions we demonstrate the accuracy of our results going well beyond standard perturbative approaches. This work provides a way to derive classical network structures within a constructive prescription, where other approaches rely on heuristics. As a specific application, we derive the structure and the time-dependent weights of equivalent ANNs in the sense of Ref. [23].

## 2 Results

In the following we compute dynamics of TFIMs of  $N$  spins with Hamiltonian

$$H = -\frac{J}{4} \sum_{\langle i,j \rangle} \sigma_i^z \sigma_j^z - \frac{h}{2} \sum_{i=1}^N \sigma_i^x, \quad (2)$$

where  $\sigma_i^{x/z}$  denote Pauli operators acting on site  $i$  and the first sum runs over neighboring lattice sites  $i$  and  $j$ . As the computational basis we choose the spin basis states  $|\vec{s}\rangle = |s_1 \dots s_N\rangle$  with  $s_i = \uparrow, \downarrow$ .

Note that dynamics of Ising models are accessible experimentally with quantum simulators, which was demonstrated recently in various setups [32–34].

In this work we are interested in the dynamics that comprise a dynamical quantum phase transition (DQPT) [35, 36]. The signature of a DQPT is a non-analyticity in the many-body dynamics analogous to equilibrium phase transitions where thermodynamic quantities behave non-analytically as function of a control parameter. DQPTs were recently observed in experiment [11, 34] and there is a series of results on TFIMs in this context [37–47].

Typically, DQPTs occur when the model is quenched across an underlying equilibrium quantum phase transition. A particularly insightful limit with this respect is a quench from  $h_0 = \infty$  to  $h/J \ll 1$ , where, e.g., universal behavior was proven in  $d = 1$  [41]. When quenching from  $h_0 = \infty$  to  $h = 0$  the TFIM in  $d = 1, 2$  exhibits DQPTs at odd multiples of  $t_c = \pi/J$ , which we choose as the unit of time throughout the paper. The ground state at  $h_0 = \infty$  is a particularly simple initial state, since  $\langle \vec{s} | \psi_0 \rangle = 2^{-N/2}$ . One could, however, go away from that limit perturbatively, e.g., by constructing a Schrieffer-Wolff transformation for an initial state with weak spin couplings.

### 2.1 Classical network via cumulant expansion

Consider a Hamiltonian of the form  $H = H_0 + \lambda V$ , where  $H_0$  is diagonal in the spin basis,  $H_0 |\vec{s}\rangle = E_{\vec{s}} |\vec{s}\rangle$ ,  $V$  an off-diagonal operator, and  $\lambda \ll 1$ . In the interaction picture the time evolution operator can be expressed as  $e^{-iHt} = e^{-iH_0 t} W_\lambda(t)$ , where  $W_\lambda(t) = \mathcal{T}_t \exp \left[ -i\lambda \int_0^t dt' V(t') \right]$ . In this setting time-evolved coefficients of the wave function (1) can be obtained perturbatively by a cumulant expansion [48]. Denoting the initial state with  $|\psi_0\rangle = \sum_{\vec{s}} \psi_0(\vec{s}) |\vec{s}\rangle$  the cumulant expansion to lowest order yields the time-evolved state  $|\psi(t)\rangle = \sum_{\vec{s}} \psi(\vec{s}, t) |\vec{s}\rangle$  with

$$\frac{\psi(\vec{s}, t)}{\psi_0(\vec{s})} = e^{-iE_{\vec{s}} t} \exp \left[ -i\lambda \int_0^t dt' \frac{\langle \vec{s} | V(t') | \psi_0 \rangle}{\langle \vec{s} | \psi_0 \rangle} + \mathcal{O}(\lambda^2) \right]. \quad (3)$$

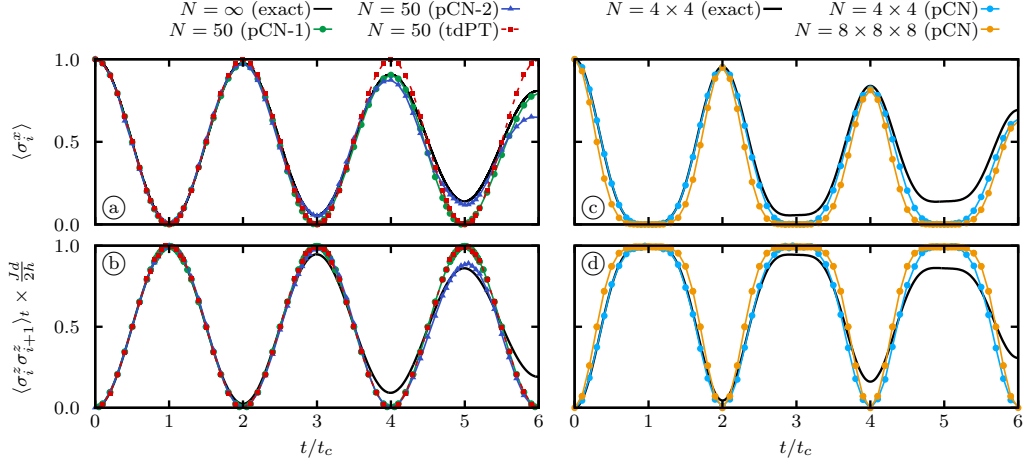


Figure 2: Time evolution of transverse magnetization (top panels) and nearest-neighbor correlation function (bottom panels) in the TFIM. (a, b) Results for  $d = 1$  obtained from the pCN with first order (pCN-1) and second order (pCN-2) expansion in comparison with the exact dynamics and time-dependent perturbation theory (tdPT). (c, d) Dynamics in  $d = 2$  (blue), and  $d = 3$  (orange) obtained from the first order pCN compared to exact results in  $d = 2$ . Data obtained with  $h/J = 0.05$ ;  $t_c = \pi/J$ .

By identifying  $\mathcal{H}(\vec{s}, t) = -iE_{\vec{s}}t - i\lambda \int_0^t dt' \frac{\langle \vec{s} | V(t') | \psi_0 \rangle}{\langle \vec{s} | \psi_0 \rangle}$  the expression above takes the desired form given in Eq. (1). Importantly, also the effective Hamilton function becomes local, whenever  $H_0$  and  $V$  are local. It will be demonstrated below that the construction via cumulant expansion yields much more accurate results than conventional perturbation theory. The approximation can be systematically improved by taking into account higher order terms. To which extent it is possible to also capture long-time dynamics using such a construction, remains an open question and, since beyond the scope of the present work, will be left for future research.

For our purposes, we identify  $H_0 = -\frac{J}{4} \sum_{\langle i,j \rangle} \sigma_i^z \sigma_j^z$  and  $\lambda V \hat{=} -\frac{\hbar}{2} \sum_i \sigma_i^x$ . Note that, e.g., a strongly anisotropic XXZ model could be treated analogously. The time-dependent  $V(t)$  is obtained by solving the Heisenberg equation of motion. The general form of the Hamilton function from the first-order cumulant expansion obtained under these assumptions is

$$\mathcal{H}^{(1)}(\vec{s}, t) = \sum_{n=0}^z C_n(t) \sum_{l=1}^N \sum_{(a_1, \dots, a_n) \in \mathcal{V}_n^l} s_l^n \prod_{r=1}^n s_{a_r}, \quad (4)$$

where  $\mathcal{V}_n^l$  denotes the set of possible combinations of  $n$  neighboring sites of lattice site  $l$ ,  $z$  is the coordination number of the lattice, and  $C_n(t)$  are time-dependent complex couplings. Classical Hamilton functions  $\mathcal{H}^{(1)}(\vec{s}, t)$  for cubic lattices in  $d = 1, 2, 3$  including explicit expressions for the couplings  $C_n(t)$  are given in Appendix A. Fig. 1 displays the structure of the pCN in 2D and the time evolution of the couplings  $C_n(t)$ . For  $d = 2, 3$   $\mathcal{H}^{(1)}(\vec{s}, t)$  already contains couplings with products of four or six spin variables, respectively. Thereby, the derived structure of the pCN markedly differs from heuristically motivated Jastrow-type wave functions, which constitute a common variational ansatz [17, 20].

The following results were obtained with  $h/J = 0.05$ ; see Appendix A for results at larger  $h/J$ .

## 2.2 Observables

Plugging Eq. (1) into the time-dependent expectation value of an observable  $\hat{O}$  with matrix elements  $\langle \vec{s} | \hat{O} | \vec{s}' \rangle = O_{\vec{s}\vec{s}'}$  results in

$$\langle \psi_0 | e^{iHt} O e^{-iHt} | \psi_0 \rangle = \sum_{\{\vec{s}\}} e^{\tilde{\mathcal{H}}(\vec{s},t)} \tilde{O}_{\vec{s}}. \quad (5)$$

with

$$\tilde{O}_{\vec{s}} = \sum_{\{\vec{s}'\}} \text{Re} \left[ O_{\vec{s}\vec{s}'} e^{\mathcal{H}(\vec{s}',t) - \mathcal{H}(\vec{s},t)} \right] \quad (6)$$

and  $\tilde{\mathcal{H}}(\vec{s},t) = 2 \text{Re}[\mathcal{H}(\vec{s},t)]$ . In this form the quantum expectation value resembles a thermal expectation value in the pCN defined by  $\mathcal{H}(\vec{s},t)$ . For an observable  $\hat{O}$  that is diagonal in the spin basis,  $\langle \vec{s} | \hat{O} | \vec{s}' \rangle = O_{\vec{s}} \delta_{\vec{s},\vec{s}'}$ , the expression above simplifies to

$$\langle \psi_0 | e^{iHt} \hat{O} e^{-iHt} | \psi_0 \rangle = \sum_{\{\vec{s}\}} e^{\tilde{\mathcal{H}}(\vec{s},t)} O_{\vec{s}}. \quad (7)$$

These expressions can be evaluated efficiently by the Metropolis algorithm [49]. Although we find empirically that the off-diagonal observables under consideration can still be sampled efficiently by Monte Carlo, it is not clear whether a sign problem can appear in other cases. Fig. 2 shows results for different local observables obtained in this way. In these and the following figures the Monte Carlo error is less than the resolution of the plot.

In Fig. 2(a,b) we compare the results from the classical network construction to exact results obtained by fermionization for the infinite system in  $d = 1$  [50–54]. Focusing for the moment on the transverse magnetization  $\sigma_i^x$  in Fig. 2(a) we find that on short times the pCN gives an accurate description of the dynamics. Upon improving our pCN construction by including the second-order contributions in the cumulant expansion, the time scale up to which the pCN captures quantitatively the real-time evolution of  $\sigma_i^x$  increases suggesting that the expansion can be systematically improved by including higher order terms. For a further benchmarking of our results we also compare the pCN results to conventional first-order time-dependent perturbation theory. Clearly, the first-order pCN provides a much more accurate approximation to the exact dynamics, which originates in an effective resummation of an infinite subseries of terms appearing in conventional time-dependent perturbation theory. In Fig. 2(b) we consider the nearest-neighbor longitudinal correlation function  $\sigma_i^z \sigma_{i+1}^z$  which is an observable diagonal in the spin basis. Compared to the offdiagonal observable studied in Fig. 2a we find much stronger deviations from the exact result which also cannot be improved upon including higher orders in the cumulant expansion. However, for correlation functions at longer distances the corrections to the first-order cumulant expansion become important; see Appendix A. The observation that the diagonal observables don't improve with the order of the pCN expansion we attribute to secular terms from resonant processes which are not appropriately captured by perturbative approaches such as the pCN. One possible strategy to incorporate such resonant processes is to impose a time-dependent variational principle [17, 55–57] on our networks in order to obtain suitably optimized coupling coefficients. Having demonstrated under which circumstances the pCN can be improved by including higher order contributions, for the remainder of the article we focus on the capabilities of the first-order pCN leaving further optimization strategies of the network open for the future.

In Fig. 2(c,d) we show our results for the same observables but now in  $d = 2$  and  $d = 3$ . Compared to  $d = 1$  we find much broader maxima and minima, respectively, close to the

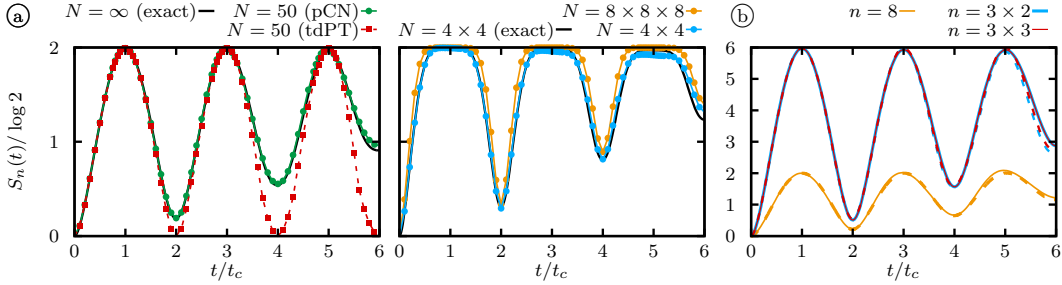


Figure 3: (a) Time evolution of the entanglement entropy for subsystems of  $n = 2$  spins obtained from the classical network by MC in comparison with exact results;  $h/J = 0.05$ . (b) Time evolution of the entanglement entropy for different subsystem shapes with  $n$  spins obtained from full wave functions  $|\psi(t)\rangle$  determined from the pCN in comparison with exact results (dashed lines). In  $d = 1$  the system size is  $N = 20$ , in  $d = 2$  it is  $N = 6 \times 3$ ;  $h/J = 0.05$ .

times where DQPTs occur at odd multiples of  $t_c = \pi/J$ . In the limit  $h/J \rightarrow 0$  the shape is given by the power law  $|t - t_c|^z$  with  $z = 2d$ . This behavior was already observed for one and two dimensional systems in Ref. [41]. For the  $d = 2$  case we have included also exact diagonalization data for a  $4 \times 4$  lattice. Overall, we observe a similar accuracy in the dynamics of these observables as compared to the  $d = 1$  results.

### 2.3 Entanglement

Having discussed the capabilities of the pCN to encode the necessary information for the dynamics of local observables and correlations, we would like to show now that it can also reproduce entanglement dynamics and thus the propagation of quantum information.

By sampling all correlation functions it is in principle possible to construct the reduced density matrix of a subsystem  $A$ ,  $\rho_A(t) = \text{tr}_B(|\psi(t)\rangle\langle\psi(t)|)$ , where  $\text{tr}_B$  denotes the trace over the complement of  $A$ , and the entanglement entropy of subsystem  $A$  given by  $S(t) = -\text{tr}(\rho_A(t) \ln \rho_A(t))$ . For subsystems with two spins at sites  $i$  and  $j$  we have  $\rho_A = \frac{1}{4} \sum_{\alpha, \alpha' \in \{0, x, y, z\}} \langle \sigma_i^\alpha \sigma_j^{\alpha'} \rangle \sigma^\alpha \otimes \sigma^{\alpha'}$ , where  $\sigma_i^0$  denotes the identity.

Figure 3(a) shows the entanglement entropy  $S_2(t)$  of two neighboring spins. We find very good agreement of the Monte Carlo data based on the first-order cumulant expansion with the exact results. In particular, for the entanglement entropy the classical network captures both the decay of the maxima close to the critical times  $(2n+1)t_c$  and the increase of the minima. As for the observables the shape in the vicinity of the maxima depends on  $d$  and is for  $h/J \rightarrow 0$  given by the same power laws. Note, that the pCN correctly captures the maximal possible entanglement  $S_2^{\text{max}} = 2 \ln 2$ . By contrast, the result from tdPT completely misses the decay of the oscillations.

In order to assess the capability of the pCN to capture the entanglement dynamics of larger subsystems we compute the whole wave function  $|\psi(t)\rangle = \sum_{\vec{s}} \psi(\vec{s}) |\vec{s}\rangle$  with the coefficients  $\psi(\vec{s})$  as given in Eq. (3) for feasible system sizes. The entanglement entropy of arbitrary bipartitions is then obtained by a Schmidt decomposition. Fig. 3(b) shows entanglement entropies obtained in this way for subsystems of different sizes  $n$  in  $d = 1, 2$ . The results imply that at these short times only spins at the surface of the subsystem become entangled with the rest of the system. The maxima for a subsystem of  $n = 8$  spins in a ring of  $N = 20$  spins in  $d = 1$  lie close to  $2 \ln 2$ , the theoretical maximum for the entanglement entropy of the two spins, which sit at the surface. This interpretation is

supported by the results for a torus of  $N = 6 \times 3$  spins with subsystems of size  $n = 3 \times 2$  and  $n = 3 \times 3$ . In that case the entanglement entropy reaches maxima of  $6 \ln 2$ , corresponding to 6 spins at the boundary. In both cases the results agree well with the exact results for times  $t < 4t_c$ . This again reflects the fact that the pCN from first-order cumulant expansion yields a good approximation of the dynamics of neighboring spins.

## 2.4 Loschmidt amplitude

Next, we aim to show that not only local but also global properties are well-captured by the classical networks. For that purpose we study the Loschmidt amplitude  $\langle \psi_0 | \psi(t) \rangle$ , which constitutes the central quantity for the anticipated DQPTs and which has been measured recently experimentally in different contexts [34, 58]. For a quench from  $h_0 = \infty$  to  $h = 0$  the Loschmidt amplitude

$$Z(t) = \frac{1}{2^N} \sum_{\vec{s} \in \{\pm 1\}^N} e^{i \frac{J}{4} t \sum_{\langle i, j \rangle} s_i s_j} \quad (8)$$

resembles the partition sum of a classical network with imaginary temperature  $\beta = -it$  [41]. This expression is not suited for MC sampling because all weights lie on the unit circle in the complex plane rendering importance sampling impractical and indicating a severe sign problem. These issues can be diminished by constructing an equivalent network with real weights. After integrating out every second spin on the sublattice  $\Lambda$ , equivalent to one decimation step [59], the partition sum takes the form

$$Z(t) = \frac{1}{2^N} \sum_{\vec{s} \in \{\pm 1\}^{N/2}} \prod_{i \in \Lambda} 2 \cos \left( \frac{J}{4} t \sum_{\langle i, j \rangle} s_j \right). \quad (9)$$

Choosing a suited ansatz the partition sum can be rewritten as  $Z(t) = \sum_{\vec{s}} e^{\mathcal{H}(\vec{s}, t)}$  with real Boltzmann weights given by an effective Hamilton function  $\mathcal{H}(\vec{s}, t)$  that defines the classical network [41, 59, 60]. Generally, the effective Hamilton function takes the form

$$\mathcal{H}(\vec{s}, t) = \sum_{n=0}^{z/2} C_n(t) \sum_{l \in \Lambda} \sum_{(a_1, \dots, a_{2n}) \in \mathcal{V}_{2n}^l} \prod_{r=1}^{2n} s_{a_r}. \quad (10)$$

The explicit expressions for  $d = 1, 2, 3$  are given in Appendix B.

It is evident from Eq. (9) that, although real, the Boltzmann weights of the classical network are not necessarily positive. The bottom panels in Fig. 4 show the real parts of the coupling constants of the effective Hamiltonians for  $d = 1, 3$ . The couplings in  $d = 3$  acquire non-vanishing imaginary parts for  $t_c/3 \leq t \leq 5t_c/3$  leading to negative weights for some configurations. The partition sum is then split into a positive and a negative part  $Z(t) = Z_+(t) + Z_-(t)$  with  $Z_+ > 0$  and  $Z_- < 0$ . In order to compute  $Z(t)$  by Monte Carlo sampling we combine a separate sampling of factor graphs [61] with parallel tempering [62] and multi-histogram reweighting [63]; see Appendix B.

As the Loschmidt amplitude is exponentially suppressed with increasing system size we study the rate function [35]  $\lambda_N(t) = -\frac{1}{N} \ln |Z(t)|$ , which is well defined in the thermodynamic limit  $N \rightarrow \infty$ . The top panel in Fig. 4(a) displays  $\lambda_N(t)$  obtained by a Monte Carlo sampling for a ring of  $N = 100$  spins together with the exact result [64], confirming the precision of the pCN approach and demonstrating the principled possibility to detect DQPTs. For the rate function in  $d = 3$  shown in Fig. 4(b) we obtained converged results in the whole interval for  $N = 4 \times 4 \times 4$  and  $N = 4 \times 4 \times 6$  physical spins. Note that there are no indications of non-analytic behavior in the Monte Carlo results at  $t = t_c/3, t_c/2$



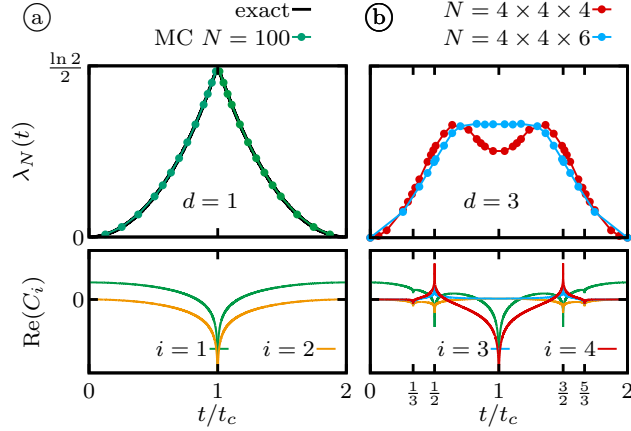


Figure 4: Time evolution of the rate function of the Loschmidt amplitude  $\lambda_N(t)$  (top panels) and corresponding couplings in the classical network (bottom panels); (a)  $d=1$ , (b)  $d=3$ .

despite the divergences of the couplings at those points. While we can reach fairly large systems in  $d=3$ , these are still not large enough to see convergence and non-analytic behavior at  $t=t_c$  as opposed to the case of  $d=1$ . It can be shown, see Appendix B, that for any dimension  $\lambda_\infty(t_c) = \ln(2)/2$  demonstrating that our data in  $d=3$  is still far from the thermodynamic limit.

## 2.5 Construction of equivalent ANNs

Finally, we present an exact mapping of the pCN obtained by a cumulant expansion to an equivalent ANN as introduced in Ref. [23]. This outlines the general potential of the pCN to guide the choice of network structures, for which otherwise no generic principle exists.

Generally, for Ising systems with translational invariance and local interactions, the cumulant expansion will yield a Hamilton function of the form

$$\mathcal{H}(\vec{s}, t) = \sum_{l=1}^N \mathcal{P}_l(\vec{s}, t) \quad (11)$$

where the functions  $\mathcal{P}_l(\vec{s}, t)$  only involve a couple of spins in the neighborhood of spin  $l$ . We call the spins involved in  $\mathcal{P}_l(\vec{s}, t)$  a *patch*. The  $\mathcal{P}_l(\vec{s}, t)$  are invariant under  $\mathbb{Z}_2$  and a number of permutations of the spins in a patch due to the lattice symmetries. In terms of the  $\mathcal{P}_l(\vec{s}, t)$  the coefficients of the wave function are given by

$$\psi(\vec{s}, t) = e^{\mathcal{H}(\vec{s}, t)} = \prod_{l=1}^N e^{\mathcal{P}_l(\vec{s}, t)}. \quad (12)$$

To find the corresponding ANN we choose a general  $\mathbb{Z}_2$  symmetric ansatz [23]

$$\psi_{ANN}(\vec{s}, t) = \left(\frac{\Omega}{2^\alpha}\right)^N \sum_{\vec{u}_1^{(1)} \dots \vec{u}_l^{(N_u)}} e^{\sum_{l,m} \sum_n W_{lm}^{(n)}(t) s_m u_l^{(n)}} \quad (13)$$

incorporating lattice symmetries in the connectivity of physical spins  $s_l$  and hidden spins  $u_l^{(n)}$  defined by the weights  $W_{lm}^{(n)}$ .  $\alpha$  denotes the number of hidden spins per physical

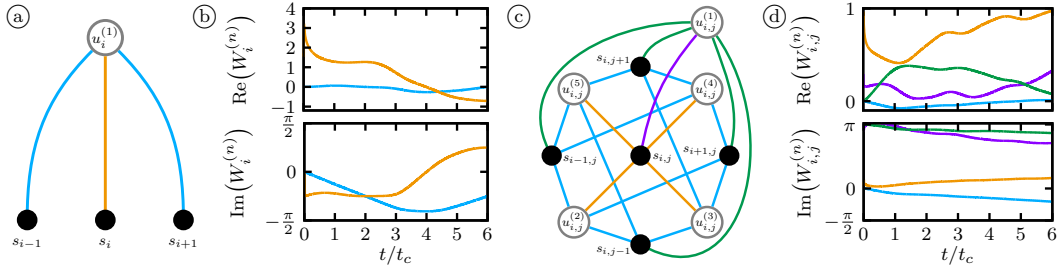


Figure 5: Structure of the ANN for the TFIM in  $d = 1, 2$  (a, c) and time evolution of the weights obtained by first-order cumulant expansion for  $h/J = 0.05$  (b, d). In the networks black dots stand for physical spins and gray circles indicate hidden spins. The couplings in (b, d) are color coded with the corresponding lines in (a, c).

spin and  $\Omega$  constitutes an overall normalization. Upon integrating out the hidden spins we obtain

$$\psi(\vec{s}, t) = \prod_{l=1}^N \prod_{n=1}^{\alpha} \cosh \left( \sum_m W_{lm}^{(n)} s_m \right). \quad (14)$$

In order to determine the ANN weights we factor-wise equate the r.h.s. of Eq. (12) and Eq. (14),

$$\prod_n \cosh \left( \sum_m W_{lm}^{(n)} s_m \right) = e^{\mathcal{P}_l(\vec{s}, t)}, \quad (15)$$

and plug in each of the distinct spin configurations of a patch. This yields a set of equations for the unknown weights  $W_{lm}^{(n)}$ , which can be solved numerically. In Appendix C procedure is outlined in detail for  $d = 1$  and  $d = 2$ .

Fig. 5 shows the structure of the ANNs and the time-dependence of the weights obtained in this way for  $d = 1$  and  $d = 2$ . In  $d = 1$  the ANN structure (Fig. 5(a)) comprises the minimal number of hidden spins that is possible subject to the lattice symmetries. Although unproven the same is expected to hold for the structure for  $d = 2$  in Fig. 5(c). Note the complex dynamics and the rapid initial change exhibited by some of the couplings. In comparison to a general all-to-all ansatz this construction provides a way to drastically reduce the number of ANN couplings in a controlled way, thereby restricting the variational subspace and lessening the computational cost for the optimization in variational algorithms.

### 3 Conclusions

For the quench parameters under consideration the state of the system remains close to classical for long times. As demonstrated in Appendix A a maximal bond dimension of  $\chi_{\max} = 4$  is sufficient to obtain converged results in  $d = 1$  for local observables using iTEBD [65]. Nevertheless, this amounts to 64 parameters, which have to be stored, whereas the first-order pCN encodes the state in three couplings, which indicates the potential efficiency of pCNs in this respect. The pCNs derived by a cumulant expansion give a good approximation of this dynamics and thereby provide a controlled benchmark for new algorithms targeting the dynamics in higher dimensions. In future work it is worth to explore whether the structure of the networks constitutes a good ansatz for numerical

time evolution based on a variational principle also in the absence of a small parameter [17, 55–57]. We expect that a variational time evolution based on the derived network structures could effectively perform the resummation of higher orders that would be necessary to overcome the problem of secular terms in the perturbative results. Moreover, the presented approach can be straightforwardly generalized to other systems and higher spin degrees of freedom. This might be particularly interesting in many-body-localized systems [9, 66–69], where the so-called local integrals of motion provide a natural basis for constructing a classical network.

## Acknowledgements

The authors acknowledge helpful discussions with S. Kehrein and M. Behr. For the numerical computations the Armadillo library [70] was used. The iTEBD algorithm was implemented using the iTensor library [71].

**Funding information** M.S. is supported by the Studienstiftung des Deutschen Volkes. M.H. acknowledges support by the Deutsche Forschungsgemeinschaft via the Gottfried Wilhelm Leibniz Prize program.

## A Perturbative classical networks

### A.1 Explicit expressions for the perturbative classical networks

For the cumulant expansion the time-evolved operator  $V(t) = e^{iH_0 t} V e^{-iH_0 t}$  is required. This can be obtained by solving the corresponding Heisenberg equation of motion  $-i \frac{d}{dt} V(t) = [H_0, V(t)]$ .

In 1D the Heisenberg EOM for  $\sigma_l^x(t)$  yields

$$\sigma_l^x(t) = \cos^2(Jt/2) \sigma_l^x - \sigma_{l-1}^z \sigma_{l+1}^z \sin^2(Jt/2) \sigma_l^x - i \frac{1}{2} \sin(Jt) (\sigma_{l-1}^z + \sigma_{l+1}^z) \sigma_l^z \sigma_l^x. \quad (16)$$

The cumulant expansion to first-order results in classical Hamilton functions of the general form

$$\mathcal{H}^{(1)}(\vec{s}, t) = -i E_{\vec{s}} t - i \lambda \sum_l \int_0^t dt' \frac{\langle \vec{s} | V(t') | \psi_0 \rangle}{\langle \vec{s} | \psi_0 \rangle} = \sum_{n=0}^z C_n(t) \sum_{l=1}^N \sum_{(a_1, \dots, a_n) \in \mathcal{V}_n^l} s_l^n \prod_{r=1}^n s_{a_r}, \quad (17)$$

where  $\mathcal{V}_n^l$  denotes the set of possible combinations of  $n$  neighboring sites of lattice site  $l$ ,  $z$  is the coordination number of the lattice, and  $C_n(t)$  are time-dependent complex couplings.

In  $d = 1$  the explicit form is

$$\mathcal{H}_{1D}^{(1)} = N C_0(t) + C_1(t) \sum_l (s_{l-1}^z s_l^z + s_l^z s_{l+1}^z) + C_2(t) \sum_l s_{l-1}^z s_{l+1}^z \quad (18)$$

with

$$\begin{aligned} C_0(t) &= i \frac{\hbar}{4J} (Jt + \sin(Jt)) , & C_1(t) &= i \frac{Jt}{8} + \frac{\hbar}{4J} (1 - \cos(Jt)) , \\ C_2(t) &= -i \frac{\hbar}{4J} (Jt - \sin(Jt)) . \end{aligned} \quad (19)$$

Analogously for  $d = 2$ ,

$$\begin{aligned} \mathcal{H}_{2D}^{(1)} = \sum_l \left[ C_0^{(1)}(t) + C_1^{(1)}(t) \sum_{a \in \mathcal{V}_1^l} s_a^z s_l^z + C_2^{(1)}(t) \sum_{(a,b) \in \mathcal{V}_2^l} s_a^z s_b^z \right. \\ \left. + C_3^{(1)}(t) \sum_{(a,b,c) \in \mathcal{V}_3^l} s_a^z s_b^z s_c^z s_l^z + C_4^{(1)}(t) \sum_{(a,b,c,d) \in \mathcal{V}_4^l} s_a^z s_b^z s_c^z s_d^z \right] \end{aligned} \quad (20)$$

where

$$\begin{aligned} C_0^{(1)}(t) &= i \frac{h}{2J} \frac{6Jt + 8 \sin(Jt) + \sin(2Jt)}{16}, & C_1^{(1)}(t) &= i \frac{Jt}{8} + \frac{h}{2J} \frac{1 - \cos^4(Jt/2)}{2J}, \\ C_2^{(1)}(t) &= -i \frac{h}{2J} \frac{2Jt - \sin(2Jt)}{16}, & C_3^{(1)}(t) &= -\frac{h}{2J} \frac{\sin^4(Jt/2)}{2J}, \\ C_4^{(1)}(t) &= i \frac{h}{2J} \frac{6Jt - 8 \sin(Jt) + \sin(2Jt)}{16}. \end{aligned} \quad (21)$$

The classical network from first-order cumulant expansion in  $d = 3$  is given by

$$\begin{aligned} \mathcal{H}_{3D}^{(1)} = \sum_l \left[ C_0^{(1)}(t) + C_1^{(1)}(t) \sum_{a \in \mathcal{V}_1^l} s_a^z s_l^z + C_2^{(1)}(t) \sum_{(a,b) \in \mathcal{V}_2^l} s_a^z s_b^z \right. \\ \left. + C_3^{(1)}(t) \sum_{(a,b,c) \in \mathcal{V}_3^l} s_a^z s_b^z s_c^z s_l^z + C_4^{(1)}(t) \sum_{(a,b,c,d) \in \mathcal{V}_4^l} s_a^z s_b^z s_c^z s_d^z \right. \\ \left. + C_5^{(1)}(t) \sum_{(a,b,c,d,e) \in \mathcal{V}_5^l} s_a^z s_b^z s_c^z s_d^z s_e^z s_l^z + C_6^{(1)}(t) \sum_{(a,b,c,d,e,f) \in \mathcal{V}_6^l} s_a^z s_b^z s_c^z s_d^z s_e^z s_f^z \right] \end{aligned} \quad (22)$$

with

$$\begin{aligned} C_0^{(1)}(t) &= i \frac{h}{2J} \frac{30Jt + 45 \sin(Jt) + 9 \sin(2Jt) + \sin(3Jt)}{96}, \\ C_1^{(1)}(t) &= i \frac{Jt}{8} + \frac{h}{2J} \frac{1 - \cos^6(Jt/2)}{3}, \\ C_2^{(1)}(t) &= -i \frac{h}{2J} \frac{6Jt + 3 \sin(Jt) - 3 \sin(2Jt) - \sin(3Jt)}{96}, \\ C_3^{(1)}(t) &= -\frac{h}{2J} \frac{\sin^4(Jt/2)(\cos(Jt) + 2)}{6}, \\ C_4^{(1)}(t) &= i \frac{h}{2J} \frac{6Jt - 3 \sin(Jt) - 3 \sin(2Jt) + \sin(3Jt)}{96}, & C_5^{(1)}(t) &= \frac{h}{2J} \frac{\sin^6(Jt/2)}{3}, \\ C_6^{(1)}(t) &= -i \frac{h}{2J} \frac{30Jt - 45 \sin(Jt) + 9 \sin(2Jt) - \sin(3Jt)}{96}. \end{aligned} \quad (23)$$

## A.2 Range of applicability and effect of higher order terms

Fig. 6 shows the time evolution of transverse magnetization and nearest-neighbor spin-spin correlation obtained from the first-order cumulant expansion for different  $h/J$ . We find that for  $ht < 1$  the results from the cumulant expansion agree with the exact results to a similar extent independent of the value of  $h/J$ . For  $ht > 1$  the cumulant expansion deviates strongly from the exact results.

To second order in the cumulant expansion the wave function coefficients are approximated by

$$\begin{aligned} \frac{\psi(\vec{s}, t)}{\psi_0(\vec{s})} &= \frac{\langle \vec{s} | e^{-iHt} | \psi_0 \rangle}{\langle \vec{s} | \psi_0 \rangle} \\ &\approx e^{-iE_{\vec{s}}t} \exp \left[ -i\lambda \int_0^t dt' \frac{\langle \vec{s} | V(t') | \psi_0 \rangle}{\langle \vec{s} | \psi_0 \rangle} \right. \\ &\quad \left. - \lambda^2 \int_0^t dt' \int_0^{t'} dt'' \left( \frac{\langle \vec{s} | V(t') V(t'') | \psi_0 \rangle}{\langle \vec{s} | \psi_0 \rangle} - \frac{\langle \vec{s} | V(t') | \psi_0 \rangle \langle \vec{s} | V(t'') | \psi_0 \rangle}{\langle \vec{s} | \psi_0 \rangle^2} \right) \right]. \end{aligned} \quad (24)$$

In one dimension this yields the effective Hamilton function of the general form

$$\mathcal{H}^{(2)}(\vec{s}, t) = \sum_{n_1=0}^z \sum_{n_2=0}^z C_{n_1 n_2}(t) \sum_{l=1}^N \sum_{(a_1, \dots, a_{n_1}) \in \mathcal{V}_{n_1}^{1l}} \sum_{(b_1, \dots, b_{n_2}) \in \mathcal{V}_{n_2}^{2l}} s_l^{n_1+n_2} \prod_{r_1=1}^{n_1} s_{a_{r_1}} \prod_{r_2=1}^{n_2} s_{b_{r_2}} \quad (25)$$

where  $\mathcal{V}_n^{dl}$  denotes the set of all groups of  $n$  spins at distance  $d$  from spin  $l$ . The coupling constants are

$$\begin{aligned} C_{00}(t) &= i \frac{h}{4J} (Jt + \sin(Jt)) - \frac{h^2}{J^2} \sin(Jt/2), \\ C_{10}(t) &= i \frac{Jt}{8} + \frac{h}{4J} (1 - \cos(Jt)) + i \frac{h^2}{8J^2} (2Jt - 4 \sin(Jt) + \sin(2Jt)), \\ C_{20}(t) &= -i \frac{h}{4J} (Jt - \sin(Jt)) - \frac{h^2}{J^2} \sin(Jt/2), \\ C_{01}(t) &= \frac{h^2}{32J^2} (9 - 2J^2t^2 - 8 \cos(Jt) - \cos(2Jt) - 4Jt \sin(Jt)), \\ C_{11}(t) &= i \frac{h^2}{32J^2} (6Jt - 8Jt \cos(Jt) + \sin(2Jt)), \quad C_{21}(t) = \frac{h^2}{16J^2} (\sin(Jt) - Jt)^2, \\ C_{02}(t) &= 0, \quad C_{12}(t) = 0, \quad C_{22}(t) = 0. \end{aligned} \quad (26)$$

We observe that taking into account the second order contribution of the cumulant expansion significantly enhances the result for the next-nearest-neighbor correlation function as shown in Fig. 7. In particular it yields corrections that are much larger than what one would expect from a naive perturbative expansion.

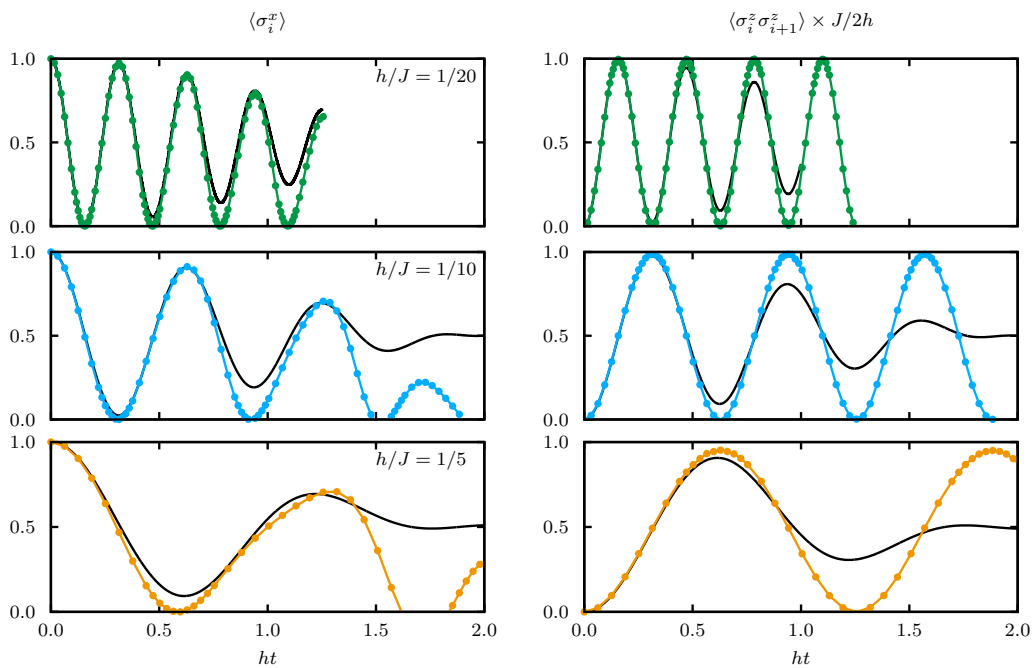


Figure 6: MC data in comparison with exact results for different  $h/J$ .

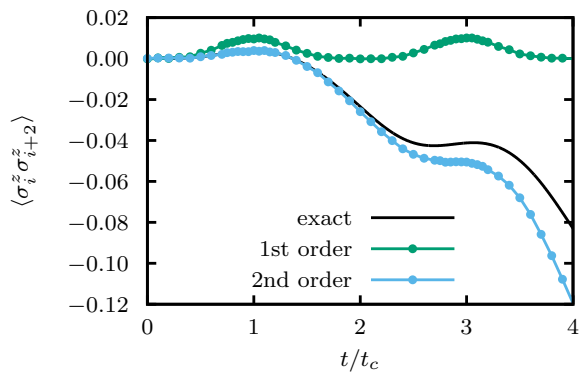


Figure 7: Next-nearest-neighbor correlation function in  $d = 1$  obtained with first-order and second-order cumulant expansion in comparison with the exact result;  $h/J = 0.05$ .



### A.3 Comparison: Complexity of the equivalent iMPS

In order to give an estimate of the complexity of the time-evolved state in terms of Matrix Product States we show the time evolution of local observables, entanglement, and bond dimension after the quench  $h_0 = \infty \rightarrow h = J/20$  computed using iTEBD [65] in Fig. 8. The bond dimension  $\chi$  was restricted to different maximal values  $\chi_{\max}$  and during the simulation Schmidt values smaller than  $10^{-10}$  were discarded. In all quantities a converged result on the time interval of interest is obtained with a maximal bond dimension of  $\chi_{\max} \geq 4$ .

For the implementation of the iTEBD algorithm the iTensor library [71] was used.

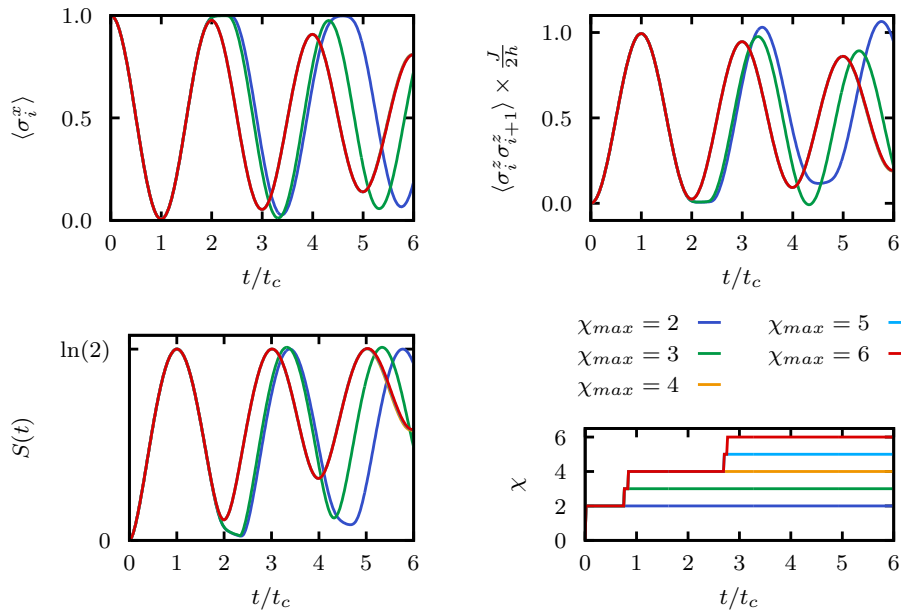


Figure 8: Dynamics for the quench from  $h_0 = \infty$  to  $h/J = 0.05$  computed with iTEBD with different maximal bond dimensions  $\chi_{\max}$ .

## B Loschmidt amplitude as classical partition function

### B.1 Real weights from decimation RG

As outlined in the results section the Loschmidt amplitude (8) after integrating out every second spin, residing on sublattice  $\Lambda$ , can be integrated out, yielding

$$Z(t) = \frac{1}{2^N} \sum_{\vec{s} \in \{\pm 1\}^{N/2}} \prod_{i \in \Lambda} 2 \cos \left( \frac{J}{4} t \sum_{\langle i, j \rangle} s_j \right). \quad (27)$$

A Hamilton function  $\mathcal{H}(\vec{s}, t)$  defining a classical network can be obtained by choosing a general ansatz including all possible  $\mathbb{Z}_2$ -symmetric couplings of spins with a common neighbor on the sublattice  $\Lambda$ , which takes the form given in Eq. (10). The Boltzmann weight of a configuration is then given by

$$e^{\mathcal{H}(\vec{s}, t)} = \prod_{l \in \Lambda} \exp \left[ \sum_{n=0}^{z/2} C_n(t) \sum_{(a_1, \dots, a_{2n}) \in \mathcal{V}_{2n}^l} \prod_{r=1}^{2n} s_{a_r} \right]. \quad (28)$$

Equating each factor in the expression above with the corresponding factor in Eq. (27) for every configuration of the involved spins yields a system of equations that determines the couplings  $C_n(t)$  [59].

In  $d = 1$  the couplings are

$$C_0(t) = \ln 2 + \frac{\ln(\cos(Jt/2))}{2}, \quad C_1(t) = \frac{\ln(\cos(Jt/2))}{2}. \quad (29)$$

The couplings in  $d = 2$  are

$$\begin{aligned} C_0(t) &= \ln 2 + \frac{\ln(\cos(Jt)) + 4 \ln(\cos(Jt/2))}{8}, & C_1(t) &= \frac{\ln(\cos(Jt))}{8}, \\ C_2(t) &= \frac{\ln(\cos(Jt)) - 4 \ln(\cos(Jt/2))}{8}. \end{aligned} \quad (30)$$

In  $d = 3$  the resulting couplings are

$$\begin{aligned} C_0(t) &= \ln 2 + \frac{\ln(\cos(3Jt/2)) + 6 \ln(\cos(Jt)) + 15 \ln(\cos(Jt/2))}{32}, \\ C_1(t) &= \frac{\ln(\cos(3Jt/2)) + 2 \ln(\cos(Jt)) - \ln(\cos(Jt/2))}{32}, \\ C_2(t) &= \frac{\ln(\cos(3Jt/2)) - 2 \ln(\cos(Jt)) - \ln(\cos(Jt/2))}{32}, \\ C_3(t) &= \frac{\ln(\cos(3Jt/2)) - 6 \ln(\cos(Jt)) + 15 \ln(\cos(Jt/2))}{32}. \end{aligned} \quad (31)$$

The time evolution of these couplings is displayed in Fig. 9.

### B.2 Monte-Carlo scheme for the Loschmidt amplitude

In order to evaluate the Loschmidt amplitude given in terms of the renormalized Boltzmann weights (28) a combination of different Monte Carlo techniques is employed. Since the Loschmidt amplitude is the normalization of the Boltzmann weights a simple Metropolis Monte Carlo sampling is not sufficient. Moreover, the Monte Carlo sampling is hindered

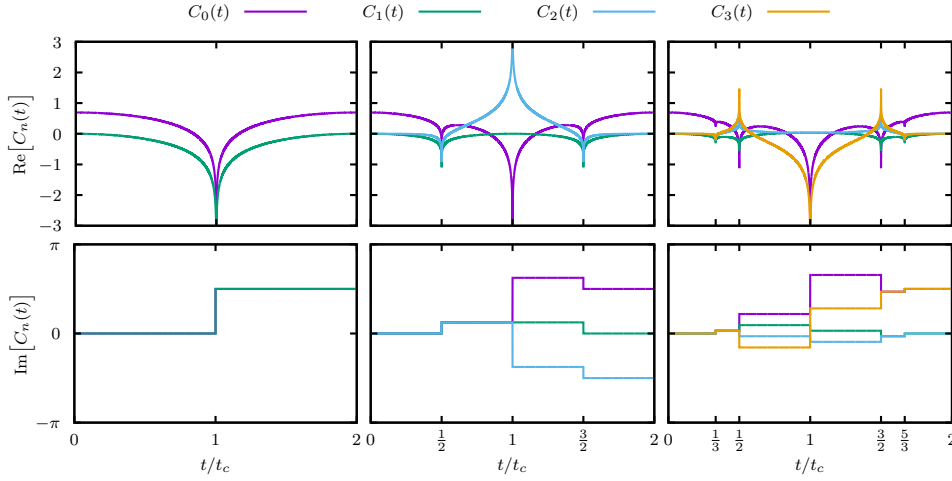


Figure 9: Time evolution of the couplings of the effective Hamiltonian function  $\mathcal{H}(\vec{s}, t)$  for the Loschmidt amplitude in one, two, and three dimensions.

by critical slowing down close to the critical times and the presence of negative weights leads to a sign problem.

The idea to deal with these issues is to sample for a given Hamiltonian function  $\mathcal{H}(\vec{s}, t)$  the energy histograms  $P_{\pm}(E) = \Omega_{\pm}(E)e^E$  where the density of states  $\Omega_{\pm}(E)$  is the number of configurations  $\vec{s}$  with energy  $E = \text{Re}\mathcal{H}(\vec{s}, t)$ . The sign index indicates the sign of the corresponding Boltzmann weight. Given a good estimate of these histograms the partition sum is simply

$$Z(t) = \sum_{E, \sigma = \pm 1} \sigma P_{\sigma}(E). \quad (32)$$

Note, however, that the histograms  $P_{\pm}(E)$  must be properly normalized in order to get the correct result for  $Z(t)$ . In order to obtain a good estimate of the normalized histogram we combine the following techniques:

1. *Separate sampling of factor graphs.* In order to overcome the sign problem the configuration space  $\mathcal{X} = \{\pm 1\}^{N'}$  is separated into  $\mathcal{X}_+ = \{\vec{s} | e^{\mathcal{H}(\vec{s}, t)} > 0\}$  and  $\mathcal{X}_- = \{\vec{s} | e^{\mathcal{H}(\vec{s}, t)} < 0\}$ ;  $N'$  is the number renormalized spins. Then the partition sum is split as

$$\begin{aligned} Z(t) &= Z_+(t) + Z_-(t), \\ Z_{\pm} &= \sum_{\vec{s} \in \mathcal{X}_{\pm}} e^{\mathcal{H}(\vec{s}, t)} = \pm \sum_E P_{\pm}(E). \end{aligned} \quad (33)$$

The partition sums  $Z_{\pm}$  can be sampled separately as described in Ref. [61].

2. *Importance sampling.* When sampling the energy  $E$  in an importance sampling scheme with weights  $e^E$  the relative frequency of samples with energy  $E$  is proportional to  $P_{\pm}(E) = \Omega_{\pm}(E)e^E$ . Therefore, a histogram of the energies sampled with Metropolis Monte Carlo updates yields the desired histograms up to normalization. Moreover, the importance sampling allows to choose the region in the energy spectrum that is sampled by introducing an artificial temperature as described next.
3. *Parallel tempering.* Parallel tempering [62] is a method to improve the sampling efficiency in strongly peaked multi-modal distributions, which occurs in our case

close to the critical times. The idea of parallel tempering is to perform a Markov Chain Monte-Carlo (MCMC) sampling on several copies of a system at different temperatures. During the sampling the system configurations are not only updated as usual but also configuration swaps between adjacent temperatures are possible. Thereby a MCMC on the temperatures is performed allowing the system to jump between different peaks of the distribution.

In the present case a distribution with weights  $w(\vec{s}, t) = e^{\mathcal{H}(\vec{s}, t)}$  shall be sampled. Introducing an artificial temperature  $\beta$  yields weights

$$w_\beta(\vec{s}, t) = e^{\beta \mathcal{H}(\vec{s}, t)} . \quad (34)$$

At  $\beta = 1$  the sampling is inefficient due to the diverging renormalized weights of the Hamilton function (see bottom panels in Fig. 4). This problem is attenuated if we sample with a parallel tempering scheme with temperatures  $1 = \beta_1 > \beta_2 > \dots > \beta_N$ . Moreover, parallel tempering is beneficial, because histograms  $P_\pm^\beta(E) = \Omega_\pm(E) e^{\beta E}$  are obtained as a byproduct, which capture different regions of the spectrum with high precision. This can be used to obtain decent precision over the whole range of energies and thereby a properly normalized histogram as described next.

4. *Multiple histogram reweighting.* In order to get a good histogram for  $P_\pm(E)$  in the whole energy range the fact that

$$P_\pm^{\beta_1}(E) = e^{(\beta_1 - \beta_0)E} P_\pm^{\beta_0}(E) \quad (35)$$

can be exploited. In the multiple histogram reweighting procedure [63] the histograms obtained at the different temperatures are combined to yield a histogram covering the whole energy range. This allows us to normalize the histogram at  $\beta = 0$ , where

$$\sum_{E, \sigma = \pm 1} |P_\sigma^{\beta=0}(E)| = 2^{N'} . \quad (36)$$

### B.3 Simplification of effective systems close to $t_c$

For times  $t$  close to the critical time  $t_c$  the effective classical networks can be simplified, because some of the couplings become very small, as evident from Fig. 4 and also Fig. 9, and the Hamilton functions dominated by the divergent contributions. This simplification can be exploited for additional insights into the behavior of the Loschmidt amplitude close to the critical time. In the following we will discuss the case  $d = 2$ , but the arguments hold similarly for  $d = 3$ .

Dropping contributions to the couplings that vanish at  $t_c$  the partition sum close to  $t_c$  can be approximated by

$$Z(t) \approx \frac{1}{2^{N'}} \sum_{\vec{s} \in \{\pm 1\}^{N'}} \sigma_{\vec{s}} e^{-\beta(t) \mathcal{H}(\vec{s})} \quad (37)$$

with an effective temperature  $\beta(t) = -\ln(\cos(Jt/2))/2$ , the number of remaining spins  $N' = N/2$ ,  $\sigma_{\vec{s}} = \pm 1$  the sign of the weight of the configuration  $\vec{s}$ , and

$$\mathcal{H}(\vec{s}) = \sum_{i,j} (1 - s_{i,j} s_{i+1,j} s_{i,j+1} s_{i+1,j+1}) . \quad (38)$$

The minimal energy of the network defined by  $\mathcal{H}(\vec{s})$  is obviously reached when the condition

$$s_{i,j} s_{i+1,j} s_{i,j+1} s_{i+1,j+1} = 1 \quad (39)$$

is fulfilled on each plaquette. This is possible in systems where the edge lengths of the system,  $N'_x$  and  $N'_y$ , are both even, to which we restrict the following discussion. To obtain a “ground state” it is sufficient to fix the spin configuration in one row and in one column. The state of the remaining spins is then determined by the condition (39). Hence, the ground state is  $2^{N'_x+N'_y-1}$ -fold degenerate.

From Eq. (27) we know that the sign of the corresponding Boltzmann weight is determined by the number of plaquettes with  $|s_{i,j} + s_{i+1,j} + s_{i,j+1} + s_{i+1,j+1}| = 4$ . If there is an even number of plaquettes with this property, the configuration has a positive Boltzmann weight, otherwise it is negative. We find that for even edge lengths the ground states always have positive Boltzmann weights.

Let us now introduce the density of states  $\Omega_{\pm}(E)$ , i.e. the number of spin configurations  $\vec{s}$  with the same real part of the energy  $E = \mathcal{H}(\vec{s}, t)$  and  $\text{sgn}(e^{\mathcal{H}(\vec{s}, t)}) = \pm 1$ , in order to rewrite the sum over configurations in Eq. (37) as a sum over energies,

$$Z(t) = \frac{1}{2^{N'}} \sum_{E, \sigma = \pm 1} \sigma \Omega_{\sigma}(E) e^{-\beta(t)E}. \quad (40)$$

From the above analysis of the ground state we know that  $\Omega_+(0) = 2^{N'_x+N'_y-1}$ . In the limit  $t \rightarrow t_c$ , or equivalently  $\beta \rightarrow \infty$ , this is the only contribution that does not vanish in the sum. Therefore,  $Z(t_c) = 2^{N'_x+N'_y-1-N'}$  and

$$\lambda_N(t_c) = \left( \frac{1}{2} - \frac{N'_x + N'_y - 1}{N} \right) \ln 2 \xrightarrow{N \rightarrow \infty} \frac{\ln 2}{2}, \quad (41)$$

which determines the value of the rate function at  $t_c$  in the thermodynamic limit and the finite size correction.

We would like to remark that classical spin systems of the form (38) were studied in the literature and can be solved analytically for real temperatures [72, 73]. We found, however, that introducing a sign into the partition sum renders the analytical summation impossible.

## C Exemplary derivation of ANN couplings from the cumulant expansion

### C.1 $d = 1$

From the cumulant expansion (18) we have

$$\mathcal{P}_l(\vec{s}, t) = C_0(t) + C_1(t)s_l(s_{l-1} + s_{l+1}) + C_2(t)s_{l-1}s_{l+1}, \quad (42)$$

i.e.

$$\psi(\vec{s}) = \prod_l \exp(C_0(t) + C_1(t)s_l(s_{l-1} + s_{l+1}) + C_2(t)s_{l-1}s_{l+1}). \quad (43)$$

A patch consists of three consecutive spins and swapping the two spins at the border leaves the weight unchanged.

A possible ansatz for the ANN with one hidden spin per lattice site (see Fig. 5(a) of the main text), that respects the symmetries, is

$$\psi(\vec{s}) = \left(\frac{\Omega}{2}\right)^N \sum_{\vec{u}^{(1)}, \vec{u}^{(2)}} \exp\left(\sum_l (W_1(s_{l-1} + s_{l+1}) + W_2 s_l) u_l\right), \quad (44)$$

where  $\Omega$  constitutes a overall normalization and phase that is irrelevant when expectation values are computed with the Metropolis algorithm. Integrating out the hidden spins yields

$$\psi(\vec{s}) = \prod_l \Omega \cosh(W_1(s_{l-1} + s_{l+1}) + W_2 s_l) \quad (45)$$

Identifying the single factors yields for the different possible spin configurations (in the following we abbreviate  $\cosh$  by  $\text{ch}$ )

$$\begin{aligned} \uparrow\uparrow\uparrow: \quad \Omega \text{ch}(2W_1 + W_2) &= \exp(C_0 + 2C_1 + C_2) \\ \uparrow\uparrow\downarrow: \quad \Omega \text{ch}(W_2) &= \exp(C_0 - C_2) \\ \uparrow\downarrow\uparrow: \quad \Omega \text{ch}(2W_1 - W_2) &= \exp(C_0 - 2C_1 + C_2) \end{aligned} \quad (46)$$

All other spin configurations are connected to these via  $\mathbb{Z}_2$  symmetry. This is an implicit equation for the ANN weights that can be solved numerically. One solution for the weights obtained from the 1st order cumulant expansion is plotted in Fig. 5(b) of the main text. Note that these equations have different possible solutions.

### C.2 $d = 2$

From the cumulant expansion (20) we have

$$\begin{aligned} \mathcal{P}_l(\vec{s}, t) &= C_0^{(1)}(t) + C_1^{(1)}(t) \sum_{a \in \mathcal{V}_1^l} s_a^z s_l^z + C_2^{(1)}(t) \sum_{(a,b) \in \mathcal{V}_2^l} s_a^z s_b^z \\ &+ C_3^{(1)}(t) \sum_{(a,b,c) \in \mathcal{V}_3^l} s_a^z s_b^z s_c^z s_l^z + C_4^{(1)}(t) \sum_{(a,b,c,d) \in \mathcal{V}_4^l} s_a^z s_b^z s_c^z s_d^z \end{aligned} \quad (47)$$



A patch consists of a central spin  $s_{i,j}$  and four neighboring spins as depicted by the black dots in Fig. 4a in the main text. Any permutation of the surrounding spins leaves  $\mathcal{P}_l(\vec{s}, t)$  unchanged.

A possible ansatz for the ANN with five hidden spins per lattice site is depicted in Fig. 5(c) of the main text. After integrating out the hidden spins the wave function is given by

$$\begin{aligned} \psi(\vec{s}) = \Omega \prod_l & \text{ch}\left(W_1^{(1)} s_{i,j}\right) \text{ch}\left(W_1^{(1)} s_{i,j} + W_2^{(1)}(s_{i,j+1} + s_{i,j-1} + s_{i+1,j} + s_{i-1,j})\right) \\ & \times \text{ch}\left(W_1^{(2)} s_{i,j} + W_2^{(2)}(s_{i,j+1} + s_{i,j-1} + s_{i+1,j})\right) \\ & \times \text{ch}\left(W_1^{(2)} s_{i,j} + W_2^{(2)}(s_{i,j+1} + s_{i,j-1} + s_{i-1,j})\right) \\ & \times \text{ch}\left(W_1^{(2)} s_{i,j} + W_2^{(2)}(s_{i+1,j} + s_{i-1,j} + s_{i,j+1})\right) \\ & \times \text{ch}\left(W_1^{(2)} s_{i,j} + W_2^{(2)}(s_{i+1,j} + s_{i-1,j} + s_{i,j-1})\right) \end{aligned} \quad (48)$$

Identifying the single factors yields for the different possible spin configurations

$$\begin{aligned} \uparrow\uparrow\uparrow\uparrow: & \quad \Omega \text{ch}\left(W_1^{(1)} + 4W_2^{(1)}\right) \text{ch}\left(W_1^{(2)} + 3W_2^{(2)}\right)^4 \\ & = \exp\left(4C_1 + 4C_3 + C_0 + 6C_2 + C_4\right) \\ \uparrow\uparrow\uparrow\downarrow: & \quad \Omega \text{ch}\left(W_1^{(1)} + 2W_2^{(1)}\right) \text{ch}\left(W_1^{(2)} + 3W_2^{(2)}\right) \text{ch}\left(W_1^{(2)} + W_2^{(2)}\right)^3 \\ & = \exp\left(2C_1 - 2C_3 + C_0 - C_4\right) \\ \uparrow\uparrow\downarrow\downarrow: & \quad \Omega \text{ch}\left(W_1^{(1)}\right) \text{ch}\left(W_1^{(2)} + W_2^{(2)}\right)^2 \text{ch}\left(W_1^{(2)} - W_2^{(2)}\right)^2 \\ & = \exp\left(C_0 - 2C_2 + C_4\right) \\ \downarrow\uparrow\uparrow\uparrow: & \quad \Omega \text{ch}\left(-W_1^{(1)} + 4W_2^{(1)}\right) \text{ch}\left(-W_1^{(2)} + 3W_2^{(2)}\right)^4 \\ & = \exp\left(-4C_1 - 4C_3 + C_0 + 6C_2 + C_4\right) \\ \downarrow\uparrow\uparrow\downarrow: & \quad \Omega \text{ch}\left(-W_1^{(1)} + 2W_2^{(1)}\right) \text{ch}\left(-W_1^{(2)} + 3W_2^{(2)}\right) \text{ch}\left(-W_1^{(2)} + W_2^{(2)}\right)^3 \\ & = \exp\left(-2C_1 + 2C_3 + C_0 - C_4\right) \end{aligned} \quad (49)$$

where the leftmost arrow in the spin configurations corresponds to the central spin of the patch. One solution for the weights obtained from the 1st order cumulant expansion is plotted in Fig. 5(d) of the main text.

## References

- [1] S. R. White, *Density matrix formulation for quantum renormalization groups*, Phys. Rev. Lett. **69**, 2863 (1992), doi:10.1103/PhysRevLett.69.2863.
- [2] U. Schollwöck, *The density-matrix renormalization group in the age of matrix product states*, Annals of Physics **326**(1), 96 (2011), doi:http://dx.doi.org/10.1016/j.aop.2010.09.012.
- [3] R. Orús, *A practical introduction to tensor networks: Matrix product states and projected entangled pair states*, Annals of Physics **349**, 117 (2014), doi:http://dx.doi.org/10.1016/j.aop.2014.06.013.
- [4] A. Georges, G. Kotliar, W. Krauth and M. J. Rozenberg, *Dynamical mean-field theory of strongly correlated fermion systems and the limit of infinite dimensions*, Rev. Mod. Phys. **68**, 13 (1996), doi:10.1103/RevModPhys.68.13.
- [5] D. Vollhardt, *Dynamical mean-field theory for correlated electrons*, Annalen der Physik **524**(1), 1 (2012), doi:10.1002/andp.201100250.
- [6] J. K. Freericks, V. M. Turkowski and V. Zlatić, *Nonequilibrium Dynamical Mean-Field Theory*, Phys. Rev. Lett. **97**, 266408 (2006), doi:10.1103/PhysRevLett.97.266408.
- [7] H. Aoki, N. Tsuji, M. Eckstein, M. Kollar, T. Oka and P. Werner, *Nonequilibrium dynamical mean-field theory and its applications*, Rev. Mod. Phys. **86**, 779 (2014), doi:10.1103/RevModPhys.86.779.
- [8] U. Schneider, L. Hackermüller, J. P. Ronzheimer, S. Will, S. Braun, T. Best, I. Bloch, E. Demler, S. Mandt, D. Rasch and A. Rosch, *Fermionic transport and out-of-equilibrium dynamics in a homogeneous Hubbard model with ultracold atoms*, Nat Phys **8**, 213 (2012), doi:10.1038/nphys2205.
- [9] J.-y. Choi, S. Hild, J. Zeiher, P. Schauß, A. Rubio-Abadal, T. Yefsah, V. Khemani, D. A. Huse, I. Bloch and C. Gross, *Exploring the many-body localization transition in two dimensions*, Science **352**(6293), 1547 (2016), doi:10.1126/science.aaf8834.
- [10] M. Mitrano, A. Cantaluppi, D. Nicoletti, S. Kaiser, A. Perucchi, S. Lupi, P. Di Pietro, D. Pontiroli, M. Riccò, S. R. Clark, D. Jaksch and A. Cavalleri, *Possible light-induced superconductivity in K3C60 at high temperature*, Nature **530**, 461 (2016), doi:10.1038/nature16522.
- [11] N. Fläschner, D. Vogel, M. Tarnowski, B. Rem, D.-S. Lühmann, M. Heyl, H. Budich, L. Mathey, K. Sengstock and C. Weitenberg, *Observation of a dynamical topological phase transition*, arXiv:1608.05616 (2016).
- [12] S. Hild, T. Fukuhara, P. Schauß, J. Zeiher, M. Knap, E. Demler, I. Bloch and C. Gross, *Far-from-Equilibrium Spin Transport in Heisenberg Quantum Magnets*, Phys. Rev. Lett. **113**, 147205 (2014), doi:10.1103/PhysRevLett.113.147205.
- [13] P. Bordia, H. Lüschen, S. Scherg, S. Gopalakrishnan, M. Knap, U. Schneider and I. Bloch, *Probing Slow Relaxation and Many-Body Localization in Two-Dimensional Quasi-Periodic Systems*, arXiv:1704.03063 (2017).
- [14] W. L. McMillan, *Ground State of Liquid He<sup>4</sup>*, Phys. Rev. **138**, A442 (1965), doi:10.1103/PhysRev.138.A442.

- [15] S. Sorella, *Wave function optimization in the variational Monte Carlo method*, Phys. Rev. B **71**, 241103 (2005), doi:10.1103/PhysRevB.71.241103.
- [16] M. Capello, F. Becca, M. Fabrizio and S. Sorella, *Superfluid to Mott-Insulator Transition in Bose-Hubbard Models*, Phys. Rev. Lett. **99**, 056402 (2007), doi:10.1103/PhysRevLett.99.056402.
- [17] G. Carleo, F. Becca, M. Schiró and M. Fabrizio, *Localization and Glassy Dynamics Of Many-Body Quantum Systems*, Scientific Reports **2**, 243 (2012), doi:10.1038/srep00243.
- [18] G. Carleo, F. Becca, L. Sanchez-Palencia, S. Sorella and M. Fabrizio, *Light-cone effect and supersonic correlations in one- and two-dimensional bosonic superfluids*, Phys. Rev. A **89**, 031602 (2014), doi:10.1103/PhysRevA.89.031602.
- [19] L. Cevolani, G. Carleo and L. Sanchez-Palencia, *Protected quasilocality in quantum systems with long-range interactions*, Phys. Rev. A **92**, 041603 (2015), doi:10.1103/PhysRevA.92.041603.
- [20] B. Blaß and H. Rieger, *Test of quantum thermalization in the two-dimensional transverse-field Ising model*, Scientific Reports **6**, 38185 (2016), doi:10.1038/srep38185.
- [21] J. Hafner, B. Blass and H. Rieger, *Light cone in the two-dimensional transverse-field ising model in time-dependent mean-field theory*, EPL (Europhysics Letters) **116**(6), 60002 (2016).
- [22] G. Carleo, L. Cevolani, L. Sanchez-Palencia and M. Holzmann, *Unitary Dynamics of Strongly Interacting Bose Gases with the Time-Dependent Variational Monte Carlo Method in Continuous Space*, Phys. Rev. X **7**, 031026 (2017), doi:10.1103/PhysRevX.7.031026.
- [23] G. Carleo and M. Troyer, *Solving the quantum many-body problem with artificial neural networks*, Science **355**(6325) (2017).
- [24] D.-L. Deng, X. Li and S. Das Sarma, *Exact Machine Learning Topological States*, arXiv:1609.09060 (2016).
- [25] D.-L. Deng, X. Li and S. Das Sarma, *Quantum Entanglement in Neural Network States*, Phys. Rev. X **7**, 021021 (2017), doi:10.1103/PhysRevX.7.021021.
- [26] Y. Huang and J. Moore, *Neural network representation of tensor network and chiral states*, arXiv:1701.06246 (2017).
- [27] J. Chen, S. Cheng, H. Xie, L. Wang and T. Xiang, *On the Equivalence of Restricted Boltzmann Machines and Tensor Network States*, arXiv:1701.04831 (2017).
- [28] G. Torlai, G. Mazzola, J. Carrasquilla, M. Troyer, R. Melko and G. Carleo, *Many-body quantum state tomography with neural networks*, arXiv:1703.05334 (2017).
- [29] Z. Cai, *Approximating quantum many-body wave-functions using artificial neural networks*, arXiv:1704.05148 (2017).
- [30] X. Gao and L.-M. Duan, *Efficient Representation of Quantum Many-Body States with Deep Neural Networks*, arXiv:1701.05039 (2017).

- [31] J. C. B. Raphael Kaubruegger, Lorenzo Pastori, *Chiral Topological Phases from Artificial Neural Networks*, arXiv:1710.04713 (2017).
- [32] H. Bernien, S. Schwartz, A. Keesling, H. Levine, A. Omran, H. Pichler, S. Choi, A. S. Zibrov, M. Endres, M. Greiner, V. Vuletić and M. D. Lukin, *Probing many-body dynamics on a 51-atom quantum simulator*, arXiv:1707.04344 (2017).
- [33] E. Guardado-Sanchez, P. T. Brown, D. Mitra, T. Devakul, D. A. Huse, P. Schauss and W. S. Bakr, *Probing quench dynamics across a quantum phase transition into a 2D Ising antiferromagnet*, arXiv:1711.00887 (2017).
- [34] P. Jurcevic, H. Shen, P. Hauke, C. Maier, T. Brydges, C. Hempel, B. Lanyon, M. Heyl, R. Blatt and C. Roos, *Direct observation of dynamical quantum phase transitions in an interacting many-body system*, arXiv:1612.06902 (2016).
- [35] M. Heyl, A. Polkovnikov and S. Kehrein, *Dynamical Quantum Phase Transitions in the Transverse-Field Ising Model*, Phys. Rev. Lett. **110**, 135704 (2013), doi:10.1103/PhysRevLett.110.135704.
- [36] M. Heyl, *Dynamical quantum phase transitions: a review*, arXiv:1709.07461 (2017).
- [37] F. Pollmann, S. Mukerjee, A. G. Green and J. E. Moore, *Dynamics after a sweep through a quantum critical point*, Phys. Rev. E **81**, 020101 (2010), doi:10.1103/PhysRevE.81.020101.
- [38] C. Karrasch and D. Schuricht, *Dynamical phase transitions after quenches in nonintegrable models*, Phys. Rev. B **87**, 195104 (2013), doi:10.1103/PhysRevB.87.195104.
- [39] J. N. Kriel, C. Karrasch and S. Kehrein, *Dynamical quantum phase transitions in the axial next-nearest-neighbor ising chain*, Phys. Rev. B **90**, 125106 (2014), doi:10.1103/PhysRevB.90.125106.
- [40] A. J. A. James and R. M. Konik, *Quantum quenches in two spatial dimensions using chain array matrix product states*, Phys. Rev. B **92**, 161111 (2015), doi:10.1103/PhysRevB.92.161111.
- [41] M. Heyl, *Scaling and Universality at Dynamical Quantum Phase Transitions*, Phys. Rev. Lett. **115**, 140602 (2015), doi:10.1103/PhysRevLett.115.140602.
- [42] N. O. Abeling and S. Kehrein, *Quantum quench dynamics in the transverse field Ising model at nonzero temperatures*, Phys. Rev. B **93**, 104302 (2016), doi:10.1103/PhysRevB.93.104302.
- [43] S. Sharma, U. Divakaran, A. Polkovnikov and A. Dutta, *Slow quenches in a quantum Ising chain: Dynamical phase transitions and topology*, Phys. Rev. B **93**, 144306 (2016), doi:10.1103/PhysRevB.93.144306.
- [44] B. Zunkovic, M. Heyl, M. Knap and A. Silva, *Dynamical Quantum Phase Transitions in Spin Chains with Long-Range Interactions: Merging different concepts of non-equilibrium criticality*, arXiv:1609.08482 (2016).
- [45] J. Halimeh and V. Zauner-Stauber, *Enriching the dynamical phase diagram of spin chains with long-range interactions*, arXiv:1610.02019 (2016).
- [46] M. Heyl, *Quenching a quantum critical state by the order parameter: Dynamical quantum phase transitions and quantum speed limits*, Phys. Rev. B **95**, 060504 (2017), doi:10.1103/PhysRevB.95.060504.

- [47] I. Homrighausen, N. O. Abeling, V. Zauner-Stauber and J. C. Halimeh, *Anomalous dynamical phase in quantum spin chains with long-range interactions*, Phys. Rev. B **96**, 104436 (2017), doi:10.1103/PhysRevB.96.104436.
- [48] R. Kubo, *Generalized Cumulant Expansion Method*, Journal of the Physical Society of Japan **17**(7) (1962).
- [49] N. Metropolis, A. Rosenbluth, M. Rosenbluth, A. Teller and E. Teller, *Equation of State Calculations by Fast Computing Machines*, The Journal of Chemical Physics **21** (1953).
- [50] E. Lieb, T. Schultz and D. Mattis, *Two soluble models of an antiferromagnetic chain*, Annals of Physics **16**(3), 407 (1961).
- [51] P. Pfeuty, *The one-dimensional Ising model with a transverse field*, Annals of Physics **57**(1), 79 (1970).
- [52] P. Calabrese, F. H. L. Essler and M. Fagotti, *Quantum quench in the transverse field Ising chain: I. Time evolution of order parameter correlators*, Journal of Statistical Mechanics: Theory and Experiment **2012**(07), P07016 (2012).
- [53] G. Vidal, J. I. Latorre, E. Rico and A. Kitaev, *Entanglement in quantum critical phenomena*, Phys. Rev. Lett. **90**(quant-ph/0211074), 227902. 5 p (2002).
- [54] J. I. Latorre, E. Rico and G. Vidal, *Ground State Entanglement in Quantum Spin Chains*, Quantum Info. Comput. **4**(1), 48 (2004).
- [55] P. A. M. Dirac, *Note on Exchange Phenomena in the Thomas Atom*, Mathematical Proceedings of the Cambridge Philosophical Society **26**(3), 376–385 (1930), doi:10.1017/S0305004100016108.
- [56] R. Jackiw and A. Kerman, *Time-dependent variational principle and the effective action*, Physics Letters A **71**(2), 158 (1979), doi:http://dx.doi.org/10.1016/0375-9601(79)90151-8.
- [57] J. Haegeman, J. I. Cirac, T. J. Osborne, I. Pizorn, H. Verschelde and F. Verstraete, *Time-Dependent Variational Principle for Quantum Lattices*, Phys. Rev. Lett. **107**, 070601 (2011), doi:10.1103/PhysRevLett.107.070601.
- [58] E. Martinez, C. Muschik, P. Schindler, D. Nigg, A. Erhard, M. Heyl, P. Hauke, M. Dalmonte, T. Monz, P. Zoller and R. Blatt, *Real-time dynamics of lattice gauge theories with a few-qubit quantum computer*, Nature **534**, 516 (2016), doi:10.1038/nature18318.
- [59] B. Hu, *Introduction to real-space renormalization-group methods in critical and chaotic phenomena*, Physics Reports **91**(5), 233 (1982), doi:https://doi.org/10.1016/0370-1573(82)90057-6.
- [60] J. Markham and T. Kieu, *Simulations with complex measure*, Nuclear Physics B **516**(3) (1998).
- [61] M. Molkaiaie and H.-A. Loelinger, *Extending Monte Carlo methods to factor graphs with negative and complex factors*, Proc. 2012 IEEE Information Theory Workshop p. 367–371 (2012).

- [62] D. Earl and M. Deem, *Parallel tempering: theory, applications, and new perspectives.*, Phys Chem Chem Phys **7**(23), 3910 (2005).
- [63] A. M. Ferrenberg and R. H. Swendsen, *Optimized Monte Carlo data analysis*, Phys. Rev. Lett. **63**, 1195 (1989), doi:10.1103/PhysRevLett.63.1195.
- [64] S. Sachdev, *Quantum Phase Transitions*, Cambridge University Press, Cambridge (2011).
- [65] J. A. Kjäll, M. P. Zaletel, R. S. K. Mong, J. H. Bardarson and F. Pollmann, *Phase diagram of the anisotropic spin-2 XXZ model: Infinite-system density matrix renormalization group study*, Phys. Rev. B **87**, 235106 (2013), doi:10.1103/PhysRevB.87.235106.
- [66] R. Nandkishore and D. A. Huse, *Many-Body Localization and Thermalization in Quantum Statistical Mechanics*, Ann Rev of Cond Matt Phys **6**(1), 15 (2015), doi:10.1146/annurev-conmatphys-031214-014726.
- [67] E. Altman and R. Vosk, *Universal Dynamics and Renormalization in Many-Body-Localized Systems*, Ann Rev of Cond Matt Phys **6**(1), 383 (2015), doi:10.1146/annurev-conmatphys-031214-014701.
- [68] M. Schreiber, S. S. Hodgman, P. Bordia, H. P. Lüschen, M. H. Fischer, R. Vosk, E. Altman, U. Schneider and I. Bloch, *Observation of many-body localization of interacting fermions in a quasirandom optical lattice*, Science **349**(6250), 842 (2015), doi:10.1126/science.aaa7432.
- [69] J. Smith, A. Lee, P. Richerme, B. Neyenhuis, P. W. Hess, P. Hauke, M. Heyl, D. A. Huse and C. Monroe, *Many-body localization in a quantum simulator with programmable random disorder*, Nat Phys **12**, 907 (2016), doi:10.1038/nphys3783.
- [70] C. Sanderson and R. Curtin, *Armadillo: a template-based C++ library for linear algebra*, Journal of Open Source Software **1**, 26 (2016).
- [71] <http://itensor.org/>, version 2.1.0.
- [72] M. Suzuki, *Solution and Critical Behavior of Some "Three-Dimensional" Ising Models with a Four-Spin Interaction*, Phys. Rev. Lett. **28**, 507 (1972), doi:10.1103/PhysRevLett.28.507.
- [73] M. Mueller, D. A. Johnston and W. Janke, *Exact solutions to plaquette Ising models with free and periodic boundaries*, Nucl Phys B **914**, 388 (2017), doi:http://dx.doi.org/10.1016/j.nuclphysb.2016.11.005.

# Chapter 4

## Irreversibility

The question of irreversibility is of elementary importance to understand the interface between the fundamental microscopic laws of motion and statistical physics. All microscopic theories of physics are symmetric under time reversal.<sup>1</sup> This means that for any process that can occur according to the laws of motion the time-inverse process is also possible. Notwithstanding this, the Second Law of thermodynamics states that as time proceeds entropy cannot decrease in a closed system. This clearly distinguishes a preferred direction of time.

The problem of irreversibility can be explained intuitively thinking of hypothetical video recordings of a flying football and a latte macchiato. Assume the recording of the football shows the ball flying through the field of view in front of a blue sky. The ball moves on a parabolic trajectory from the left to the right edge of the screen. Subsequently the recording is played in reverse and the screen shows the ball flying from the right to the left. Can the spectator decide in which of both cases the video was played in the actual direction of recording? The answer is no. Only based on the trajectory of the ball it is impossible to tell what is the direction of time. This fact is a manifestation of the time reversal symmetry of Newton's equation of motion. Considering the recording of a latte macchiato, instead, the spectator will easily be able to tell whether the recording is played forward or backward. If the initially separate layers of milk and coffee mix to form a brown sludge the video is with certainty played forward – a brown sludge spontaneously unmixing to form two separate layers was as of yet never observed. Although intuitive, this fact is at first surprising, since after all the single molecules in the latte macchiato observe the same laws of nature as the football.

The emergence of irreversibility in classical systems is understood as a consequence of chaotic dynamics, as will be outlined in Section 4.1. This understanding is, however, not directly transferable to quantum systems. In the subsequent sections a possible definition of irreversibility in quantum many-body systems based on imperfect effective time reversal is proposed and investigated in different settings. The results suggest relations to out-of-time-order correlators, which are close to equilibrium known as probe of a quantum butterfly effect and as indicators of loss of local information under time evolution. To investigate possible connections, out-of-time-order correlators are studied far from equilibrium in Section

---

<sup>1</sup> An exception is the weak force, which is, however, irrelevant for typical many-body phenomena.



4.5. Finally, in Section 4.6 the echo dynamics of the Sachdev-Ye-Kitaev model, which is of particular interest in studies of quantum chaos, is analyzed using a semiclassical approach.

## 4.1 Emergence of effective irreversibility despite time reversal invariance

The origin of irreversible dynamics on the macroscopic level in spite of the time reversal symmetry of the underlying microscopic laws of motion already intrigued the founding fathers of thermodynamics and statistical mechanics. In a seminal work Boltzmann derived the  $H$ -theorem (Boltzmann, 1872), which states that in a gas of colliding particles the entropy  $S$  cannot decrease over time,

$$\frac{dS}{dt} \geq 0 . \quad (4.1)$$

In his article Boltzmann claimed that his derivation provided an analytical proof of the Second Law. This result, however, puzzled Loschmidt, who in response hinted at the time reversal symmetry of Newton’s equations of motion (Loschmidt, 1876). He pointed out that in any system of classical particles the dynamics can be inverted by inverting all momenta. Due to this effective time reversal the system should evolve back to its initial state. Tradition has it, though, that Boltzmann’s plain response was “Then try and do it!”. This quotation essentially gets to the heart of the matter as it was also explained more elaborately in (Boltzmann, 1877) and by (Thompson, 1874).

The modern understanding of irreversibility makes use of the notion of chaos, which was only developed in the twentieth century (Lorenz, 1963; Strogatz, 2014). Systems with many degrees of freedom are typically chaotic, i.e., the dynamics exhibits an exponential sensitivity to small perturbations. This means that any small imperfection that occurs when manipulating the system in order to invert the momenta will grow exponentially in the course of time and therefore inhibit the recovery of the initial state. Since imperfections are inevitable in any experimental realization, it is understood that classical many-body systems are irreversible for all practical purposes although the microscopic dynamics is not.

The irreversible nature of the dynamics is very prominently revealed when considering an ordered initial state and a time evolution that is effectively reverted at some point including a small imperfection. Fig. 4.1 displays an example simulation of suchlike dynamics. The system consists of classical hard spheres in a box, which interact by elastic collisions. Initially all spheres are located in the bottom half of the box and only one moves with a momentum indicated by the attached arrow. The moving particle kicks off the others, which subsequently distribute uniformly over the box as shown in the momentary configurations at time slices  $t = 5, 10, 15, 20$ . At time  $t = 20$  the momenta of all particles are inverted with six-digit precision (an imperfection not resolvable by the eye). In the following the system partially recovers the initial order in that at times  $t = 35$  and  $t = 40$  there is an overbalance of particles in the bottom half; but, clearly, there is a strong discrepancy between the initial ordered configuration and the configuration reached after imperfect effective time reversal at time  $t = 40$ . The dynamics of the system is effectively irreversible.

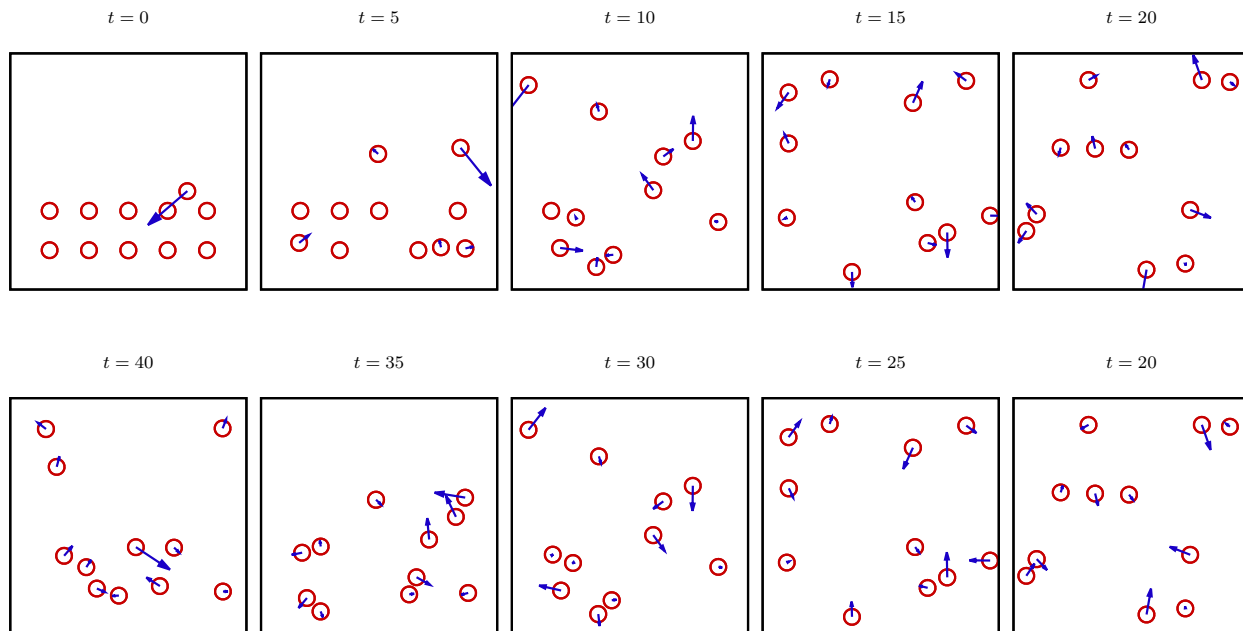


**Fig. 4.1:** Imperfect effective time reversal in a classical system. The initially ordered state at  $t = 0$  evolves to a uniform state at  $t = 20$ . As is evident from the configuration at  $t = 40$  a tiny perturbation in the time-reversal operation at  $t = 20$  prevents the system from returning to the initial state due to the chaotic nature of the dynamics.

For the effective time reversal protocols the chaotic nature of the dynamics does not only imply a deviation from perfect recovery that grows exponentially with the waiting time. In addition, any effort to improve the manipulation precision in order to get closer to the initial state is ultimately futile. The chaotic dynamics is characterized by a maximal *Lyapunov exponent* that determines the divergence of initially close-by trajectories. This rate is independent of the distance between the two initial configurations. As a consequence, aiming at a fixed degree to which the initial state is recovered when performing effective time reversal any effort to enhance the precision only extends the possible waiting time logarithmically. In this sense classical chaos imposes an exponential barrier that inhibits recovery of the initial state in practice.

In order to explain the origin of irreversibility in quantum systems it is not possible to directly transfer the knowledge about classical systems. The chaotic dynamics of classical systems originates in the nonlinearity of the equations of motion. By contrast, the time evolution of quantum systems at the level of the wave function is inherently linear. Since it is moreover unitary, the resemblance of two states quantified by their overlap is unchanged under the dynamics. Hence, in the view of overlaps the divergence of close-by initial states is not just slower than exponential – it is completely absent. In the context of quantum systems it is thus not only unclear how irreversibility arises, but also what is actually meant by it.

One way to probe the sensitivity of quantum dynamics to perturbations was proposed by Peres (Peres, 1984). Inspired by the historic discussion of irreversibility he suggested to study

effective time reversal, which is in a quantum mechanical system achieved by simply changing the sign of the Hamiltonian. The imperfection is in the proposed protocol introduced as a perturbation to the Hamiltonian during the backwards evolution. The whole protocol can be summarized as

$$|\psi_0\rangle \xrightarrow{e^{-i\hat{H}\tau}} |\psi(\tau)\rangle \xrightarrow{e^{i(\hat{H}-\epsilon\hat{V})\tau}} |\psi(2\tau)\rangle \stackrel{?}{\approx} |\psi_0\rangle, \quad (4.2)$$

where  $\epsilon\hat{V}$  constitutes a small perturbation of the Hamiltonian  $\hat{H}$ .

In order to quantify the resemblance of the time-evolved to the initial state Peres suggested to resort to the overlap of both,

$$\mathcal{L}(\tau) = |\langle\psi_0|e^{i(\hat{H}-\epsilon\hat{V})\tau}e^{-i\hat{H}\tau}|\psi_0\rangle|^2, \quad (4.3)$$

which was in remembrance of the historic discussion named *Loschmidt echo*. The decay characteristics of the Loschmidt echo have been studied extensively, in particular considering systems with few degrees of freedom, which can be attributed a classical counterpart (Gorin *et al.*, 2006; Jacquod and Petitjean, 2009). Generally, in systems with classically chaotic counterpart the Loschmidt echo decays exponentially or with a Gaussian law as function of the waiting time  $\tau$ . A crossover between both decay laws can occur as function of the perturbation strength  $\epsilon$ . In systems which are instead regular in the classical limit the Loschmidt echo was found to decay algebraically. Hence, a Loschmidt echo that decays exponentially or faster can be interpreted as signature of irreversible dynamics in few-body systems.

For systems with many degrees of freedom, however, overlaps like the Loschmidt echo (4.3) have only limited significance for the physical resemblance of states. The ETH, which was discussed in Section 1.2.1, relies on the observation that, although orthogonal, energy eigenstates are practically indistinguishable in terms of physical observables. Whether the overlap of the time-evolved and the initial state becomes large after an effective inversion of the dynamics is, hence, not necessarily meaningful for the question whether the system as observed in the laboratory resembles the initial condition. Any definition of irreversibility applicable to many-body systems should therefore be based on physical observables.

Note that effective time reversal in quantum many-body systems is indeed not just of theoretical interest. Echo dynamics can for example be realized in nuclear magnetic resonance experiments on spin systems. The simplest case is the Hahn spin echo (Hahn, 1950), where an initial macroscopic spin polarization is after dephasing by field inhomogeneities recovered through the application of  $\pi$ -pulses. The spin dynamics in Hahn echo experiments is governed by a Hamiltonian of the form

$$\hat{H} = \sum_l \vec{B}_l \cdot \vec{S}_l + \hat{H}_{\text{int}}. \quad (4.4)$$

Here  $\vec{B}_l$  denotes a large magnetic field that is slightly inhomogeneous coupled to the spins  $\vec{S}_l$ .  $\hat{H}_{\text{int}}$  comprises additional contributions like couplings between spins or coupling of the spins to the environment. The spin polarization, initially parallel to the external field, is rotated into the perpendicular plane by application of a suited electromagnetic pulse. The

subsequent precession results in a dephasing of the polarization due to inhomogeneities of the external field. After some time another pulse (the  $\pi$ -pulse) is applied, which flips all spins and thereby effectively inverts the single spin term in Eq. (4.4). In the following the polarization is partially restored, because the dephasing due to field inhomogeneities is reverted. However, the relaxation caused by additional contributions to the Hamiltonian inhibits a perfect recovery of the initial polarization. The decay of the echo allows to infer the natural line width from such measurements. Interestingly, more sophisticated pulse sequences allow for the effective sign change of interaction terms: Using a so-called magic echo technique the sign of a dipolar coupled spin Hamiltonian can be inverted with good precision (Schneider and Schmiedel, 1969; Rhim *et al.*, 1971; Hafner *et al.*, 1996). Other candidate setups for the realization of effective time reversal are the quantum simulators discussed in Section 1.1, where the excellent control the parameters of the Hamiltonian could be further exploited. A recent numerical analysis demonstrated how the spin dynamics of an antiferromagnetic Mott insulator can be effectively inverted by subjecting it to a fast external drive (Mentink *et al.*, 2015).

In Sections 4.2, 4.3, and 4.4 the dynamics of observable echoes under imperfect effective time reversal is studied. It is demonstrated that in generic systems imperfections lead to a decay of the observable echoes with a rate that is independent of the perturbation. This implies that also in quantum many-body systems any practical effort to improve the accuracy in a time reversal experiment is in vain, just like in irreversible classical systems.

An alternative view of the loss of information about the initial state under dynamics that obtained increasing interest recently is *scrambling*. Originally motivated by studies of the information paradox of black holes it is in this context investigated how much information about the initial state can be inferred from local measurements on the time-evolved state. In a system that scrambles all information is after sufficiently long time completely delocalized such that local observations yield no insight about the initial state.

So called *out-of-time-order correlators* (OTOCs) were suggested as a probe of scrambling and exponential sensitivity of the dynamics to small perturbations (Shenker and Stanford, 2014; Kitaev, 2014). An OTOC is a correlation function of the form

$$\langle V(t)^\dagger W(0)^\dagger V(t) W(0) \rangle_\beta, \quad (4.5)$$

where  $V(t)$  and  $W(t)$  are operators in the Heisenberg picture. These correlation functions occur when taking the square of the commutator of both operators,  $\langle [V(t), W(0)]^\dagger [V(t), W(0)] \rangle_\beta$ . Choosing momentum  $\hat{p}$  and position  $\hat{q}$  as the pair of operators and taking the classical limit by replacing the commutator by Poisson brackets one finds that in a chaotic system  $\langle [\hat{p}(t), \hat{q}(0)]^2 \rangle \sim \hbar^2 e^{2\lambda_L t}$  with the Lyapunov exponent  $\lambda_L$  (Larkin and Ovchinnikov, 1969). In fact, it was found that the OTOCs in a black hole theory grow exponentially with the maximal possible growth rate  $\lambda_L = \frac{2\pi}{\beta}$  (Maldacena *et al.*, 2016). Besides that, OTOCs in systems with spin-1/2 degrees of freedom can be related to an information-theoretic measure for the delocalization of initially local information (Hosur *et al.*, 2016). Thereby, it can be decided based on the long time limit of the OTOC whether a system scrambles or not.

Out-of-time-order structures occur naturally when considering echo dynamics under imperfect time reversal as described above. These are investigated with focus on a possible relation to scrambling in Section 4.5 and a semiclassical analysis of echo dynamics presented

in Section 4.6 indicates that similar to OTOCs out-of-time-order double commutators can exhibit exponential growth in time, which allows to introduce the notion of a Lyapunov exponent.

## 4.2 *Publication:* Effective time reversal and echo dynamics in the transverse field Ising model

Markus Schmitt and Stefan Kehrein

EPL **115** 50001 (2016)

<https://doi.org/10.1209/0295-5075/115/50001>

**Author contributions** M. S. performed all analytical and numerical calculations and wrote the manuscript. Both authors discussed the results and contributed to the design of the study. S. K. suggested to study echo dynamics in this model, devised the pulse Hamiltonian and revised the manuscript.

---

# Effective time reversal and echo dynamics in the transverse field Ising model

MARKUS SCHMITT and STEFAN KEHREIN

*Institute for Theoretical Physics, Georg-August-Universität Göttingen - Friedrich-Hund-Platz 1, Göttingen 37077, Germany*

PACS 05.30.-d – Quantum statistical mechanics

PACS 03.65.-w – Quantum mechanics

PACS 05.45.Mt – Quantum chaos

**Abstract** – The question of thermalisation in closed quantum many-body systems has received a lot of attention in the past few years. An intimately related question is whether a closed quantum system shows irreversible dynamics. However, irreversibility and what we actually mean by this in a quantum many-body system with unitary dynamics has been explored very little. In this work we investigate the dynamics of the Ising model in a transverse magnetic field involving an imperfect effective time reversal. We propose a definition of irreversibility based on the echo peak decay of observables. Inducing the effective time reversal by different protocols we find algebraic decay of the echo peak heights or an ever persisting echo peak indicating that the dynamics in this model is well reversible.

---

**Introduction.** – During the last decades enormous advances in the experimental realisation of highly controllable quantum simulators [1–4] have triggered a lot of activity in theoretically investigating the out of equilibrium dynamics of quantum many-body systems. In particular the equilibration of closed many-body systems and the process of thermalisation as fundamental questions of quantum statistical mechanics aroused a lot of interest [5–14]. Nevertheless, albeit being intimately related to thermalisation the question of irreversibility in quantum many-body systems has to date hardly been addressed.

In the context of classical systems this question was already discussed during the development of thermodynamics. Regarding Boltzmann’s H-theorem [15] Loschmidt pointed out that in his derivation of the Second Law Boltzmann had obviously broken the time reversal invariance of the underlying microscopic laws of motion [16]. Specifically, he argued that if one performs an effective time reversal on a classical gas by inverting the velocities of all particles at some point in time the system must necessarily return to its initial state after twice that time. With this example at hand the emergence of irreversibility in classical systems is nowadays easily understood: A system with sufficiently many degrees of freedom will generically exhibit chaotic dynamics and therefore any time reversal

operation will be practically infeasible due to the exponential sensitivity of the dynamics to inevitable errors. This is also a way to understand the loss of information about the initial state during the time evolution, which is essential for thermalisation. In a chaotic many-body system with irreversible dynamics there is no realisable protocol that would allow to return it to the initial state.

Referring to the knowledge about classical irreversibility Peres suggested to study the Loschmidt echo

$$\mathcal{L}(\tau) = |\langle \psi_0 | e^{i(H+\epsilon V)\tau} e^{-iH\tau} | \psi_0 \rangle|^2 \quad (1)$$

in order to quantify irreversibility of quantum systems [17]. The Loschmidt echo is the overlap of the initial state with the forward and backward time evolved state when including a small deviation  $\epsilon V$  in the time evolution operator of the backwards evolution. As such it quantifies how well the initial state is resembled after an imperfect effective time reversal. The Loschmidt echo turned out to be a very interesting measure when studying systems with few degrees of freedom, exhibiting a variety of possible decay characteristics [18, 19].

However, in generic quantum many-body systems the Loschmidt echo is not a measurable quantity. If the prerequisite of the Eigenstate Thermalisation Hypothesis (ETH) [20–22] pertains, which all numerical evidence in-



icates [7, 23, 24], then expectation values of local observables  $O_E = \langle E|\hat{O}|E\rangle$  are smooth functions of the energy  $E$ . This means that even orthogonal states cannot necessarily be distinguished experimentally. This argument carries over to integrable systems when the observable expectation value is considered as a function of all integrals of motion instead of only the energy [25]. Therefore a definition of irreversibility with respect to the Loschmidt-echo cannot meaningfully differentiate between reversible and irreversible dynamics in many-body systems. It should also be noted that generally the Loschmidt echo is of large deviation form,  $\mathcal{L}(\tau) \sim e^{-Nl(\tau)}$  with some rate function  $l(\tau)$ , i.e. it is exponentially suppressed with increasing system size  $N$ .

In our work, when addressing the question of irreversibility in many-body systems we focus on observable echoes that are produced under imperfect effective time reversal, i.e.

$$\begin{aligned} \langle O \rangle_\tau &= \langle \psi(\tau) | \hat{O} | \psi(\tau) \rangle, \\ |\psi(\tau)\rangle &= e^{i(H+\epsilon V)\tau} e^{-iH\tau} |\psi_0\rangle. \end{aligned} \quad (2)$$

We propose a definition of irreversibility based on the decay of the echo peak as the waiting time  $\tau$  is increased. With respect to that we consider the dynamics of systems exhibiting an algebraic decay reversible, whereas systems with exponentially or faster than exponentially decaying echo peaks are irreversible.

Obviously, echoes in the expectation values of observables will depend on the choice of the observables. Thus, the conclusions that can be drawn regarding the irreversibility of the dynamics will have to be decided on a case by case basis. However, to the best of the current knowledge fundamental issues of thermalisation, in particular the description of stationary expectation values in unitarily evolved pure states after long times by thermal density matrices, can likewise only be understood for specific classes of observables [13, 14].

Recently, an alternative definition for chaos in quantum systems was put forward, which is based on the behaviour of out-of-time-order (OTO) correlators of the form  $\langle W(t)V(0)W(t)V(0) \rangle$ . These OTO correlators probe a system's sensitivity to small perturbations [26]. Moreover, they are closely related to the phenomenon of scrambling, i.e. the complete delocalisation of initially local information under time evolution [27]. The relation between both definitions should be investigated systematically in future work.

An important experimental application of effective time reversal are NMR experiments. The dynamics of non-interacting spins can be reverted by the Hahn echo technique [28] or by the application of more sophisticated pulse sequences [29, 30]. Moreover, it is possible to realise effective time reversal in certain dipolar coupled spin systems by the so called magic echo technique [31–33]. Particularly notable are various experimental and theoretical works on the refocussing of a local excitation by effective time re-

versal in NMR setups [34–37]. Besides that we expect that effective time reversal can be realised in quantum simulators [3, 4]; and recently there were proposals for effective time reversal by periodic driving [38] or by spin flips in cold atom setups with spin-orbit coupling [39].

Results for the echo dynamics in many-body systems might also be interesting from other points of view. For example, there are proposals for the identification of many-body localised phases using spin echoes [40] or for the certification of quantum simulators using effective time reversal [41].

In this letter we report results for effective time reversal in the transverse field Ising model (TFIM). This simple model Hamiltonian is diagonal in terms of fermionic degrees of freedom and all quantities of interest can be computed analytically in the thermodynamic limit. Thus, it has well known properties and, in particular, the stationary state it approaches in the long time limit is well understood [10, 42]. As such the TFIM is ideally suited as a starting point to study irreversibility theoretically from the aforementioned point of view. On top of this, the TFIM can be realised experimentally in circuit QED [43].

**Dynamics in the transverse field Ising model.** – The Ising model in a transverse magnetic field is defined by the Hamiltonian

$$H(h) = -J \sum_{i=1}^N S_i^z S_{i+1}^z + h \sum_{i=1}^N S_i^x, \quad (3)$$

where  $S_i^{x/z}$  denotes the Pauli spin operators acting on lattice site  $i$ ,  $N$  the number of lattice sites, and  $h$  the magnetic field strength [44]. For our purposes we consider periodic boundary conditions. A Jordan-Wigner transform allows to map this spin Hamiltonian to a quadratic Hamiltonian in momentum space

$$H(g) = J \sum_{k>0} \begin{pmatrix} c_k^\dagger & c_{-k} \end{pmatrix} \begin{pmatrix} d_k^z(g) & -id_k^y(g) \\ id_k^y(g) & -d_k^z(g) \end{pmatrix} \begin{pmatrix} c_k \\ c_{-k}^\dagger \end{pmatrix} \quad (4)$$

with fermionic operators  $c_k^\dagger, c_k$  and coefficient functions  $d_k^y(g) = \sin(k)/2$  and  $d_k^z(g) = g - \cos(k)/2$ , where  $g = h/J$ . The Bogoliubov rotation

$$\begin{pmatrix} \lambda_k \\ \lambda_{-k}^\dagger \end{pmatrix} = R^x(\theta_k^g) \begin{pmatrix} c_k \\ c_{-k}^\dagger \end{pmatrix} \quad (5)$$

with Bogoliubov angle  $\theta_k^g = \arctan(d_k^y/d_k^z(g))$  diagonalises the Hamiltonian yielding

$$H(g) = \sum_{k>0} \epsilon_k^g \lambda_k^\dagger \lambda_k \quad (6)$$

with energy spectrum  $\epsilon_k^g = J \sqrt{d_k^y(g)^2 + d_k^z(g)^2}$ . The gap closing point at  $g = 1/2$  indicates the quantum phase transition between paramagnet and ferromagnet.

Above a family of unitary matrices,

$$R^\alpha(\phi) = \mathbf{1} \cos \frac{\phi}{2} + i\sigma^\alpha \sin \frac{\phi}{2}, \quad \alpha \in \{x, y, z\}, \quad (7)$$

with the Pauli matrices  $\sigma^\alpha$  was introduced for later convenience.

After mapping the spin degrees of freedom to free fermions expectation values of many observables are – thanks to Wick’s theorem – given in terms of block Toeplitz (correlation) matrices  $\Gamma_{ij} \equiv \Gamma_{(i-j)}$ , where

$$\Gamma_l = \begin{pmatrix} f_l & g_l \\ -g_{-l} & -f_l \end{pmatrix} \quad (8)$$

with

$$g_l \equiv i\langle a_i b_{i+l-1} \rangle, \quad (9)$$

$$f_l \equiv i\langle a_i a_{i+l} \rangle - i\delta_{l0} = i\langle b_{i+l} b_i \rangle - i\delta_{l0}, \quad (10)$$

and Majorana operators  $a_i = c_i^\dagger + c_i$ ,  $b_i = i(c_i^\dagger - c_i)$  [45–49]. Here  $\langle \cdot \rangle$  denotes the expectation value for a given state  $|\psi\rangle$ , i.e.  $\langle \cdot \rangle \equiv \langle \psi | \cdot | \psi \rangle$ . Since, due to translational invariance,

$$g_l = \frac{i}{N} \sum_k e^{-ik(l-1)} \langle b_k a_{-k} \rangle \equiv \frac{1}{N} \sum_k e^{-ikl} \hat{g}_k, \quad (11)$$

$$f_l = \frac{i}{N} \sum_k e^{-ikl} \langle a_k a_{-k} \rangle \equiv \frac{1}{N} \sum_k e^{-ikl} \hat{f}_k, \quad (12)$$

where  $a_k = \frac{1}{\sqrt{N}} \sum_l e^{-ikl} a_l$  and  $b_k = \frac{1}{\sqrt{N}} \sum_l e^{-ikl} b_l$ , the Toeplitz matrix  $\Gamma_{ij}$  is fully determined by its symbol

$$\hat{\Gamma}_k = \begin{pmatrix} \hat{f}_k & \hat{g}_k \\ -\hat{g}_{-k} & -\hat{f}_k \end{pmatrix} \quad (13)$$

via  $\Gamma_l = \sum_k e^{-ikl} \hat{\Gamma}_k$ .

For our purposes we consider the transverse magnetisation

$$\langle m_x \rangle \equiv \frac{1}{N} \sum_i \langle S_i^x \rangle = -\frac{1}{2} g_1 \quad (14)$$

and the longitudinal spin-spin correlation

$$\rho_n^{zz} \equiv \langle S_i^z S_{i+n}^z \rangle = \frac{1}{4} \text{Pf} [\Gamma^n], \quad (15)$$

where  $\text{Pf}[\cdot]$  denotes the Pfaffian and  $\Gamma^n$  is the correlation matrix consisting of blocks  $\Gamma_{ij}$  with  $|i-j| < n$  (cf. eq. (8)). Moreover, we will study the entanglement entropy  $S_n$  of a strip  $A_n$  of  $n$  adjacent spins with the rest of the system, which is given by

$$S_n \equiv \text{Tr} [\rho_{A_n} \ln(\rho_{A_n})] = \sum_{l=1}^n H_2 \left( \frac{1 + \nu_l}{2} \right) \quad (16)$$

where  $\rho_{A_n}$  is the reduced density matrix of the subsystem  $A_n$ ,  $\pm i\nu_l$  are the eigenvalues of  $\Gamma^n$ , and  $H_2(x) \equiv -x \log(x) - (1-x) \log(1-x)$  [50, 51].

In the following we will be interested in time evolution which is induced by quenching the magnetic field  $g$  at  $t = 0$ . This means the initial state  $|\psi_0\rangle$  is the ground state of the Hamiltonian  $H(g_0)$  and for  $t > 0$  the time

evolution is driven by a Hamiltonian  $H(g)$  with  $g \neq g_0$ . To compute the time evolution for this protocol it is convenient to introduce operators

$$\vec{\Omega}_i \equiv \begin{pmatrix} \omega_i^+ \\ \omega_i^- \end{pmatrix} \equiv \sqrt{2} R^y(\pi/2) \begin{pmatrix} c_i^\dagger \\ c_i \end{pmatrix} \quad (17)$$

in terms of which the correlators (9) and (10) are  $i\langle a_i a_j \rangle = i\langle \omega_i^+ \omega_j^+ \rangle$  and  $i\langle a_i b_j \rangle = -\langle \omega_i^+ \omega_j^- \rangle$ .  $\Gamma^n$  is then fully determined by the correlation matrix

$$\langle \vec{\Omega}_k \vec{\Omega}_k^\dagger \rangle_t = \begin{pmatrix} \langle \omega_k^+ \omega_{-k}^+ \rangle_t & -\langle \omega_k^+ \omega_{-k}^- \rangle_t \\ \langle \omega_k^- \omega_{-k}^+ \rangle_t & -\langle \omega_k^- \omega_{-k}^- \rangle_t \end{pmatrix}. \quad (18)$$

where  $\langle \cdot \rangle_t$  is the expectation value with respect to the time evolved state  $|\psi(t)\rangle$ . For the abovementioned quench the expectation values with  $|\psi(t)\rangle = \exp(-iH(g)t) |\psi_0\rangle$  can be evaluated [52], yielding

$$\langle \vec{\Omega}_k \vec{\Omega}_k^\dagger \rangle_t = \frac{1}{2} \tilde{U}_k(t) (\sigma^z + 1) \tilde{U}_k(t)^\dagger, \quad (19)$$

where  $\tilde{U}_k(t) = \sqrt{2} R^y(\frac{\pi}{2}) R^x(\theta_k^g) R^z(2\epsilon_k^g t) R^x(\phi_k^{g, g_0})$  with  $R^\alpha(\phi)$  as defined in eq. (7) and  $\phi_k^{g, g_0} \equiv \theta_k^g - \theta_k^{g_0}$ . In the following we will employ straightforward generalisations of this formalism for situations of imperfect effective time reversal, generally yielding coefficients  $\Sigma_\alpha^k(t) \equiv \Sigma_\alpha^k(t, g_0, g, \dots)$  with which

$$\langle \vec{\Omega}_k \vec{\Omega}_k^\dagger \rangle_t = \mathbf{1} + \sum_{\alpha \in \{x, y, z\}} \Sigma_\alpha^k(t) \sigma^\alpha, \quad (20)$$

where  $\sigma^\alpha$  denote the Pauli matrices. Although derived straightforwardly, the expressions for  $\Sigma_\alpha^k(t)$  become very lengthy for the time reversal protocols under consideration in this work. The full expressions can be found in the supplemental material [53].

**Quantifying initial state resemblance.** – In the following we will study the resemblance of a time evolved state to the initial state when different kinds of imperfect effective time reversal are employed at  $t = \tau$ . For this purpose we compute different time dependent quantities  $X_t$ , namely observables and entanglement entropy. For  $t \rightarrow \infty$  these quantities approach a stationary value  $X_\infty$ . However, due to the applied time reversal protocol the deviation  $|X_t - X_\infty|$  will show a distinguished (local) maximum at  $t_e \approx 2\tau$ , which we call the echo peak. We will consider the normalised echo peak height

$$E_\tau^*[X] = \max_{t > \tau} \left| \frac{X_t - X_\infty}{X_0 - X_\infty} \right| \quad (21)$$

as measure for the initial state resemblance.

According to eqs. (11), (12), and (20) the quantities of interest will in the thermodynamic limit ( $N \rightarrow \infty$ ) be determined by integrals  $\int_{-\pi}^{\pi} dk e^{-ink} \Sigma_\alpha^k / 2\pi$ , where the time-dependent parts of  $\Sigma_\alpha^k$  oscillate more and more quickly as function of  $k$  with increasing  $t$ . Therefore, the stationary

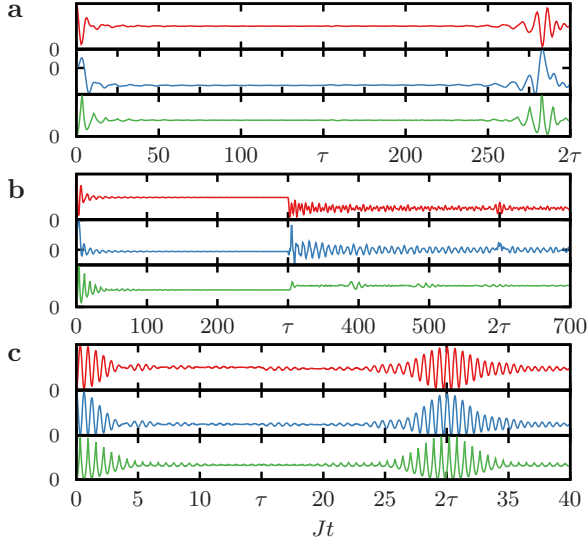


Fig. 1: Exemplary time evolution of the transverse magnetisation  $\langle m_x \rangle_t$  (red curves), the longitudinal spin-spin correlation  $\langle S_i^z S_{i+2}^z \rangle_t$  (blue curves), and the rate function of the fidelity  $l(t) = \lim_{N \rightarrow \infty} \ln(|\langle \psi_0 | \psi(t) \rangle|)/N$  (green curves) for the three different echo protocols: (a) by explicit sign change,  $g_0 = 5$ ,  $g = 0.2$ ,  $\delta g = 0.025$ , (b) by pulse,  $g_0 = 1$ ,  $g = 0.15$ ,  $\alpha t_P = 50$ , (c) generalised Hahn echo,  $g_0 = 0$ ,  $g = 5$ .

values  $X_\infty$  are given by the corresponding integrals over only the time-independent contributions to  $\Sigma_\alpha^k$  [52].

In this work we restrict the discussion to systems in the thermodynamic limit. Since the limits  $\tau \rightarrow \infty$  and  $N \rightarrow \infty$  do not commute, generic results for the bulk can only be obtained when taking  $N \rightarrow \infty$  first. When considering finite systems a crossover is to be expected at some  $\tau$  proportional to the systems size, where the details depend on the specific boundary conditions.

In what follows we discuss three different time reversal protocols, namely time reversal by explicit sign change of the Hamiltonian,  $H(g) \rightarrow -H(g + \delta g)$ , time reversal by application of a Loschmidt pulse  $U_P$ ,  $H(g) \rightarrow U_P^\dagger H(g) U_P$ , and a generalised Hahn echo protocol,  $H(g) \rightarrow H(-g)$ . All three protocols yield algebraically decaying or even ever persisting echo peak heights.

**Time reversal by explicit sign change.** – As a first echo protocol we consider effective time reversal induced by an explicit sign change of the Hamiltonian at time  $\tau$  and a well controlled deviation in the backward evolution through a slight variation  $\delta g$  of the magnetic field, i.e. for  $t > \tau$

$$U(t) = \exp(iH(g_\delta)(t - \tau)) \exp(-iH(g)\tau), \quad (22)$$

where  $g_\delta \equiv g + \delta g$  was introduced.

In order to reliably assess how well an initial state can be recovered by imperfect effective time reversal we choose initial states, which exhibit distinguishable expectation values of some observables. These are ground states of

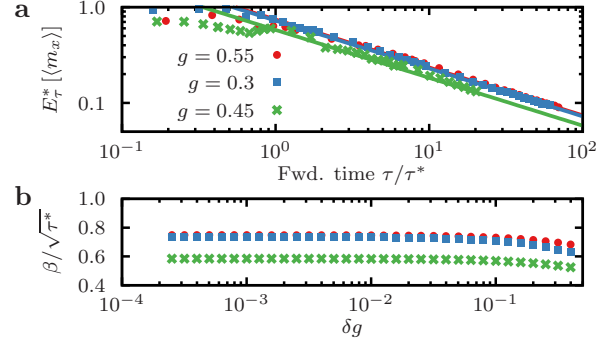


Fig. 2: (a) Echo peak height of the transverse magnetisation for three different quenches. The dots are exact results, the lines are the asymptotes  $\propto \tau^{-1/2}$  given by eq. (23). (b) Estimation of the echo peak height at the onset of the algebraic decay based on the stationary phase approximation. The echo protocol parameters are  $g_0 = 1$  and  $\delta g = 0.02$ .

$H(g)$  for  $g = 0$  or  $g \gg 1$ , respectively, which show large spin-spin correlations.

Under the time reversal protocol described above the energy spectrum  $\epsilon_k^{g_\delta}$  is deformed as compared to  $\epsilon_k^g$  and, consequently, the quasiparticle velocities,  $v_k = \frac{d\epsilon_k}{dk}$ , during forward and backward evolution can differ. Therefore, the closest resemblance of the time evolved state to the initial state does not necessarily occur at  $t = 2\tau$ . This becomes evident in the exemplary time evolution displayed in fig. 1a. In addition to observables fig. 1a shows the time evolution of the rate function of the fidelity,  $l(t) = \lim_{N \rightarrow \infty} \ln(|\langle \psi_0 | \psi(t) \rangle|^2)/N$ . A minimum of this quantity corresponds to a large overlap of the time evolved state with the initial state for finite  $N$ . Note as an aside that the time evolution exhibits dynamical quantum phase transitions, which aroused a lot of interest recently [54], in the forward as well as in the backward evolution.

Let us first consider echoes in the transverse magnetisation. For this observable a stationary phase approximation reveals an algebraic decay of the echo peak height with

$$|\langle m_x \rangle_{t_e} - \langle m_x \rangle_\infty| \approx \kappa_{k^*}(\tau) \beta_{k^*}^{g, g_0, g_\delta} \tau^{-1/2}, \quad (23)$$

where  $\kappa_{k^*}(\tau) = \cos(2(\epsilon_{k^*}^g - \nu_{k^*}^{g, g_\delta} \epsilon_{k^*}^{g_\delta})\tau + \pi/4)$ ,

$$\beta_{k^*}^{g, g_0, g_\delta} = \frac{\zeta_{k^*}^{g, g_\delta, g_0}}{2\sqrt{\pi} |\xi_{k^*}^{g, g_\delta}|^{1/2}}, \quad (24)$$

$$\zeta_k^{g, g_\delta, g_0} \equiv \sin \theta_{k^*}^{g_\delta} \sin \phi_{k^*}^{g, g_0} \frac{\cos \phi_{k^*}^{g_\delta, g} + 1}{2}, \quad (25)$$

$$\xi_{k^*}^{g, g_\delta} \equiv \left. \frac{d^2}{dk^2} (\epsilon_k^g - \nu_{k^*}^{g, g_\delta} \epsilon_k^{g_\delta}) \right|_{k=k^*}, \quad (26)$$

and the echo peak time is  $t_e = (1 + \nu_{k^*}^{g, g_\delta})\tau$  with  $k^* = \text{argmax}_k |\beta_k^{g, g_0, g_\delta}|$ . From the stationary phase approximation the onset of the algebraic decay can be expected at  $\tau \approx \tau^*$  with  $\tau^* = \frac{d}{dk} \zeta_{k^*}^{g, g_\delta, g_0} \Big|_{k=k^*} / \xi_{k^*}^{g, g_\delta}$ . A detailed derivation of this result is given in the supplement [53]. Fig.

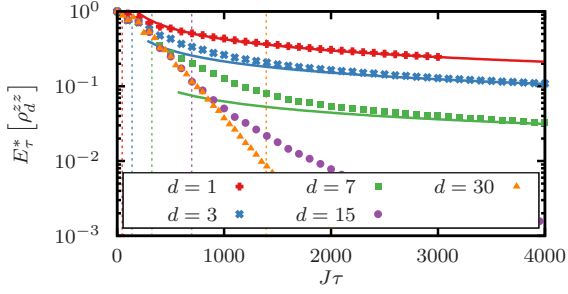


Fig. 3: Echo peak height of the longitudinal spin-spin correlation for different distances  $d$  with quench parameters  $g_0 = 0, g = 1, \delta g = 0.05$ . The dots are exact results, the solid lines are  $\propto \tau^{-1/2}$  and the dashed lines mark the forward times  $\tau = d/\tilde{v}_{\max}$  for the different  $d$ , respectively.

2a shows the decay of the echo peak height of the transverse magnetisation as a function of the forward time  $\tau$  for three different quenches starting in the paramagnetic phase. In all cases the initial magnetisation is almost perfectly recovered for forward times  $\tau \lesssim \tau^*$ , whereas it decays algebraically for  $\tau \gg \tau^*$ . Moreover, the evaluation of  $\beta_{k^*}^{g, g_0, g_s}$  and  $\tau^*$  as function of the deviation  $\delta g$  yields  $\beta_{k^*}^{g, g_0, g_s} \propto \delta g^{-1/2}$  and  $\tau^* \propto \delta g^{-1}$  for a wide range of perturbation strengths  $\delta g$ . As a result,  $\beta_{k^*}^{g, g_0, g_s} (\tau^*)^{-1/2}$  is almost constant (cf. fig. 2b) meaning that generally a very pronounced echo peak can be expected until the onset of the algebraic decay and the height of which is independent of the imperfection in the backwards evolution. Hence, the echo peak decay is ultimately induced by dephasing due to the deformed spectrum in the backwards evolution.

Fig. 3 shows the longitudinal spin-spin correlation  $\rho_d^{zz}$  computed according to eq. (15) for different distances  $d$ . For this quantity we also observe an algebraic decay of the echo peak height,  $E_\tau^*[\rho_d^{zz}] \propto \tau^{-1/2}$  for large  $\tau$ . However, before the onset of the algebraic decay there is a distance-dependent regime of exponential-looking decay, which increases with increasing spin-separation  $d$ . Similar behaviour is known for the decay of correlation functions after a simple quench without time reversal [10, 49]. In that case the decay law can be rigorously derived by identifying an space-time scaling regime where  $v_{\max} t \sim d$  with  $v_{\max}$  the maximal propagation velocity. Due to the similar algebraic structure in the echo dynamics we expect a similar explanation for the intermediate regime in the decay of the echo peak of  $\rho_d^{zz}$  with a different effective velocity  $\tilde{v}_{\max} = \max_{k \in [0, \pi]} \frac{d}{dk} (\epsilon_k^g - \nu_{k^*}^{g, g_s} \epsilon_k^{g_s})$ . At late times all entries of the correlation matrix (8) will just like the transverse magnetisation decay algebraically with exponent  $-1/2$ , and therefore the leading term of the Pfaffian will decay with the same power law, which explains that  $E_\tau^*[\rho_d^{zz}] \propto \tau^{-1/2}$  for  $\tilde{v}_{\max} \tau \gg d$ . In this sense the quasiparticle picture which already yielded insights in various other contexts [49, 55–57] is also useful to analyse the echo dynamics. Considering the order parameter  $\langle m_z \rangle^2 = \lim_{d \rightarrow \infty} \rho_d^{zz}$ , our

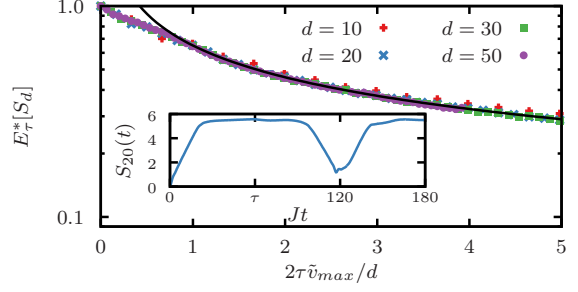


Fig. 4: Decay of the echo peak height of the entanglement entropy for different subsystem sizes  $d$ ,  $g_0 = 1, g = 0.5, \delta g = 0.05$ . After long waiting times the echo peak height decays algebraically  $\propto \tau^{-1/2}$  (black line). The inset shows an exemplary time evolution of the entanglement entropy under effective time reversal for  $d = 20$  and  $g_0 = 2.5, g = 0.55, \delta g = 0.05, \tau = 30$ .

result implies an exponential decay of the echo peak height for all forward times  $\tau \gg 1$ .

Another interesting question is how far the entanglement produced during the time evolution can be reduced again by the effective time reversal protocol. After quenching the magnetic field the entanglement entropy increases until it saturates at a level that is determined by the subsystem size [55]. Therefore, an echo peak  $E_\tau^*[S_d] = 1$  means that the state  $|\psi(t_e)\rangle$  has the same low entanglement as the initial state, whereas for  $E_\tau^*[S_d] < 1$  some additional entanglement remains. Fig. 4 displays the echo peak height of the entanglement entropy  $S_n$  of a subsystem  $A_d$  consisting of  $d$  adjacent spins with the rest of the chain as defined in eq. (16). Again we observe an initial  $d$ -dependent regime of exponential-looking decay crossing over to algebraic decay with  $E_\tau^*[S_d] \propto \tau^{-1/2}$  for  $\tau \gg d/2\tilde{v}_{\max}$ .

**Time reversal by a Loschmidt pulse.** – Another possibility to invert the course of the dynamics in the TFIM is the application of a pulse similar to the  $\pi$ -pulses applied to the system in a Hahn echo experiment. Consider the Hamiltonian

$$H_P = -\alpha \sum_j (S_j^x S_{j+1}^y + h.c.) . \quad (27)$$

In terms of the Jordan-Wigner fermions in momentum space this reads  $H_P = 2\alpha \sum_k \sin k (c_k^\dagger c_{-k}^\dagger + c_{-k} c_k)$  and the structure does not change under Bogoliubov rotation, since  $c_k^\dagger c_{-k}^\dagger + c_{-k} c_k = \lambda_k^\dagger \lambda_{-k}^\dagger + \lambda_{-k} \lambda_k$ . The time evolution operator for this Hamiltonian in the diagonal basis is

$$e^{-iH_P t} = \prod_k [\cos(2\alpha t \sin k) - i \sin(2\alpha t \sin k) (\lambda_k^\dagger \lambda_{-k}^\dagger + \lambda_{-k} \lambda_k)] \quad (28)$$

For a given pulse time  $t_P$  this operator perfectly inverts the population of modes  $k_n^*$  with  $2\alpha t_P \sin k_n^* = (2n + 1)\pi/2, n \in \mathbb{Z}$ , whereas the population of other modes is only partially inverted or remains unchanged. Thereby,

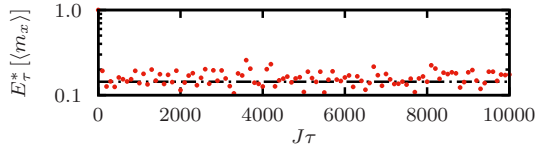


Fig. 5: Echo peak heights (red dots) for the transverse magnetisation  $m_x$  when applying the pulse Hamiltonian (27) together with residual peak height given by eq. (30) (dashed line). Parameters:  $g_0 = 1, g = 0.3$ , and  $\alpha t_P = 25$ .

the evolution of the system under the Hamiltonian (27) for a pulse time  $t_p$  leads to an imperfect effective time reversal, i.e.  $e^{iH_P t_P} e^{-iH\tau} e^{-iH_P t_P} = e^{i(H+\epsilon V)\tau}$ , by an imperfect inversion of the mode occupation. Note that in the notation introduced above the pulse operator in one  $k$ -sector is  $\tilde{U}_k^P(2\alpha t) \equiv R^x(4\alpha t \sin k)^\dagger$ .

With this protocol the forward and backward time evolution are generated by the same Hamiltonian; hence, the echo peak after time reversal at time  $\tau$  appears at  $t_e = 2\tau$ , which can be seen in the exemplary time evolution in fig. 1b. In particular, we find that at  $t_e = 2\tau$  the transverse magnetisation can be split into three parts,

$$\langle m_x \rangle_{t_e=2\tau} = \langle m_x \rangle_\infty + \langle m_x \rangle_E + \langle m_x \rangle_\tau, \quad (29)$$

where  $\langle m_x \rangle_\infty$  is the stationary value reached at  $t \rightarrow \infty$ ,  $\langle m_x \rangle_E$  is an additional  $\tau$ -independent contribution, and  $\langle m_x \rangle_\tau$  are the time-dependent contributions, which vanish for  $\tau \rightarrow \infty$ . This means we find an echo peak at  $t_e = 2\tau$ , which never decays. The residual peak height is given by

$$\langle m_x \rangle_E = \frac{1}{2} \int_{-\pi}^{\pi} \frac{dk}{2\pi} \sin \phi_k^{g, g_0} \left( 1 - \cos(4\alpha t_P \sin k) \right) \quad (30)$$

An example of this ever persisting echo is depicted in fig. 5, where the dots show the exact result and the dashed line shows the echo peak height expected when only considering the time-independent contributions in eq. (29).

**Time reversal by generalised Hahn echo.** – The Hamiltonian of the TFIM (3) allows for an echo protocol very similar to the way the effective time reversal is induced in a Hahn echo experiment [28], namely by a sign inversion of the Zeeman term. For large magnetic fields changing the sign of the field can be considered an effective time reversal with small imperfection given by the Ising term,  $\epsilon V = 2J \sum_i S_i^z S_{i+1}^z$ . In contrast to the original Hahn echo setup, where an initial magnetisation decays due to field inhomogeneities, the decay in the TFIM will be due to the coupling of the physical degrees of freedom.

The stationary phase analysis for the echo dynamics under this protocol unveils that it combines two properties of the previously discussed protocols. Since the switching of the magnetic field corresponds to a shift of the energy spectrum,  $\epsilon_k^g = \epsilon_{k+\pi}^{-g}$ , the quasiparticle velocities are perfectly inverted, yielding echo peaks at  $t_e = 2\tau$ ; nevertheless, for large  $\tau$  the echo peak height decays algebraically

with exponent  $-1/2$ . A detailed derivation is given in the supplementary material [53].

**Relation to thermalisation.** – The fact that it is well possible to produce pronounced echoes in the TFIM also after long waiting times matches the absence of thermalisation in the conventional sense. The dynamics of the system is constrained by infinitely many integrals of motion, which keep a lot of information about the initial state. Especially, these integrals of motion determine the stationary value of local observables through the corresponding generalised Gibbs ensemble (GGE) [10], i.e. the reduced density matrix of a strip of length  $l$ ,  $\rho_l(t)$ , converges to a density matrix given by a GGE,  $\rho_{GGE,l}$ , for  $t \rightarrow \infty$ . Note that the distance of both density matrices decreases as  $\mathcal{D}(\rho_l(t), \rho_{GGE,l}) \propto l^2 t^{-3/2}$  [11], whereas the expectation value of an observable at  $t = 2\tau$  is determined by  $\langle O \rangle_{2\tau} = \text{tr}[O(\tau)\rho(\tau)]$ . In the latter expression  $\rho(\tau) = e^{-iH\tau} |\psi_0\rangle \langle \psi_0| e^{iH\tau}$  approaches a GGE as mentioned above but  $O(\tau) = e^{-i(H+\epsilon V)\tau} O e^{i(H+\epsilon V)\tau}$  becomes increasingly non-local. Therefore, the fact that echoes are possible after arbitrarily long waiting times does not contradict the convergence to a GGE.

**Discussion.** – We proposed a definition of irreversibility based on the decay of observable echoes under imperfect effective time reversal and presented different ways to induce the time reversal in the TFIM. As a result we find an algebraic decay of the echo peak height after long forward times for all observables under consideration due to dephasing whenever the imperfection comes along with a deformation of the energy spectrum. In the case of an unchanged spectrum during forward and backward evolution there is a residual contribution to the echo peak, which never decays.

Based on these results we conclude that the dynamics in the TFIM can be considered well reversible. This finding matches the fact that the TFIM has an infinite number of integrals of motion, which preserve a lot of information about the initial state throughout the course of the dynamics and also prevent the equilibration to a conventional Gibbs ensemble.

An important point of future work will be to understand the dynamics of non-quadratic Hamiltonians under imperfect effective time reversal. Work along these lines is in progress.

\*\*\*

The authors thank S. Sondhi for the interesting suggestion to study the entanglement entropy under effective time reversal as well as M. Medvedyeva, M. Heyl, M. Fagotti, and D. Fioretto for helpful discussions and N. Abeling for proofreading the manuscript. This work was supported through SFB 1073 (project B03) of the Deutsche Forschungsgemeinschaft (DFG) and the Studienstiftung des Deutschen Volkes. For the numerical computations the Armadillo library [58] was used.

## REFERENCES

- [1] GREINER M., MANDEL O., ESSLINGER T., HANSCH T. W. and BLOCH I., *Nature*, **415** (2002) 39 .
- [2] KINOSHITA T., WENGER T. and WEISS D. S., *Nature*, **440** (2006) 900 .
- [3] BLOCH I., DALIBARD J. and NASCIMBENE S., *Nat Phys*, **8** (2012) 267 .
- [4] GEORGESCU I. M., ASHHAB S. and NORI F., *Rev. Mod. Phys.*, **86** (2014) 153.
- [5] MANMANA S. R., WESSEL S., NOACK R. M. and MURAMATSU A., *Phys. Rev. Lett.*, **98** (2007) 210405.
- [6] RIGOL M., DUNJKO V., YUROVSKY V. and OLSHANII M., *Phys. Rev. Lett.*, **98** (2007) 050405.
- [7] RIGOL M., DUNJKO V. and OLSHANII M., *Nature*, **452** (2008) 854.
- [8] MOECKEL M. and KEHREIN S., *Phys. Rev. Lett.*, **100** (2008) 175702.
- [9] REIMANN P., *Phys. Rev. Lett.*, **101** (2008) 190403.
- [10] CALABRESE P., ESSLER F. H. L. and FAGOTTI M., *Phys. Rev. Lett.*, **106** (2011) 227203.
- [11] FAGOTTI M. and ESSLER F. H. L., *Phys. Rev. B*, **87** (2013) 245107.
- [12] CAUX J.-S. and ESSLER F. H. L., *Phys. Rev. Lett.*, **110** (2013) 257203.
- [13] POLKOVNIKOV A., SENGUPTA K., SILVA A. and VENGALATTORE M., *Rev. Mod. Phys.*, **83** (2011) 863.
- [14] EISERT J., FRIESDORF M. and GOGOLIN C., *Nat Phys*, **11** (2015) 124.
- [15] BOLTZMANN L., *Sitzungsberichte der Akademie der Wissenschaften zu Wien*, **66** (1872) 275.
- [16] LOSCHMIDT J., *Sitzungsberichte der Akademie der Wissenschaften zu Wien*, **73** (1876) 128.
- [17] PERES A., *Phys. Rev. A*, **30** (1984) 1610.
- [18] GORIN T., PROSEN T., SELIGMAN T. H. and NIDARI M., *Physics Reports*, **435** (2006) 33 .
- [19] JACQUOD P. and PETITJEAN C., *Advances in Physics*, **58** (2009) 67.
- [20] DEUTSCH J. M., *Phys. Rev. A*, **43** (1991) 2046.
- [21] SREDNICKI M., *Phys. Rev. E*, **50** (1994) 888.
- [22] SREDNICKI M., *Journal of Physics A: Mathematical and General*, **29** (1996) L75.
- [23] STEINIGEWEG R., KHODJA A., NIEMEYER H., GOGOLIN C. and GEMMER J., *Phys. Rev. Lett.*, **112** (2014) 130403.
- [24] BEUGELING W., MOESSNER R. and HAQUE M., *Phys. Rev. E*, **89** (2014) 042112.
- [25] CASSIDY A. C., CLARK C. W. and RIGOL M., *Phys. Rev. Lett.*, **106** (2011) 140405.
- [26] MALDACENA J., SHENKER S. and STANFORD D., *arXiv:1503.01409*, (2015) .
- [27] HOSUR P., QI X.-L., ROBERTS D. A. and YOSHIDA B., *Journal of High Energy Physics*, **2016** (2016) 1.
- [28] HAHN E. L., *Phys. Rev.*, **80** (1950) 580.
- [29] HAEBERLEN U., *Academic Press, New York*, (1976) 12.
- [30] UHRIG G. S., *Phys. Rev. Lett.*, **98** (2007) 100504.
- [31] SCHNEIDER H. and SCHMIEDEL H., *Physics Letters A*, **30** (1969) 298.
- [32] RHIM W., PINES A. and WAUGH J., *Physical Review B*, **3** (1971) 684.
- [33] HAFNER S., DEMCO D. E. and KIMMICH R., *Solid state nuclear magnetic resonance*, **6** (1996) 275.
- [34] ZHANG S., MEIER B. H. and ERNST R. R., *Phys. Rev. Lett.*, **69** (1992) 2149.
- [35] PASTAWSKI H. M., LEVSTEIN P. R. and USAJ G., *Phys. Rev. Lett.*, **75** (1995) 4310.
- [36] LEVSTEIN P. R., USAJ G. and PASTAWSKI H. M., *The Journal of Chemical Physics*, **108** (1998) 2718.
- [37] ZANGARA P. R., BENDERSKY D. and PASTAWSKI H. M., *Phys. Rev. A*, **91** (2015) 042112.
- [38] MENTINK J. H., BALZER K. and ECKSTEIN M., *Nat Commun*, **6** (2015) 6708.
- [39] ENGL T., URBINA J., RICHTER K. and SCHLAGHECK P., *arXiv:1409.5684*, (2014) .
- [40] SERBYN M., KNAP M., GOPALAKRISHNAN S., PAPIĆ Z., YAO N. Y., LAUMANN C. R., ABANIN D. A., LUKIN M. D. and DEMLER E. A., *Phys. Rev. Lett.*, **113** (2014) 147204.
- [41] WIEBE N., GRANADE C., FERRIE C. and CORY D. G., *Phys. Rev. Lett.*, **112** (2014) 190501.
- [42] CALABRESE P., ESSLER F. H. L. and FAGOTTI M., *Journal of Statistical Mechanics: Theory and Experiment*, **2012** (2012) P07022.
- [43] VIEHMANN O., VON DELFT J. and MARQUARDT F., *Phys. Rev. Lett.*, **110** (2013) 030601.
- [44] PFEUTY P., *ANNALS of Physics*, **57** (1970) 79.
- [45] LIEB E., SCHULTZ T. and MATTIS D., *ANNALS of Physics*, **16** (1961) 407.
- [46] CALANIELLO E. R. and FUBINI S., *Il Nuovo Cimento*, **9** (1952) 1218.
- [47] BAROUCH E., MCCOY B. M. and DRESDEN M., *Physical Review A*, **2** (1970) 1075.
- [48] BAROUCH E. and MCCOY B. M., *Physical Review A*, **3** (1971) 786.
- [49] CALABRESE P., ESSLER F. H. L. and FAGOTTI M., *Journal of Statistical Mechanics: Theory and Experiment*, **2012** (2012) P07016.
- [50] VIDAL G., LATORRE J. I., RICO E. and KITAEV A., *Phys. Rev. Lett.*, **90** (2002) 227902. 5 p.
- [51] LATORRE J. I., RICO E. and VIDAL G., *Quantum Info. Comput.*, **4** (2004) 48.
- [52] SENGUPTA K., POWELL S. and SACHDEV S., *Physical Review A*, **69** (2004) .
- [53] See supplemental material at [URL inserted by EPL].
- [54] HEYL M., POLKOVNIKOV A. and KEHREIN S., *Phys. Rev. Lett.*, **110** (2013) 135704.
- [55] CALABRESE P. and CARDY J., *Journal of Statistical Mechanics: Theory and Experiment*, **2005** (2005) P04010.
- [56] CALABRESE P. and CARDY J., *Phys. Rev. Lett.*, **96** (2006) 136801.
- [57] IGLÓI F. and RIEGER H., *Phys. Rev. Lett.*, **106** (2011) 035701.
- [58] SANDERSON C. and CURTIN R., *Journal of Open Source Software*, **1** (2016) 26.

# Effective time reversal and echo dynamics in the transverse field Ising model - Supplementary material

Markus Schmitt and Stefan Kehrein  
(Dated: July 20, 2016)

## I. COMPUTING ECHO TIME EVOLUTION IN THE TRANSVERSE FIELD ISING MODEL

As mentioned in the main text the time evolution of all observables of interest is essentially determined by the correlation matrix

$$\langle \vec{\Omega}_k \vec{\Omega}_k^\dagger \rangle_t = \begin{pmatrix} \langle \omega_k^+ \omega_{-k}^+ \rangle_t & -\langle \omega_k^+ \omega_{-k}^- \rangle_t \\ \langle \omega_k^- \omega_{-k}^+ \rangle_t & -\langle \omega_k^- \omega_{-k}^- \rangle_t \end{pmatrix}, \quad (\text{S1})$$

which is for the case of quenching from the ground state determined by

$$\langle \vec{\Omega}_k \vec{\Omega}_k^\dagger \rangle_t = \frac{1}{2} \tilde{U}_k(t) (\sigma^z + 1) \tilde{U}_k(t)^\dagger \quad (\text{S2})$$

with  $\tilde{U}_k(t) = \sqrt{2} R^y \left( \frac{\pi}{2} \right) R^x(\theta_k^g) R^z(2\epsilon_k^g t) R^x(\phi_k^{g,g_0})$  the time evolution operator of the corresponding  $k$ -sector in expressed in the basis of the initial Hamiltonian (see main text for references). Recall the definition

$$R^\alpha(\phi) = \mathbb{1} \cos \frac{\phi}{2} + i\sigma^\alpha \sin \frac{\phi}{2}, \quad \alpha \in \{x, y, z\}. \quad (\text{S3})$$

The correlation matrices can generally be written as

$$\langle \vec{\Omega}_k \vec{\Omega}_k^\dagger \rangle_t = \mathbb{1} + \sum_{\alpha=1}^3 \Sigma_\alpha^k(t) \sigma^\alpha \quad (\text{S4})$$

with suited coefficients  $\Sigma_\alpha^k(t)$ ,  $\alpha \in \{x, y, z\}$ , and the Pauli matrices  $\sigma^\alpha$ . The formalism for a simple quench is straightforwardly generalised for the different echo protocols discussed in the main text. In the following subsections we give the corresponding coefficient functions  $\Sigma_\alpha^k$ .

### A. $\Sigma_\alpha$ for echoes through explicit sign change

For the time reversal by explicit sign change, where the Hamiltonian is switched from  $H(g)$  to  $-H(g + \delta g)$  at  $t = \tau$ ,  $\tilde{U}_k(t)$  generalises to

$$\tilde{U}_k(t) = \sqrt{2} R^y \left( \frac{\pi}{2} \right) \left\{ \begin{array}{l} R^x(\theta_k^g) \\ R^x(\theta_k^{g\delta}) R^z(-2\epsilon_k^{g\delta}(t-\tau))^\dagger R^x(\phi_k^{g\delta,g})^\dagger \end{array} \right., \quad \begin{array}{l} t < \tau \\ t > \tau \end{array} \left. \right\} R^z(2\epsilon_k^g t)^\dagger R^x(\phi_k^{g,g_0})^\dagger \quad (\text{S5})$$

yielding

$$\begin{aligned} \Sigma_x^k = & - [(\cos \phi_k^{g,g_0} \sin \phi_k^{g\delta,g} + \sin \phi_k^{g,g_0} \cos \phi_k^{g\delta,g} \cos(2\epsilon_k^g \tau)) \cos(2\epsilon_k^{g\delta}(t-\tau)) \\ & + \sin \phi_k^{g,g_0} \sin(2\epsilon_k^g \tau) \sin(2\epsilon_k^{g\delta}(t-\tau))] \sin \theta_k^{g\delta} \\ & - [\cos \phi_k^{g,g_0} \cos \phi_k^{g\delta,g} - \sin \phi_k^{g,g_0} \sin \phi_k^{g\delta,g} \cos(2\epsilon_k^g \tau)] \cos \theta_k^{g\delta}, \end{aligned} \quad (\text{S6})$$

$$\begin{aligned} \Sigma_y^k = & - [(\cos \phi_k^{g,g_0} \sin \phi_k^{g\delta,g} + \sin \phi_k^{g,g_0} \cos \phi_k^{g\delta,g} \cos(2\epsilon_k^g \tau)) \cos(2\epsilon_k^{g\delta}(t-\tau)) \\ & + \sin \phi_k^{g,g_0} \sin(2\epsilon_k^g \tau) \sin(2\epsilon_k^{g\delta}(t-\tau))] \cos \theta_k^{g\delta} \\ & + [\cos \phi_k^{g,g_0} \cos \phi_k^{g\delta,g} - \sin \phi_k^{g,g_0} \sin \phi_k^{g\delta,g} \cos(2\epsilon_k^g \tau)] \sin \theta_k^{g\delta}, \end{aligned} \quad (\text{S7})$$

$$\begin{aligned} \Sigma_z^k = & \sin \phi_k^{g,g_0} \sin(2\epsilon_k^g \tau) \cos(2\epsilon_k^{g\delta}(t-\tau)) \\ & - (\cos \phi_k^{g,g_0} \sin \phi_k^{g\delta,g} + \sin \phi_k^{g,g_0} \cos \phi_k^{g\delta,g} \cos(2\epsilon_k^g \tau)) \sin(2\epsilon_k^{g\delta}(t-\tau)). \end{aligned} \quad (\text{S8})$$



for  $t > \tau$ . For  $t \rightarrow \infty$  and  $\tau < t$  the stationary value after application of the time reversal is determined by the time-independent contributions

$$\Sigma_x^k = -\cos \phi_k^{g,g_0} \cos \phi_k^{g,g_s} \cos \theta_k^g, \quad (\text{S9})$$

$$\Sigma_y^k = \cos \phi_k^{g,g_0} \cos \phi_k^{g,g_s} \sin \theta_k^g, \quad (\text{S10})$$

$$\Sigma_z^k = 0. \quad (\text{S11})$$

### B. $\Sigma_\alpha$ for echoes through pulse Hamiltonian

In the case of time reversal by application of a pulse operator  $\tilde{U}_k^P(2\alpha t) = R^x(4\alpha t \sin k)^\dagger$  we obtain

$$\Omega(t) = \sqrt{2} R^y \left( \frac{\pi}{2} \right) R^x(\theta_k^g) \begin{cases} R^z(2\epsilon_k^g t)^\dagger & , \quad t < \tau \\ R^x(4\alpha t_p \sin k) R^z(2\epsilon_k^g(t-\tau))^\dagger R^x(4\alpha t_p \sin k)^\dagger R^z(2\epsilon_k^g \tau)^\dagger & , \quad t > \tau \end{cases} \cdot R^x(\phi_k^{g,g_0})^\dagger \begin{pmatrix} \gamma_k \\ \gamma_{-k} \end{pmatrix} \quad (\text{S12})$$

In terms of eq. (S4) we get for  $t > \tau$

$$\Sigma_x^k = \left( A \cos \chi_k^{\alpha t_p} + B \sin \chi_k^{\alpha t_p} \right) \sin \theta_k^g - \left( -A \sin \chi_k^{\alpha t_p} + B \cos \chi_k^{\alpha t_p} \right) \cos \theta_k^g, \quad (\text{S13})$$

$$\Sigma_y^k = \left( A \cos \chi_k^{\alpha t_p} + B \sin \chi_k^{\alpha t_p} \right) \cos \theta_k^g + \left( -A \sin \chi_k^{\alpha t_p} + B \cos \chi_k^{\alpha t_p} \right) \sin \theta_k^g, \quad (\text{S14})$$

$$\Sigma_z^k = \sin \phi_k^{g,g_0} \sin(2\epsilon_k(g)\tau) \cos(2\epsilon_k(g)(t-\tau)) + \left( \sin \phi_k^{g,g_0} \cos(2\epsilon_k(g)\tau) \cos(\chi_k^{\alpha t_p}) - \cos \phi_k^{g,g_0} \sin(\chi_k^{\alpha t_p}) \right) \sin(2\epsilon_k(g)(t-\tau)), \quad (\text{S15})$$

where  $\chi_k^{\alpha t_p} = 4\alpha t_p \sin k$  was introduced and

$$A = \sin \phi_k^{g,g_0} \sin(2\epsilon_k(g)\tau) \sin(2\epsilon_k(g)(t-\tau)) - \left( \sin \phi_k^{g,g_0} \cos(2\epsilon_k(g)\tau) \cos \chi_k^{\alpha t_p} - \cos \phi_k^{g,g_0} \sin \chi_k^{\alpha t_p} \right) \cos(2\epsilon_k(g)(t-\tau)), \quad (\text{S16})$$

$$B = \sin \phi_k^{g,g_0} \cos(2\epsilon_k(g)\tau) \sin \chi_k^{\alpha t_p} + \cos \phi_k^{g,g_0} \cos \chi_k^{\alpha t_p} \quad (\text{S17})$$

### C. $\Sigma_\alpha$ for generalised Hahn echo

In the generalised Hahn echo protocol the time reversal is at  $t = \tau$  induced by a sign change of the magnetic field,  $g \rightarrow -g$ . In this case the time evolution operator is

$$\tilde{U}_k(t) = \sqrt{2} R^y \left( \frac{\pi}{2} \right) \begin{cases} R^x(\theta_k^g) & , \quad t < \tau \\ R^x(\theta_k^{-g}) R^z(2\epsilon_k^{-g}(t-\tau))^\dagger R^x(\phi_k^{-g,g})^\dagger & , \quad t > \tau \end{cases} R^z(2\epsilon_k^g t)^\dagger R^x(\phi_k^{g,g_0})^\dagger \quad (\text{S18})$$

and the corresponding coefficients for the correlation matrix are

$$\Sigma_x^k = - \left[ (\cos \phi_k^{g,g_0} \sin \phi_k^{-g,g} + \sin \phi_k^{g,g_0} \cos \phi_k^{-g,g} \cos(2\epsilon_k^g \tau)) \cos(2\epsilon_k^{-g}(t-\tau)) - \sin \phi_k^{g,g_0} \sin(2\epsilon_k^g \tau) \sin(2\epsilon_k^{-g}(t-\tau)) \right] \sin \theta_k^{-g} - \left[ \cos \phi_k^{g,g_0} \cos \phi_k^{-g,g} - \sin \phi_k^{g,g_0} \sin \phi_k^{-g,g} \cos(2\epsilon_k^g \tau) \right] \cos \theta_k^{-g}, \quad (\text{S19})$$

$$\Sigma_y^k = - \left[ (\cos \phi_k^{g,g_0} \sin \phi_k^{-g,g} + \sin \phi_k^{g,g_0} \cos \phi_k^{-g,g} \cos(2\epsilon_k^g \tau)) \cos(2\epsilon_k^{-g}(t-\tau)) - \sin \phi_k^{g,g_0} \sin(2\epsilon_k^g \tau) \sin(2\epsilon_k^{-g}(t-\tau)) \right] \cos \theta_k^{-g} + \left[ \cos \phi_k^{g,g_0} \cos \phi_k^{-g,g} - \sin \phi_k^{g,g_0} \sin \phi_k^{-g,g} \cos(2\epsilon_k^g \tau) \right] \sin \theta_k^{-g}, \quad (\text{S20})$$

$$\Sigma_z^k = \sin \phi_k^{g,g_0} \sin(2\epsilon_k^g \tau) \cos(2\epsilon_k^{-g}(t-\tau)) + (\cos \phi_k^{g,g_0} \sin \phi_k^{-g,g} + \sin \phi_k^{g,g_0} \cos \phi_k^{-g,g} \cos(2\epsilon_k^g \tau)) \sin(2\epsilon_k^{-g}(t-\tau)). \quad (\text{S21})$$

## II. STATIONARY PHASE APPROXIMATION FOR THE DECAY AFTER LONG WAITING TIMES

### A. Transverse magnetisation for time reversal by explicit sign change

The echo in the transverse magnetisation is given by

$$\langle m_x \rangle_{t_e} = - \int_{-\pi}^{\pi} \frac{dk}{4\pi} (\Sigma_x^k(t_e) + i\Sigma_y^k(t_e)) . \quad (\text{S22})$$

Since  $\theta_k^g$  is an odd function of  $k$  and so is  $\phi_k^{g,g'}$ , whereas  $\epsilon_k^g$  is even, the imaginary part does not contribute,  $\int_{-\pi}^{\pi} dk \Sigma_y^k = 0$ . Thus,

$$\langle m_x \rangle_{t_e} = - \int_{-\pi}^{\pi} \frac{dk}{4\pi} \Sigma_x^k \quad (\text{S23})$$

$$\begin{aligned} &= \langle m_x \rangle_{\infty} + \int \frac{dk}{4\pi} \sin \theta_k^{g\delta} \cos \phi_k^{g,g_0} \sin \phi_k^{g\delta,g} \cos(2\epsilon_k^{g\delta} \nu \tau) + \int \frac{dk}{4\pi} \sin \theta_k^{g\delta} \sin \phi_k^{g,g_0} \cos \phi_k^{g\delta,g} \cos(2\epsilon_k^g \tau) \cos(2\epsilon_k^{g\delta} \nu \tau) \\ &+ \int \frac{dk}{4\pi} \sin \phi_k^{g,g_0} \sin(2\epsilon_k^g \tau) \sin(2\epsilon_k^{g\delta} \nu \tau) \sin \theta_k^{g\delta} - \int \frac{dk}{4\pi} \cos \theta_k^{g\delta} \sin \phi_k^{g,g_0} \sin \phi_k^{g\delta,g} \cos(2\epsilon_k^g \tau) , \end{aligned} \quad (\text{S24})$$

where  $\nu \equiv (t_e - \tau)/\tau$  was introduced. This expression contains two types of integrands, namely two integrals including only a single trigonometric function of time and two integrals including a product of two trigonometric functions of time with slightly differing spectra  $\epsilon_k^{g/g\delta}$ .

Consider the first type. For large  $\tau$  the integrands become highly oscillatory and the main contribution to the integral is given by the stationary points  $k^*$  of  $\epsilon_k^g$ ,

$$\left. \frac{d\epsilon_k^g}{dk} \right|_{k=k^*} = 0 \Rightarrow k^* = 0, \pm\pi . \quad (\text{S25})$$

At the stationary points  $\phi_{k^*} = \theta_{k^*} = 0$  and expanding the respective test functions  $f(k)$  around the stationary points yields

$$\int_{-\pi}^{\pi} \frac{dk}{2\pi} f(k) \cos(2\epsilon_k \tau) \approx \sum_{k^* \in \{0, \pi\}} \int_{-\infty}^{\infty} \frac{dk}{2\pi} \frac{f''(k^*)}{2} (k - k^*)^2 \cos(\epsilon_{k^*}'' (k - k^*)^2 \tau) \quad (\text{S26})$$

$$= \sum_{k^* \in \{0, \pi\}} \frac{1}{\tau^{3/2}} \int_{-\infty}^{\infty} \frac{dq}{2\pi} \frac{f''(k^*)}{2} q^2 \cos(\epsilon_{k^*}'' q^2) \propto \frac{\cos(2\epsilon_{k^*} \tau + \pi/4)}{\tau^{3/2}} \quad (\text{S27})$$

Thus, at long forward times these parts give contributions with a decay law  $\propto \tau^{-3/2}$ .

Now consider the terms including products of trigonometric functions of time. Here we can get rid of the products via the identities

$$2 \cos(2\epsilon_k^g \tau) \cos(2\epsilon_k^{g\delta} \nu \tau) = \cos(2(\epsilon_k^g + \nu \epsilon_k^{g\delta}) \tau) + \cos(2(\epsilon_k^g - \nu \epsilon_k^{g\delta}) \tau) , \quad (\text{S28})$$

$$2 \sin(2\epsilon_k^g \tau) \sin(2\epsilon_k^{g\delta} \nu \tau) = -\cos(2(\epsilon_k^g + \nu \epsilon_k^{g\delta}) \tau) + \cos(2(\epsilon_k^g - \nu \epsilon_k^{g\delta}) \tau) . \quad (\text{S29})$$

Allowing for  $0 < \nu \neq 1$  relevant saddle points for the above integrals are determined by

$$\left. \frac{d}{dk} (\epsilon_k^g \pm \nu \epsilon_k^{g\delta}) \right|_{k=k^*} = \left( \left( \frac{g}{\epsilon_k^g} \pm \nu \frac{g\delta}{\epsilon_k^{g\delta}} \right) \sin k \right) \Big|_{k=k^*} = 0 \quad (\text{S30})$$

yielding  $k^* = 0, \pi$  for both signs, and additionally

$$k_-^* = \pm \arccos \left( \frac{\nu^2 g_\delta^2 (1 + g^2) - g^2 (1 + g_\delta^2)}{2g\nu^2 g_\delta^2 - 2g_\delta g^2} \right) \quad (\text{S31})$$

for the negative sign. These additional saddle points coincide with  $k^* = 0, \pi$  for

$$\nu_0 = \frac{g|1 + g_\delta|}{g_\delta|1 + g|} , \quad \nu_\pi = \frac{g|1 - g_\delta|}{g_\delta|1 - g|} , \quad (\text{S32})$$

respectively. In the search of an echo peak  $\nu \in [\nu_0, \nu_\pi]$  can be tuned to create any saddle point  $k^* \in [0, \pi]$  via

$$\nu_{k^*}^{g, g\delta} = \frac{g\epsilon_{k^*}^{g\delta}}{g\delta\epsilon_{k^*}^g}. \quad (\text{S33})$$

Thus, for sufficiently long forward times with  $t_e = (1 + \nu)\tau$  and considering the equal contributions of both stationary points

$$\langle m_x \rangle_{t_e} - \langle m_x \rangle_\infty \approx - \int_{-\pi}^{\pi} \frac{dk}{2\pi} \left[ \sin \theta_k^{g\delta} \sin \phi_k^{g, g_0} \frac{\cos \phi_k^{g\delta, g} + 1}{2} \right] \cos(2(\epsilon_k^g - \nu \epsilon_k^{g\delta})\tau) + \gamma\tau^{-3/2} \quad (\text{S34})$$

$$\approx - \beta_\nu^{g, g_0, g\delta} \frac{\kappa_{k^*}(\tau)}{\tau^{1/2}} + \gamma\tau^{-3/2} \quad (\text{S35})$$

where  $\kappa_{k^*}(\tau) = \cos(2(\epsilon_{k^*}^g - \nu \epsilon_{k^*}^{g\delta})\tau + \pi/4)$  varies very slowly,

$$\beta_{k^*}^{g, g_0, g\delta} = \frac{\zeta_{k^*}^{g, g\delta, g_0}}{2\sqrt{\pi} |\xi_{k^*}^{g, g\delta}|^{1/2}}, \quad (\text{S36})$$

$$\zeta_k^{g, g\delta, g_0} \equiv \sin \theta_k^{g\delta} \sin \phi_k^{g, g_0} \frac{\cos \phi_k^{g\delta, g} + 1}{2}, \quad (\text{S37})$$

$$\xi_{k^*}^{g, g\delta} \equiv \left. \frac{d^2}{dk^2} (\epsilon_k^g - \nu_{k^*}^{g, g\delta} \epsilon_k^{g\delta}) \right|_{k=k^*}, \quad (\text{S38})$$

and the echo peak appears at  $t_e = (1 + \nu_{k^*}^{g, g\delta})\tau$ , where

$$k^* = \operatorname{argmax}_{k^*} |\beta_{k^*}^{g, g_0, g\delta}|. \quad (\text{S39})$$

The stationary phase approximation is valid if the test function  $\zeta_k^{g, g\delta, g_0} \approx \zeta_{k^*}^{g, g\delta, g_0} + \frac{d}{dk} \zeta_k^{g, g\delta, g_0} \Big|_{k=k^*} (k - k^*)$  does not vary too much on the interval  $[k - \Delta k, k + \Delta k]$ , where  $\Delta k$  is given by the width of the saddle point,  $(\tau \xi_{k^*}^{g, g\delta})^{-1}$ , i.e. we expect the approximation to be good for  $\tau > \tau^* = \frac{d}{dk} \zeta_k^{g, g\delta, g_0} \Big|_{k=k^*} / \xi_{k^*}^{g, g\delta}$ . Moreover, the period of  $\kappa_{k^*}(\tau)$  is determined by the difference of the spectra and, hence, very large compared to  $\tau^*$ .

## B. Longitudinal correlator for time reversal by generalised Hahn echo

We consider the case of starting from the ground state of  $H(g_0 = 0)$ . The echo in the transverse magnetisation is given by

$$\langle S_i^z S_{i+1}^z \rangle_{t_e} = \int_{-\pi}^{\pi} \frac{dk}{8\pi} e^{-ik} (\Sigma_x^k(t_e) + i\Sigma_y^k(t_e)) = \int_{-\pi}^{\pi} \frac{dk}{8\pi} (\Sigma_x^k(t_e) \cos k + \Sigma_y^k(t_e) \sin k). \quad (\text{S40})$$

The analysis of these integrals is mainly analogous to the previous section; however, for the Hahn echo protocol the relevant saddle points are contributed by the integrals containing  $\cos(2(\epsilon_k^g + \epsilon_k^{-g})\tau)$  without a shift of the echo time ( $\nu = (t_e - \tau)/\tau = 1$ ). Since with  $k_\pm^* = \pm\pi/2$

$$\left. \frac{d}{dk} (\epsilon_k^g + \epsilon_k^{-g}) \right|_{k=k_\pm^*} = \pm \left( \frac{1}{\epsilon_{k_\pm^*}^g} - \frac{1}{\epsilon_{k_\pm^*}^{-g}} \right) = 0 \quad (\text{S41})$$

and the corresponding test function  $\sin k_\pm^* \cos \theta_{k_\pm^*}^{-g} \sin \phi_{k_\pm^*}^{g, g_0} (\cos \phi_{k_\pm^*}^* + 1)/2 \neq 0$ , the stationary phase approximation yields

$$\langle S_i^z S_{i+1}^z \rangle_{t_e} - \langle S_i^z S_{i+1}^z \rangle_\infty \approx \tilde{\beta}^{g_0, g} \frac{\tilde{\kappa}(\tau)}{\tau^{1/2}} \quad (\text{S42})$$

with

$$\tilde{\kappa}(\tau) \equiv \cos(2(\epsilon_{\pi/2}^g + \epsilon_{\pi/2}^{-g})\tau + \pi/4) , \quad (\text{S43})$$

$$\tilde{\beta}^g \equiv \frac{\zeta^g}{4\sqrt{\pi}|\tilde{\xi}^g|^{1/2}} , \quad (\text{S44})$$

$$\tilde{\zeta}^g \equiv \cos \theta_{\pi/2}^{-g} \frac{\cos \phi_{\pi/2}^{-g,g} + 1}{2} , \quad (\text{S45})$$

$$\tilde{\xi}^g \equiv \left. \frac{d^2}{dk^2} (\epsilon_k^g + \epsilon_k^{-g}) \right|_{k=\pi/2} . \quad (\text{S46})$$

Note that in this case the frequency of the oscillatory term  $\tilde{\kappa}(\tau)$  is given by the sum of the spectra and for  $g \gg 1$   $\epsilon_{\pi/2}^g + \epsilon_{\pi/2}^{-g} \approx g$ . Therefore, the echo peak height at  $t_e = 2\tau$  oscillates with a high frequency, but the amplitude of the oscillations follows a power law with exponent  $-1/2$ .

## 4.3 Effective time reversal with perturbed Hamiltonian in generic many-body systems

In the previous section the echo decay under imperfect effective time reversal was studied by analytical means in a spin chain with quadratic Hamiltonian, which yielded a detailed understanding. It was found that the echoes decay only slowly with an algebraic decay law and that under certain conditions it is even possible to obtain ever persisting echoes. In this section we will explore whether this behavior of the free system is under the identical echo protocol contrasted by different behavior in nonintegrable systems, which are expected to be truly irreversible.

### 4.3.1 The effect of adding interactions

The integrability of the transverse-field Ising model studied in the previous section can be broken by adding a longitudinal component to the external magnetic field, i.e., extending the Hamiltonian to

$$\hat{H} = -J \sum_l \hat{S}_l^z \hat{S}_{l+1}^z + h_x \sum_l \hat{S}_l^x + h_z \sum_l \hat{S}_l^z . \quad (4.6)$$

By varying  $h_z$  this Hamiltonian can be continuously tuned between the integrable point  $h_z = 0$  and the nonintegrable system.

The lack of symmetries strongly restricts the system sizes feasible with exact diagonalization, where it is hard to differentiate between the general oscillations under time evolution and echo peaks. Therefore, we resort to iTEBD (cf. Section 3.1.2) in order to compute the dynamics.

As initial state we choose the ground state at  $h_x = \infty$ , which is distinguished by a full polarization  $\langle m_x \rangle = \frac{1}{N} \sum_l \langle S_l^x \rangle = 1/2$ . Fig. 4.2 displays the time evolution when the transverse field component is quenched to  $h_x = 0.3J$  and the imperfection is introduced to the backward evolution via a slight perturbation of  $h_x$  by  $\delta h_x = 0.05J$ . Fig. 4.2(a) shows the result for the noninteracting system with  $h_z = 0$  and the dynamics in the interacting regime at  $h_z = 0.1$  is displayed in Fig. 4.2(b). The plots contain the full time evolution of the transverse magnetization  $m_x$  under the echo protocol introduced in the previous section for different waiting times  $J\tau = 5, 10, 15, 20, 25, 30$ . In the case of the free system there is no decay of the echo peaks perceptible up to the maximal waiting time. The variation of the echo peak height is due to a node in the dynamics, which can be attributed to the beating of the transverse polarization that dominates the dynamics (see Section 3.2, where a similar quench was considered). The maximum of the envelope enclosing the single curves for different waiting times only changes marginally. By contrast the results for the interacting system in Fig. 4.2(b) clearly show a decaying echo peak height already on the considered time scale. The decay characteristics under the imperfect effective time reversal protocol change drastically as interactions are introduced. The echo peaks decay notably faster, indicating that it is much harder to effectively revert the dynamics. Note that even a very small longitudinal field component is sufficient to cause this change.

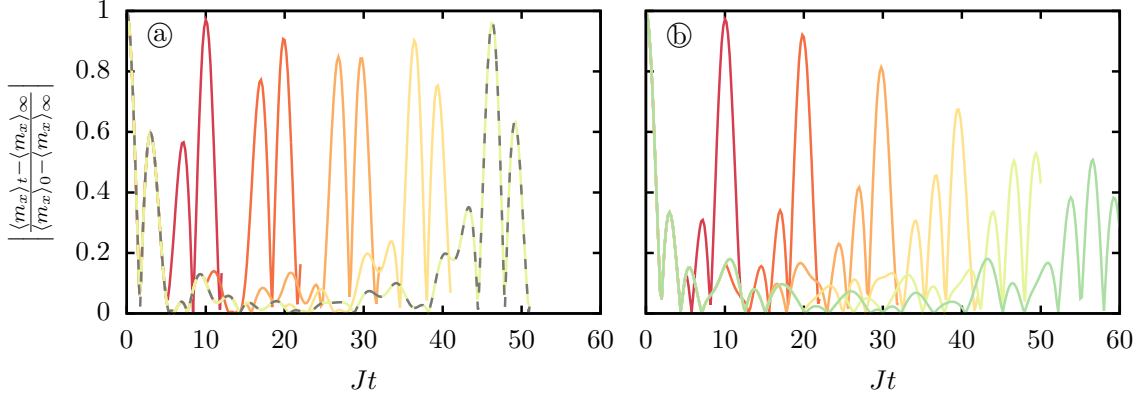


**Fig. 4.2:** Comparison of the decay of echoes in the integrable and the nonintegrable Ising chain (4.6). **(a)** In the transverse field Ising model ( $h_x = 0.3J$ ,  $h_z = 0$ ,  $\delta h_x = 0.05J$ ) the echo shows no recognizable decay on the considered time scale. The dashed line indicates the exact result from fermionization to demonstrate the accuracy of the other results obtained by iTEBD. **(b)** Adding a small longitudinal component  $h_z = 0.1J$  suffices to induce a clear decay of the echo signal.

Since the maximal times accessible with iTEBD are restricted due to the growth of entanglement, this method is not suited to extract decay laws from the computed dynamics with sufficient reliability. In the next section this question will be addressed by applying exact diagonalization to suited model Hamiltonians.

### 4.3.2 Decay laws

In order to investigate decay laws occurring under imperfect effective time reversal in interacting many-body systems we consider in the following a dimerized anisotropic spin-1/2 Heisenberg chain with next-nearest-neighbor interactions,

$$\begin{aligned} \hat{H}(J, J_z, \delta, \lambda) = & J \sum_l (1 + (-1)^l \delta) (\hat{S}_l^x \hat{S}_{l+1}^x + \hat{S}_l^y \hat{S}_{l+1}^y) + J_z \sum_l \hat{S}_l^z \hat{S}_{l+1}^z \\ & + \lambda \left[ J \sum_l (\hat{S}_l^x \hat{S}_{l+2}^x + \hat{S}_l^y \hat{S}_{l+2}^y) + J_z \sum_l \hat{S}_l^z \hat{S}_{l+2}^z \right]. \end{aligned} \quad (4.7)$$

With periodic boundary conditions this family of Hamiltonians obeys a number of symmetries restricting the dynamics to a smaller sector of the total Hilbert space (cf. Section 3.1.1). Exploiting these symmetries allows to access larger system sizes, which is crucial to identify echo peaks at late times. In small systems large oscillations in the dynamics cannot be distinguished from the echo at late times. These oscillations are suppressed by increasing system size.

The different parameters of the Hamiltonian (4.7) allow to tune interactions and integrability.  $\hat{H}(J, 0, 0, 0)$  is a quadratic Hamiltonian by virtue of Jordan-Wigner transform, namely the XX model (Lieb *et al.*, 1961). Note that this is, however, not suited for the echo protocol under consideration as it lacks a second parameter that can be used to introduce an imperfection to the backwards evolution without changing basic system properties. The

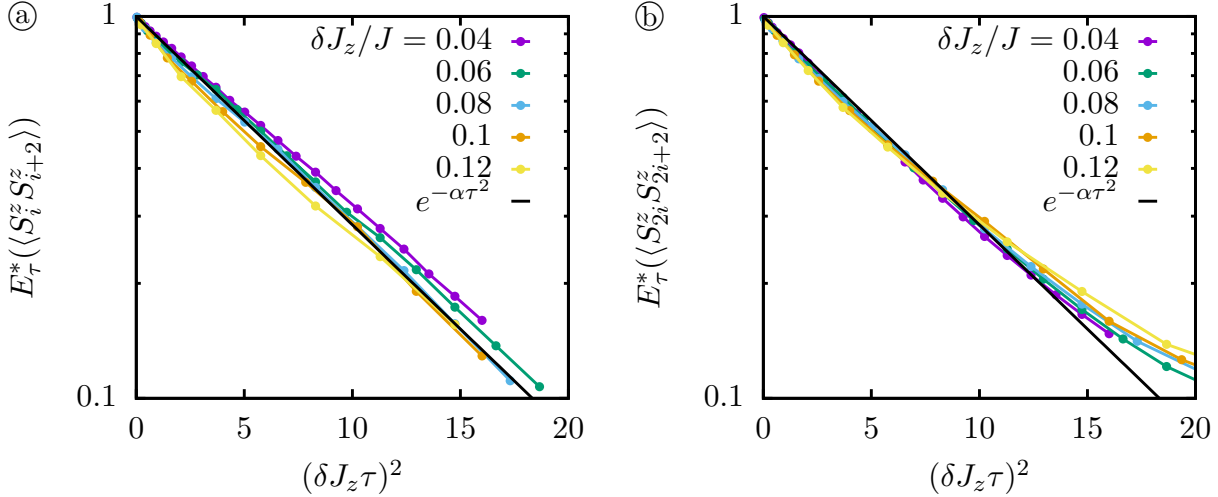


**Fig. 4.3:** Echo peak decay in an integrable spin chain with  $N = 28$  spins. **(a)** Decay in the integrable  $XXZ$  chain with  $J_z = 0.3J$ . **(b)** Decay in the nonintegrable dimerized chain with  $J_z = 0.3J$  and  $\delta = 0.2$ . In both cases the echo peak decay is compatible with a Gaussian decay law on the accessible time scale.

Hamiltonian  $\hat{H}(J, J_z, 0, 0)$  constitutes the  $XXZ$  model, which is integrable and solvable by Bethe ansatz (Bethe, 1931; Korepin *et al.*, 1993). The integrability is broken by introducing a dimerization  $\delta > 0$  or next-nearest neighbor interactions  $\lambda > 0$ .

In the following the imperfection in the backward evolution will always be introduced through a slight perturbation to the anisotropy  $\delta J_z$ . As initial state we choose the symmetrized Néel state

$$|\psi_0\rangle = \frac{1}{\sqrt{2}} \left( |\uparrow\downarrow\uparrow \dots \uparrow\downarrow\rangle + |\downarrow\uparrow\downarrow \dots \downarrow\uparrow\rangle \right), \quad (4.8)$$

which is the ground state at strong anisotropy. Distinct observables suited to probe the order of this state are spin-spin correlations functions  $\langle \hat{S}_l^z \hat{S}_{l+n}^z \rangle$ .

We first consider the system without next-nearest neighbor interactions,  $\lambda = 0$ , and anisotropy  $J_z = 0.3J$ . Fig. 4.3 shows the echo peak heights in the observable  $\langle \hat{S}_l^z \hat{S}_{l+2}^z \rangle$  extracted for the integrable system without dimerization (Fig. 4.3(a)) and the nonintegrable system with dimerization  $\delta = 0.2$  (Fig. 4.3(b)). In both cases the results are compatible with a Gaussian decay law  $E_\tau^*(\langle \hat{S}_l^z \hat{S}_{l+2}^z \rangle) \propto e^{-\alpha\tau^2}$ , which is indicated by the black line.<sup>1</sup> Note that the results for different perturbation strengths  $\delta J_z$  collapse due to a rescaling of the time axis by  $\delta J_z^2$ . This means that the decay rate depends on the perturbation strength as  $\alpha \propto \delta J_z^2$ .

The echo peak decay in the nonintegrable model begins to deviate from the Gaussian law at late times. We attribute this to the finite size of the system. In order to substantiate this allegation we turn to the system with next-nearest neighbor interactions  $\lambda > 0$ , where the boundaries become important at earlier times and the crossover can be separated from the effect of finite size oscillations in the numerical data.

<sup>1</sup> The normalized echo peak height  $E_\tau^*(X)$  is defined in Eq. (21) of Section 4.2.



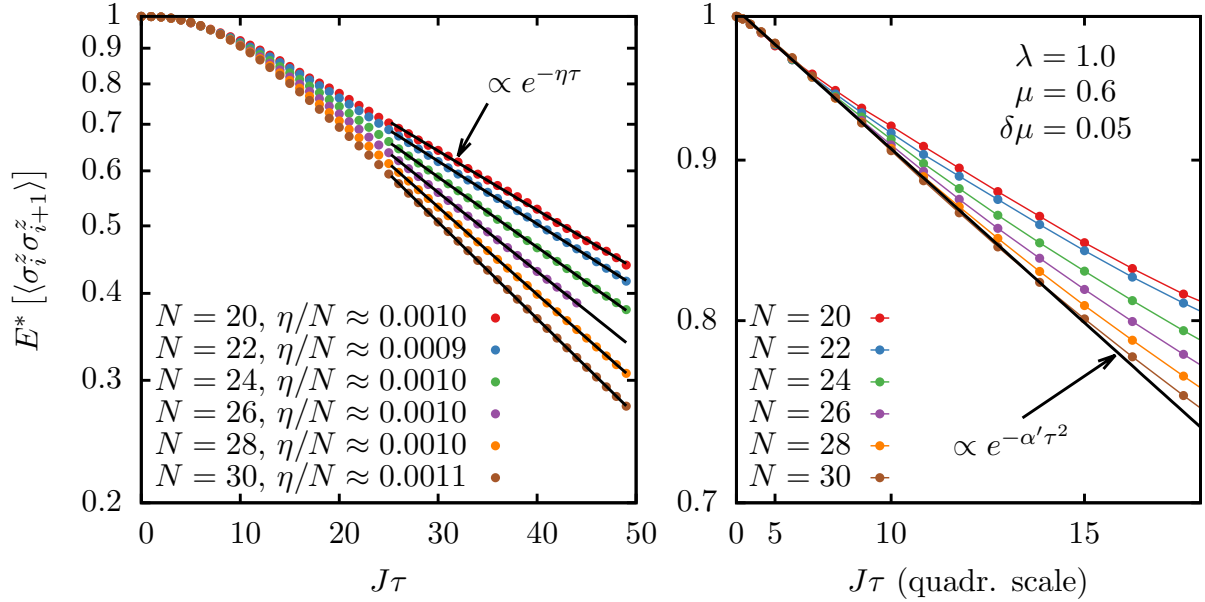


**Fig. 4.4:** Echo peak decay in the integrable spin chain with next-nearest-neighbor coupling  $\lambda = 1$ ,  $J_z = 0.6J$ , and perturbation  $\delta J_z = 0.05J$ . Plotted on a log-linear scale (left panel) it is evident that the decay is exponential at long times with a rate  $\eta$  that is proportional to the system size  $N$ . In a log-quadratic plot it seems that the decay is Gaussian for a short initial period that extends as the system size is increased.

Fig. 4.4 displays the echo peak decay obtained with the Hamiltonian  $H(J = 1, J_z = 0.6, \delta = 0, \lambda = 1)$  for different system sizes. The log-linear plot in Fig. 4.4(a) reveals that the echoes decay exponentially at late times. Moreover, the decay rate is proportional to the system size  $\eta \propto N$ . The same data is plotted with a quadratic scaling of the time axis in Fig. 4.4(b). In this case it appears that the echoes initially decay in a Gaussian fashion for a time interval that grows as the system size is increased. This observation gives rise to the conjecture that in finite systems the decay law of the echo peaks is of the form

$$E_\tau^* \sim e^{-\min(\tau, \nu N) \times \alpha \tau} . \quad (4.9)$$

with some constant  $\nu$ . In the thermodynamic limit  $N \rightarrow \infty$  this means a Gaussian decay of the echo peak heights for all times.

In the integrable system the decay was always found to be Gaussian. There was no crossover to exponential decay observed. Since the maximal times that can be analyzed in the finite system are, however, restricted due to the general oscillations in the time evolution, we cannot exclude that such a crossover occurs at later times.

In studies of the Loschmidt echo (Gorin *et al.*, 2006) analytical insight into the origin of different decay laws could be gained by considering expansions of the echo operator in powers of the perturbation, i.e.,

$$\hat{U}_E(\tau) = e^{i(\hat{H} + \epsilon \hat{V})\tau} e^{-i\hat{H}\tau} = \mathcal{T}_t \exp \left( -i\epsilon \int_0^\tau dt \hat{V}(t) \right) , \quad (4.10)$$

where  $\mathcal{T}_t$  is the time ordering operator and  $\hat{V}(t) = e^{i\hat{H}t}\hat{V}e^{-i\hat{H}t}$ . This analysis, however, relies on the fact that the echo occurs at  $t_e = 2\tau$ . It was already found in Section 4.2 that due to variations in the quasiparticle dispersion between forward and backward evolution observable echoes in many-body systems do not necessarily occur at  $t_e = 2\tau$ . This is also the case in the interacting systems under consideration in this section. Fig. 4.5 shows exemplarily that also in these models the echo peak shifts systematically away from  $2\tau$  as  $\tau$  is increased. Hence, it is crucial to identify the correct echo time  $t_e$  in order to find the decay laws discussed above. It is at this point not clear how to include the shift of the echo peak in a related analysis.

In conclusion, we find that the echo peak heights in interacting systems decay much faster than in noninteracting systems, namely with a Gaussian decay law in the thermodynamic limit. The decay law is the same for an interacting integrable system and the generic systems. Hence, we conclude that interactions crucially impede the possibility to restore the initial state by a time reversal protocol. However, the decay law observed after imperfect time reversal with a perturbation of the Hamiltonian lacks a central property that is required to motivate true irreversibility, namely perturbation independence. The decay rate was found to scale quadratically with the perturbation strength. This means that aiming at a given resemblance to the initial state the endeavor to improve the manipulation precision resulting in a smaller perturbation to the Hamiltonian is rewarded by an extension of the achievable waiting time that is proportional to the reduction of the perturbation. In other words: The improvement warrants the effort.

In the following section it will be demonstrated that considering perturbations that affect the state at the point of time reversal instead of the Hamiltonian throughout the backwards evolution results in perturbation-independent decay rates. These lead to an interpretation analogous to classical systems meaning that the dynamics of quantum many-body systems is irreversible for all practical purposes, because precise time reversal is prohibitively expensive.

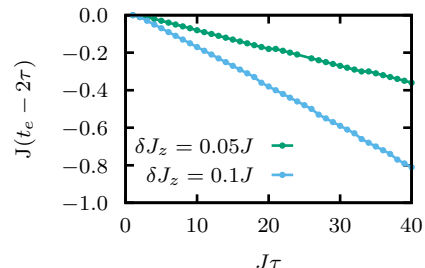


**Fig. 4.5:** In the considered echo protocol the echo time  $t_e$  is systematically shifted away from  $2\tau$ , which can be ascribed to a modified quasiparticle dispersion in the backwards evolution;  $J_z = 0.2J$ ,  $\lambda = 0.5$ ,  $\delta = 0$  (cf. Eq. (4.7)).

## 4.4 *Preprint:* Irreversible dynamics in quantum many-body systems

Markus Schmitt and Stefan Kehrein

arXiv:1711.00015; submitted.

<https://arxiv.org/abs/1711.00015>

**Author contributions** The authors conceived the approach based on perturbations of the many-body state in joint discussions. M. S. performed the numerical analysis and wrote the manuscript. S. K. revised the manuscript.

# Irreversible dynamics in quantum many-body systems

Markus Schmitt\* and Stefan Kehrein

*Institute for Theoretical Physics, Georg-August-Universität Göttingen,  
Friedrich-Hund-Platz 1 - 37077 Göttingen, Germany*

(Dated: October 31, 2017)

Irreversibility, despite being a necessary condition for thermalization, still lacks a sound understanding in the context of quantum many-body systems. In this work we approach this question by studying the behavior of generic many-body systems under imperfect effective time reversal, where the imperfection is introduced as a perturbation of the many-body state at the point of time reversal. Based on numerical simulations of the full quantum dynamics we demonstrate that observable echos occurring in this setting decay exponentially with a rate that is intrinsic to the system meaning that the dynamics is effectively irreversible.

*Introduction.* The recent development of experimental techniques to realize and precisely manipulate closed quantum systems with many degrees of freedom [1–4] motivated a lot of theoretical activity aimed at understanding the dynamics of quantum many-body systems far from equilibrium. A fundamental question that arose in this context is how and in what sense closed quantum many-body systems thermalize when initially prepared far from thermal equilibrium. This has been investigated with great efforts in recent years [5, 6]. Closely related is the question of irreversibility, which, however, did to date not receive much attention.

For classical systems the origin of irreversibility despite microscopically reversible dynamics was already discussed by Boltzmann and Loschmidt [7–9] and was essentially understood in a modern sense by Thompson [10]. Classical systems typically exhibit chaotic dynamics if composed of many degrees of freedom. Hence, any practical efforts to revert the dynamics, e.g. by inverting the momenta, are ultimately futile due to the exponential sensitivity of the dynamics to small imperfections. In particular, the dominant rate with which initially nearby trajectories diverge, called Lyapunov exponent, is independent of the perturbation strength. Therefore, any improvement of the accuracy in the time reversal protocol can only affect the prefactor of the exponential law.

This practical understanding of irreversibility in classical systems led Peres [11] to introduce the Loschmidt echo

$$\mathcal{L}(t) = |\langle \psi_0 | e^{i(\hat{H} + \epsilon \hat{V})t} e^{-i\hat{H}t} | \psi_0 \rangle|^2 \quad (1)$$

as measure for irreversibility in quantum systems. The Loschmidt echo is the overlap of a wave function evolved forward in time with Hamiltonian  $\hat{H}$  and subsequently backwards with a slightly perturbed Hamiltonian  $\hat{H} + \epsilon \hat{V}$ , thereby quantifying the resemblance of the time evolved state with the initial state. This quantity proved very useful in the analysis of the dynamics of quantum systems with few degrees of freedom [12, 13].

In generic quantum many-body systems, however, overlaps like the Loschmidt echo have only limited significance for the resemblance of states in physical terms.

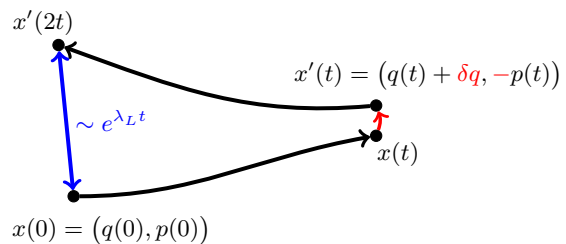


FIG. 1. Classical analog of the time reversal protocol under consideration.

According to the eigenstate thermalization hypothesis (ETH) [14–17] energy expectation values of few-body observables  $\mathcal{O}_E = \langle E | \hat{O} | E \rangle$  are smooth functions of the eigenstate energy  $E$ . More precisely, the assumption is that the difference of the expectation value in neighboring eigenstates,  $|\mathcal{O}_{E_n} - \mathcal{O}_{E_{n+1}}|$ , is exponentially suppressed with increasing system size, which is strongly supported by numerical evidence from different studies [18–21]. Since all experimentally measurable quantities are related to the above-mentioned class of observables this means that energetically close-by eigenstates of a generic Hamiltonian  $\hat{H}$ , although orthogonal, are by all practical means indistinguishable in experiment. The same holds for integrable systems if the further integrals of motion are taken into account in addition to the energy [22]. Therefore, any definition of irreversibility in many-body systems should be based on observables, which are accessible in experiment [23–27].

Connected to the question of irreversibility so called out-of-time-order correlators (OTOCs) of the form  $\langle \hat{A}^\dagger(0) \hat{B}^\dagger(t) \hat{A}(0) \hat{B}(t) \rangle_\beta$  were recently suggested to probe scrambling, i.e. the complete delocalization of initially local information, and exponential sensitivity of the dynamics to small perturbations [28, 29]. Based on this a black hole theory and a holographic model of Majorana fermions were identified as maximally chaotic systems [30–32]. Moreover, OTOCs can directly be related to an information-theoretic measure for the delocalization of initially local information [33]. These ideas were seized in a number of subsequent works to investigate signatures

of chaos and scrambling in the dynamics of local lattice models [33–38].

*Scope of this work.* In this Letter we propose a probe of irreversible dynamics based on observable echos under imperfect effective time reversal. A first investigation in an integrable model was done in Ref. [26]. In that work it was found that the echos in an integrable spin chain decay not faster than algebraically indicating that the dynamics is well reversible. Under a certain protocol even ever-persisting echos were found. In the present work we demonstrate that in generic non-integrable systems the observable echos under imperfect time reversal decay exponentially as would be expected when the dynamics is chaotic and – importantly – that the decay is primarily governed by the intrinsic properties of the system. This finding contrasts the aforementioned algebraic decay found in an integrable spin chain. In the considered protocol the imperfection is introduced as a perturbation of the many-body state at the point of time reversal. Hence, the proposed probe of irreversibility directly corresponds with the understanding of classical irreversibility as a consequence of the butterfly effect, but it is applicable to generic quantum many-body systems far from any semi-classical limit.

*Time reversal protocol.* Irreversibility in classical systems is understood to be a consequence of chaotic dynamics, i.e. the fact that trajectories diverge exponentially if the coordinates are slightly changed initially. This leads to the fact that the final coordinates deviate exponentially from the initial coordinates if an imperfect time reversal protocol as sketched in Fig. 1 is applied.

An analogous situation in quantum systems is the perturbation of the quantum state at the point of time reversal, i.e. applying a unitary perturbation operator  $\hat{P}_\epsilon$  to the time-evolved state  $|\psi(t)\rangle = e^{-i\hat{H}t}|\psi_0\rangle$ ,

$$|\psi(t)\rangle \rightarrow |\psi'(t)\rangle = \hat{P}_\epsilon |\psi(t)\rangle, \quad (2)$$

where  $\epsilon$  is a parameter for the magnitude of the perturbation. For many-body systems it is crucial at this point to regard physical observables as measure for the smallness of the perturbation and not the overlap of the states. Due to the unitarity of the time evolution there will always be a part of the dynamics that is perfectly reverted if the states before and after applying the perturbation have a non-vanishing overlap. A natural operation  $\hat{P}_\epsilon$  that leaves observables almost unchanged while making the state orthogonal is time evolution with a local Hamiltonian  $\hat{H}_p$  for short time  $\delta t$ . In a many-body system with  $N$  degrees of freedom the overlap of a time-evolved state with the initial state generally takes the form  $|\langle \psi_0 | e^{-i\hat{H}t} | \psi_0 \rangle|^2 = e^{-Nr(t)}$  with a system size independent rate function  $r(t)$ , i.e. the overlap vanishes at arbitrarily short times in the thermodynamic limit  $N \rightarrow \infty$ . Observables, instead, change smoothly under time evolution with a physical Hamiltonian.

In the following we study the dynamics of a many-body system when a time reversal protocol motivated by these considerations is applied. The system is prepared in an initial state  $|\psi_0\rangle$  that exhibits some significant features distinguishing it from an equilibrium state of the Hamiltonian  $\hat{H}$ , like, e.g., a strong magnetic order in a disordered phase. This state is time-evolved for a waiting time  $\tau$ , yielding  $|\psi(\tau)\rangle = e^{-i\hat{H}\tau}|\psi_0\rangle$ . At this point a perturbation operator  $\hat{P}_{\delta t} = e^{-i\hat{H}_p\delta t}$  given by some other Hamiltonian  $\hat{H}_p$  is applied for a short time  $\delta t$ , resulting in  $|\psi'(\tau)\rangle = \hat{P}_{\delta t}|\psi(\tau)\rangle$ . Subsequently,  $|\psi'(\tau)\rangle$  is evolved backwards in time until the echo time  $t^* \approx 2\tau$ , where the resemblance of the time evolved state to the initial state is largest in terms of the observables under consideration, i.e. these observables show an extremum, which we call an echo peak. The existence of these echo peaks can be inferred by considering the case of  $\delta t = 0$ , where a perfect revival is produced independent of the waiting time  $\tau$ , and assuming a smooth behavior of the dynamics as  $\delta t$  is increased. We propose to declare a system irreversible if the decay of echos as a function of the waiting time  $\tau$  is exponential or faster than exponential and if the decay rate is an intrinsic property of the system, i.e. unaffected by reducing the perturbation strength. This definition means that substantial improvement of the reconstruction of the initial state by manipulating with enhanced precision is practically impossible.

Note that by identifying  $\hat{A}(0) \equiv \hat{O}$  and  $\hat{B}(\tau) \equiv e^{i\hat{H}\tau}\hat{P}_{\delta t}e^{-i\hat{H}\tau}$  this protocol effectively results in the measurement of an OTOC as introduced above if the initial state  $|\psi_0\rangle$  is an eigenstate of observable under consideration,  $\hat{O}|\psi_0\rangle = O|\psi_0\rangle$ . A key difference is, however, the fact that the echo protocol takes into account the expectation value in the pure initial state far from equilibrium, whereas the OTOC is defined with respect to a thermal density matrix.

*Model Hamiltonians.* As minimal examples of generic quantum many-body systems we study spin-1/2 systems defined by the Hamiltonian

$$\hat{H} = \sum_{i \neq j} J_{ij} (\hat{\sigma}_i^x \hat{\sigma}_j^x + \hat{\sigma}_i^y \hat{\sigma}_j^y), \quad (3)$$

where the  $\hat{\sigma}_i^\alpha$ ,  $\alpha = x, y$ , denote the Pauli spin operators acting on lattice sites  $i = 1, \dots, N$ . In this work we focus on two versions of this Hamiltonian, namely a Hamiltonian  $\hat{H}_{\text{loc}}$  with local couplings

$$J_{ij}^{\text{loc}} = J \begin{cases} 2^{1-|i-j|} & , \text{ for } 0 < |i-j| \leq 2 \\ 0 & , \text{ else} \end{cases} \quad (4)$$

and a fully connected random Hamiltonian  $\hat{H}_{\text{fc}}$  with  $J_{ij}^{\text{fc}} = J_{ji}^{\text{fc}} = JR_{ij}/N$ , where  $R_{ij}$  is drawn from the standard normal distribution. We found that altering the interaction range of the local Hamiltonian and introducing an (anisotropic) Heisenberg-type coupling left

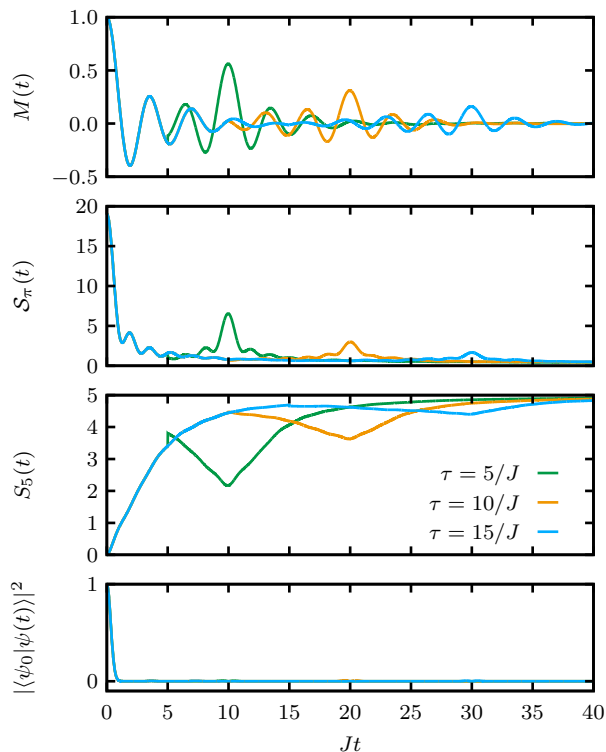


FIG. 2. Time evolution of staggered magnetization  $M(t)$ , spin structure factor  $\mathcal{S}_\pi(t)$ , entanglement entropy  $S_5(t)$ , and return probability  $|\langle \psi_0 | \psi(t) \rangle|^2$  under the imperfect time reversal protocol for different forward times  $\tau$  obtained with the Hamiltonian  $H_{\text{loc}}$ . The observables and the entanglement entropy show clear echos at  $t = 2\tau$  that decay as  $\tau$  is increased, whereas the return probability does not show any signal. The perturbation strength is  $\delta t/J = 0.05$ .

the results qualitatively unchanged. However, the restriction of the couplings to shorter distances or strongly anisotropic couplings, respectively, introduce large oscillations to the dynamics, which complicates the identification of echo peaks. As initial state we choose the Néel state  $|\psi_0\rangle = |\uparrow\downarrow\uparrow\dots\rangle$ . For this state the staggered magnetization  $M = \frac{1}{N} \sum_n (-1)^n \langle \hat{\sigma}_n^z \rangle$  and the spin structure factor  $\mathcal{S}_\pi = \frac{1}{N} \sum_{i,j} e^{i(i-j)\pi/N} \langle \vec{\sigma}_i \cdot \vec{\sigma}_j \rangle$  constitute suited observables for the echo protocol described above. Moreover, we will investigate the dynamics of the entanglement entropy of bipartitions into subsystems  $A$  and  $B$  defined by  $S_A = -\text{tr}(\hat{\rho}_A \log_2 \hat{\rho}_A)$ , where  $\hat{\rho}_A = \text{tr}_B(|\psi(t)\rangle\langle\psi(t)|)$  is the reduced density matrix of the subsystem  $A$ .

The Hamiltonian that defines the perturbation is chosen to be a local random Hamiltonian

$$\hat{H}_p = \sum_{i=1}^{N-1} J_i (\hat{\sigma}_i^x \hat{\sigma}_{i+1}^x + \hat{\sigma}_i^y \hat{\sigma}_{i+1}^y) \quad (5)$$

with real couplings  $J_i$  drawn from the standard normal distribution.

*Numerical realization and finite size effects.* In the following we will resort to exact diagonalization and Lanczos propagation [39] in order to compute the time evolution. This limits the accessible systems to sizes far from the thermodynamic limit; due to the numerical expense the maximal system size we consider is  $N = 22$ . For any finite system, however, the echos produced under the envisaged imperfect effective time reversal will generally not decay to zero for long waiting times  $\tau$ . Introducing the eigenbasis of the Hamiltonian,  $(\hat{H} - E_\alpha)|\alpha\rangle = 0$ , the time evolution of observables under the time reversal protocol is

$$\begin{aligned} \langle \hat{O} \rangle_{t_1, t_2} &= \langle \psi_0 | e^{i\hat{H}t_1} \hat{P}_{\delta t}^\dagger e^{-i\hat{H}t_2} \hat{O} e^{i\hat{H}t_2} \hat{P}_{\delta t} e^{-i\hat{H}t_1} | \psi_0 \rangle \\ &= \sum_{\alpha, \alpha', \beta, \beta'} \langle \psi_0 | \alpha \rangle (P_{\delta t}^\dagger)_{\alpha, \alpha'} O_{\alpha' \beta} (P_{\delta t})_{\beta \beta'} \langle \beta' | \psi_0 \rangle \\ &\quad \times e^{i(E_\alpha - E_{\beta'})t_1 + i(E_\beta - E_{\alpha'})t_2}, \end{aligned} \quad (6)$$

where  $X_{\alpha\beta} = \langle \alpha | \hat{X} | \beta \rangle$  with  $\hat{X} = \hat{O}, \hat{P}_{\delta t}, \hat{P}_{\delta t}^\dagger$  denotes the matrix elements of the respective operators. Clearly, for any  $t_1, t_2$  terms with  $\alpha = \beta'$  and  $\beta = \alpha'$  are time-independent. These terms yield the stationary value that is reached at long times  $t_1 \neq t_2$ . At  $t_1 = t_2$  there is, however, an additional time-independent contribution of the terms with  $\alpha = \alpha'$  and  $\beta = \beta'$ , where the diagonal elements of the perturbation operator  $(P_{\delta t})_{\alpha\alpha} = \langle \alpha | e^{-i\hat{H}_p \delta t} | \alpha \rangle$  appear. Most prominent among these contributions at small  $N$  is the identity that gives rise to the non-vanishing overlap  $\langle \psi(\tau) | \hat{P}_{\delta t} | \psi(\tau) \rangle$  in the finite system. As discussed above the modulus of overlaps of the form  $\langle \alpha | e^{-i\hat{H}_p \delta t} | \alpha \rangle$  vanishes at arbitrarily short times in the thermodynamic limit. Hence, this non-decaying contribution to echos at  $t_1 = t_2$  vanishes for  $N \rightarrow \infty$ .

In the finite systems we analyze the decay of the echo peaks towards these stationary values, which is the universal behavior that survives in the thermodynamic limit. In practice we discard the parallel component of the perturbed state,  $|\psi_\parallel(\tau)\rangle = \langle \psi(\tau) | \psi'(\tau) \rangle |\psi(\tau)\rangle$ , before starting the backward evolution. When analyzing the decay laws we additionally subtract the remaining stationary value from the echo peak heights that is estimated by a long time average.

Fig. 2 displays an exemplary time evolution with  $\hat{H}_{\text{loc}}$  of staggered magnetization  $M(t)$ , spin structure factor  $\mathcal{S}_\pi(t)$ , entanglement entropy  $S_n(t)$  of  $n = 5$  spins at one end of the spin chain, and overlap with the initial state  $|\langle \psi_0 | \psi(t) \rangle|^2$  for a system of  $N = 20$  spins, where the perturbation with  $J\delta t = 0.05$  is applied at different waiting times  $\tau$ . The perturbation causes only a minimal shift of the observables although the perturbed state is orthogonal to the state before the perturbation. The dynamics exhibit a pronounced maximum at  $t_e \approx 2\tau$ , whereas the entanglement entropy becomes minimal at this point. Note that in contrast to the results for imperfect time reversal with a perturbed Hamiltonian [26] the echo time

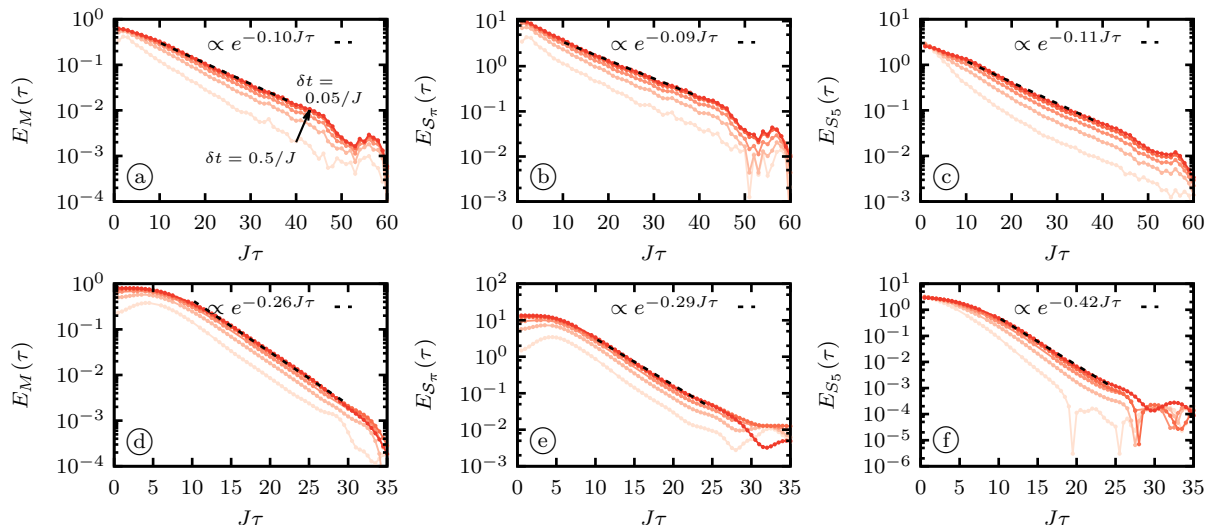


FIG. 3. Decay of the echo peak heights of staggered magnetization  $M$ , spin structure factor  $S_\pi$ , and entanglement entropy of five consecutive spins  $S_5$  after imperfect effective time reversal for both the local Hamiltonian  $\hat{H}_{\text{loc}}$  (a)-(c) and the fully connected Hamiltonian  $\hat{H}_{\text{fc}}$  (d)-(f). The perturbation Hamiltonian is the same realization of  $\hat{H}_p$  in all cases, whereas the plotted perturbation strengths are  $J\delta t = 0.5, 0.35, 0.25, 0.15, 0.05$ . The dashed lines indicate exponential fits to the results for  $\delta t = 0.05/J$ .

under the present time reversal protocol is always very close to  $2\tau$  and does not exhibit any systematic shift away from that.

*Echo peak decay.* As is evident from the exemplary time evolution in Fig. 2 the resemblance of the time-evolved state to the initial state in terms of the observables decreases as the waiting time is increased. In order to extract laws of decay we introduce the echo peak height of an observable  $\hat{O}$ ,

$$E_O(t) = \max_{t' > t} |\langle \hat{O} \rangle_{t', t} - O_\infty|, \quad (7)$$

where the maximum occurs at the echo time  $t_e \approx 2t$  and  $O_\infty$  is the stationary value reached after long times.

Fig. 3 displays the decay of the echo peak heights for the observables and the entanglement entropy for both the local Hamiltonian  $H_{\text{loc}}$  and the fully connected random Hamiltonian  $H_{\text{fc}}$ . The decay for a single realization of the perturbation Hamiltonian  $H_p$  is shown for different perturbation strengths  $\delta t$ . In all cases the echo peak heights exhibit a marked exponential decay at long waiting times  $\tau$ . The decay rate varies only weakly as  $\delta t$  is changed. In particular, the curves converge as  $\delta t \rightarrow 0$ . In each plot an exponential fit to the data with the smallest perturbation strength ( $\delta t = 0.05$ ) is included. For the local Hamiltonian the fitted decay rates for both observables and the entanglement entropy are almost identical. In the fully connected system the observable echos decay with similar rates, whereas the echos in the entanglement entropy decay slightly faster. While the relation of the decay rates to microscopic properties of the systems is as of yet unclear, we find that they do not coincide with the

decay rates occurring after a simple quench. The decay of the entanglement entropy shows that although recoverable at short times the information about the genuinely quantal structure of the initial state is lost in the same fashion as the information about observables.

For different realizations of the random perturbation Hamiltonian  $\hat{H}_p$  and fixed  $\delta t$  we observed variations of the decay rate of about 15%. We attribute these variations to the small system size and expect them to vanish in the thermodynamic limit.

*Discussion.* In this work results from numerical simulations of the full quantum dynamics are reported. Our results show that generic quantum many-body systems exhibit exponential decay of observable echo peaks under imperfect effective time reversal. This is in contrast to algebraically decaying echos found in an integrable system [26]. Importantly, the decay rate in the non-integrable quantum many-body models studied here was found to be largely independent of the perturbation strength. This implies that any practical effort to improve the accuracy in a time reversal experiment is in the end futile, just like in irreversible classical systems.

The presented results give rise to further questions, which are beyond the scope of this work and are therefore left for future research. It was found that the decay rate of the echos is an intrinsic property of the Hamiltonian that determines the time evolution. However, it is at this point not clear how said rate is related to the microscopic details of the system. Moreover, possible relations to other definitions of quantum chaos and irreversibility, e.g. the one based on OTOCs [28, 29], should be investigated.

This work was supported through SFB 1073 (project



B03) of the Deutsche Forschungsgemeinschaft (DFG). M.S. acknowledges support by the Studienstiftung des Deutschen Volkes. For the numerical computations the Armadillo library [40] was used.

---

\* markus.schmitt@theorie.physik.uni-goettingen.de

- [1] M. Greiner, O. Mandel, T. Esslinger, T. W. Hansch, and I. Bloch, *Nature* **415**, 39 (2002).
- [2] T. Kinoshita, T. Wenger, and D. S. Weiss, *Nature* **440**, 900 (2006).
- [3] J.-y. Choi, S. Hild, J. Zeiher, P. Schauß, A. Rubio-Abadal, T. Yefsah, V. Khemani, D. A. Huse, I. Bloch, and C. Gross, *Science* **352**, 1547 (2016).
- [4] P. Jurcevic, H. Shen, P. Hauke, C. Maier, T. Brydges, C. Hempel, B. P. Lanyon, M. Heyl, R. Blatt, and C. F. Roos, *Phys. Rev. Lett.* **119**, 080501 (2017).
- [5] J. Eisert, M. Friesdorf, and C. Gogolin, *Nat Phys* **11**, 124 (2015).
- [6] L. D'Alessio, Y. Kafri, A. Polkovnikov, and M. Rigol, *Advances in Physics* **65**, 239 (2016).
- [7] L. Boltzmann, *Sitzungsberichte der Akademie der Wissenschaften zu Wien* **66**, 275 (1872).
- [8] J. Loschmidt, *Sitzungsberichte der Akademie der Wissenschaften zu Wien* **73**, 128 (1876).
- [9] L. Boltzmann, *Sitzungsberichte der Akademie der Wissenschaften zu Wien* **75**, 67 (1877).
- [10] W. Thompson, *Proceedings of the Royal Society of Edinburgh* **8**, 325 (1874).
- [11] A. Peres, *Phys. Rev. A* **30**, 1610 (1984).
- [12] T. Gorin, T. Prosen, T. H. Seligman, and M. Žnidarič, *Physics Reports* **435**, 33 (2006).
- [13] P. Jacquod and C. Petitjean, *Advances in Physics* **58**, 67 (2009).
- [14] J. M. Deutsch, *Phys. Rev. A* **43**, 2046 (1991).
- [15] M. Srednicki, *Phys. Rev. E* **50**, 888 (1994).
- [16] M. Srednicki, *Journal of Physics A: Mathematical and General* **29**, L75 (1996).
- [17] M. Rigol, V. Dunjko, and M. Olshanii, *Nature* **452**, 854 (2008).
- [18] R. Steinigeweg, J. Herbrych, and P. Prelovšek, *Phys. Rev. E* **87**, 012118 (2013).
- [19] W. Beugeling, R. Moessner, and M. Haque, *Phys. Rev. E* **89**, 042112 (2014).
- [20] H. Kim, T. N. Ikeda, and D. A. Huse, *Phys. Rev. E* **90**, 052105 (2014).
- [21] R. Mondaini, K. R. Fratus, M. Srednicki, and M. Rigol, *Phys. Rev. E* **93**, 032104 (2016).
- [22] A. C. Cassidy, C. W. Clark, and M. Rigol, *Phys. Rev. Lett.* **106**, 140405 (2011).
- [23] B. V. Fine, T. A. Elsayed, C. M. Kropf, and A. S. de Wijn, *Phys. Rev. E* **89**, 012923 (2014).
- [24] P. R. Zangara, D. Bendersky, and H. M. Pastawski, *Phys. Rev. A* **91**, 042112 (2015).
- [25] T. A. Elsayed and B. V. Fine, *Physica Scripta* **2015**, 014011 (2015).
- [26] M. Schmitt and S. Kehrein, *EPL* **115**, 50001 (2016).
- [27] A. E. Tarkhov, S. Wimberger, and B. V. Fine, *Phys. Rev. A* **96**, 023624 (2017).
- [28] S. Shenker and D. Stanford, *Journal of High Energy Physics* **2014**, 46 (2014).
- [29] A. Kitaev, “Hidden correlations in the Hawking radiation and thermal noise,” (2014), (Talk given at the Fundamental Physics Prize Symposium).
- [30] J. Maldacena, S. Shenker, and D. Stanford, *Journal of High Energy Physics* **2016**, 106 (2016).
- [31] A. Kitaev, “A simple model of quantum holography,” <http://online.kitp.ucsb.edu/online/entangled15/kitaev/>; <http://online.kitp.ucsb.edu/online/entangled15/kitaev2/>.
- [32] J. Maldacena and D. Stanford, *Phys. Rev. D* **94**, 106002 (2016).
- [33] P. Hosur, X.-L. Qi, D. Roberts, and B. Yoshida, *Journal of High Energy Physics* **2016**, 4 (2016).
- [34] A. Bohrdt, C. B. Mendl, M. Endres, and M. Knap, *New Journal of Physics* **19**, 063001 (2017).
- [35] E. Iyoda and T. Sagawa, arXiv:1704.04850.
- [36] B. Swingle and D. Chowdhury, *Phys. Rev. B* **95**, 060201 (2017).
- [37] H. Shen, P. Zhang, R. Fan, and H. Zhai, *Phys. Rev. B* **96**, 054503 (2017).
- [38] Y. Huang, Y.-L. Zhang, and X. Chen, *Annalen der Physik* (2016), 10.1002/andp.201600318.
- [39] T. J. Park and J. C. Light, *The Journal of Chemical Physics* **85**, 5870 (1986).
- [40] C. Sanderson and R. Curtin, *Journal of Open Source Software* **1**, 26 (2016).

## 4.5 Relation to out-of-time-order correlators

In the search for dynamical signatures of many-body chaos in quantum systems out-of-time-order correlators (OTOCs, cf. Eq. (4.5)) attracted a lot of interest recently (Shenker and Stanford, 2014; Kitaev, 2014). The echo protocol described in the previous section effectively amounts to an OTOC if the initial state is an eigenstate of the observable, i.e.,  $(\hat{O}-\mu)|\psi_0\rangle = 0$ . Introducing the echo evolution operator

$$\hat{U}_E(\tau) = e^{i\hat{H}\tau} e^{-i\hat{H}_p\delta t} e^{-i\hat{H}\tau} \quad (4.11)$$

the observable echo resembles the form of an OTOC as introduced in Eq. (4.5),

$$\langle\psi_0|\hat{U}_E(\tau)^\dagger\hat{O}\hat{U}_E(\tau)|\psi_0\rangle = \frac{1}{\mu}\langle\psi_0|\hat{O}\hat{U}_E(\tau)^\dagger\hat{O}\hat{U}_E(\tau)|\psi_0\rangle. \quad (4.12)$$

Other than in the conventional definition, however, the OTOC emerging in the echo protocol is an expectation value in the initial nonequilibrium state instead of a thermal expectation value.

In fact, for small  $\delta t$  the dominant contribution can be ascribed to the OTOC of  $\hat{H}_p$  and  $\hat{O}$ . Expanding the exponential yields

$$\begin{aligned} \langle\psi_0|\hat{U}_E(\tau)^\dagger\hat{O}\hat{U}_E(\tau)|\psi_0\rangle &= \langle\psi_0|\hat{O}|\psi_0\rangle + i\delta t\langle\psi_0|[\hat{H}_p(\tau), \hat{O}]|\psi_0\rangle \\ &\quad - \frac{\delta t^2}{2}\langle\psi_0|[\hat{H}_p(\tau), [\hat{H}_p(\tau), \hat{O}]]|\psi_0\rangle + \mathcal{O}(\delta t^3). \end{aligned} \quad (4.13)$$

The  $\delta t$ -dependent terms in this expansion describe the deviation from a perfect echo due to the imperfection of the time reversal. Correspondingly, the contributions relevant for the echo decay observed in the previous sections have to be growing as a function of  $\tau$ . The single commutator occurring in the linear term, however, corresponds to linear response and, hence, decays as  $\tau$  is increased. The first contribution that can account for sensitivity to the introduced perturbation is the quadratic term; and, indeed, expanding the commutator yields

$$\frac{1}{2}\langle\psi_0|[\hat{H}_p(\tau), [\hat{H}_p(\tau), \hat{O}]]|\psi_0\rangle = \mu\langle\psi_0|\hat{H}_p(\tau)^2|\psi_0\rangle - \frac{1}{\mu}\langle\psi_0|\hat{O}\hat{H}_p(\tau)\hat{O}\hat{H}_p(\tau)|\psi_0\rangle, \quad (4.14)$$

where the OTOC of the observable and the perturbation Hamiltonian appears. This observation suggests that there exists a close relation between imperfect effective time reversal as a probe of irreversibility and a possible quantum butterfly effect and scrambling, which is probed by OTOCs. In the remainder of this section and in Section 4.6.2 this possible relation will be examined from different perspectives.

The behavior of conventional OTOCs with thermal states was studied in different contexts including microscopic many-body systems. It was shown that there exists a system of strongly interacting (Majorana) fermions, the Sachdev-Ye-Kitaev model, which is maximally chaotic in the sense that OTOCs grow exponentially with the maximal possible Lyapunov exponent  $\lambda_L = \frac{2\pi}{\beta}$  (Kitaev, 2015; Maldacena and Stanford, 2016). Based on the analysis above the

expectation is that imperfect effective time reversal can be used to probe this butterfly effect. Possible relations will be examined in a semiclassical approach to the echo dynamics of the Sachdev-Ye-Kitaev model in Section 4.6 with a particular focus on the growth of the out-of-time-order double commutator occurring in Eq. (4.13).

In the remainder of this section we will shed some light on another aspect, namely the possibility to probe the spreading of information and scrambling. First, a particularly notable relation between OTOCs and an information theoretic measure of scrambling is reviewed in Section 4.5.1, including some new results. Subsequently, in Section 4.5.2 the behavior of OTOCs far from equilibrium is compared to conventional OTOCs. Finally, the behavior of double commutators as motivated by the echo dynamics is compared to that of OTOCs in an analogous setting in Section 4.5.3.

### 4.5.1 Out-of-time-order correlators and scrambling

As a probe for the spreading of information and scrambling in microscopic lattice systems OTOCs have been studied in a series of works (Hosur *et al.*, 2016; Huang *et al.*, 2016; Bohrdt *et al.*, 2017; Iyoda and Sagawa, 2017; Swingle and Chowdhury, 2017). Particularly notable is the fact that in spin-1/2 systems there exists a rigorous relation between OTOCs and tripartite information, which quantifies how much information about the initial state is fully delocalized in that it can only be retrieved by global measurements (Hosur *et al.*, 2016). In this context the time evolution operator acting on a chain of  $N$  spins,

$$\hat{U}(t) = \sum_{i,j} u_{ij} |i\rangle\langle j|, \quad (4.15)$$

which would commonly be interpreted as a tensor with  $N$  input and  $N$  output legs as depicted in Fig. 4.6 (cf. also Section 3.1.2), is thought of as a state in doubled Hilbert space,

$$|U(t)\rangle = \frac{1}{2^{n/2}} \sum_{i,j} u_{ij} |i\rangle_{\text{out}} \otimes |j\rangle_{\text{in}}. \quad (4.16)$$

In this language the reduced density matrix of the input subsystem,  $\hat{\rho}_{\text{in}} = \text{tr}_{\text{out}}(|U(t)\rangle\langle U(t)|)$ , corresponds to a uniform ensemble of states of the physical system, whereas the reduced density matrix of the output subsystem,  $\hat{\rho}_{\text{out}} = \text{tr}_{\text{in}}(|U(t)\rangle\langle U(t)|)$ , corresponds to the time-evolved initial density matrix,  $\hat{\rho}_{\text{out}} = \hat{U}(t)\hat{\rho}_{\text{in}}\hat{U}(t)^\dagger$ .

In this view it is possible to consider more general input ensembles  $\hat{\rho}_{\text{in}} = \sum_j p_j |\psi_j\rangle\langle\psi_j|$  given by probabilities  $p_j$  and a set of orthonormal states  $\{|\psi_j\rangle\}$ . The corresponding state

$$|\Psi(t)\rangle = \sum_j \sqrt{p_j} |\psi_j\rangle_{\text{in}} \otimes \hat{U}(t) |\psi_j\rangle_{\text{out}} \quad (4.17)$$

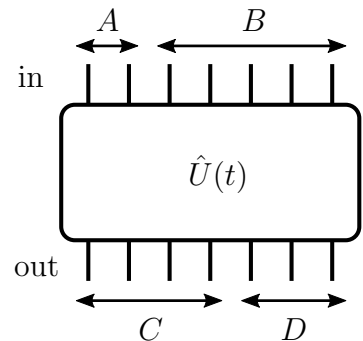


**Fig. 4.6:** To define tripartite information as a measure of scrambling the unitary operator  $\hat{U}(t)$  is viewed as a state in doubled Hilbert space with “in” and “out” degrees of freedom.

contains all information about the time evolution, in this case with a possible weighting of the input ensemble. A possible choice is  $|\psi_j\rangle = |E_j\rangle$  and  $p_j = e^{-\beta E_j}$  for which  $|\Psi(0)\rangle$  is a thermofield double state corresponding to a thermal initial density matrix.

In the doubled system it is possible to define mutual information of spins on the input and on the output side. Considering bipartitions of the input and the output subsystem into parts  $A, B, C$  and  $D$  as depicted in Fig. 4.6 the mutual information of, e.g.,  $A$  and  $C$  is defined as

$$I(A : C) = S_A + S_C - S_{AC} \quad (4.18)$$

where

$$S_A = -\text{tr}(\hat{\rho}_A \log \hat{\rho}_A) \quad (4.19)$$

with the reduced density matrix  $\hat{\rho}_A = \text{tr}_{\bar{A}}(|\Psi(t)\rangle\langle\Psi(t)|)$ . On this basis the *tripartite information*

$$I_3(A : C : D) = I(A : C) + I(A : D) - I(A : CD) \quad (4.20)$$

quantifies how much information about  $A$  is after time evolution hidden nonlocally in  $CD$  and cannot be detected by local measurements just on  $C$  or  $D$ . If a system scrambles initially local information, the tripartite information will take a negative value with large magnitude. Therefore, in contrast to OTOCs the tripartite information allows to diagnose scrambling based only on properties of the time evolution operator, thereby avoiding ambiguities that can occur due to the choice of observables.<sup>1</sup>

Strikingly, however, the tripartite information in spin-1/2 systems can be bounded by the so-called OTOC average

$$\overline{\langle \hat{O}_D(t) \hat{O}_A \hat{O}_D(t) \hat{O}_A \rangle_\beta} = \frac{1}{4^{a+d}} \sum_{i,j} \langle \hat{D}_i(t) \hat{A}_j \hat{D}_i(t) \hat{A}_j \rangle_\beta. \quad (4.21)$$

In this expression  $\{\hat{A}_i\}$  (equivalently  $\{\hat{D}_i\}$ ) denotes a complete basis of operators on subsystem  $A$  satisfying the orthonormality condition  $\text{tr}(\hat{A}_i \hat{A}_j) = 2^a \delta_{ij}$  with  $a$  the number of spins in  $A$ . For  $a = 1$  a possible choice is  $\{\hat{1}, \hat{\sigma}_x, \hat{\sigma}_y, \hat{\sigma}_z\}$ . At infinite temperature,  $\beta = 0$ , (Hosur *et al.*, 2016) show that if the OTOC average at long times approaches a constant  $\epsilon > 0$ , the tripartite information is bounded by

$$I_3(A : C : D) \leq -2a + \log_2 \frac{\epsilon}{\epsilon_{\min}} \quad (4.22)$$

with the theoretical minimum  $\epsilon_{\min} = 2^{-2a}$ . This means that a saturation of the OTOC average (4.21) close to  $\epsilon_{\min}$  implies scrambling.

As an example (Hosur *et al.*, 2016) studied the dynamics of the Ising model with tunable magnetic field orientation as defined in Eq. (4.6). They found that considering an infinite

---

<sup>1</sup>Note that the tripartite information (4.20) defined on the doubled Hilbert space is identical with the topological entanglement entropy introduced by (Kitaev and Preskill, 2006). Until now it is, however, unclear whether this resemblance has further implications.

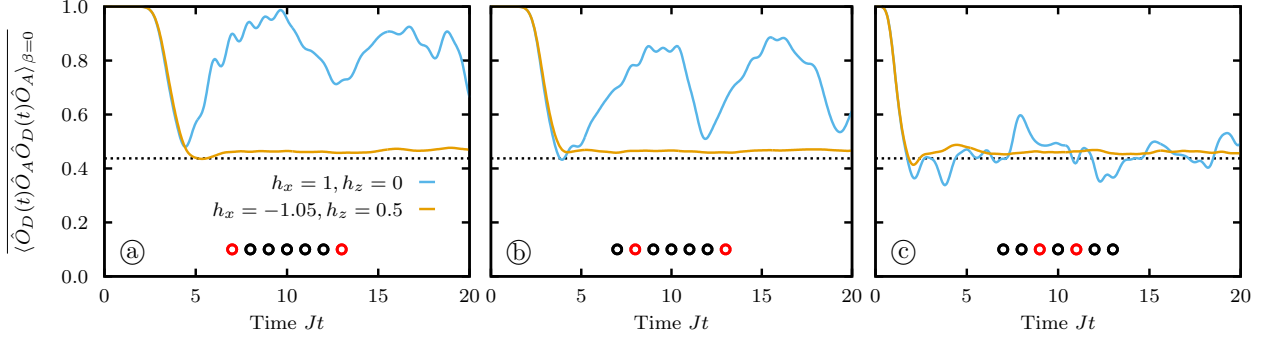


**Fig. 4.7:** Dynamics of the OTOC average the a quadratic and the nonintegrable Ising spin chain with magnetic field for different choices of the subsystem partitioning. The displayed circles represent the chain of  $N = 7$  spins, where the red circles indicate the positions of the one-spin-subsystems  $A$  and  $D$ , respectively. The dashed line corresponds to the Haar scrambled value. In (a) results from (Hosur *et al.*, 2016) are reproduced, showing that the noninteracting system is a scrambler, whereas the free one is not. (b) and (c) reveal that the long time behavior in the free system strongly depends on the choice of subsystems.

temperature initial state the tripartite information and the OTOC average clearly distinguish between the quadratic transverse-field Ising model and the nonintegrable system at tilted field orientation. Fig. 4.7(a) shows a reproduction of the results reported in (Hosur *et al.*, 2016) obtained by exact diagonalization. The dashed line indicates the value attained under *Haar scrambling*, which is considered maximally chaotic and corresponds to the vanishing of all nontrivial contributions in Eq. (4.21). In accordance with the general expectation the interacting system scrambles, whereas the free one does not. Note that this is compatible with the observations in Section 4.3.1, where it was found that breaking integrability renders the dynamics irreversible.

When considering the further results in Fig. 4.7(b) and (c) it becomes, however, evident that even if operator-dependence is largely eliminated the signature of nonscrambling dynamics delicately depends on the partitioning of the Hilbert space: As the subsystems  $A$  and  $D$  are moved away from the boundary of the spin chain the distinction between the free and the nonintegrable system become less clear. In particular in Fig. 4.7(c) the OTOC average of both systems remains close to the Haar scrambled value for most times. By contrast, when considering a partitioning of the Hilbert space into modes of the free system instead of lattice sites one would expect that a corresponding OTOC average of the corresponding operators does not change at all over time, because the mode occupation is conserved.

The observations in Fig. 4.7 suggest to declare those systems scrambling, in which the OTOC average approaches the Haar value for any partitioning of the Hilbert space; if instead a partitioning can be found in which the OTOC deviates from the Haar value at long times the system is not a scrambler.

The comparison of the results for different subsystem positions shows that in the study of scrambling a characteristic velocity appears. The time at which the OTOC average starts to deviate from the initial value is proportional to the distance of the subsystems. In the literature the corresponding velocity is referred to as “butterfly velocity” (Hosur *et al.*, 2016;

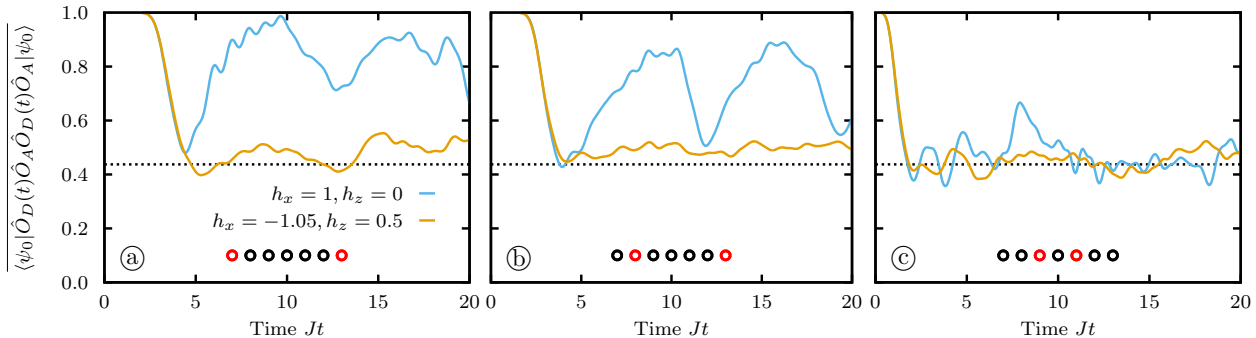


**Fig. 4.8:** Dynamics of the OTOC average far from equilibrium. The plots show data for the same situations as in Fig. 4.7, where in the definition of the OTOC average (4.21) the thermal average  $\langle \cdot \rangle_\beta$  was replaced the average  $\langle \psi_0 | \cdot | \psi_0 \rangle$  in a nonequilibrium initial state. Overall a very similar signature is obtained.

Bohrdt *et al.*, 2017). In the free system this velocity can directly be related to the Lieb-Robinson velocity (cf. Section 1.2.2), because a Wick theorem is applicable meaning that any signal in an OTOC must be related to a signal in the conventional correlation functions.

## 4.5.2 Out-of-time-order correlators far from equilibrium

We will now address the question whether nonequilibrium OTOCs, which are motivated by echo protocols, show a similar sensitivity to integrability as the conventional OTOC average. Fig. 4.8 displays results for the OTOC average where the thermal expectation value  $\langle \cdot \rangle_\beta$  in Eq. (4.21) is replaced by the expectation value in a nonequilibrium state,  $\langle \psi_0 | \cdot | \psi_0 \rangle$ . In this case the initial state is the Neel state  $|\psi_0\rangle = |\uparrow\downarrow\uparrow \dots\rangle$ . The parameters and the choice of subsystems is identical with the cases shown in Fig. 4.7. Comparing the results for the conventional OTOC average in Fig. 4.7 and for the OTOC average far from equilibrium in Fig. 4.8 one finds that both results are very similar. In particular the curves for the free system in the left panels, respectively, are almost identical. For the nonintegrable system the OTOC average far from equilibrium shows stronger oscillations around the approximately stationary value. Again the behavior of the free system at long times strongly depends on the choice of subsystems.

In order to include also a Bethe integrable system into the analysis we now turn to the extended XXZ Hamiltonian introduced in Eq. (4.7). Fig. 4.9(a) shows the time evolution of the OTOC average at characteristically distinct points in the parameter space of this system with subsystems  $A$  and  $D$  at the boundary of the spin chain. Similar to the Ising chain with transverse field the free XX model obtained at  $J_z = \delta = \lambda = 0$  does not scramble. The OTOC average even returns to the initial value from time to time, which would by virtue of the bound (4.22) allow for excellent recovery of information about the initial state by local measurements. If integrability is broken by either introducing a dimerization  $\delta \neq 0$  or next-nearest-neighbor coupling  $\lambda \neq 0$  the OTOC average indicates that the system becomes a scrambler (Note how adding longer distance couplings increases the butterfly velocity in comparison to the nearest-neighbor coupled systems). The signature of the OTOC average

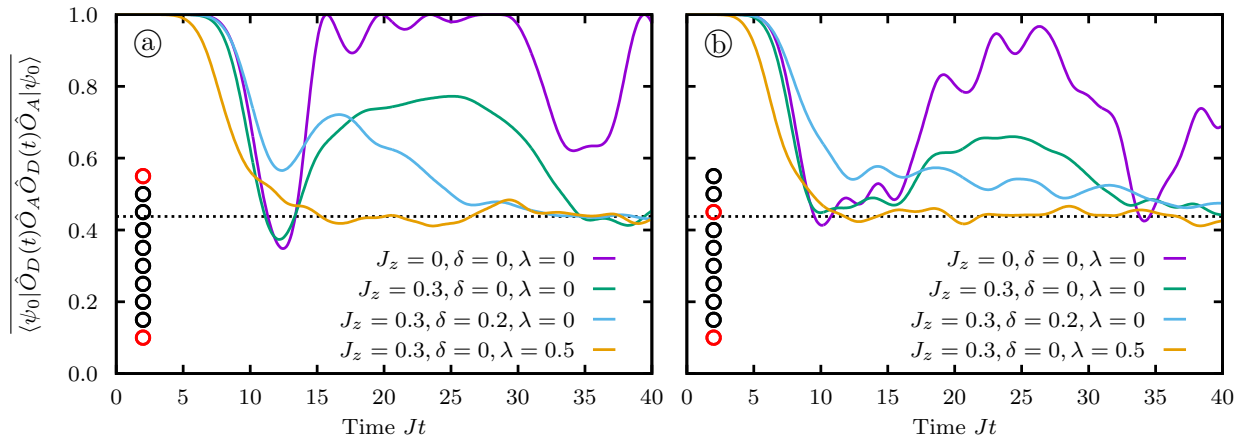


**Fig. 4.9:** Time evolution of the OTO average after a quench in an extended XXZ model defined in Eq. (4.7). The circles inside the plots represent the spin chains of length 10 and the red circles indicate the subsystems on which the operators act. The dashed line indicates the Haar-scrambled value that is approached in the long time limit if the system scrambles.

for the integrable XXZ chain,  $J_z \neq 0$  and  $\delta = \lambda = 0$ , is less clear. After a dip at  $Jt \approx N$  the OTOC average at first shows a strong deviation from the Haar scrambled value similar to the free system. However, after the signal traversed the system a second time, i.e., for  $Jt \gtrsim 30$ , the OTOC decreases again and subsequently remains close to the Haar scrambled value. Therefore, it can on this basis not be decided unambiguously whether the Bethe integrable system scrambles or not. Besides this, Fig. 4.9(b) again demonstrates that the behavior of the OTOCs strongly differs in particular for the nonscrambling systems if the choice of subsystems is varied. In cases where both subsystems are located in the bulk the dynamics is almost identical for all choices of parameters, similar to Fig. 4.8(c) (not shown).

We can conclude that with the nonequilibrium initial state, which, chosen as the Néel state, is a high energy state, the resulting OTOCs essentially reflect the properties of OTOCs in equilibrium at high temperature.

### 4.5.3 Double commutators

In order to assess whether the double commutator occurring in Eq. (4.13) probe chaotic dynamics similar to OTOCs we will now consider a double commutator average in analogy to the OTOC average discussed in the previous section. For two subsystems  $A$  and  $B$  consisting of  $a$  and  $b$  lattice sites, respectively, and corresponding sets of operators  $\{\hat{A}_i\}$  and  $\{\hat{B}_j\}$  we define

$$DC_{AB}^{|\psi_0\rangle}(t) = \sqrt{\frac{1}{4^{a+b}} \sum_{i,j} \langle \psi_0 | [\hat{A}_i(t), [\hat{A}_i(t), \hat{B}_j]] | \psi_0 \rangle^2}. \quad (4.23)$$

Note that the double commutator expectation values can be negative. With the echo dynamics in mind a situation where the double commutator becomes negative can occur when



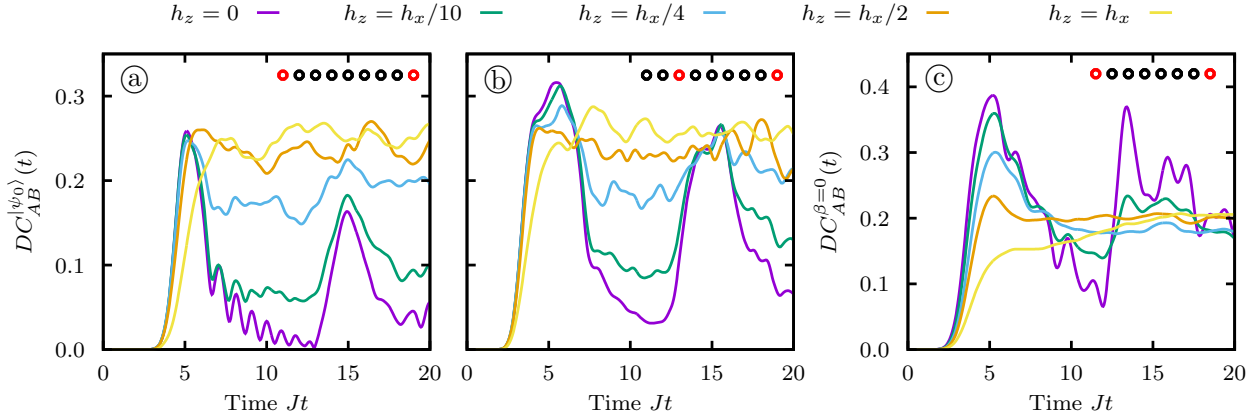


**Fig. 4.10:** Dynamics of double commutator averages in the Ising model with magnetic field (4.6). In all cases  $h_x = J$ . The locations of the single spin subsystems are indicated by the red circles. **(a,b)** Double commutator average  $DC_{AB}^{|\psi_0\rangle}(t)$  as defined in Eq. (4.23) with nonequilibrium initial state  $|\psi_0\rangle = |\uparrow\downarrow\uparrow\dots\rangle$ . **(c)** Double commutator average  $DC_{AB}^{\beta}(t)$  as defined in Eq. (4.24) at infinite temperature  $\beta = 0$ .

the observable has an initial value that is smaller than the value attained after relaxation. In order to probe the magnitude of the double commutators, they are squared in the expression above.

Fig. 4.10(a,b) shows  $DC_{AB}^{|\psi_0\rangle}(t)$  for different magnetic field orientations of the Ising chain (4.6). The behavior of the double commutators is very similar to the OTOCs. In Fig. 4.10(a) the subsystems are located at the boundaries of the spin chain. For the quadratic Hamiltonian  $h_z = 0$  the double commutator shows a strong signal after the spread of information covered the distance between the subsystems. Subsequently, this signal decays to zero before a finite-size echo appears. If the integrability is broken by tilting the magnetic field orientation the double commutator approaches a stationary value larger than zero. This distinction between the quadratic and the nonintegrable system is just as in the case of the OTOC average diminished if the subsystems are moved away from the boundary, as for example in Fig. 4.10(b).

Fig. 4.10(c) shows the dynamics of a *thermal* double commutator average,

$$DC_{AB}^{\beta}(t) = \sqrt{\frac{1}{4^{a+b}} \sum_{i,j} \text{tr}(\hat{\rho}_{\beta}[\hat{A}_i(t), [\hat{A}_i(t), \hat{B}_j]])^2}, \quad (4.24)$$

where  $\hat{\rho}_{\beta}$  is the thermal density matrix at temperature  $\beta$ . This average in the thermal state at infinite temperature behaves quite similar to the average in the nonequilibrium state. In the nonintegrable regime the double commutator deviates from zero once the information about the perturbation at the other end of the chain arrived and it quickly saturates at a nonzero value that only slightly varies for the different  $h_z$ . In the quadratic model at  $h_z = 0$  there is a strong signal on the “light cone”, which decays afterwards. It is, however, not possible to tell unambiguously from these data whether it approaches zero, because the decay is interrupted by a finite size echo. Note that compared to the nonequilibrium state

the double commutators in the thermal state of the nonintegrable system show only much weaker traces of finite-size echoes.

In this analysis of the dynamics of double commutators  $[\hat{O}_A(t), [\hat{O}_A(t), \hat{O}_B]]$  involving operators  $\hat{O}_{A/B}$  with support on spatially separate regions  $A$  and  $B$  the focus was on the behavior at late times. In the following section it will be demonstrated for a semiclassical model that the double commutator as it occurs in the echo dynamics (4.13) is at short times sensitive to the butterfly effect.

## 4.6 Semiclassical echo dynamics and Lyapunov exponents in the Sachdev-Ye-Kitaev model

For systems in the semiclassical limit quantum dynamics can be treated with good accuracy in a phase space approach. Wigner-Weyl quantization provides a systematic prescription to construct the phase space for a given quantum model and the resulting equations of motion can be solved in the Truncated Wigner Approximation (TWA); see Section 4.6.1. As the result is a generic classical Hamiltonian system one can expect that the dynamics intrinsically exhibit an exponential sensitivity to small perturbations. In the following it will be investigated how this affects the echo dynamics.

With regards to chaos the Sachdev-Ye-Kitaev model (SYK model) is a particularly interesting quantum system. It is defined by the Hamiltonian

$$\hat{H}_{\text{SYK}} = \frac{1}{(2N)^{3/2}} \sum_{i,j,k,l=1}^N J_{ijkl} \hat{c}_i^\dagger \hat{c}_j^\dagger \hat{c}_k \hat{c}_l, \quad (4.25)$$

where  $J_{ijkl}$  is a complex Gaussian random variable with zero mean and variance  $\sigma^2 = \langle |J_{ijkl}|^2 \rangle$ ; the  $\hat{c}_i^\dagger$  and  $\hat{c}_i$  are fermionic creation and annihilation operators. The SYK model has a number of interesting properties (Kitaev, 2015; Maldacena and Stanford, 2016). First of all, it is exactly solvable in the limit of large  $N$  despite the fact that it is strongly interacting (the only energy scale is the standard deviation of the couplings,  $\sigma$ ). Moreover, it exhibits approximate conformal symmetry at low energies indicating the existence of a holographic dual. The SYK model is maximally chaotic in the sense that OTOCs grow exponentially with a rate saturating the bound  $\lambda_L = 2\pi/\beta$ , which was argued to constitute the maximal possible Lyapunov exponent in gravity (Maldacena *et al.*, 2016).

A study of the relaxation dynamics of the SYK model using the TWA found very good agreement of the phase space approach with exact quantum dynamics, indicating that the dynamics of the SYK model is essentially classical (Davidson *et al.*, 2017). Note, however, that in another work it was concluded that the effective classical system does not correctly capture the full quantum dynamics (Scaffidi and Altman, 2017).

The results presented in the following were obtained in a collaboration with A. Polkovnikov<sup>1</sup>, S. Kehrein, D. Sels<sup>1</sup>, and S. Davidson<sup>1</sup>.

---

<sup>1</sup> Condensed Matter Theory Group, Boston University.

### 4.6.1 Phase space dynamics with Truncated Wigner Approximation

In order to formulate quantum dynamics in phase space it is required to find a consistent mapping of operators to phase space variables. A possible generic prescription to obtain a phase space formulation is the so-called Wigner-Weyl transformation. For simplicity we will first consider position and momentum operators  $\hat{q}$  and  $\hat{p}$ , which act on a Hilbert space spanned by position eigenstates  $|q\rangle$  and fulfil the canonical commutation relation  $[\hat{p}, \hat{q}] = i\hbar$ . For any operator  $\hat{\Omega}(\hat{q}, \hat{p})$  the *Weyl symbol* is defined as

$$\Omega_W(q, p) = (\hat{\Omega}(\hat{q}, \hat{p}))_W = \int d\xi \langle q - \xi/2 | \hat{\Omega}(\hat{q}, \hat{p}) | q + \xi/2 \rangle e^{ip\xi/\hbar}. \quad (4.26)$$

This transformation is constructed to yield the correct classical limit,  $\Omega_W(q, p) \xrightarrow{\hbar \rightarrow 0} \Omega(q, p)$ , and to satisfy the canonical commutation relation,

$$(\hat{p}\hat{q})_W - (\hat{q}\hat{p})_W = i\hbar. \quad (4.27)$$

Furthermore, introducing the *Wigner function* as the Weyl symbol of the density matrix,

$$W(q, p) = (\hat{\rho})_W \quad (4.28)$$

quantum mechanical expectation values are given by

$$\langle \hat{\Omega} \rangle = \text{tr}(\hat{\rho}\hat{\Omega}) = \int \frac{dpdq}{2\pi} W(q, p) \Omega_W(q, p) \quad (4.29)$$

(Wigner, 1932). In this form the quantum expectation value expressed in the phase space formulation resembles an expectation value of  $\Omega_W(q, p)$  with probability function  $W(q, p)$ . However, as it is not necessarily positive, the Wigner function is in general not a probability density.

In order to capture the noncommutativity of operator multiplication the *Moyal product* (Groenewold, 1946) is introduced, which gives the Weyl symbol of the product of two operators  $\hat{\Omega}_1$  and  $\hat{\Omega}_2$ ,

$$(\hat{\Omega}_1\hat{\Omega}_2)_W = (\hat{\Omega}_1)_W \exp\left(-\frac{i\hbar}{2}\Lambda_P\right) (\hat{\Omega}_2)_W, \quad (4.30)$$

where

$$\Lambda_P = \overleftarrow{\frac{\partial}{\partial p}} \frac{\partial}{\partial q} - \frac{\overleftarrow{\frac{\partial}{\partial q}} \partial}{\partial p} \quad (4.31)$$

is the Poisson operator with the arrows indicating that the corresponding derivative acts to the left. Based on this one can introduce the *Moyal bracket*, which is the Weyl symbol of the commutator,

$$-i\hbar\{(\hat{\Omega}_1)_W, (\hat{\Omega}_2)_W\}_M = ([\hat{\Omega}_1, \hat{\Omega}_2])_W = -2i(\hat{\Omega}_1)_W \sin\left(\frac{\hbar}{2}\Lambda_P\right) (\hat{\Omega}_2)_W. \quad (4.32)$$

An alternative way to obtain the Weyl symbol of an operator  $\hat{\Omega}(\hat{q}, \hat{p})$  is to use *Bopp operators* (Bopp, 1956)

$$\hat{q} = q + \frac{i\hbar}{2} \frac{\partial}{\partial p}, \quad \hat{p} = p - \frac{i\hbar}{2} \frac{\partial}{\partial q} \quad (4.33)$$

which yield the Weyl symbol via

$$\Omega_W(q, p) = \Omega\left(q + \frac{i\hbar}{2} \frac{\partial}{\partial p}, p - \frac{i\hbar}{2} \frac{\partial}{\partial q}\right) 1. \quad (4.34)$$

Using the Moyal bracket the von Neumann equation (1.2) for time evolution of the density matrix with a Hamiltonian  $\hat{H}$  is readily translated to an equation of motion for the Wigner function,

$$\frac{d}{dt} W = \{(\hat{H})_W, W\}_M, \quad (4.35)$$

and similarly the Heisenberg equation of motion for arbitrary operators translates to

$$\frac{d}{dt} \Omega_W = \{(\hat{H})_W, \Omega_W\}_M. \quad (4.36)$$

In general these equations of motion are difficult to solve, because they contain arbitrarily high derivatives. However, if  $\hbar$  can be considered a small parameter, i.e., in the semiclassical limit, the Moyal bracket can be truncated at leading order in  $\hbar$ , which means that it reduces to the Poisson bracket

$$\{A, B\}_P = A\Lambda_P B \quad (4.37)$$

known from classical mechanics. This constitutes the *Truncated Wigner Approximation*. The resulting dynamics respects a Liouville theorem, which means that time evolved expectation values can be computed by the method of characteristics from individual trajectories in phase space,

$$\langle \hat{O} \rangle \approx \langle \hat{O} \rangle_{\text{TWA}} = \int \frac{dpdq}{2\pi} W(q_0, p_0) O_W(q(t), p(t)), \quad (4.38)$$

where  $W(q_0, p_0)$  is the Wigner function of the initial density matrix and  $q(t)$  and  $p(t)$  are time-evolved phase space coordinates with  $q(0) = q_0$  and  $p(0) = p_0$ . The numerical results presented later in this section were obtained by integrating the TWA equations using an adaptive Dormand-Prince integrator (Dormand and Prince, 1980) with initial conditions sampled from the Wigner function.

So far we discussed the phase space approach in coordinate-momentum representation. An analogous construction is possible with slight modifications in a coherent state representation based on bosonic creation and annihilation operators (Polkovnikov, 2010). In that case the effective  $\hbar$  is the inverse average occupation  $1/N$  indicating that TWA is good at high densities. A recent development is the formulation of phase space dynamics for fermionic systems (Davidson *et al.*, 2017). In the following section we will make use of this technique to compute echo dynamics of the SYK model.

## 4.6.2 Semiclassical dynamics of the Sachdev-Ye-Kitaev model

Other than the position and momentum operators and the bosonic operators discussed in the previous section, fermionic operators obey canonical *anti*-commutation relations. Therefore, a Wigner-Weyl transformation of the basic operators does not yield a suited phase space representation in this case. However, the fermionic TWA (fTWA) developed by (Davidson *et al.*, 2017) relies on the fact that any physical observable can only be made up from bilinears of the fermionic operators, which obey specific commutation relations. It is thus possible (and sufficient) to find a phase space formulation of the dynamics of these bilinears. In the following the fTWA formalism is briefly sketched; the reader is referred to (Davidson *et al.*, 2017) and (Davidson, 2017) for further details.

Given a set of fermionic operators  $\hat{c}_i, \hat{c}_i^\dagger$  with the properties

$$\{\hat{c}_i, \hat{c}_j^\dagger\} = \hat{c}_i \hat{c}_j^\dagger + \hat{c}_j^\dagger \hat{c}_i = \delta_{i,j}, \quad \{\hat{c}_i, \hat{c}_j\} = \{\hat{c}_i^\dagger, \hat{c}_j^\dagger\} = 0 \quad (4.39)$$

the different possible bilinears are

$$\hat{E}_{\alpha\beta} = \hat{c}_\alpha \hat{c}_\beta, \quad \hat{E}^{\alpha\beta} = \hat{c}_\alpha^\dagger \hat{c}_\beta^\dagger, \quad \hat{E}_\beta^\alpha = \frac{1}{2}(\hat{c}_\alpha^\dagger \hat{c}_\beta - \hat{c}_\beta \hat{c}_\alpha^\dagger). \quad (4.40)$$

These operators obey the commutation relations of  $so(2N)$ , i.e., for a suited relabelling  $\{\hat{E}_{\alpha\beta}, \hat{E}^{\alpha\beta}, \hat{E}_\beta^\alpha\} \rightarrow \{\hat{X}_a\}$  one finds  $[\hat{X}_a, \hat{X}_b] = i f_{abc} \hat{X}_c$  with  $f_{abc}$  the structure constants of  $so(2N)$  (Fukutome, 1981). Then, generalizing the Moyal product by replacing the Poisson operator (4.31) with

$$\Lambda_c = i \frac{\overleftarrow{\partial}}{\partial(\hat{X}_a)_W} (\hat{X}_c)_W f_{abc} \frac{\partial}{\partial(\hat{X}_b)_W} \quad (4.41)$$

a suited phase space representation is obtained. Here and in the following doubly occurring indices are summed over. Moreover, we denote the Weyl symbols as

$$\tau_{\alpha\beta} = (\hat{E}_{\alpha\beta})_W = -(\hat{E}^{\alpha\beta})_W^*, \quad \rho_{\alpha\beta} = (\hat{E}_\beta^\alpha)_W. \quad (4.42)$$

In terms of these variables the fTWA equations for the dynamics driven by a Hamiltonian with Weyl symbol  $\mathcal{H} = (\hat{H})_W$  are

$$i \frac{d}{dt} \rho_{\alpha\beta} = \left( -\frac{\partial \mathcal{H}}{\partial \rho_{\gamma\alpha}} \rho_{\gamma\beta} + \frac{\partial \mathcal{H}}{\partial \tau_{\gamma\alpha}} \tau_{\beta\gamma} - \frac{\partial \mathcal{H}}{\partial \tau_{\alpha\gamma}} \tau_{\beta\gamma} \right) - \left( \alpha \leftrightarrow \beta \right)^*. \quad (4.43)$$

$$i \frac{d}{dt} \tau_{\alpha\beta} = \left( \frac{\partial \mathcal{H}}{\partial \rho_{\alpha\gamma}} \tau_{\gamma\beta} + \frac{\partial \mathcal{H}}{\partial \tau_{\gamma\alpha}^*} \rho_{\gamma\beta} - \frac{\partial \mathcal{H}}{\partial \tau_{\alpha\gamma}^*} \tau_{\gamma\beta} \right) - \left( \alpha \leftrightarrow \beta \right), \quad (4.44)$$

where in both equations the second bracket on the right hand side is the same as the first, but with  $\alpha$  and  $\beta$  exchanged.

A suited Hamilton function  $\mathcal{H}_{\text{SYK}}$  for the SYK model (4.25) was derived by (Davidson *et al.*, 2017). Note that the quartic form of the interaction can be expressed by different

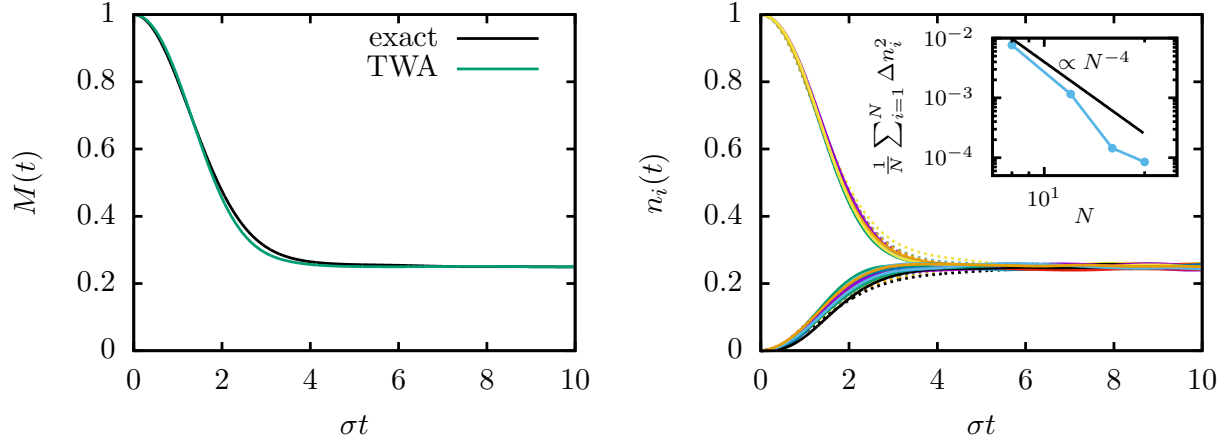


**Fig. 4.11:** Comparison of TWA results with exact dynamics. For an SYK model with  $N = 20$  fermionic modes at quarter filling the TWA is in good agreement with the exact dynamics for the occupation imbalance  $M(t)$  (left panel) and the individual occupations  $n_i(t)$  (right panel; dashed lines are exact). The inset shows the average squared deviation of the TWA results for the individual occupations from the exact results as a function of  $N$ . The decay compatible with  $N^{-4}$  indicates that TWA becomes exact for  $N \rightarrow \infty$ .

choices of the fermion bilinears (4.40) resulting in different Hamilton functions. It turns out that choosing the “superconducting” variables  $\tau$  yields accurate results, whereas the Hamilton function in terms of  $\rho$ -variables does not (Davidson *et al.*, 2017; Davidson, 2017). The Hamilton function obtained by combining the fermionic operators to pairing operators and calculating the Weyl symbol is

$$\mathcal{H}_{\text{SYK}} = \frac{1}{(2N)^{3/2}} \sum_{ijkl} J_{ijkl} \left( \tau_{ji}^* \tau_{kl} + \frac{1}{2} \rho_{jk} \delta_{il} - \frac{1}{2} \rho_{jl} \delta_{ik} + \frac{1}{2} \rho_{il} \delta_{kj} - \frac{1}{2} \rho_{ik} \delta_{jl} \right). \quad (4.45)$$

In order to compute dynamics the Wigner function of the initial density matrix must be known. However, the exact Wigner function is often hard to treat numerically, because it is not necessarily positive. In the following we consider simple initial states that are characterized by a single particle density matrix  $\hat{\rho}_0$ , which is diagonal,  $(\hat{\rho}_0)_{\alpha\beta} = \delta_{\alpha\beta}(n_\alpha - 1/2)$ , with the orbital occupation numbers  $n_\alpha = \langle c_\alpha^\dagger c_\alpha \rangle$ . In that case the Wigner function is well approximated by a multivariate Gaussian distribution fixed by the first and second moments (Davidson, 2017)

$$\begin{aligned} \langle \rho_{\alpha\beta} \rangle &= \delta_{\alpha\beta} \left( n_\alpha - \frac{1}{2} \right), \\ \langle \tau_{\alpha\beta} \rangle &= 0, \\ \langle \rho_{\alpha\beta}^* \rho_{\mu\nu} \rangle_c &= \frac{1}{2} \delta_{\alpha\mu} \delta_{\beta\nu} (n_\alpha + n_\beta - 2n_\alpha n_\beta), \\ \langle \tau_{\alpha\beta}^* \tau_{\mu\nu} \rangle_c &= \frac{1}{2} (\delta_{\alpha\mu} \delta_{\beta\nu} - \delta_{\beta\mu} \delta_{\alpha\nu}) (1 + 2n_\alpha n_\beta - n_\alpha - n_\beta). \end{aligned} \quad (4.46)$$

Initial states that can be described in this form and which are suited to study echo dynamics are those, in which a part of the orbitals is occupied, while the rest is empty, i.e.,

$$n_\alpha = \begin{cases} 1, & \alpha \leq m \\ 0, & \text{else} \end{cases} . \quad (4.47)$$

An observable that distinguishes these initial states is the occupation imbalance

$$\hat{M} = \frac{1}{N} \sum_{l=1}^N n_l (2\hat{c}_l^\dagger \hat{c}_l - 1) \quad (4.48)$$

with Weyl symbol

$$(\hat{M})_W = \frac{2}{N} \sum_{l=1}^N n_l \rho_{ll} . \quad (4.49)$$

Fig. 4.11 displays results for the dynamics in an SYK model with  $N = 20$  fermionic modes, of which initially  $m = 5$  are occupied and the rest is empty. Under time evolution the system relaxes to equal occupation of all modes and the TWA results are in good agreement with the exact results. In order to quantitatively assess the accuracy the inset in the right panel shows the average of the integrated deviations

$$\Delta n_i^2 = \frac{1}{T} \int_0^T dt (n_i^{\text{TWA}}(t) - n_i^{\text{exact}}(t))^2 . \quad (4.50)$$

A decay of the integrated deviations compatible with  $N^{-4}$  is observed indicating that TWA becomes exact in the limit  $N \rightarrow \infty$ .

### Chaos in individual TWA trajectories

The SYK Hamilton function (4.45) yields a set of nonlinear TWA equations of motion. Said nonlinearity leads to an exponential sensitivity of individual trajectories to small perturbations. This behavior becomes evident when studying derivatives of the form

$$\frac{\partial x_i(t)}{\partial x_j(0)} = \lim_{\Delta \rightarrow 0} \frac{x_i(t) - x_i^\Delta(t)}{\Delta} , \quad (4.51)$$

where the  $x_i \in \{\tau_{\alpha\beta}, \rho_{\gamma\delta}\}$  denote some coordinate and  $x_i(t)$  is computed from the initial condition  $x_i(0)$ , whereas  $x_i^\Delta$  is computed from the initial condition  $x_i^\Delta(0) = x_i(0) + \delta_{ij}\Delta$ .

Fig. 4.12(a-c) displays numerical results for different choices of  $x_i$  and  $x_j$ , where the derivative (4.51) was approximated by a difference quotient. As a function of time the finite difference approximations of  $\frac{\partial x_i(t)}{\partial x_j(0)}$  show exponential growth over a period that is extended as  $\Delta$  is reduced. The growth rate is very similar for all choices of coordinates.

With echo dynamics and effective time reversal in mind one can define  $\frac{\partial x_i(0)}{\partial x_j(t)}$  in analogy to Eq. (4.51), where the variation  $\Delta$  is introduced at time  $t$  before the TWA equations are



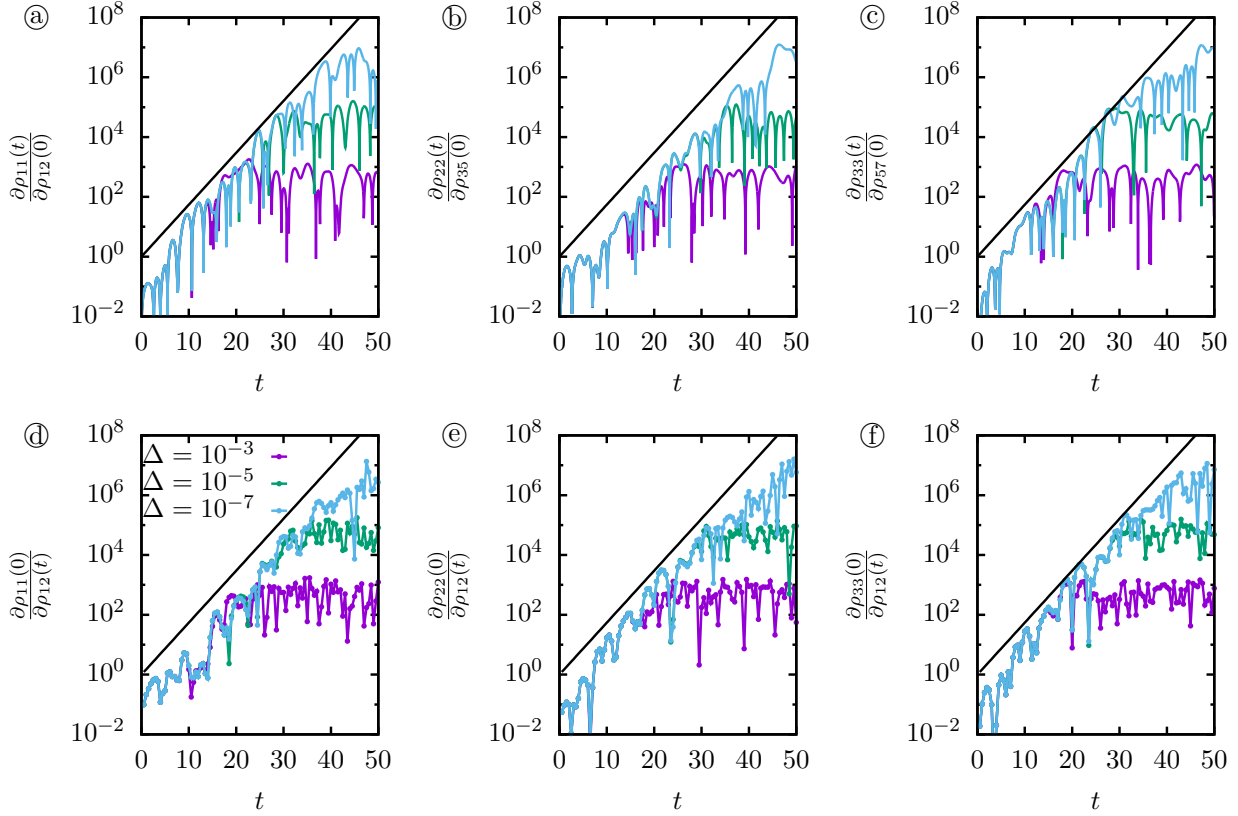


**Fig. 4.12:** Butterfly effect in individual TWA trajectories. The divergence is quantified by  $\frac{\partial x_i(t_1)}{\partial x_j(t_2)}$  as defined in Eq. (4.51). **(a-c)** Divergence of trajectories perturbed at time  $t = 0$ . **(d-f)** Divergence of trajectories perturbed at time  $t$ . The black line indicates an exponential  $\propto e^{0.4t}$ .

integrated backwards to  $t = 0$ . As shown in Fig. 4.12(d-f) the results under these conditions are very similar to the outcomes when perturbing at  $t = 0$ . This indicates that the growth rate of the divergence of trajectories is roughly constant on the energy hypersurface that is sampled, when the perturbation is introduced at varying times  $t$ .

In conclusion, we find that both  $\frac{\partial x_i(t)}{\partial x_j(0)}$  and  $\frac{\partial x_i(0)}{\partial x_j(t)}$  show clear signatures of chaotic behavior in the semiclassical TWA dynamics of the SYK model.

## Echo dynamics

We will now turn to the echo protocol defined in Eq. (4.13). Note that in the following analysis, other than in Section 4.4, we do not include a projection on the orthogonal component of the perturbed state. Since we nevertheless consider the SYK model with finite  $N$  this means that there will be a contribution to the echo peak that never decays. Moreover, we will in this case address the deviation from a perfect echo at short times. Hence, choosing the observable  $\hat{M}$  given in Eq. (4.48) and “classical” initial states with  $m$  occupied and  $N - m$  empty sites as given by Eq. (4.47) the quantity of interest is

$$\Delta M(\tau) = \langle \psi_0 | \hat{M} | \psi_0 \rangle - \langle \psi_0 | \hat{U}_E(\tau)^\dagger \hat{M} \hat{U}_E(\tau) | \psi_0 \rangle. \quad (4.52)$$

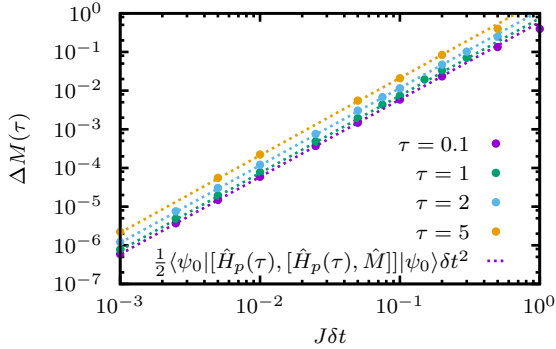


**Fig. 4.13:** Deviation from the perfect echo for different  $t$  as function of the perturbation strength  $\delta t$ . The prefactor of the dashed lines is given by the respective expectation value of the double commutator.

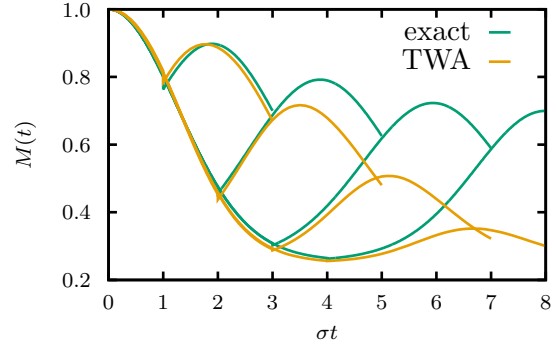


**Fig. 4.14:** Comparison of the full echo dynamics obtained by TWA with exact results. The TWA misses the persisting echo, which is a genuine quantum feature. Here,  $N = 20$  with quarter filling and  $J\delta t = 0.25$ .

As perturbation Hamiltonian we choose

$$\hat{H}_p = \sum_l J_l (c_l^\dagger c_{l+1} + h.c.) , \quad (4.53)$$

where the  $J_l$  are real Gaussian random couplings with standard deviation  $J = \sqrt{\langle J_l^2 \rangle}$ . The corresponding Weyl symbol is

$$(\hat{H}_p)_W = 2 \sum_l J_l \rho_{l,l+1} \quad (4.54)$$

Note that this is a quadratic Hamiltonian for which TWA is exact because the higher derivatives of the Moyal bracket vanish identically.

The first observation is that up to very long times only the second order contribution in Eq. (4.13), i.e., the double commutator  $[\hat{H}_p(\tau), [\hat{H}_p(\tau), \hat{M}]]$ , plays a role for the echo. This is demonstrated by the results in Fig. 4.13, which were obtained by exact simulation of the echo dynamics of an SYK model with  $N = 16$ .<sup>1</sup> The plot shows  $\Delta M(t)$  for different times  $\tau$  as a function of the perturbation strength  $\delta t$ . The dots are the exact data. The prefactor of the dashed lines is determined by the double commutator, which was also obtained from the exact simulation. They perfectly coincide with the observed echoes. Only at large perturbations  $\delta t$  and for long waiting times  $\tau$  deviations become evident.

Let us now turn to the semiclassical echo dynamics. Fig. 4.14 shows the full time evolution with imperfect time reversal at different times obtained with TWA and the exact dynamics as comparison. It is evident the height of the exact echo soon saturates at a nonvanishing value, because the perturbed state is not orthogonal to the state before the perturbation (cf. Section 4.4). In the TWA simulation, however, the echo decays to zero. This can be

<sup>1</sup> Here and in the following we consider a single realization of the SYK model, because we observe that the variation of the results with different realizations is only marginal indicating that the large number of random couplings is already sufficient for self-averaging to a large extent.

understood in the sense that the existence of a component in the perturbed state that leads to a perfect echo, because it is parallel to the unperturbed state, is a genuine quantum property. The TWA does not capture this; hence, the echo decays to zero also for small  $N$ . With increasing  $N$  the persisting echo peak height in the exact dynamics will vanish and, moreover, the accuracy of the TWA will improve. Therefore, we assume that at large  $N$  TWA gives accurate results for the echo dynamics.

The plot in Fig. 4.15 displays TWA results at quarter filling for  $\Delta M(\tau)$  with perturbation strength  $J\delta t = 10^{-1}$  in comparison with exact dynamics. Both agree well at short times before the exact  $\Delta M(\tau)$  saturates due to the persisting echo. After the short time dynamics the TWA result crosses over to an exponential increase with a growth rate  $\lambda \approx 1.24\sigma$ . Also the TWA data saturate, because  $\Delta M(\tau) \xrightarrow{\tau \rightarrow \infty} 3/4$ . The regime of exponential growth is, however, extended when the perturbation  $\delta t$  is reduced, as is shown for  $J\delta t = 10^{-2}$ . This finding hints at an important feature in the small perturbation expansion of the echo operator (4.13): The exponential divergence from the perfect echo can only occur over an extended period of time, because the perturbation strength as a small parameter suppresses the corresponding terms sufficiently to allow growth over several orders of magnitude. In large- $N$  theories, where Lyapunov exponents were identified in OTOCs, a similar role is played by  $1/N$  as small parameter (Maldacena and Stanford, 2016).

Finally, when computing the dynamics with TWA much larger system sizes are accessible than with exact simulations. In Fig. 4.16  $\Delta M(\tau)$  computed with perturbation strength  $J\delta t = 0.01$  is plotted for  $N = 20$  and  $N = 40$ . The result indicates that the Lyapunov exponent occurring in the echo dynamics is largely independent of the system size  $N$ . The short time dynamics is, however, affected by varying  $N$ , which leads to the fact that both results do not coincide despite normalization.

In conclusion, we find that in the echo dynamics of the SYK model the deviation from a perfect echo is governed by the double commutator  $[\hat{H}_p(\tau), [\hat{H}_p(\tau), \hat{M}]]$ . The perturbed echo diverges exponentially as a function of the waiting time  $\tau$  and the regime of exponential

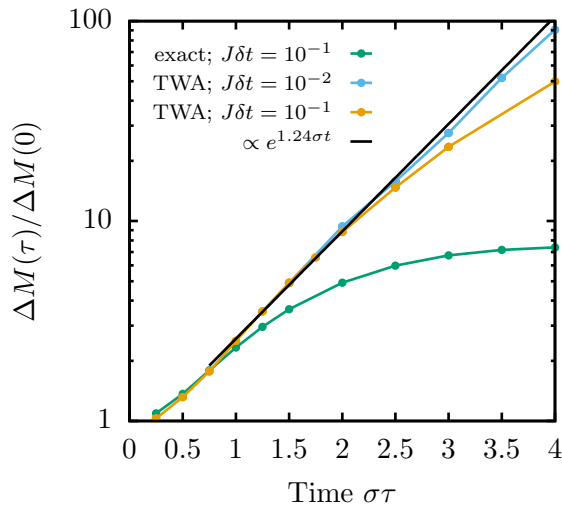


**Fig. 4.15:** Divergence from the perfect echo  $\Delta M(\tau)$  obtained from TWA in comparison with exact dynamics. For small perturbation  $\delta t$  there is a pronounced regime of exponential growth between initial short time dynamics and saturation at late times.

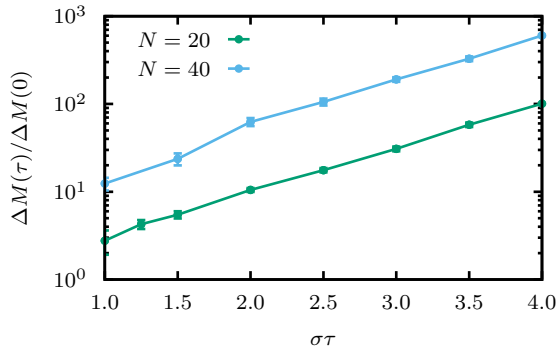


**Fig. 4.16:** TWA results for the divergence  $\Delta M(\tau)$  for different  $N$  and  $J\delta t = 10^{-2}$ .

growth is extended as the perturbation strength  $\delta t$  is reduced. In analogy to classical chaos the corresponding growth rate can be interpreted as a Lyapunov exponent.

These results and those found in Section 4.5 suggest that double commutators motivated by echo dynamics might be a suited measure that is sensitive to a possible quantum butterfly effect. These objects might be a convenient probe, because other than OTOCs, which are hard to measure experimentally, the double commutators occur in comparably simple protocols for imperfect effective time reversal. In view of a more profound understanding, a series of ensuing questions emerges, which should be addressed in future research. For example, it would be desirable to identify Lyapunov exponents and possible bounds on which in the double commutators by analytical means.

# Chapter 5

## Summary and outlook

Within this thesis different aspects of the nonequilibrium dynamics of closed quantum many-body systems have been studied. Different kinds of dynamical criticality were investigated and the questions of effective time reversal, quantum butterfly effect, and irreversibility were addressed. Moreover, the possibility to encode quantum dynamics in classical networks was explored in a perturbative approach.

In Chapter 2 two different types of nonequilibrium phase transitions have been studied. In Section 2.1 the quench dynamics of the Kitaev honeycomb model has been analyzed regarding the occurrence of dynamical quantum phase transitions and their characteristics. In the analytically solvable model various aspects of DQPTs were investigated. As a central result it was found that in this two-dimensional model the distribution of Fisher zeros in the complex time plane characteristically differs from one-dimensional systems in that the zeros form areas instead of lines. In a formal analogy the density of Fisher zeros corresponds to a density of electrical charge meaning that the nonanalytic behavior of the dynamical free energy density at the boundaries of the domains of zeros can be deduced in the same way as the nonanalyticities of the electric field at the boundary of a charge distribution. This analysis yields that in two dimensions DQPTs occur as discontinuities of the second derivative of the dynamical free energy density.

In Sections 2.2.1 and 2.2.2 the asymptotic state of Chern insulators at long times after quenching a parameter that drives topological transitions in the ground state was studied. In this setting a topologically driven nonequilibrium phase transition can be identified, which is signaled by a nonanalyticity of the Hall conductance as function of the quench parameter. It was demonstrated that irrespective of further microscopic details for gapped initial states any system with Dirac-like gap closing points exhibits a universal logarithmic singularity at the transition. If the initial state is critical, the transition occurs as a jump of definite height. The analysis in Section 2.2.2 showed that this behavior pertains in Floquet topological insulators, which are candidates for the experimental observation of the nonequilibrium transition. So far, the study of the quenched Chern insulators was undertaken in an ideal limit of a clean noninteracting system allowing for the measurement of linear response at infinite times after the quench. In future research it should be investigated whether and how the transition can be identified when relaxing these conditions.

Chapter 3 dealt with the possibility to represent quantum many-body states as networks of

classical degrees of freedom. In Section 3.2 a new approach was introduced to perturbatively derive classical networks that encode a time-evolved wave function. Using this construction the transient dynamics of transverse-field Ising models in one, two, and three dimensions was computed including local observables, entanglement production, and Loschmidt amplitudes. This demonstrates the potential capability of this approach to address dynamics in intermediate dimensions, which is hard to do with existing methods. The perturbatively derived network structures allow for a precise encoding of the wave function at short times. In the future it should be investigated whether these structures constitute a good ansatz for variational time evolution.

The last part of this thesis, Chapter 4, was about the question of irreversibility. Starting from the approach that any useful definition of irreversibility should be based on experimentally observable quantities the decay of observable echoes under imperfect effective time reversal was studied in different settings. A key finding presented in Section 4.4 is that echoes in generic many-body systems decay exponentially with a rate that is largely independent of the magnitude of the introduced imperfection. This leads to the conclusion that the dynamics is irreversible for all practical purposes, because any effort to enhance the precision of the induced time reversal is ultimately futile. This behavior of generic systems is contrasted by algebraic decay of the echoes, which was found in the analysis of an integrable spin chain in Section 4.2.

The results of further investigations presented in Sections 4.5 and 4.6 indicate that out-of-time-order double commutators, which occur naturally when considering imperfect effective time reversal, might constitute an alternative probe of the quantum butterfly effect and scrambling in addition to OTOCs. A convenient property of these objects is that they are accessible in experiment with comparatively simple effective time reversal protocols.

The aim of further research will be to understand the origin of the perturbation-independent decay of echoes under imperfect effective time reversal in more detail, including the behavior of out-of-time-order double commutators. One possible route could be to expand the investigation of relations to out-of-time-order correlators and scrambling considering quantum lattice models in the spirit of Section 4.5. A way to gain more insights into connections to a genuine butterfly effect might be to extend the studies of semiclassical echo dynamics as in Section 4.6 and to identify Lyapunov exponents in out-of-time-order double commutators by analytical means in suited models.

# Bibliography

- D. A. Abanin and Z. Papić. *Recent progress in many-body localization*. *Annalen der Physik* **529**(7), 1700169 (2017). doi:10.1002/andp.201700169. 1700169.  
URL <http://dx.doi.org/10.1002/andp.201700169>
- N. Abelung, L. Cevolani, and S. Kehrein. *Analysis of the buildup of spatiotemporal correlations and their bounds outside of the light cone*. arXiv:1707.02328 (2017).  
URL <https://arxiv.org/abs/1707.02328>
- G. Akemann, J. Baik, and P. Di Francesco (editors). *The Oxford Handbook of Random Matrix Theory*. Oxford University Press, Oxford (2011).
- F. B. Anders and A. Schiller. *Real-Time Dynamics in Quantum-Impurity Systems: A Time-Dependent Numerical Renormalization-Group Approach*. *Phys. Rev. Lett.* **95**, 196801 (2005). doi:10.1103/PhysRevLett.95.196801.  
URL <https://link.aps.org/doi/10.1103/PhysRevLett.95.196801>
- P. W. Anderson. *Absence of Diffusion in Certain Random Lattices*. *Phys. Rev.* **109**, 1492 (1958). doi:10.1103/PhysRev.109.1492.  
URL <https://link.aps.org/doi/10.1103/PhysRev.109.1492>
- F. Andraschko and J. Sirker. *Dynamical quantum phase transitions and the Loschmidt echo: A transfer matrix approach*. *Phys. Rev. B* **89**, 125120 (2014). doi:10.1103/PhysRevB.89.125120.  
URL <https://link.aps.org/doi/10.1103/PhysRevB.89.125120>
- H. Aoki, N. Tsuji, M. Eckstein, M. Kollar, T. Oka, and P. Werner. *Nonequilibrium dynamical mean-field theory and its applications*. *Rev. Mod. Phys.* **86**, 779 (2014). doi:10.1103/RevModPhys.86.779.  
URL <https://link.aps.org/doi/10.1103/RevModPhys.86.779>
- Y. Y. Atas, E. Bogomolny, O. Giraud, and G. Roux. *Distribution of the Ratio of Consecutive Level Spacings in Random Matrix Ensembles*. *Phys. Rev. Lett.* **110**, 084101 (2013). doi:10.1103/PhysRevLett.110.084101.  
URL <https://link.aps.org/doi/10.1103/PhysRevLett.110.084101>
- B. B. Nachtergaele and R. Sims. *Lieb-Robinson Bounds in Quantum Many-Body Physics*. In *Entropy and the Quantum*, volume 529 of *Contemporary Mathematics*, p. 141. American Mathematical Society (2010).



- M. C. Bañuls, J. I. Cirac, and M. B. Hastings. *Strong and Weak Thermalization of Infinite Nonintegrable Quantum Systems*. Phys. Rev. Lett. **106**, 050405 (2011). doi:10.1103/PhysRevLett.106.050405.  
URL <https://link.aps.org/doi/10.1103/PhysRevLett.106.050405>
- J. H. Bardarson, F. Pollmann, and J. E. Moore. *Unbounded Growth of Entanglement in Models of Many-Body Localization*. Phys. Rev. Lett. **109**, 017202 (2012). doi:10.1103/PhysRevLett.109.017202.  
URL <https://link.aps.org/doi/10.1103/PhysRevLett.109.017202>
- T. Barthel and U. Schollwöck. *Dephasing and the Steady State in Quantum Many-Particle Systems*. Phys. Rev. Lett. **100**, 100601 (2008). doi:10.1103/PhysRevLett.100.100601.  
URL <https://link.aps.org/doi/10.1103/PhysRevLett.100.100601>
- D. Basko, I. Aleiner, and B. Altshuler. *Metal-insulator transition in a weakly interacting many-electron system with localized single-particle states*. Annals of Physics **321**(5), 1126 (2006). doi:<https://doi.org/10.1016/j.aop.2005.11.014>.  
URL <http://www.sciencedirect.com/science/article/pii/S0003491605002630>
- J. Bell. *On the Einstein Podolsky Rosen Paradox*. Physics **1**(3), 195 (1964).  
URL [http://inspirehep.net/record/31657/files/vol1p195-200\\_001.pdf](http://inspirehep.net/record/31657/files/vol1p195-200_001.pdf)
- J. Berges, S. Borsányi, and C. Wetterich. *Prethermalization*. Phys. Rev. Lett. **93**, 142002 (2004). doi:10.1103/PhysRevLett.93.142002.  
URL <https://link.aps.org/doi/10.1103/PhysRevLett.93.142002>
- B. A. Bernevig, T. L. Hughes, and S.-C. Zhang. *Quantum Spin Hall Effect and Topological Phase Transition in HgTe Quantum Wells*. Science **314**(5806), 1757 (2006). doi:10.1126/science.1133734.  
URL <http://science.sciencemag.org/content/314/5806/1757>
- M. V. Berry and M. Tabor. *Level clustering in the regular spectrum*. Proceedings of the Royal Society of London A: Mathematical, Physical and Engineering Sciences **356**(1686), 375 (1977). doi:10.1098/rspa.1977.0140.  
URL <http://rspa.royalsocietypublishing.org/content/356/1686/375>
- B. Bertini, F. H. L. Essler, S. Groha, and N. J. Robinson. *Prethermalization and Thermalization in Models with Weak Integrability Breaking*. Phys. Rev. Lett. **115**, 180601 (2015). doi:10.1103/PhysRevLett.115.180601.  
URL <https://link.aps.org/doi/10.1103/PhysRevLett.115.180601>
- H. Bethe. *Zur Theorie der Metalle*. Zeitschrift für Physik **71**(3), 205 (1931). doi:10.1007/BF01341708.  
URL <https://doi.org/10.1007/BF01341708>
- W. Beugeling, R. Moessner, and M. Haque. *Finite-size scaling of eigenstate thermalization*. Phys. Rev. E **89**, 042112 (2014). doi:10.1103/PhysRevE.89.042112.  
URL <https://link.aps.org/doi/10.1103/PhysRevE.89.042112>

- U. Bhattacharya and A. Dutta. *Emergent topology and dynamical quantum phase transitions in two-dimensional closed quantum systems*. Phys. Rev. B **96**, 014302 (2017). doi:10.1103/PhysRevB.96.014302.  
URL <https://link.aps.org/doi/10.1103/PhysRevB.96.014302>
- F. R. A. Biebl and S. Kehrein. *Thermalization rates in the one-dimensional Hubbard model with next-to-nearest neighbor hopping*. Phys. Rev. B **95**, 104304 (2017). doi:10.1103/PhysRevB.95.104304.  
URL <https://link.aps.org/doi/10.1103/PhysRevB.95.104304>
- B. Blaß and H. Rieger. *Test of quantum thermalization in the two-dimensional transverse-field Ising model*. Scientific Reports **6**, 38185 (2016). doi:10.1038/srep38185.  
URL <http://dx.doi.org/10.1038/srep38185>
- I. Bloch, J. Dalibard, and S. Nascimbene. *Quantum simulations with ultracold quantum gases*. Nat Phys **8**, 267 (2012). doi:10.1038/nphys2259.  
URL <http://dx.doi.org/10.1038/nphys2259>
- I. Bloch, J. Dalibard, and W. Zwerger. *Many-body physics with ultracold gases*. Rev. Mod. Phys. **80**, 885 (2008). doi:10.1103/RevModPhys.80.885.  
URL <https://link.aps.org/doi/10.1103/RevModPhys.80.885>
- O. Bohigas, M. J. Giannoni, and C. Schmit. *Characterization of Chaotic Quantum Spectra and Universality of Level Fluctuation Laws*. Phys. Rev. Lett. **52**, 1 (1984). doi:10.1103/PhysRevLett.52.1.  
URL <https://link.aps.org/doi/10.1103/PhysRevLett.52.1>
- A. Bohrdt, C. B. Mendl, M. Endres, and M. Knap. *Scrambling and thermalization in a diffusive quantum many-body system*. New Journal of Physics **19**(6), 063001 (2017). doi:10.1088/1367-2630/aa719b.  
URL <http://stacks.iop.org/1367-2630/19/i=6/a=063001>
- L. Boltzmann. *Weitere Studien über das Wärmegleichgewicht unter Gasmolekülen*. Sitzungsberichte der Akademie der Wissenschaften zu Wien **66**, 275 (1872).
- L. Boltzmann. *Über die Beziehung eines allgemeinen mechanischen Satzes zum zweiten Hauptsatze der Wärmetheorie*. Sitzungsberichte der Akademie der Wissenschaften zu Wien **75**, 67 (1877).
- F. Bopp. *La mécanique quantique est-elle une mécanique statistique classique particulière*. Annales de l'institut Henri Poincaré **15**(2), 81 (1956).  
URL [http://www.numdam.org/item?id=AIHP\\_1956\\_\\_15\\_2\\_81\\_0](http://www.numdam.org/item?id=AIHP_1956__15_2_81_0)
- J. C. Budich and M. Heyl. *Dynamical topological order parameters far from equilibrium*. Phys. Rev. B **93**, 085416 (2016). doi:10.1103/PhysRevB.93.085416.  
URL <https://link.aps.org/doi/10.1103/PhysRevB.93.085416>

- L. A. Bunimovich. *On the ergodic properties of nowhere dispersing billiards*. *Comm. Math. Phys.* **65**(3), 295 (1979).  
URL <https://projecteuclid.org:443/euclid.cmp/1103904878>
- M. D. Caio, N. R. Cooper, and M. J. Bhaseen. *Hall response and edge current dynamics in Chern insulators out of equilibrium*. *Phys. Rev. B* **94**, 155104 (2016). doi:10.1103/PhysRevB.94.155104.  
URL <https://link.aps.org/doi/10.1103/PhysRevB.94.155104>
- P. Calabrese and J. Cardy. *Entanglement entropy and quantum field theory*. *Journal of Statistical Mechanics: Theory and Experiment* **2004**(06), P06002 (2004).  
URL <http://stacks.iop.org/1742-5468/2004/i=06/a=P06002>
- P. Calabrese and J. Cardy. *Evolution of entanglement entropy in one-dimensional systems*. *Journal of Statistical Mechanics: Theory and Experiment* **2005**(04), P04010 (2005).  
URL <http://stacks.iop.org/1742-5468/2005/i=04/a=P04010>
- P. Calabrese and J. Cardy. *Time Dependence of Correlation Functions Following a Quantum Quench*. *Phys. Rev. Lett.* **96**, 136801 (2006). doi:10.1103/PhysRevLett.96.136801.  
URL <https://link.aps.org/doi/10.1103/PhysRevLett.96.136801>
- P. Calabrese, F. H. L. Essler, and M. Fagotti. *Quantum Quench in the Transverse-Field Ising Chain*. *Phys. Rev. Lett.* **106**, 227203 (2011). doi:10.1103/PhysRevLett.106.227203.  
URL <https://link.aps.org/doi/10.1103/PhysRevLett.106.227203>
- P. Calabrese, F. H. L. Essler, and M. Fagotti. *Quantum quenches in the transverse field Ising chain: II. Stationary state properties*. *Journal of Statistical Mechanics: Theory and Experiment* **2012**(07), P07022 (2012). doi:10.1088/1742-5468/2012/07/P07022.  
URL <http://stacks.iop.org/1742-5468/2012/i=07/a=P07022>
- E. Canovi, P. Werner, and M. Eckstein. *First-Order Dynamical Phase Transitions*. *Phys. Rev. Lett.* **113**, 265702 (2014). doi:10.1103/PhysRevLett.113.265702.  
URL <https://link.aps.org/doi/10.1103/PhysRevLett.113.265702>
- M. Capello, F. Becca, M. Fabrizio, and S. Sorella. *Superfluid to Mott-Insulator Transition in Bose-Hubbard Models*. *Phys. Rev. Lett.* **99**, 056402 (2007). doi:10.1103/PhysRevLett.99.056402.  
URL <https://link.aps.org/doi/10.1103/PhysRevLett.99.056402>
- G. Carleo, F. Becca, L. Sanchez-Palencia, S. Sorella, and M. Fabrizio. *Light-cone effect and supersonic correlations in one- and two-dimensional bosonic superfluids*. *Phys. Rev. A* **89**, 031602 (2014). doi:10.1103/PhysRevA.89.031602.  
URL <https://link.aps.org/doi/10.1103/PhysRevA.89.031602>
- G. Carleo, F. Becca, M. Schiró, and M. Fabrizio. *Localization and Glassy Dynamics Of Many-Body Quantum Systems*. *Scientific Reports* **2**, 243 (2012). doi:10.1038/srep00243.  
URL <http://dx.doi.org/10.1038/srep00243>

- G. Carleo, L. Cevolani, L. Sanchez-Palencia, and M. Holzmann. *Unitary Dynamics of Strongly Interacting Bose Gases with the Time-Dependent Variational Monte Carlo Method in Continuous Space*. Phys. Rev. X **7**, 031026 (2017). doi:10.1103/PhysRevX.7.031026.  
URL <https://link.aps.org/doi/10.1103/PhysRevX.7.031026>
- G. Carleo and M. Troyer. *Solving the quantum many-body problem with artificial neural networks*. Science **355**(6325), 602 (2017). doi:10.1126/science.aag2302.
- A. C. Cassidy, C. W. Clark, and M. Rigol. *Generalized Thermalization in an Integrable Lattice System*. Phys. Rev. Lett. **106**, 140405 (2011). doi:10.1103/PhysRevLett.106.140405.  
URL <https://link.aps.org/doi/10.1103/PhysRevLett.106.140405>
- J.-S. Caux and J. Mossel. *Remarks on the notion of quantum integrability*. J. Stat. Mech. p. P02023 (2011). doi:10.1088/1742-5468/2011/02/P02023.  
URL <https://doi.org/10.1088/1742-5468/2011/02/P02023>
- M. A. Cazalilla. *Effect of Suddenly Turning on Interactions in the Luttinger Model*. Phys. Rev. Lett. **97**, 156403 (2006). doi:10.1103/PhysRevLett.97.156403.  
URL <https://link.aps.org/doi/10.1103/PhysRevLett.97.156403>
- L. Cevolani, G. Carleo, and L. Sanchez-Palencia. *Protected quasilocality in quantum systems with long-range interactions*. Phys. Rev. A **92**, 041603 (2015). doi:10.1103/PhysRevA.92.041603.  
URL <https://link.aps.org/doi/10.1103/PhysRevA.92.041603>
- A. Chandran, A. Nanduri, S. S. Gubser, and S. L. Sondhi. *Equilibration and coarsening in the quantum  $O(N)$  model at infinite  $N$* . Phys. Rev. B **88**, 024306 (2013). doi:10.1103/PhysRevB.88.024306.  
URL <https://link.aps.org/doi/10.1103/PhysRevB.88.024306>
- M. Cheneau, P. Barmettler, D. Poletti, M. Endres, P. Schauß, T. Fukuhara, C. Gross, I. Bloch, C. Kollath, and S. Kuhr. *Light-cone-like spreading of correlations in a quantum many-body system*. Nature **481**, 484 (2012). doi:10.1038/nature10748.  
URL <https://www.nature.com/articles/nature10748>
- L. Childress, M. V. Gurudev Dutt, J. M. Taylor, A. S. Zibrov, F. Jelezko, J. Wrachtrup, P. R. Hemmer, and M. D. Lukin. *Coherent Dynamics of Coupled Electron and Nuclear Spin Qubits in Diamond*. Science **314**(5797), 281 (2006). doi:10.1126/science.1131871.  
URL <http://science.sciencemag.org/content/314/5797/281>
- J.-y. Choi, S. Hild, J. Zeiher, P. Schauß, A. Rubio-Abadal, T. Yefsah, V. Khemani, D. A. Huse, I. Bloch, and C. Gross. *Exploring the many-body localization transition in two dimensions*. Science **352**(6293), 1547 (2016). doi:10.1126/science.aaf8834.  
URL <http://science.sciencemag.org/content/352/6293/1547>
- S. Choi, J. Choi, R. Landig, G. Kucsko, H. Zhou, J. Isoya, F. Jelezko, S. Onoda, H. Sumiya, V. Khemani, C. von Keyserlingk, N. Y. Yao, E. Demler, and M. D. Lukin. *Observation of*

- discrete time-crystalline order in a disordered dipolar many-body system.* Nature **543**, 221 (2017). doi:10.1038/nature21426.  
URL <http://dx.doi.org/10.1038/nature21426>
- G. Cohen, E. Gull, D. R. Reichman, and A. J. Millis. *Taming the Dynamical Sign Problem in Real-Time Evolution of Quantum Many-Body Problems.* Phys. Rev. Lett. **115**, 266802 (2015). doi:10.1103/PhysRevLett.115.266802.  
URL <https://link.aps.org/doi/10.1103/PhysRevLett.115.266802>
- N. R. da Silva, M. Möller, A. Feist, H. Ulrichs, C. Ropers, and S. Schäfer. *Nanoscale mapping of ultrafast magnetization dynamics with femtosecond Lorentz microscopy.* arXiv:1710.03307 (2017).  
URL <https://arxiv.org/abs/1710.03307>
- L. D'Alessio, Y. Kafri, A. Polkovnikov, and M. Rigol. *From Quantum Chaos and Eigenstate Thermalization to Statistical Mechanics and Thermodynamics.* Advances in Physics **65**, 239 (2016). doi:10.1080/00018732.2016.1198134.  
URL <https://dx.doi.org/10.1080/00018732.2016.1198134>
- S. M. Davidson. *Novel phase-space methods to simulate strongly-interacting many-body quantum dynamics.* Ph.D. thesis, Boston University School of Arts & Sciences (2017).  
URL <https://open.bu.edu/handle/2144/24091>
- S. M. Davidson, D. Sels, and A. Polkovnikov. *Semiclassical approach to dynamics of interacting fermions.* Annals of Physics **384**, 128 (2017). doi:https://doi.org/10.1016/j.aop.2017.07.003.  
URL <http://www.sciencedirect.com/science/article/pii/S0003491617301926>
- H. Dehghani, T. Oka, and A. Mitra. *Out-of-equilibrium electrons and the Hall conductance of a Floquet topological insulator.* Phys. Rev. B **91**, 155422 (2015). doi:10.1103/PhysRevB.91.155422.  
URL <https://link.aps.org/doi/10.1103/PhysRevB.91.155422>
- D.-L. Deng, X. Li, and S. Das Sarma. *Exact Machine Learning Topological States.* arXiv:1609.09060 (2016).  
URL <https://arxiv.org/abs/1609.09060>
- D.-L. Deng, X. Li, and S. Das Sarma. *Quantum Entanglement in Neural Network States.* Phys. Rev. X **7**, 021021 (2017). doi:10.1103/PhysRevX.7.021021.  
URL <https://link.aps.org/doi/10.1103/PhysRevX.7.021021>
- J. M. Deutsch. *Quantum statistical mechanics in a closed system.* Phys. Rev. A **43**, 2046 (1991). doi:10.1103/PhysRevA.43.2046.  
URL <https://link.aps.org/doi/10.1103/PhysRevA.43.2046>



- P. A. M. Dirac. *Note on Exchange Phenomena in the Thomas Atom*. Mathematical Proceedings of the Cambridge Philosophical Society **26**(3), 376–385 (1930). doi:10.1017/S0305004100016108.  
URL <https://doi.org/10.1017/S0305004100016108>
- M. W. Doherty, N. B. Manson, P. Delaney, F. Jelezko, J. Wrachtrup, and L. C. L. Hollenberg. *The nitrogen-vacancy colour centre in diamond*. Physics Reports **528**, 1 (2013). doi:10.1016/j.physrep.2013.02.001.  
URL <https://doi.org/10.1016/j.physrep.2013.02.001>
- A. Doikou, S. Evangelisti, G. Feverati, and N. Karaiskos. *Introduction to quantum integrability*. International Journal of Modern Physics A **25**(17), 3307 (2010). doi:10.1142/S0217751X10049803.  
URL <http://www.worldscientific.com/doi/abs/10.1142/S0217751X10049803>
- J. Dormand and P. Prince. *A family of embedded Runge-Kutta formulae*. Journal of Computational and Applied Mathematics **6**(1), 19 (1980). doi:[https://doi.org/10.1016/0771-050X\(80\)90013-3](https://doi.org/10.1016/0771-050X(80)90013-3).  
URL <http://www.sciencedirect.com/science/article/pii/0771050X80900133>
- F. J. Dyson. *Statistical Theory of the Energy Levels of Complex Systems. I*. Journal of Mathematical Physics **3**(1), 140 (1962). doi:10.1063/1.1703773.  
URL <http://dx.doi.org/10.1063/1.1703773>
- L. D'Alessio and M. Rigol. *Dynamical preparation of Floquet Chern insulators*. Nat. Commun. **6**, 8336 (2015). doi:10.1038/ncomms9336.  
URL <http://dx.doi.org/10.1038/ncomms9336>
- M. Eckstein, M. Kollar, and P. Werner. *Thermalization after an Interaction Quench in the Hubbard Model*. Phys. Rev. Lett. **103**, 056403 (2009). doi:10.1103/PhysRevLett.103.056403.  
URL <https://link.aps.org/doi/10.1103/PhysRevLett.103.056403>
- A. Einstein, B. Podolsky, and N. Rosen. *Can Quantum-Mechanical Description of Physical Reality Be Considered Complete?* Phys. Rev. **47**, 777 (1935). doi:10.1103/PhysRev.47.777.  
URL <https://link.aps.org/doi/10.1103/PhysRev.47.777>
- J. Eisert, M. Cramer, and M. B. Plenio. *Colloquium: Area laws for the entanglement entropy*. Rev. Mod. Phys. **82**, 277 (2010). doi:10.1103/RevModPhys.82.277.  
URL <https://link.aps.org/doi/10.1103/RevModPhys.82.277>
- F. H. L. Essler, S. Kehrein, S. R. Manmana, and N. J. Robinson. *Quench dynamics in a model with tuneable integrability breaking*. Phys. Rev. B **89**, 165104 (2014). doi:10.1103/PhysRevB.89.165104.  
URL <https://link.aps.org/doi/10.1103/PhysRevB.89.165104>

- M. Fagotti and F. H. L. Essler. *Reduced density matrix after a quantum quench*. Phys. Rev. B **87**, 245107 (2013). doi:10.1103/PhysRevB.87.245107.  
URL <https://link.aps.org/doi/10.1103/PhysRevB.87.245107>
- U. Fano. *Effects of Configuration Interaction on Intensities and Phase Shifts*. Phys. Rev. **124**, 1866 (1961). doi:10.1103/PhysRev.124.1866.  
URL <https://link.aps.org/doi/10.1103/PhysRev.124.1866>
- H. Feshbach. *A unified theory of nuclear reactions. II*. Annals of Physics **19**(2), 287 (1962). doi:http://dx.doi.org/10.1016/0003-4916(62)90221-X.  
URL <http://www.sciencedirect.com/science/article/pii/000349166290221X>
- R. P. Feynman. *Simulating physics with computers*. International Journal of Theoretical Physics **21**(6), 467 (1982). doi:10.1007/BF02650179.  
URL <https://doi.org/10.1007/BF02650179>
- G. E. Fisher. *Lectures in Theoretical Physics*, volume 7 of *Lectures in Theoretical Physics: Lectures Delivered at the Summer Institute for Theoretical Physics, University of Colorado, Boulder*. Interscience (1965).
- M. E. Fisher. *The renormalization group in the theory of critical behavior*. Rev. Mod. Phys. **46**, 597 (1974). doi:10.1103/RevModPhys.46.597.  
URL <https://link.aps.org/doi/10.1103/RevModPhys.46.597>
- N. Fläschner, D. Vogel, M. Tarnowski, B. S. Rem, M. Lühmann, D-S Heyl, J. C. Budich, L. Mathey, K. Sengstock, and C. Weitenberg. *Observation of a dynamical topological phase transition*. arXiv:1608.05616 (2016).
- J. K. Freericks, V. M. Turkowski, and V. Zlatić. *Nonequilibrium Dynamical Mean-Field Theory*. Phys. Rev. Lett. **97**, 266408 (2006). doi:10.1103/PhysRevLett.97.266408.  
URL <https://link.aps.org/doi/10.1103/PhysRevLett.97.266408>
- H. Fukutome. *The Group Theoretical Structure of Fermion Many-Body Systems Arising from the Canonical Anticommutation Relation. I Lie Algebras of Fermion Operators and Exact Generator Coordinate Representations of State Vectors*. Progress of Theoretical Physics **65**(3), 809 (1981). doi:10.1143/PTP.65.809.  
URL <http://dx.doi.org/10.1143/PTP.65.809>
- A. Gambassi and P. Calabrese. *Quantum quenches as classical critical films*. EPL (Europhysics Letters) **95**(6), 66007 (2011).  
URL <http://stacks.iop.org/0295-5075/95/i=6/a=66007>
- A. Gambassi and A. Silva. *Large Deviations and Universality in Quantum Quenches*. Phys. Rev. Lett. **109**, 250602 (2012). doi:10.1103/PhysRevLett.109.250602.  
URL <https://link.aps.org/doi/10.1103/PhysRevLett.109.250602>



- X. Gao and L.-M. Duan. *Efficient Representation of Quantum Many-Body States with Deep Neural Networks*. arXiv:1701.05039 (2017).  
URL <https://arxiv.org/abs/1701.05039>
- A. Georges, G. Kotliar, W. Krauth, and M. J. Rozenberg. *Dynamical mean-field theory of strongly correlated fermion systems and the limit of infinite dimensions*. Rev. Mod. Phys. **68**, 13 (1996). doi:10.1103/RevModPhys.68.13.  
URL <https://link.aps.org/doi/10.1103/RevModPhys.68.13>
- I. M. Georgescu, S. Ashhab, and F. Nori. *Quantum simulation*. Rev. Mod. Phys. **86**, 153 (2014). doi:10.1103/RevModPhys.86.153.  
URL <https://link.aps.org/doi/10.1103/RevModPhys.86.153>
- C. Gogolin and J. Eisert. *Equilibration, thermalisation, and the emergence of statistical mechanics in closed quantum systems*. Reports on Progress in Physics **79**(5), 056001 (2016).  
URL <http://stacks.iop.org/0034-4885/79/i=5/a=056001>
- C. Gogolin, M. P. Müller, and J. Eisert. *Absence of Thermalization in Nonintegrable Systems*. Phys. Rev. Lett. **106**, 040401 (2011). doi:10.1103/PhysRevLett.106.040401.  
URL <https://link.aps.org/doi/10.1103/PhysRevLett.106.040401>
- T. Gorin, T. Prosen, T. H. Seligman, and M. Žnidarič. *Dynamics of Loschmidt echoes and fidelity decay*. Physics Reports **435**(2–5), 33 (2006). doi:http://dx.doi.org/10.1016/j.physrep.2006.09.003.  
URL <http://www.sciencedirect.com/science/article/pii/S0370157306003310>
- I. V. Gornyi, A. D. Mirlin, and D. G. Polyakov. *Interacting Electrons in Disordered Wires: Anderson Localization and Low-T Transport*. Phys. Rev. Lett. **95**, 206603 (2005). doi:10.1103/PhysRevLett.95.206603.  
URL <https://link.aps.org/doi/10.1103/PhysRevLett.95.206603>
- M. Greiner, O. Mandel, T. W. Hansch, and I. Bloch. *Collapse and revival of the matter wave field of a Bose-Einstein condensate*. Nature **419**, 51 (2002). doi:10.1038/nature00968.  
URL <http://dx.doi.org/10.1038/nature00968>
- R. Grimm, M. Weidemüller, and Y. B. Ovchinnikov. *Optical Dipole Traps for Neutral Atoms*. Adv. At., Mol., Opt. Phys. **42**, 95 (2000).  
URL [https://doi.org/10.1016/S1049-250X\(08\)60186-X](https://doi.org/10.1016/S1049-250X(08)60186-X)
- M. Gring, M. Kuhnert, T. Langen, T. Kitagawa, B. Rauer, M. Schreitl, I. Mazets, D. A. Smith, E. Demler, and J. Schmiedmayer. *Relaxation and Prethermalization in an Isolated Quantum System*. Science **337**(6100), 1318 (2012). doi:10.1126/science.1224953.  
URL <http://science.sciencemag.org/content/337/6100/1318>
- H. Groenewold. *On the principles of elementary quantum mechanics*. Physica **12**(7), 405 (1946). doi:https://doi.org/10.1016/S0031-8914(46)80059-4.  
URL <http://www.sciencedirect.com/science/article/pii/S0031891446800594>

- C. Gross and I. Bloch. *Quantum simulations with ultracold atoms in optical lattices*. *Science* **357**(6355), 995 (2017). doi:10.1126/science.aal3837.  
URL <http://science.sciencemag.org/content/357/6355/995>
- E. Gull, A. J. Millis, A. I. Lichtenstein, A. N. Rubtsov, M. Troyer, and P. Werner. *Continuous-time Monte Carlo methods for quantum impurity models*. *Rev. Mod. Phys.* **83**, 349 (2011). doi:10.1103/RevModPhys.83.349.  
URL <https://link.aps.org/doi/10.1103/RevModPhys.83.349>
- A. Hackl and S. Kehrein. *Real time evolution in quantum many-body systems with unitary perturbation theory*. *Phys. Rev. B* **78**, 092303 (2008). doi:10.1103/PhysRevB.78.092303.  
URL <https://link.aps.org/doi/10.1103/PhysRevB.78.092303>
- A. Hackl and S. Kehrein. *A unitary perturbation theory approach to real-time evolution problems*. *Journal of Physics: Condensed Matter* **21**(1), 015601 (2009).  
URL <http://stacks.iop.org/0953-8984/21/i=1/a=015601>
- J. Haegeman, J. I. Cirac, T. J. Osborne, I. Pižorn, H. Verschelde, and F. Verstraete. *Time-Dependent Variational Principle for Quantum Lattices*. *Phys. Rev. Lett.* **107**, 070601 (2011). doi:10.1103/PhysRevLett.107.070601.  
URL <https://link.aps.org/doi/10.1103/PhysRevLett.107.070601>
- J. Hafner, B. Blass, and H. Rieger. *Light cone in the two-dimensional transverse-field Ising model in time-dependent mean-field theory*. *EPL (Europhysics Letters)* **116**(6), 60002 (2016).  
URL <http://stacks.iop.org/0295-5075/116/i=6/a=60002>
- S. Hafner, D. Demco, and R. Kimmich. *Magic echoes and NMR imaging of solids*. *Solid State Nuclear Magnetic Resonance* **6**(4), 275 (1996). doi:[https://doi.org/10.1016/0926-2040\(96\)01234-9](https://doi.org/10.1016/0926-2040(96)01234-9).  
URL <http://www.sciencedirect.com/science/article/pii/0926204096012349>
- E. L. Hahn. *Spin Echoes*. *Phys. Rev.* **80**, 580 (1950). doi:10.1103/PhysRev.80.580.  
URL <https://link.aps.org/doi/10.1103/PhysRev.80.580>
- F. D. M. Haldane. *Model for a Quantum Hall Effect without Landau Levels: Condensed-Matter Realization of the “Parity Anomaly”*. *Phys. Rev. Lett.* **61**, 2015 (1988). doi:10.1103/PhysRevLett.61.2015.  
URL <https://link.aps.org/doi/10.1103/PhysRevLett.61.2015>
- B. Hensen, H. Bernien, A. E. Dreau, A. Reiserer, N. Kalb, M. S. Blok, J. Ruitenber, R. F. L. Vermeulen, R. N. Schouten, C. Abellan, W. Amaya, V. Pruneri, M. W. Mitchell, M. Markham, D. J. Twitchen, D. Elkouss, S. Wehner, T. H. Taminiau, and R. Hanson. *Loophole-free Bell inequality violation using electron spins separated by 1.3 kilometres*. *Nature* **526**, 682 (2015). doi:10.1038/nature15759.  
URL <http://dx.doi.org/10.1038/nature15759>

- M. Heyl. *Dynamical Quantum Phase Transitions in Systems with Broken-Symmetry Phases*. Phys. Rev. Lett. **113**, 205701 (2014). doi:10.1103/PhysRevLett.113.205701.  
URL <https://link.aps.org/doi/10.1103/PhysRevLett.113.205701>
- M. Heyl. *Scaling and Universality at Dynamical Quantum Phase Transitions*. Phys. Rev. Lett. **115**, 140602 (2015). doi:10.1103/PhysRevLett.115.140602.  
URL <https://link.aps.org/doi/10.1103/PhysRevLett.115.140602>
- M. Heyl. *Dynamical quantum phase transitions: a review*. arXiv:1709.07461 (2017).  
URL <https://arxiv.org/abs/1709.07461>
- M. Heyl, A. Polkovnikov, and S. Kehrein. *Dynamical Quantum Phase Transitions in the Transverse-Field Ising Model*. Phys. Rev. Lett. **110**, 135704 (2013). doi:10.1103/PhysRevLett.110.135704.  
URL <https://link.aps.org/doi/10.1103/PhysRevLett.110.135704>
- K. Hornik. *Approximation Capabilities of Multilayer Feedforward Networks*. Neural Netw. **4**(2), 251 (1991). doi:10.1016/0893-6080(91)90009-T.  
URL [http://dx.doi.org/10.1016/0893-6080\(91\)90009-T](http://dx.doi.org/10.1016/0893-6080(91)90009-T)
- P. Hosur, X.-L. Qi, D. Roberts, and B. Yoshida. *Chaos in quantum channels*. Journal of High Energy Physics **2016**(2), 4 (2016). doi:10.1007/JHEP02(2016)004.  
URL <https://link.springer.com/article/10.1007%2FJHEP02%282016%29004>
- Y. Hu, P. Zoller, and J. C. Budich. *Dynamical Buildup of a Quantized Hall Response from Nontopological States*. Phys. Rev. Lett. **117**, 126803 (2016). doi:10.1103/PhysRevLett.117.126803.  
URL <https://link.aps.org/doi/10.1103/PhysRevLett.117.126803>
- Y. Huang and J. Moore. *Neural network representation of tensor network and chiral states*. arXiv:1701.06246 (2017).  
URL <https://arxiv.org/abs/1701.06246>
- Y. Huang, Y.-L. Zhang, and X. Chen. *Out-of-time-ordered correlators in many-body localized systems*. Annalen der Physik (2016). doi:10.1002/andp.201600318.  
URL <http://dx.doi.org/10.1002/andp.201600318>
- Z. Huang and A. V. Balatsky. *Dynamical Quantum Phase Transitions: Role of Topological Nodes in Wave Function Overlaps*. Phys. Rev. Lett. **117**, 086802 (2016). doi:10.1103/PhysRevLett.117.086802.  
URL <https://link.aps.org/doi/10.1103/PhysRevLett.117.086802>
- J. Hubbard. *Electron correlations in narrow energy bands*. Proceedings of the Royal Society of London A: Mathematical, Physical and Engineering Sciences **276**(1365), 238 (1963). doi:10.1098/rspa.1963.0204.  
URL <http://rspa.royalsocietypublishing.org/content/276/1365/238>

- D. A. Huse, R. Nandkishore, and V. Oganesyan. *Phenomenology of fully many-body-localized systems*. Phys. Rev. B **90**, 174202 (2014). doi:10.1103/PhysRevB.90.174202.  
URL <https://link.aps.org/doi/10.1103/PhysRevB.90.174202>
- E. Iyoda and T. Sagawa. *Scrambling of Quantum Information in Quantum Many-Body Systems*. arXiv:1704.04850 (2017).  
URL <https://arxiv.org/abs/1704.04850>
- R. Jackiw and A. Kerman. *Time-dependent variational principle and the effective action*. Physics Letters A **71**(2), 158 (1979). doi:http://dx.doi.org/10.1016/0375-9601(79)90151-8.  
URL <http://www.sciencedirect.com/science/article/pii/0375960179901518>
- P. Jacquod and C. Petitjean. *Decoherence, entanglement and irreversibility in quantum dynamical systems with few degrees of freedom*. Advances in Physics **58**(2), 67 (2009). doi:10.1080/00018730902831009.  
URL <http://dx.doi.org/10.1080/00018730902831009>
- R. Jastrow. *Many-Body Problem with Strong Forces*. Phys. Rev. **98**, 1479 (1955). doi:10.1103/PhysRev.98.1479.  
URL <https://link.aps.org/doi/10.1103/PhysRev.98.1479>
- E. T. Jaynes. *Information Theory and Statistical Mechanics*. Phys. Rev. **106**, 620 (1957a). doi:10.1103/PhysRev.106.620.  
URL <https://link.aps.org/doi/10.1103/PhysRev.106.620>
- E. T. Jaynes. *Information Theory and Statistical Mechanics. II*. Phys. Rev. **108**, 171 (1957b). doi:10.1103/PhysRev.108.171.  
URL <https://link.aps.org/doi/10.1103/PhysRev.108.171>
- R. V. Jensen and R. Shankar. *Statistical Behavior in Deterministic Quantum Systems with Few Degrees of Freedom*. Phys. Rev. Lett. **54**, 1879 (1985). doi:10.1103/PhysRevLett.54.1879.  
URL <https://link.aps.org/doi/10.1103/PhysRevLett.54.1879>
- G. Jotzu, M. Messer, R. Desbuquois, M. Lebrat, T. Uehlinger, D. Greif, and T. Esslinger. *Experimental realization of the topological Haldane model with ultracold fermions*. Nature **515**, 237 (2014). doi:10.1038/nature13915.  
URL <http://dx.doi.org/10.1038/nature13915>
- P. Jurcevic, B. P. Lanyon, P. Hauke, C. Hempel, P. Zoller, R. Blatt, and C. F. Roos. *Quasi-particle engineering and entanglement propagation in a quantum many-body system*. Nature **511**, 202 (2014). doi:10.1038/nature13461.  
URL <http://dx.doi.org/10.1038/nature13461>
- P. Jurcevic, H. Shen, P. Hauke, C. Maier, T. Brydges, C. Hempel, B. P. Lanyon, M. Heyl, R. Blatt, and C. F. Roos. *Direct Observation of Dynamical Quantum Phase Transitions in an Interacting Many-Body System*. Phys. Rev. Lett. **119**, 080501 (2017). doi:10.1103/

- PhysRevLett.119.080501.  
URL <https://link.aps.org/doi/10.1103/PhysRevLett.119.080501>
- C. L. Kane and E. J. Mele. *Quantum Spin Hall Effect in Graphene*. Phys. Rev. Lett. **95**, 226801 (2005). doi:10.1103/PhysRevLett.95.226801.  
URL <https://link.aps.org/doi/10.1103/PhysRevLett.95.226801>
- C. Karrasch and D. Schuricht. *Dynamical phase transitions after quenches in nonintegrable models*. Phys. Rev. B **87**, 195104 (2013). doi:10.1103/PhysRevB.87.195104.  
URL <https://link.aps.org/doi/10.1103/PhysRevB.87.195104>
- R. Kaubruegger, L. Pastori, and J. C. Budich. *Chiral Topological Phases from Artificial Neural Networks*. arXiv:1710.04713 (2017).  
URL <https://arxiv.org/abs/1710.04713>
- S. Kehrein. *The Flow Equation Approach to Many-Particle Systems*. Springer, Berlin (2006). doi:10.1007/3-540-34068-8.
- H. Kim, T. N. Ikeda, and D. A. Huse. *Testing whether all eigenstates obey the eigenstate thermalization hypothesis*. Phys. Rev. E **90**, 052105 (2014). doi:10.1103/PhysRevE.90.052105.  
URL <https://link.aps.org/doi/10.1103/PhysRevE.90.052105>
- T. Kinoshita, T. Wenger, and D. S. Weiss. *A quantum Newton's cradle*. Nature **440**, 900 (2006). doi:10.1038/nature04693.  
URL <http://dx.doi.org/10.1038/nature04693>
- A. Kitaev. *Hidden correlations in the Hawking radiation and thermal noise* (2014). (Talk given at the Fundamental Physics Prize Symposium).
- A. Kitaev. *A simple model of quantum holography* (2015). <http://online.kitp.ucsb.edu/online/entangled15/kitaev/>; <http://online.kitp.ucsb.edu/online/entangled15/kitaev2/> .
- A. Kitaev and J. Preskill. *Topological Entanglement Entropy*. Phys. Rev. Lett. **96**, 110404 (2006). doi:10.1103/PhysRevLett.96.110404.  
URL <https://link.aps.org/doi/10.1103/PhysRevLett.96.110404>
- J. A. Kjäll, M. P. Zaletel, R. S. K. Mong, J. H. Bardarson, and F. Pollmann. *Phase diagram of the anisotropic spin-2 XXZ model: Infinite-system density matrix renormalization group study*. Phys. Rev. B **87**, 235106 (2013). doi:10.1103/PhysRevB.87.235106.  
URL <https://link.aps.org/doi/10.1103/PhysRevB.87.235106>
- M. Kollar and M. Eckstein. *Relaxation of a one-dimensional Mott insulator after an interaction quench*. Phys. Rev. A **78**, 013626 (2008). doi:10.1103/PhysRevA.78.013626.  
URL <https://link.aps.org/doi/10.1103/PhysRevA.78.013626>

- M. Kollar, F. A. Wolf, and M. Eckstein. *Generalized Gibbs ensemble prediction of prethermalization plateaus and their relation to nonthermal steady states in integrable systems*. Phys. Rev. B **84**, 054304 (2011). doi:10.1103/PhysRevB.84.054304.  
URL <https://link.aps.org/doi/10.1103/PhysRevB.84.054304>
- C. Kollath, G. Roux, G. Biroli, and A. M. Läuchli. *Statistical properties of the spectrum of the extended Bose–Hubbard model*. Journal of Statistical Mechanics: Theory and Experiment **2010**(08), P08011 (2010). doi:0.1088/1742-5468/2010/08/P08011.  
URL <http://stacks.iop.org/1742-5468/2010/i=08/a=P08011>
- M. König, S. Wiedmann, C. Brüne, A. Roth, H. Buhmann, L. W. Molenkamp, X.-L. Qi, and S.-C. Zhang. *Quantum Spin Hall Insulator State in HgTe Quantum Wells*. Science **318**(5851), 766 (2007). doi:10.1126/science.1148047.  
URL <http://science.sciencemag.org/content/318/5851/766>
- V. E. Korepin, N. M. Bogoliubov, and A. G. Izergin. *Quantum Inverse Scattering Method and Correlation Functions*. Cambridge Monographs on Mathematical Physics. Cambridge University Press (1993). doi:10.1017/CBO9780511628832.
- V. K. B. Kota (editor). *Embedded Random Matrix Ensembles in Quantum Physics*, volume 884 of *Lecture Notes in Physics*. Springer International Publishing (2014). doi:10.1007/978-3-319-04567-2.  
URL <http://www.springer.com/us/book/9783319045665>
- J. N. Kriel, C. Karrasch, and S. Kehrein. *Dynamical quantum phase transitions in the axial next-nearest-neighbor Ising chain*. Phys. Rev. B **90**, 125106 (2014). doi:10.1103/PhysRevB.90.125106.  
URL <https://link.aps.org/doi/10.1103/PhysRevB.90.125106>
- R. Kubo. *The fluctuation-dissipation theorem*. Reports on Progress in Physics **29**(1), 255 (1966).  
URL <http://stacks.iop.org/0034-4885/29/i=1/a=306>
- C. Lanczos. *An iteration method for the solution of the eigenvalue problem of linear differential and integral operators*. J. Res. Nat'l Bur. Std. **45**, 255 (1950).
- T. Langen, S. Erne, R. Geiger, B. Rauer, T. Schweigler, M. Kuhnert, W. Rohringer, I. E. Mazets, T. Gasenzer, and J. Schmiedmayer. *Experimental observation of a generalized Gibbs ensemble*. Science **348**(6231), 207 (2015). doi:10.1126/science.1257026.  
URL <http://science.sciencemag.org/content/348/6231/207>
- T. Langen, T. Gasenzer, and J. Schmiedmayer. *Prethermalization and universal dynamics in near-integrable quantum systems*. Journal of Statistical Mechanics: Theory and Experiment **2016**(6), 064009 (2016).  
URL <http://stacks.iop.org/1742-5468/2016/i=6/a=064009>



- T. Langen, R. Geiger, M. Kuhnert, B. Rauer, and J. Schmiedmayer. *Local emergence of thermal correlations in an isolated quantum many-body system*. Nat Phys **9**, 640 (2013). doi:10.1038/nphys2739.  
URL <http://dx.doi.org/10.1038/nphys2739>
- A. Larkin and Y. Ovchinnikov. *Quasiclassical method in the theory of superconductivity*. Sov. Phys. JETP **28**, 1200 (1969).  
URL <http://www.jetp.ac.ru/cgi-bin/e/index/e/28/6/p1200?a=list>
- A. Läuchli, J. Sudan, and R. Moessner. *The  $S = 1/2$  Kagome Heisenberg Antiferromagnet Revisited*. arXiv:1611.06990 (2016).  
URL <https://arxiv.org/abs/1611.06990>
- N. Le Roux and Y. Bengio. *Representational power of restricted boltzmann machines and deep belief networks*. Neural Comput. **20**(6), 1631 (2008). doi:10.1162/neco.2008.04-07-510.  
URL <https://www.ncbi.nlm.nih.gov/pubmed/18254699>
- J. L. Lebowitz and O. Penrose. *Modern ergodicity theory*. Physics Today **26**, 23 (1973). doi:10.1063/1.3127948.  
URL <https://doi.org/10.1063/1.3127948>
- A. LeClair, G. Mussardo, H. Saleur, and S. Skorik. *Boundary energy and boundary states in integrable quantum field theories*. Nuclear Physics B **453**(3), 581 (1995). doi:https://doi.org/10.1016/0550-3213(95)00435-U.  
URL <http://www.sciencedirect.com/science/article/pii/055032139500435U>
- Y. Lemonik and A. Mitra. *Entanglement properties of the critical quench of  $O(N)$  bosons*. Phys. Rev. B **94**, 024306 (2016). doi:10.1103/PhysRevB.94.024306.  
URL <https://link.aps.org/doi/10.1103/PhysRevB.94.024306>
- E. Leviatan, F. Pollmann, J. Bardarson, and E. Altman. *Quantum thermalization dynamics with Matrix-Product States*. arXiv:1702.08894 (2017).  
URL <https://arxiv.org/abs/1702.08894>
- E. Lieb, T. Schultz, and D. Mattis. *Two soluble models of an antiferromagnetic chain*. Annals of Physics **16**(3), 407 (1961). doi:https://doi.org/10.1016/0003-4916(61)90115-4.  
URL <http://www.sciencedirect.com/science/article/pii/0003491661901154>
- E. H. Lieb and D. W. Robinson. *The finite group velocity of quantum spin systems*. Communications in Mathematical Physics **28**(3), 251 (1972). doi:10.1007/BF01645779.  
URL <https://doi.org/10.1007/BF01645779>
- E. N. Lorenz. *Deterministic Nonperiodic Flow*. Journal of the Atmospheric Sciences **20**(2), 130 (1963). doi:10.1175/1520-0469(1963)020<0130:DNF>2.0.CO;2.  
URL [https://doi.org/10.1175/1520-0469\(1963\)020<0130:DNF>2.0.CO;2](https://doi.org/10.1175/1520-0469(1963)020<0130:DNF>2.0.CO;2)



- J. Loschmidt. *Über den Zustand des Wärmegleichgewichtes eines Systems von Körpern mit Rücksicht auf die Schwerkraft*. Sitzungsberichte der Akademie der Wissenschaften zu Wien **73**, 128 (1876).
- J. Lux, J. Müller, A. Mitra, and A. Rosch. *Hydrodynamic long-time tails after a quantum quench*. Phys. Rev. A **89**, 053608 (2014). doi:10.1103/PhysRevA.89.053608.  
URL <https://link.aps.org/doi/10.1103/PhysRevA.89.053608>
- A. M. Läuchli and C. Kollath. *Spreading of correlations and entanglement after a quench in the one-dimensional Bose–Hubbard model*. Journal of Statistical Mechanics: Theory and Experiment **2008**(05), P05018 (2008).  
URL <http://stacks.iop.org/1742-5468/2008/i=05/a=P05018>
- T. Maier, M. Jarrell, T. Pruschke, and M. H. Hettler. *Quantum cluster theories*. Rev. Mod. Phys. **77**, 1027 (2005). doi:10.1103/RevModPhys.77.1027.  
URL <https://link.aps.org/doi/10.1103/RevModPhys.77.1027>
- J. Maldacena, S. Shenker, and D. Stanford. *A bound on chaos*. Journal of High Energy Physics **2016**(8), 106 (2016). doi:10.1007/JHEP08(2016)106.  
URL [https://link.springer.com/article/10.1007/JHEP08\(2016\)106](https://link.springer.com/article/10.1007/JHEP08(2016)106)
- J. Maldacena and D. Stanford. *Remarks on the Sachdev–Ye–Kitaev model*. Phys. Rev. D **94**, 106002 (2016). doi:10.1103/PhysRevD.94.106002.  
URL <https://link.aps.org/doi/10.1103/PhysRevD.94.106002>
- S. R. Manmana, S. Wessel, R. M. Noack, and A. Muramatsu. *Time evolution of correlations in strongly interacting fermions after a quantum quench*. Phys. Rev. B **79**, 155104 (2009). doi:10.1103/PhysRevB.79.155104.  
URL <https://link.aps.org/doi/10.1103/PhysRevB.79.155104>
- S. Mathias, S. Eich, J. Urbancic, S. Michael, A. V. Carr, S. Emmerich, A. Stange, T. Popmintchev, T. Rohwer, M. Wiesenmayer, A. Ruffing, S. Jakobs, S. Hellmann, P. Matyba, C. Chen, L. Kipp, M. Bauer, H. C. Kapteyn, H. C. Schneider, K. Rossnagel, M. M. Murnane, and M. Aeschlimann. *Self-amplified photo-induced gap quenching in a correlated electron material*. Nat Comm **7**, 12902 (2016). doi:10.1038/ncomms12902.  
URL <http://dx.doi.org/10.1038/ncomms12902>
- W. L. McMillan. *Ground State of Liquid He<sup>4</sup>*. Phys. Rev. **138**, A442 (1965). doi:10.1103/PhysRev.138.A442.  
URL <https://link.aps.org/doi/10.1103/PhysRev.138.A442>
- M. Medvedyeva, A. Hoffmann, and S. Kehrein. *Spatiotemporal buildup of the Kondo screening cloud*. Phys. Rev. B **88**, 094306 (2013). doi:10.1103/PhysRevB.88.094306.  
URL <https://link.aps.org/doi/10.1103/PhysRevB.88.094306>
- J. H. Mentink, K. Balzer, and M. Eckstein. *Ultrafast and reversible control of the exchange interaction in Mott insulators*. Nature Communications **6**, 6708 (2015). doi:10.1038/

- ncomms7708.  
URL <http://dx.doi.org/10.1038/ncomms7708>
- N. Metropolis, A. Rosenbluth, M. Rosenbluth, A. Teller, and E. Teller. *Equation of State Calculations by Fast Computing Machines*. The Journal of Chemical Physics **21** (1953).  
URL <http://dx.doi.org/10.1063/1.1699114>
- W. Metzner and D. Vollhardt. *Correlated Lattice Fermions in  $d = \infty$  Dimensions*. Phys. Rev. Lett. **62**, 324 (1989). doi:10.1103/PhysRevLett.62.324.  
URL <https://link.aps.org/doi/10.1103/PhysRevLett.62.324>
- M. Mitrano, A. Cantaluppi, D. Nicoletti, S. Kaiser, A. Perucchi, S. Lupi, P. Di Pietro, D. Pontiroli, M. Riccò, S. R. Clark, D. Jaksch, and A. Cavalleri. *Possible light-induced superconductivity in  $K_3C_{60}$  at high temperature*. Nature **530**, 461 (2016). doi:10.1038/nature16522.  
URL <http://dx.doi.org/10.1038/nature16522>
- R. Modak and S. Mukerjee. *Finite size scaling in crossover among different random matrix ensembles in microscopic lattice models*. New J. Phys. **16**, 093016 (2014). doi:10.1088/1367-2630/16/9/093016.  
URL <https://doi.org/10.1088/1367-2630/16/9/093016>
- R. Modak, S. Mukerjee, and S. Ramaswamy. *Universal power law in crossover from integrability to quantum chaos*. Phys. Rev. B **90**, 075152 (2014). doi:10.1103/PhysRevB.90.075152.  
URL <https://link.aps.org/doi/10.1103/PhysRevB.90.075152>
- M. Moeckel and S. Kehrein. *Interaction Quench in the Hubbard Model*. Phys. Rev. Lett. **100**, 175702 (2008). doi:10.1103/PhysRevLett.100.175702.  
URL <https://link.aps.org/doi/10.1103/PhysRevLett.100.175702>
- M. Moeckel and S. Kehrein. *Real-time evolution for weak interaction quenches in quantum systems*. Annals of Physics **324**(10), 2146 (2009). doi:https://doi.org/10.1016/j.aop.2009.03.009.  
URL <http://www.sciencedirect.com/science/article/pii/S0003491609000712>
- M. Moeckel and S. Kehrein. *Crossover from adiabatic to sudden interaction quenches in the Hubbard model: prethermalization and non-equilibrium dynamics*. New Journal of Physics **12**(5), 055016 (2010).  
URL <http://stacks.iop.org/1367-2630/12/i=5/a=055016>
- R. Mondaini, K. R. Fratus, M. Srednicki, and M. Rigol. *Eigenstate thermalization in the two-dimensional transverse field Ising model*. Phys. Rev. E **93**, 032104 (2016). doi:10.1103/PhysRevE.93.032104.  
URL <https://link.aps.org/doi/10.1103/PhysRevE.93.032104>
- B. Neyenhuis, J. Smith, A. Lee, J. Zhang, P. Richerme, P. Hess, Z.-X. Gong, A. Gorshkov, and C. Monroe. *Observation of Prethermalization in Long-Range Interacting Spin Chains*.

- arXiv:1608.00681 (2016).  
URL <https://arxiv.org/abs/1608.00681>
- M. A. Nielsen and I. L. Chuang. *Quantum Computation and Quantum Information*. Cambridge University Press. Cambridge University Press (2010). doi:10.1017/CBO9780511976667.  
URL <https://doi.org/10.1017/CBO9780511976667>
- T. J. Park and J. C. Light. *Unitary quantum time evolution by iterative Lanczos reduction*. The Journal of Chemical Physics **85**(10), 5870 (1986). doi:10.1063/1.451548.  
URL <https://doi.org/10.1063/1.451548>
- R. Penrose. *Applications of Negative Dimensional Tensors*. In *Combinatorial Mathematics and its Applications*. Academic Press, Burlington (1971).
- A. Peres. *Stability of quantum motion in chaotic and regular systems*. Phys. Rev. A **30**, 1610 (1984). doi:10.1103/PhysRevA.30.1610.  
URL <https://link.aps.org/doi/10.1103/PhysRevA.30.1610>
- P. Pfeuty. *The one-dimensional Ising model with a transverse field*. Annals of Physics **57**(1), 79 (1970). doi:https://doi.org/10.1016/0003-4916(70)90270-8.  
URL <http://www.sciencedirect.com/science/article/pii/0003491670902708>
- A. Polkovnikov. *Phase space representation of quantum dynamics*. Annals of Physics **325**(8), 1790 (2010). doi:https://doi.org/10.1016/j.aop.2010.02.006.  
URL <http://www.sciencedirect.com/science/article/pii/S0003491610000382>
- F. Pollmann. *Efficient Numerical Simulations Using Matrix-Product States* (2016).  
URL [http://quantumtensor.pks.mpg.de/wp-content/uploads/2016/06/notes\\_1.pdf](http://quantumtensor.pks.mpg.de/wp-content/uploads/2016/06/notes_1.pdf)
- F. Pollmann, S. Mukerjee, A. G. Green, and J. E. Moore. *Dynamics after a sweep through a quantum critical point*. Phys. Rev. E **81**, 020101 (2010). doi:10.1103/PhysRevE.81.020101.  
URL <https://link.aps.org/doi/10.1103/PhysRevE.81.020101>
- D. Porras and J. I. Cirac. *Effective Quantum Spin Systems with Trapped Ions*. Phys. Rev. Lett. **92**, 207901 (2004). doi:10.1103/PhysRevLett.92.207901.  
URL <https://link.aps.org/doi/10.1103/PhysRevLett.92.207901>
- J. Preskill. *Lecture Notes for Physics 229: Quantum Information and Computation* (2016).  
URL <http://www.theory.caltech.edu/people/preskill/ph229/>
- P. Reimann. *Foundation of Statistical Mechanics under Experimentally Realistic Conditions*. Phys. Rev. Lett. **101**, 190403 (2008). doi:10.1103/PhysRevLett.101.190403.  
URL <https://link.aps.org/doi/10.1103/PhysRevLett.101.190403>
- P. Reimann. *Equilibration of isolated macroscopic quantum systems under experimentally realistic conditions*. Physica Scripta **86**(5), 058512 (2012).  
URL <http://stacks.iop.org/1402-4896/86/i=5/a=058512>

- W.-K. Rhim, A. Pines, and J. S. Waugh. *Time-Reversal Experiments in Dipolar-Coupled Spin Systems*. Phys. Rev. B **3**, 684 (1971). doi:10.1103/PhysRevB.3.684.  
URL <https://link.aps.org/doi/10.1103/PhysRevB.3.684>
- P. Richerme, Z.-X. Gong, A. Lee, C. Senko, J. Smith, M. Foss-Feig, S. Michalakis, A. V. Gorshkov, and C. Monroe. *Non-local propagation of correlations in quantum systems with long-range interactions*. Nature **511**, 198 (2014). doi:10.1038/nature13450.  
URL <http://dx.doi.org/10.1038/nature13450>
- A. Riera, C. Gogolin, and J. Eisert. *Thermalization in Nature and on a Quantum Computer*. Phys. Rev. Lett. **108**, 080402 (2012). doi:10.1103/PhysRevLett.108.080402.  
URL <https://link.aps.org/doi/10.1103/PhysRevLett.108.080402>
- M. Rigol, V. Dunjko, and M. Olshanii. *Thermalization and its mechanism for generic isolated quantum systems*. Nature **452**, 854 (2008). doi:10.1038/nature06838.  
URL <http://dx.doi.org/10.1038/nature06838>
- M. Rigol, V. Dunjko, V. Yurovsky, and M. Olshanii. *Relaxation in a Completely Integrable Many-Body Quantum System: An Ab Initio Study of the Dynamics of the Highly Excited States of 1D Lattice Hard-Core Bosons*. Phys. Rev. Lett. **98**, 050405 (2007). doi:10.1103/PhysRevLett.98.050405.  
URL <https://link.aps.org/doi/10.1103/PhysRevLett.98.050405>
- M. Rigol, A. Muramatsu, and M. Olshanii. *Hard-core bosons on optical superlattices: Dynamics and relaxation in the superfluid and insulating regimes*. Phys. Rev. A **74**, 053616 (2006). doi:10.1103/PhysRevA.74.053616.  
URL <https://link.aps.org/doi/10.1103/PhysRevA.74.053616>
- M. Rigol and L. F. Santos. *Quantum chaos and thermalization in gapped systems*. Phys. Rev. A **82**, 011604 (2010). doi:10.1103/PhysRevA.82.011604.  
URL <https://link.aps.org/doi/10.1103/PhysRevA.82.011604>
- Z. Rudnick. *What is Quantum Chaos*. Notices of the AMS **55**(1), 32 (2008).  
URL <http://www.math.tau.ac.il/~rudnick/papers/whatisQCfinal.pdf>
- S. Sachdev. *Quantum Phase Transitions*. Cambridge University Press, Cambridge (2011).
- A. W. Sandvik. *Computational Studies of Quantum Spin Systems*. AIP Conference Proceedings **1297**(1), 135 (2010). doi:10.1063/1.3518900.  
URL <http://aip.scitation.org/doi/abs/10.1063/1.3518900>
- L. F. Santos, F. Borgonovi, and F. M. Izrailev. *Chaos and Statistical Relaxation in Quantum Systems of Interacting Particles*. Phys. Rev. Lett. **108**, 094102 (2012). doi:10.1103/PhysRevLett.108.094102.  
URL <https://link.aps.org/doi/10.1103/PhysRevLett.108.094102>

- L. F. Santos and M. Rigol. *Onset of quantum chaos in one-dimensional bosonic and fermionic systems and its relation to thermalization*. Phys. Rev. E **81**, 036206 (2010). doi:10.1103/PhysRevE.81.036206.  
URL <https://link.aps.org/doi/10.1103/PhysRevE.81.036206>
- T. Scaffidi and E. Altman. *Semiclassical Theory of Many-Body Quantum Chaos and its Bound*. arXiv:1711.04768 (2017).  
URL <https://arxiv.org/abs/1711.04768>
- A. Schadschneider. *Cellular automata models of highway traffic*. Physica A: Statistical Mechanics and its Applications **372**(1), 142 (2006). doi:http://dx.doi.org/10.1016/j.physa.2006.05.011. Common Trends in Traffic Systems.  
URL <http://www.sciencedirect.com/science/article/pii/S0378437106005954>
- M. Schiró and M. Fabrizio. *Time-Dependent Mean Field Theory for Quench Dynamics in Correlated Electron Systems*. Phys. Rev. Lett. **105**, 076401 (2010). doi:10.1103/PhysRevLett.105.076401.  
URL <https://link.aps.org/doi/10.1103/PhysRevLett.105.076401>
- M. Schmitt and S. Kehrein. *Dynamical quantum phase transitions in the Kitaev honeycomb model*. Phys. Rev. B **92**, 075114 (2015). doi:10.1103/PhysRevB.92.075114.  
URL <https://link.aps.org/doi/10.1103/PhysRevB.92.075114>
- M. Schmitt and S. Kehrein. *Effective time reversal and echo dynamics in the transverse field Ising model*. EPL **115**(5), 50001 (2016).  
URL <http://iopscience.iop.org/article/10.1209/0295-5075/115/50001/meta;jsessionid=D18A178E31B34BA243B2502709197F2D.ip-10-40-2-120>
- M. Schmitt and P. Wang. *Universal nonanalytic behavior of the nonequilibrium Hall conductance in Floquet topological insulators*. Phys. Rev. B **96**, 054306 (2017). doi:10.1103/PhysRevB.96.054306.  
URL <https://link.aps.org/doi/10.1103/PhysRevB.96.054306>
- H. Schneider and H. Schmiedel. *Negative time development of a nuclear spin system*. Physics Letters A **30**(5), 298 (1969). doi:https://doi.org/10.1016/0375-9601(69)91005-6.  
URL <http://www.sciencedirect.com/science/article/pii/0375960169910056>
- U. Schollwöck. *The density-matrix renormalization group*. Rev. Mod. Phys. **77**, 259 (2005). doi:10.1103/RevModPhys.77.259.  
URL <https://link.aps.org/doi/10.1103/RevModPhys.77.259>
- U. Schollwöck. *The density-matrix renormalization group in the age of matrix product states*. Annals of Physics **326**(1), 96 (2011). doi:https://doi.org/10.1016/j.aop.2010.09.012. January 2011 Special Issue.  
URL <http://www.sciencedirect.com/science/article/pii/S0003491610001752>



- M. Schreiber, S. S. Hodgman, P. Bordia, H. P. Lüschen, M. H. Fischer, R. Vosk, E. Altman, U. Schneider, and I. Bloch. *Observation of many-body localization of interacting fermions in a quasirandom optical lattice*. *Science* **349**(6250), 842 (2015). doi:10.1126/science.aaa7432. URL <http://science.sciencemag.org/content/349/6250/842>
- B. Sciolla and G. Biroli. *Quantum Quenches and Off-Equilibrium Dynamical Transition in the Infinite-Dimensional Bose-Hubbard Model*. *Phys. Rev. Lett.* **105**, 220401 (2010). doi:10.1103/PhysRevLett.105.220401. URL <https://link.aps.org/doi/10.1103/PhysRevLett.105.220401>
- B. Sciolla and G. Biroli. *Quantum quenches, dynamical transitions, and off-equilibrium quantum criticality*. *Phys. Rev. B* **88**, 201110 (2013). doi:10.1103/PhysRevB.88.201110. URL <https://link.aps.org/doi/10.1103/PhysRevB.88.201110>
- M. Serbyn, Z. Papić, and D. A. Abanin. *Local Conservation Laws and the Structure of the Many-Body Localized States*. *Phys. Rev. Lett.* **111**, 127201 (2013). doi:10.1103/PhysRevLett.111.127201. URL <https://link.aps.org/doi/10.1103/PhysRevLett.111.127201>
- S. Shenker and D. Stanford. *Multiple shocks*. *Journal of High Energy Physics* **2014**(12), 46 (2014). doi:10.1007/JHEP12(2014)046. URL <https://link.springer.com/article/10.1007%2FJHEP12%282014%29046>
- J. F. Sherson, C. Weitenberg, M. Endres, M. Cheneau, I. Bloch, and S. Kuhr. *Single-atom-resolved fluorescence imaging of an atomic Mott insulator*. *Nature* **467**, 68 (2010). doi:10.1038/nature09378. URL <http://dx.doi.org/10.1038/nature09378>
- P. Smacchia, M. Knap, E. Demler, and A. Silva. *Exploring dynamical phase transitions and prethermalization with quantum noise of excitations*. *Phys. Rev. B* **91**, 205136 (2015). doi:10.1103/PhysRevB.91.205136. URL <https://link.aps.org/doi/10.1103/PhysRevB.91.205136>
- S. Sorella. *Wave function optimization in the variational Monte Carlo method*. *Phys. Rev. B* **71**, 241103 (2005). doi:10.1103/PhysRevB.71.241103. URL <https://link.aps.org/doi/10.1103/PhysRevB.71.241103>
- M. Srednicki. *Chaos and quantum thermalization*. *Phys. Rev. E* **50**, 888 (1994). doi:10.1103/PhysRevE.50.888. URL <https://link.aps.org/doi/10.1103/PhysRevE.50.888>
- M. Srednicki. *Thermal fluctuations in quantized chaotic systems*. *Journal of Physics A: Mathematical and General* **29**(4), L75 (1996). URL <http://stacks.iop.org/0305-4470/29/i=4/a=003>
- M. Srednicki. *The approach to thermal equilibrium in quantized chaotic systems*. *Journal of Physics A: Mathematical and General* **32**(7), 1163 (1999). URL <http://stacks.iop.org/0305-4470/32/i=7/a=007>

- H. Stanley. *Introduction to Phase Transitions and Critical Phenomena*. International Series of Monogr. Oxford University Press (1971).
- M. Stark and M. Kollar. *Thermalization rates in the one-dimensional Hubbard model with next-to-nearest neighbor hopping*. Kinetic description of thermalization dynamics in weakly interacting quantum systems (2013).  
URL <https://arxiv.org/abs/1308.1610>
- R. Steinigeweg, A. Khodja, H. Niemeyer, C. Gogolin, and J. Gemmer. *Pushing the Limits of the Eigenstate Thermalization Hypothesis towards Mesoscopic Quantum Systems*. Phys. Rev. Lett. **112**, 130403 (2014). doi:10.1103/PhysRevLett.112.130403.  
URL <https://link.aps.org/doi/10.1103/PhysRevLett.112.130403>
- S. H. Strogatz. *Nonlinear Dynamics and Chaos: With Applications to Physics, Biology, Chemistry, and Engineering*. Westview Press, Boulder, 2nd edition (2014).
- B. Swingle and D. Chowdhury. *Slow scrambling in disordered quantum systems*. Phys. Rev. B **95**, 060201 (2017). doi:10.1103/PhysRevB.95.060201.  
URL <https://link.aps.org/doi/10.1103/PhysRevB.95.060201>
- H. Tasaki. *The Hubbard model - an introduction and selected rigorous results*. Journal of Physics: Condensed Matter **10**(20), 4353 (1998).  
URL <http://stacks.iop.org/0953-8984/10/i=20/a=004>
- W. Thompson. *The kinetic theory of the dissipation of energy*. Proceedings of the Royal Society of Edinburgh **8**, 325 (1874).
- D. J. Thouless, M. Kohmoto, M. P. Nightingale, and M. den Nijs. *Quantized Hall Conductance in a Two-Dimensional Periodic Potential*. Phys. Rev. Lett. **49**, 405 (1982). doi:10.1103/PhysRevLett.49.405.  
URL <https://link.aps.org/doi/10.1103/PhysRevLett.49.405>
- N. Tsuji, M. Eckstein, and P. Werner. *Nonthermal Antiferromagnetic Order and Nonequilibrium Criticality in the Hubbard Model*. Phys. Rev. Lett. **110**, 136404 (2013). doi:10.1103/PhysRevLett.110.136404.  
URL <https://link.aps.org/doi/10.1103/PhysRevLett.110.136404>
- S. Vajna and B. Dóra. *Topological classification of dynamical phase transitions*. Phys. Rev. B **91**, 155127 (2015). doi:10.1103/PhysRevB.91.155127.  
URL <https://link.aps.org/doi/10.1103/PhysRevB.91.155127>
- R. van den Berg, B. Wouters, S. Eliëns, J. De Nardis, R. M. Konik, and J.-S. Caux. *Separation of Time Scales in a Quantum Newton's Cradle*. Phys. Rev. Lett. **116**, 225302 (2016). doi:10.1103/PhysRevLett.116.225302.  
URL <https://link.aps.org/doi/10.1103/PhysRevLett.116.225302>



- F. Verstraete and J. I. Cirac. *Matrix product states represent ground states faithfully*. Phys. Rev. B **73**, 094423 (2006). doi:10.1103/PhysRevB.73.094423.  
URL <https://link.aps.org/doi/10.1103/PhysRevB.73.094423>
- L. Vidmar and M. Rigol. *Generalized Gibbs ensemble in integrable lattice models*. Journal of Statistical Mechanics: Theory and Experiment **2016**(6), 064007 (2016).  
URL <http://stacks.iop.org/1742-5468/2016/i=6/a=064007>
- S. Vogelgesang, G. Storeck, J. G. Horstmann, T. Diekmann, M. Siviş, S. Schramm, K. Rossnagel, S. Schäfer, and C. Ropers. *Phase ordering of charge density waves traced by ultrafast low-energy electron diffraction*. Nature Physics (2017). doi:10.1038/nphys4309.  
URL <http://dx.doi.org/10.1038/nphys4309>
- D. Vollhardt. *Dynamical mean-field theory for correlated electrons*. Annalen der Physik **524**(1), 1 (2012). doi:10.1002/andp.201100250.  
URL <http://dx.doi.org/10.1002/andp.201100250>
- J. von Delft and H. Schoeller. *Bosonization for beginners — refermionization for experts*. Annalen der Physik **7**(4), 225 (1998). doi:10.1002/(SICI)1521-3889(199811)7:4<225::AID-ANDP225>3.0.CO;2-L.  
URL [http://dx.doi.org/10.1002/\(SICI\)1521-3889\(199811\)7:4<225::AID-ANDP225>3.0.CO;2-L](http://dx.doi.org/10.1002/(SICI)1521-3889(199811)7:4<225::AID-ANDP225>3.0.CO;2-L)
- K. von Klitzing, G. Dorda, and M. Pepper. *New Method for High-Accuracy Determination of the Fine-Structure Constant Based on Quantized Hall Resistance*. Phys. Rev. Lett. **45**, 494 (1980). doi:10.1103/PhysRevLett.45.494.  
URL <https://link.aps.org/doi/10.1103/PhysRevLett.45.494>
- J. von Neumann. *Proof of the Quasi-Ergodic Hypothesis*. PNAS **18**(1), 70 (1932). doi:10.1073/pnas.18.1.70.  
URL <http://www.pnas.org/content/18/1/70.extract>
- R. Vosk and E. Altman. *Dynamical Quantum Phase Transitions in Random Spin Chains*. Phys. Rev. Lett. **112**, 217204 (2014). doi:10.1103/PhysRevLett.112.217204.  
URL <https://link.aps.org/doi/10.1103/PhysRevLett.112.217204>
- B. Žunkovič, M. Heyl, M. Knap, and A. Silva. *Dynamical Quantum Phase Transitions in Spin Chains with Long-Range Interactions: Merging different concepts of non-equilibrium criticality*. arxiv:1609.08482 (2016).  
URL <https://arxiv.org/abs/1609.08482>
- P. Wang and S. Kehrein. *Phase transitions in the diagonal ensemble of two-band Chern insulators*. New Journal of Physics **18**(5), 053003 (2016).  
URL <http://stacks.iop.org/1367-2630/18/i=5/a=053003>
- P. Wang, M. Schmitt, and S. Kehrein. *Universal nonanalytic behavior of the Hall conductance in a Chern insulator at the topologically driven nonequilibrium phase transition*. Phys. Rev.

- B **93**, 085134 (2016). doi:10.1103/PhysRevB.93.085134.  
 URL <https://link.aps.org/doi/10.1103/PhysRevB.93.085134>
- P. Wang and G. Xianlong. *Connecting dynamical quantum phase transitions and topological steady-state transitions by tuning the energy gap*. arxiv:1707.02509 (2017).  
 URL <https://arxiv.org/abs/1707.02509>
- C. Weitenberg, M. Endres, J. F. Sherson, M. Cheneau, P. Schausz, T. Fukuhara, I. Bloch, and S. Kuhr. *Single-spin addressing in an atomic Mott insulator*. Nature **471**, 319 (2011).  
 doi:10.1038/nature09827.  
 URL <http://dx.doi.org/10.1038/nature09827>
- X.-G. Wen. *Topological Order: From Long-Range Entangled Quantum Matter to a Unified Origin of Light and Electrons*. ISRN Condensed Matter Physics (2013). doi:10.1155/2013/198710.  
 URL <http://dx.doi.org/10.1155/2013/198710>
- J. Wettlaufer. *The universe in a cup of coffee*. Physics Today **64**(5), 66 (2011). doi:  
<http://dx.doi.org/10.1063/1.3592018>.  
 URL <http://physicstoday.scitation.org/doi/10.1063/1.3592018>
- S. R. White. *Density matrix formulation for quantum renormalization groups*. Phys. Rev. Lett. **69**, 2863 (1992). doi:10.1103/PhysRevLett.69.2863.  
 URL <https://link.aps.org/doi/10.1103/PhysRevLett.69.2863>
- E. Wigner. *On the Quantum Correction For Thermodynamic Equilibrium*. Phys. Rev. **40**, 749 (1932). doi:10.1103/PhysRev.40.749.  
 URL <https://link.aps.org/doi/10.1103/PhysRev.40.749>
- E. P. Wigner. *Characteristic Vectors of Bordered Matrices With Infinite Dimensions*. Annals of Mathematics **62**(3), 548 (1955).  
 URL <http://www.jstor.org/stable/1970079>
- E. P. Wigner. *Characteristics Vectors of Bordered Matrices with Infinite Dimensions II*. Annals of Mathematics **65**(2), 203 (1957).  
 URL <http://www.jstor.org/stable/1969956>
- E. P. Wigner. *On the Distribution of the Roots of Certain Symmetric Matrices*. Annals of Mathematics **67**(2), 325 (1958).  
 URL <http://www.jstor.org/stable/1970008>
- K. G. Wilson. *The renormalization group: Critical phenomena and the Kondo problem*. Rev. Mod. Phys. **47**, 773 (1975). doi:10.1103/RevModPhys.47.773.  
 URL <https://link.aps.org/doi/10.1103/RevModPhys.47.773>
- D. Wintgen and H. Friedrich. *Classical and quantum-mechanical transition between regularity and irregularity in a Hamiltonian system*. Phys. Rev. A **35**, 1464 (1987). doi:10.1103/

PhysRevA.35.1464.

URL <https://link.aps.org/doi/10.1103/PhysRevA.35.1464>

C. N. Yang and T. D. Lee. *Statistical Theory of Equations of State and Phase Transitions. I. Theory of Condensation*. Phys. Rev. **87**, 404 (1952). doi:10.1103/PhysRev.87.404.

URL <http://link.aps.org/doi/10.1103/PhysRev.87.404>

E. A. Yuzbashyan, O. Tsypliyatyev, and B. L. Altshuler. *Relaxation and Persistent Oscillations of the Order Parameter in Fermionic Condensates*. Phys. Rev. Lett. **96**, 097005 (2006). doi:10.1103/PhysRevLett.96.097005.

URL <https://link.aps.org/doi/10.1103/PhysRevLett.96.097005>

J. Zhang, P. W. Hess, A. Kyprianidis, P. Becker, A. Lee, J. Smith, G. Pagano, I.-D. Potirniche, A. C. Potter, A. Vishwanath, N. Y. Yao, and C. Monroe. *Observation of a discrete time crystal*. Nature **543**, 217 (2017). doi:10.1038/nature21413.

URL <http://dx.doi.org/10.1038/nature21413>

A. A. Zvyagin. *Dynamical quantum phase transitions (Review Article)*. Low Temperature Physics **42**(11), 971 (2016). doi:10.1063/1.4969869.

URL <http://dx.doi.org/10.1063/1.4969869>

# Acknowledgments

First of all, I would like to thank my supervisor Prof. Stefan Kehrein, who supported my scientific development throughout the past years in many ways. He taught me a lot about physics and scientific conduct and he was a reliable guide whenever I couldn't see the wood for the trees. I enjoyed very much the freedom to explore diverse physical issues and I am very grateful for the encouragement to make new scientific contacts, not least by generously supported participation in many conferences, workshops, and schools. I would also like to thank my co-supervisor Prof. Reiner Kree for interesting comments and for assuming the duties as Second Referee.

Large parts of this thesis would not exist without my collaborators. First of all I would like to thank Markus Heyl for many inspiring discussions about physics and also for advice and support regarding my scientific career. I am grateful to Prof. Pei Wang for fruitful exchange and his hospitality during my visit in China. Furthermore, it was a pleasure to work with Prof. Anatoli Polkovnikov, Dries Sels, and Shainen Davidson.

At the institute all members of the CMT groups contributed to a pleasant atmosphere. In particular, I would like to thank Nils Abelung, who was good company as office mate and on all the journeys; due to our local rainforest rearing program we can for sure declare our dissertations carbon-neutral with a clear conscience. I am grateful to Salvatore Manmana, who always had an open ear for physical and administrative issues. Thomas Köhler was a reliable aide, who did not even flinch from the nastiest computer problems. And of course thanks to all the others for many interesting seminars, discussions, and group outings: Fabian Biebl, Lorenzo Cevolani, Davide Fioretto, Kristof Harms, Ingo Homrighausen, Ebad Kamil, Manuel Kreye, Benjamin Lenz, Mariya Medvedyeva, Johannes Oberreuter, Sebastian Paeckel, Oskar Schnaack, Florian Sohn, and Alexander Tiegel. Special thanks to Frau Schubert, who managed the most confusing travel expense reports with great patience.

Finally, it remains to thank those people, whose support was less professional, but who were of great help in the endeavor to maintain mental sanity, while spending large fractions of the working hours searching minus signs and factors of two. First of all thanks to Merle, who is my greatest backing. Thanks for a lot of patience when physics occupied me also after hours and thanks for sharing frustration and joy as it occurred in the course of my PhD. Many thanks also to all friends for good times and distraction; in particular, it was an honor to be member of the Theoretikerstammtisch – although its main purpose was of course not leisure, but to contemplate the most fundamental questions of theoretical physics. Thanks to Thomas, Tobi, and Burkhard, who, moreover, excelled as legal scholars, flatmates, and house mathematicians. Last but not least, I am glad that I could always rely on the backing by my parents.

# Curriculum vitae

## Markus Schmitt

Nationality: German

**PhD student.** Georg-August-Universität Göttingen, *date of thesis defense: Jan 11, 2018*  
Title of the project: *Dynamics of isolated quantum many-body systems far from equilibrium*  
(Supervisor: Prof. Dr. S. Kehrein)

## Academic education

- 2014 **M. Sc. in Physics** Georg-August-Universität Göttingen  
Thesis: *Dynamical Quantum Phase Transitions in the Kitaev Honeycomb Model*  
(Supervisor: Prof. Dr. S. Kehrein)
- 2013 **M. Sc. in High Performance Computing** University of Edinburgh  
Thesis: *Diagrammatic determinantal quantum Monte Carlo calculations on GPUs*  
(Supervisors: I. Bethune and Prof. Dr. T. Pruschke)
- 2012 **B. Sc. in Physics** Georg-August-Universität Göttingen  
Thesis: *Quantum dynamics of the Bose-Hubbard model on a fully connected lattice*  
(Supervisor: Prof. Dr. S. Kehrein)

## Publications & Preprints

- (1) **M. Schmitt** and S. Kehrein, *Dynamical Quantum Phase Transitions in the Kitaev Honeycomb Model*, [Phys. Rev. B \*\*92\*\* 075114 \(2015\)](#)
- (2) P. Wang, **M. Schmitt**, and S. Kehrein, *Universal nonanalytic behavior of the Hall conductance in a Chern insulator at the topologically driven nonequilibrium phase transition*, [Phys. Rev. B \*\*93\*\* 085134 \(2016\)](#)
- (3) **M. Schmitt** and S. Kehrein, *Effective time reversal and echo dynamics in the transverse field Ising model*, [EPL \*\*115\*\* 50001 \(2016\)](#)
- (4) **M. Schmitt** and P. Wang, *Universal non-analytic behavior of the non-equilibrium Hall conductance in Floquet topological insulators*, [Phys. Rev. B \*\*96\*\*, 054306 \(2017\)](#)
- (5) **M. Schmitt** and M. Heyl, *Quantum dynamics in transverse-field Ising models from classical networks*, [arXiv:1707.06656](#)
- (6) **M. Schmitt** and S. Kehrein, *Irreversible dynamics in quantum many-body systems*, [arXiv:1711.00015](#)